



HAL
open science

Scale-up of gas-liquid agitated bioreactors Three-dimensional modeling of hydrodynamics, mass transfer and kinetics

Vincenzo Cappello

► **To cite this version:**

Vincenzo Cappello. Scale-up of gas-liquid agitated bioreactors Three-dimensional modeling of hydrodynamics, mass transfer and kinetics. Chemical and Process Engineering. Université Clermont Auvergne [2017-2020], 2020. English. NNT : 2020CLFAC040 . tel-03159254

HAL Id: tel-03159254

<https://theses.hal.science/tel-03159254>

Submitted on 4 Mar 2021

HAL is a multi-disciplinary open access archive for the deposit and dissemination of scientific research documents, whether they are published or not. The documents may come from teaching and research institutions in France or abroad, or from public or private research centers.

L'archive ouverte pluridisciplinaire **HAL**, est destinée au dépôt et à la diffusion de documents scientifiques de niveau recherche, publiés ou non, émanant des établissements d'enseignement et de recherche français ou étrangers, des laboratoires publics ou privés.



Université Clermont-Auvergne

École Doctorale Sciences Pour l'Ingénieur

Thèse de doctorat

**Extrapolation des réacteurs agités
gaz-liquide par modélisation tridimensionnelle
de l'hydrodynamique, transferts et cinétique**

Vincenzo Cappello

Spécialité de doctorat : Génie des Procédés

Soutenue publiquement le 17 Juin 2020

Membres du jury :

Mme. Caroline Gentric, Professeur, GEPEA, Université de Nantes	<i>Rapporteur</i>
Mme. Giuseppina Montante, Professeur, Université de Bologne	<i>Rapporteur</i>
M. Arnaud Cockx, Professeur, INSA Toulouse	<i>Examineur</i>
Mme. Cécile Plais, Dr., Ingénieur de recherche, IFPEN, Lyon	<i>Encadrant de thèse</i>
M. Frédéric Augier, Dr., Ingénieur de recherche, HDR, IFPEN, Lyon	<i>Co-directeur de thèse</i>
M. Christophe Vial, Professeur, Université Clermont Auvergne	<i>Directeur de thèse</i>

Résumé

Dans le cadre de la production de bio-carburants, les fermenteurs agités aérés sont utilisés la culture de micro-organismes car ils permettent d'assurer un bon transfert d'oxygène entre gaz et liquide, tout en homogénéisant de manière efficace la concentration en substrats. Dans le cas de la production d'enzyme par le champignon filamenteux *Trichoderma reesei* (une étape clef de la production d'éthanol 2G), le transfert d'oxygène est dégradé par la rhéologie non-newtonienne du moût fermentaire. Par ailleurs, les volumes fermentaires nécessaires aux futures unités de production de bioéthanol sont tellement élevés, de l'ordre de plusieurs centaines de m³ ou plus, que l'homogénéité des substrats n'est plus assurée.

Dans ce contexte, la finalité des travaux présentés était de développer un outil de prédiction de performances et d'extrapolation des fermenteurs aérés, basé sur la mécanique des fluides numériques (ou CFD : Computational Fluid Dynamics), et permettant de coupler l'hydrodynamique, la rhéologie, le transfert de matière ainsi que le métabolisme simplifié des microorganismes. Pour arriver à cela, plusieurs étapes expérimentales ont été préalablement menées.

Les tailles de bulles présentes dans divers milieux (filtrat fermentaire, milieux modèles) ont été caractérisées à l'aide d'une technique de sonde optique développée à IFPEN lors de travaux antérieurs, mais encore jamais appliquée aux milieux non-newtoniens. Ces mesures inédites de tailles de bulles ont été complétées par la caractérisation du transfert gaz/liquide ($k_L a$) dans chaque système étudié, et la combinaison des différents résultats a permis de développer un modèle de coefficient de transfert (k_L) à implémenter dans le modèle CFD. Par ailleurs, des caractérisations hydrodynamiques de type Temps de mélange (par colorimétrie et traitement d'image) et Vélométrie (par tube de Pavlov) ont été menées dans les milieux visqueux aérés pour valider les simulations hydrodynamiques.

Le modèle développé, basé sur une approche diphasique Eulérienne, et une description moyennée des champs de vitesse (approche dite RANS : Reynolds Averaged Navier-Stokes équations) est utilisé pour illustrer la dégradation du mélange lors de l'extrapolation de la production d'enzymes. Ce phénomène se traduit par l'apparition de gradients de concentrations en substrats (sucres, oxygène dissous). Les résultats issus du modèle seront utilisés pour guider les futurs développements technologiques de fermenteurs, ainsi que pour mener des cultures biologiques représentatives de type scale-down, en fermenteurs multi-zones. Les simulations numériques et les expériences de scale-down permettront d'évaluer la résistance des microorganismes aux gradients de concentrations en substrats subis dans les fermenteurs industriels.

Mots clefs: transfert gaz-liquide, fermenteurs aérés, CFD, fluides non-newtoniens, taille de bulles.

Abstract

Mechanically-agitated reactors are widely used in aerobic fermentation, because they provide good mixing of reactants and high performance in terms of oxygen mass transfer. In the enzyme production process by filamentous fungi *Trichoderma reesei*, the mass transfer is hindered by the complex rheology of the fermentation broth. This process is a key step in the production of second-generation ethanol; however, because of the high fermentation volumes ($\sim 100\text{m}^3$) required for future bioethanol production units, the reactor scale-up is challenging. In fact, by increasing the size of the fermenter, large scale substrate gradients tend to appear.

In this framework, the objective of this study is to develop a predictive tool based on Computational Fluid Dynamics (CFD) for the design and scale-up of aerated reactors. The numerical model here proposed, allows one to characterize such systems by coupling hydrodynamics, rheology, mass transfer, and a simplified metabolic model. To assess the fidelity of the model, several experimental analyses were carried out. Bubble size in shear-thinning liquids and in fermentation broth was measured thanks to a novel techniques that was previously developed at IFPEN. This measuring technique is based on phase-detective optical probes, and its use in stirred tank reactors and in viscous liquids was validated during this study. Bubble size measurements were supplemented with gas-liquid transfer coefficient ($k_L a$) and gas holdup measurements. By combining these data, it was possible to develop a dimensional model for the liquid-side mass transfer coefficient (k_L), that served to model the mass transfer mechanism in the CFD simulations.

Moreover, the reactor hydrodynamics was characterized in terms of mixing time (via colorimetric method and image processing), and liquid velocity (with the Pavlov tube). These data were then used to quantify the accuracy of the simulations. The numerical model — based on the two-phase Eulerian model, and on Reynolds-averaged Navier-Stokes equations — was used to highlight the mixing degradation that accompanies the scale-up of the protein production process. Results from coupled simulations (distribution of substrate and oxygen concentrations) will be used to guide future design and technology optimization of fermenters, as well as to develop more representative scale-down models for microbial cultures. CFD simulations and scale-down data will assess the microorganisms' resistance to exposure to substrate content variation inside industrial reactors.

Key words: gas-liquid mass transfer, aerobic fermenter, CFD, non-Newtonian fluid, bubble size.

Contents

Résumé	i
Abstract	ii
1 Introduction	1
1.1 Production of biofuels and challenges to the replacement of fossil fuels	1
1.2 Biofuels	2
1.3 Production process of second-generation bioethanol	4
1.3.1 Production of cellulase from <i>Trichoderma reesei</i> : IFPEN procedure	8
1.4 Objectives of the research	9
1.5 Structure of this manuscript	12
2 Theoretical aspects of agitated reactors	13
2.1 Introduction	13
2.2 Hydrodynamics of aerated stirred tanks	14
2.2.1 Gas flow patterns	18
2.3 Key aspects of mass transfer	22
2.3.1 Mass transfer coefficient	22
2.4 Bubble size in aerated stirred tanks	26
2.5 Mixing time calculation in agitated tanks	32
2.6 Scale-up of bioreactors	34
2.7 Numerical simulations of stirred tanks	36
2.7.1 Governing equations and multiphase modeling	39

2.7.2	Turbulence modeling	39
2.7.3	Viscosity for non-Newtonian liquids	43
2.7.4	Multiphase modeling	44
2.7.5	Use of CFD in bioreactors simulations	49
2.7.6	Scale-down models from CFD	52
2.8	Conclusions	54
3	Experimental setup	55
3.1	The stirred tanks	56
3.2	Model fluids	57
3.3	Bubble size measurement	59
3.4	Gas holdup	62
3.5	Volumetric mass transfer coefficient	62
3.6	Mixing time	63
3.7	Liquid velocity	65
4	Experimental results	69
4.1	Validation of the optical probe measurement	70
4.2	Spatial distribution of gas holdup and bubble size and effect of the tank size	71
4.3	Effect of rheology and additives on bubble size and mass transfer	71
4.3.1	Sauter mean diameter	72
4.3.2	Gas holdup	79
4.3.3	Volumetric mass transfer coefficient	80
4.3.4	Liquid-side mass transfer coefficient	81
4.4	Mixing time measurement	87
4.5	Liquid velocity measurement	89
4.6	Conclusions	93
5	Validation of multiphase CFD models	95
5.1	Numerical setup	96
5.1.1	Solver configuration	96

5.1.2	Computational grid and boundary conditions	97
5.2	Un aerated tank simulations	98
5.2.1	Mesh sensitivity	98
5.2.2	Rheology modeling: definition of shear rate	102
5.2.3	Mixing time in ungassed reactor: rheology effect	104
5.3	Air-water simulations	107
5.3.1	Drag model screening for the air-water case	107
5.3.2	Mixing in air-water: effect of gas rate and tank scale	112
5.4	Multiphase simulations of non-Newtonian liquids	116
5.4.1	Drag models for shear-thinning liquids	116
5.4.2	Hydrodynamics in air-xanthan cases	117
5.5	Conclusions	119
6	Applications to bioreactors	121
6.1	Prediction of mass transfer coefficient	121
6.2	CFD analysis of <i>Trichoderma reesei</i> fermentation	125
6.2.1	Coupling of hydrodynamics and bio-kinetics	128
6.2.2	Influence of hydrodynamics on substrate distribution	131
6.3	Conclusions	147
	General conclusions and perspectives	149
	Nomenclature	155
	References	159
	List of publications	174
	Acknowledgments	176

List of Figures

1.1	Production of ethanol and biodiesel (Mtoe) for countries in 2016 and 2006. Extracted from BP (2017).	2
1.2	Production of bioethanol from biomass. Comparison between first and second generation process. From Brandt et al. (2013).	4
1.3	Structure of the cell walls of a lignocellulosic plant (Brandt et al., 2013).	5
1.4	Morphological structures of filamentous fungi (Amanullah et al., 2000).	7
1.5	Lateral and top view of the impeller developed to measure the viscosity of filamentous suspensions (Hardy et al., 2015).	7
1.6	Evolution of the concentration of strain in the fermentative broth over time (1) and of apparent viscosity (at $\dot{\gamma} = 220 \text{ s}^{-1}$) as a function of the strain concentration (2) (Hardy et al., 2015).	8
1.7	Logic chart showing the physical models necessary to characterize a bioreactor. The main experimental data used for the validation of the model are listed as well.	11
2.1	Typical configuration of an aerated stirred tank, with description of the main elements. Meaning of initials: D_T , tank diameter; H_L , liquid height; D_S , impeller diameter; C_i , impeller clearance; D_S , sparger diameter; S_S , distance between the sparger and impeller; L_B, W_B , blade length and width; W_{BF} , baffle width; C_{BF} , baffle distance from vessel's walls. Image adapted from Doran (2013).	15
2.2	Power number as a function of Reynolds number for seven types of impellers. From Paul et al. (2004)	18
2.3	Flow regimes transition for a standard geometry; from left to right: (a) flooding, (b) loading, and (c) fully dispersed regimes. Diagram extracted from Doran (2013).	19

2.4	Flow map for a single Rushton turbine. (1) below minimum dispersion speed; (2) vortex cavities, no recirculation; (3) vortex cavities with recirculation; (4) flooded; (5) loaded with large cavities; (6) large cavities with recirculation. Extracted from Paul et al. (2004).	20
2.5	Evolution at increasing gas flow rate F_g of gas cavity structure behind the blades of a Rushton turbine. Original image from Nienow (1998), adapted by Doran (2013).	21
2.6	Representation of two-film theory of Lewis-Whitman.	23
2.7	Eddy-bubble interactions: (a) interaction with several eddies, (b) interaction with the outer edge of an eddy, (c) transport within a big eddy, (d) collision with opposite eddies.	28
2.8	Liquid film drainage between two colliding bubbles and subsequent coalescence (Martín et al. 2010).	29
2.9	Main classification of multiphase flow: separated flow (left) and dispersed flow (right) (Andersson et al., 2011).	44
2.10	CFD analysis of <i>Saccharomyces cerevisiae</i> fermentation. (a) Distribution of substrate uptake; (b) from the top: signal of specific substrate uptake, regimes series, and regimes transition patterns. Images from Haringa et al. (2016).	51
2.11	Scale-down configurations to recreate dissolved oxygen heterogeneities. Figure from Paul et al. (2004).	53
3.1	Geometrical details of the tank.	57
3.2	Detail of the moving trail support that was mounted in the tank T_{60}	58
3.3	Detail of the optical probe and its plastic protection (left) and shape of the signal when a bubble is detected by the sensor (right).	59
3.4	Locations investigated with the optical probes inside the tanks T_{60} (a) and T_{30} (b). In the small tank, the point II was also used for mass transfer coefficient measurement.	61
3.5	Frames acquired in water (left) and in a solution of CMC 0.50% (right) at the same operating conditions. Only bubbles with a sharp outline were measured.	62
3.6	Mask creation for image treatment from the first frame of the video (a). The software registered pixels' brightness in each of the white zones (b).	64
3.7	Log variance versus time plot. The horizontal line represents a level of mixedness of 95%.	65

3.8	Working scheme of the two-dimensional Pavlov tube.	66
3.9	Detail of the measuring tip of the Pavlov tube.	66
3.10	Quantification of vibrations. In black continuous line, the instantaneous velocity, whereas the mean value is represented with the white dashed line.	67
4.1	Mean Sauter diameter measured with the optical probe and from image analysis. Data refers to: water (\circ), CMC 0.25% and 0.50% (\diamond), $\pm 12\%$ (----), parity line (—).	70
4.2	Sauter mean diameter in mm and gas holdup (in brackets) in the large tank. Data were collected for $N = 8.3 \text{ s}^{-1}$ and for $U_g = 8 \text{ mm s}^{-1}$ (a) and $U_g = 20 \text{ mm s}^{-1}$ (b). The probe locations are also indicated.	72
4.3	Sauter mean diameter at several superficial gas velocities in: tap water (\circ), demineralized water (\triangle), XG 0.25% (\square) and XG 0.50% (\diamond).	73
4.4	Effect of additives on the bubble Sauter mean diameter. Data collected at several superficial gas velocities in: broth (\circ), water + ethanol (\square), broth + XG 0.50% (\diamond), XG 0.50% + ethanol (\triangle), and XG 0.25% + ethanol (\times).	74
4.5	Presence of microbubbles in aerated broth.	75
4.6	Comparison between different correlations to measure the mean bubble size. This work: water (\circ), XG (\square); Bhavaraju et al. (1978): water (\diamond), XG (\triangle); Alves et al. (2002): water (\times); $\pm 10\%$ (----), parity line (—).	76
4.7	Effect of HFBII concentration on the Sauter mean bubble diameter for $N = 11.7 \text{ s}^{-1}$. Water (\bullet), filtered broth (\blacksquare), water + HFBII 1 mg L^{-1} (\diamond), water + HFBII 5 mg L^{-1} (\triangle), water + HFBII 20 mg L^{-1} (\times), water + HFBII 50 mg L^{-1} (∇).	77
4.8	Foam stability over time for <i>Trichoderma reesei</i> sample (—), water + HFBII (----), and water + BSA (---).	78
4.9	Effect of BSA concentration on the Sauter mean bubble diameter for $N = 11.7 \text{ s}^{-1}$. Water (\bullet), filtered (\blacksquare), water + BSA 25 mg L^{-1} (\diamond), water + BSA 50 mg L^{-1} (\triangle).	78
4.10	Global gas holdup at different superficial gas velocities measured in: tap water (\circ), demineralized water (\triangle), XG 0.25% (\square), and XG 0.50% (\diamond).	80
4.11	Global gas holdup at different superficial gas velocities in: broth (\circ), water + ethanol (\square), broth + XG 0.50% (\diamond), XG 0.50% + ethanol (\triangle), and XG 0.25% + ethanol (\times).	81

4.12	Influence of dissipated power and gas flow rate on the volumetric mass transfer coefficient. Data obtained in: tap water (\circ), demineralized water (\triangle), water + ethanol (\oplus), XG 0.25% (\square), XG 0.25% + ethanol (\times), XG 0.50% (\diamond), and XG 0.50% + ethanol (+).	82
4.13	Liquid-side mass transfer coefficient as a function of the dissipated power (a) and the apparent viscosity (b). Data obtained in: water (\circ), water + ethanol (\triangle), XG 0.25% (\square), XG 0.25% + ethanol (\times), XG 0.50% (\diamond), and XG 0.50% + ethanol (+). For every fluid, error bars ($\pm 16\%$) around the mean value are also reported.	83
4.14	Liquid-side mass transfer coefficient at different gas velocities. Data for: water (\circ), XG 0.25% (\square), XG 0.50% (\diamond), Equation (4.5) (—), Kawase et al. (1992) (----), Calderbank & Moo-Young (1961) (---).	84
4.15	Comparison between different correlations to estimate the oxygen transfer rate. Equation (4.5) (\circ), Kawase et al. (1992) (\square), Calderbank & Moo-Young (1961) (\diamond), $\pm 10\%$ (----), parity line (—).	86
4.16	Predicted volumetric coefficient versus experimental values. Values obtained in this thesis were integrated by measurements with different impeller configurations and fluids reported in Gabelle (2012). Symbols: k_{La} (\circ), parity line (—).	87
4.17	Image sequence of the mixing phenomenon in water captured by the camera, from the initial time at which the tracer is being injected (a) to the complete mixing of the tracer (d).	88
4.18	Mixing time calculated inside T_{30} for water and 0.25% xanthan gum, at different gas flow rates. Without aeration: water (\circ), XG 0.25% (\blacktriangle); $U_g = 8 \text{ mm s}^{-1}$: water (\square), XG 0.25% (+); $U_g = 40 \text{ mm s}^{-1}$: water (\diamond), XG 0.50% (\times).	88
4.19	Impeller discharge profile of the radial component in water for $N = 1.3 \text{ s}^{-1}$. Holes diameter: 0.5 mm (\bullet), 1.0 mm (\blacksquare), Venneker et al. (2010) (—).	89
4.20	Radial profile of the mean velocities in water at the impeller disk level. Normalized radial velocity: experimental (\circ), Venneker et al. (2010) (—); normalized axial velocity: experimental (\square), Venneker et al. (2010) (----).	90
4.21	Impeller discharge profile of the radial component in water at different rotation speed. 2.5 s^{-1} (\circ), 5.0 s^{-1} (\square), 5.8 s^{-1} (\diamond), Venneker et al. (2010) (—).	91
4.22	Influence of the gas dispersion on radial velocity at the impeller discharge region in water, for $N = 5.8 \text{ s}^{-1}$. Single phase flow (\circ), $U_g = 1 \text{ mm s}^{-1}$ (\square), $U_g = 4 \text{ mm s}^{-1}$ (\diamond), Venneker et al. (2010) (—), Rousar & Van den Akker (1994) ($U_g = 1 \text{ mm s}^{-1}$) (----), Rousar & Van den Akker (1994) ($U_g = 4 \text{ mm s}^{-1}$) (---).	92

4.23	Effect of viscosity on radial velocity in gassed conditions at $N = 5.8 \text{ s}^{-1}$. Without gas: water (●), XG 0.1% (■), Venneker et al. (2010) (—); $U_g = 4 \text{ mm s}^{-1}$: water (○), XG 0.1% (□), Rousar & Van den Akker (1994) (----).	92
5.1	View of the mesh #2 (see table 5.1) used in most part of the simulations. Refinement of the mesh in the rotating zone and along the sparger walls can be noticed. The MRF volume is also highlighted.	97
5.2	Impeller power number computed with different grids and definitions. Symbols: N_{P_r} 1 st order (○), N_{P_ε} 1 st order (□), N_{P_r} 2 nd order (●), N_{P_ε} 2 nd order (■), Bujalski et al. (—).	99
5.3	Effect of mesh resolution on normalized velocity profiles in T_{60} at $N = 8.33 \text{ s}^{-1}$ ($Re = 3 \cdot 10^5$). Radial profiles at the impeller disk height of: axial velocity (a), radial velocity (b), tangential velocity (c); radial velocity along the impeller blade (d). Legend: mesh 1 (○), mesh 2 (□), mesh 3 (◇), mesh 4 (△), Venneker et al. (2010) (—), experimental (▼).	101
5.4	Gas cavity structures in T_{30} at $U_g = 8 \text{ mm s}^{-1}$ and $N = 13.3 \text{ s}^{-1}$ by using MRF (a) and SM models (b). A sixth of the domain was simulated in the case of the MRF approach; to facilitate the comparison, the partial geometry was repeated in post-processing to represent the full tank.	102
5.5	Apparent and turbulent viscosity for XG 0.25% at $N = 5 \text{ s}^{-1}$ computed with different shear rate models: from velocity gradients (a) and from turbulent dissipation rate (b).	104
5.6	CFD mixing time in T_{60} without aeration. Data: water (○), XG 0.25% (□), XG 0.50% (◇), Grenville (—), Grenville & Nienow (XG 0.25%) (----), Grenville & Nienow (XG 0.50%) (----).	106
5.7	Gas volume fraction in the plane between the baffle and the periodic plane at $N = 8.3 \text{ s}^{-1}$ and $U_g = 8 \text{ mm s}^{-1}$. The contours were obtained by using: universal drag law (a), Grace (b), and Scargiali et al. (c). Vectors of air velocity in standard reference of frame are also represented.	109
5.8	Gas volume fraction at the impeller height. The contours were obtained at $N = 8.3 \text{ s}^{-1}$ and $U_g = 8 \text{ mm s}^{-1}$ by using: universal drag laws (a), Grace (b), and Scargiali et al. (2007) (c).	110

5.9	CFD and experimental gas fraction in water at $N = 8.3 \text{ s}^{-1}$ and $U_g = 8 \text{ mm s}^{-1}$; data were taken in T_{60} at different heights: impeller height (a), 200 mm (b) and 350 mm above the impeller disk (c). Symbols: experimental (●), Grace (○), Scargiali et al. (2007) (□), universal (◇).	111
5.10	Contours of gas fraction in the VC regime based on CFD simulation (a) and measured by Bombač et al. (1997) (b).	112
5.11	Numerical and measured gas holdup against superficial gas velocity for two tanks with different diameters. T_{30} , $N = 13.3 \text{ s}^{-1}$: CFD (●), experimental (○); T_{60} , $N = 8.3 \text{ s}^{-1}$: CFD (■), experimental (□).	113
5.12	Relative power demand for two tank diameters at several gas velocities. CFD data: T_{30} , $N = 13.3 \text{ s}^{-1}$ (○), T_{60} , $N = 8.3 \text{ s}^{-1}$ (□); Eq. (2.17): T_{30} (—), T_{60} (----).	113
5.13	Isosurface of gas fraction at $U_g = 1 \text{ mm s}^{-1}$ (a) and $U_g = 4 \text{ mm s}^{-1}$ (b) in the tank T_{60} at $N = 8.3 \text{ s}^{-1}$	114
5.14	Regime flow map for T_{60} cases already reported in figure 5.12 (□). Expected cavity shapes (vortex cavity, VC; larger cavity, LC) are highlighted, as well as the transitions from flooding to loading (—), and from partial to fully recirculated regime (----).	114
5.15	Profile of radial velocity for T_{60} at the impeller tip in air-water system at $N = 5.8 \text{ s}^{-1}$. Experimental data: $U_g = 0$ (○), $U_g = 1 \text{ mm s}^{-1}$ (□), $U_g = 4 \text{ mm s}^{-1}$ (◇); simulation: $U_g = 0$ (—), $U_g = 1 \text{ mm s}^{-1}$ (----), $U_g = 4 \text{ mm s}^{-1}$ (---).	115
5.16	Effect of turbulent Schmidt number on computed mixing time for T_{30} at $U_g = 8 \text{ mm s}^{-1}$. Comparison with experimental data in T_{30} (Section 4.4). Symbols: experimental (●), $Sc_t = 0.7$ (□), $Sc_t = 0.1$ (◇).	116
5.17	Contour of gas volume fraction in XG 0.50% at $U_g = 8 \text{ mm s}^{-1}$	117
5.18	Numerical and measured gas holdup in XG against superficial gas velocity for T_{30} at $N = 13.3 \text{ s}^{-1}$. XG 0.25%: CFD (○), experimental (●); XG 0.50%: CFD (□), experimental (■).	118
5.19	Relative power demand in T_{30} at $N = 13.3 \text{ s}^{-1}$ for XG solutions. XG 0.25% (○), XG 0.50% (□), Eq. (2.17) (—).	118
5.20	Mixing time in XG 0.25% at $U_g = 8 \text{ mm s}^{-1}$ with different Schmidt numbers. Experimental (●), $Sc = 0.7$ (□), $Sc = 0.2$ (◇), $Sc = 0.1$ (○).	119
6.1	Average mass transfer coefficient in water at several operating conditions. Data are reported for CFD (dark bar) and experiments (light bar). For the experimental results, $\pm 20\%$ error bar is displayed.	122

6.2	Average mass transfer coefficient in solutions of xanthan gum 0.25% (a) and 0.50% (b) at several operating conditions. Data are reported for CFD (dark bar) and experiments (light bar). For the experimental results, $\pm 20\%$ error bar is displayed.	123
6.3	Contours of gas fraction in xanthan gum 0.50% at $N = 13.3 \text{ s}^{-1}$ and $U_g = 40 \text{ mm s}^{-1}$	124
6.4	Influence of the substrate concentration on the specific production rate q_P (—) and specific growth rate μ_X (----) at $C_{O_2} = 0.008 \text{ g L}^{-1}$	126
6.5	Concentration of species over time during lab-scale fermentation of <i>Trichoderma reesei</i> . The fed-batch started after 30 h, at a constant $Q_{feed} = 0.03 \text{ gs/gX/h}$. Experimental concentrations: biomass (\circ), protein (\square); model: biomass (—), protein (----), substrate (----).	127
6.6	Rheology of fermentative broth at different biomass concentrations and during the growth phase (a) and the production phase (b). Data: $C_X = 10 \text{ g L}^{-1}$ (\circ), $C_X = 20 \text{ g L}^{-1}$ (\square), $C_X = 30 \text{ g L}^{-1}$ (\diamond), xanthan gum 0.25% (—), and xanthan gum 0.50% (----).	128
6.7	Scheme of the reactor with four Rushton turbines. On the right, details on the mesh used to model a sixth section of the tank.	130
6.8	Contours of gas fraction in water in the VC regime based on CFD simulation for T_{30} (a) and for 1B (b). In order to compare the different cases, the same Froude and Flow numbers were considered.	130
6.9	Substrate concentration distribution for the cases 1S (a) and 1B (b). A broader distribution of substrate was obtained in the big tank, which led to formation of a low-productivity area under the impeller (d).	132
6.10	Substrate distribution (a) for the cases 1S (dark area) and 1B (empty area). In the graph at the bottom, q_P^* (—) and μ^* (----) are represented.	134
6.11	Density distribution of normalized production rate. The area in black represents the data for the small tank, whereas data for the big tank are represented by the empty area.	134
6.12	Species concentrations, normalized production and growth rates for the 4R.	136
6.13	Substrate distribution for the configuration 4R (a). At the bottom, q_P^* (—) and μ^* (----) are reported.	137
6.14	Density distribution of the normalized production rate. The dark area represents data for 1S, while the empty area is used for 1B.	137

6.15 Substrate concentration at q_{feed}^{II} (a) and at q_{feed}^{III} (c). From the darker to the white area, data refer to 1S, 1B, and 4R, respectively; q_P^* (—) and μ^* (----) are also reported (b,d). 138

6.16 q_P^* at q_{feed}^{II} (a) and at q_{feed}^{III} (b) is represented for cases 1S (black area), 1B (gray area with horizontal lines), and 4R (empty area). 138

6.17 Substrate distribution (a) in the configurations 1S (dark area) and 4R (empty area). At the bottom, q_P^* (—) and μ^* (----) are represented. 139

6.18 Density distributions of normalized production rate (a) and growth rate (b). Areas filled in black refer to 1S, whereas the empty areas represent data for 4R. . 140

6.19 Isovalues contours of species concentrations, q_P^* , and μ^* for 4R case. 141

6.20 Nutrients concentration (a,b) and normalized production (c) and growth (d) rates for the case q_{feed}^{IV} . CFD and perfect-mixing values are reported in white and gray, respectively. The hatched bars represent estimated values at $k_L a = 200 \text{ h}^{-1}$ 142

6.21 Substrate (a) and dissolved oxygen distributions (b) for the case at $C_X = 20 \text{ g L}^{-1}$ (empty area) and at $C_X = 30 \text{ g L}^{-1}$ (dark area). 143

6.22 Density distribution of normalized production rate. The area in black represents the data at $C_X = 30 \text{ g L}^{-1}$, whereas data at $C_X = 20 \text{ g L}^{-1}$ are represented by the empty area. 144

6.23 Isovalues contours of species concentrations, q_P^* , and μ^* at $C_X = 30 \text{ g L}^{-1}$ 145

List of Tables

1.1	Fractional content of cellulose, hemicellulose and lignin in different lignocellulosic biomasses. The missing fraction is due to residual extractives (e.g. waxes and lipids) and ash. Extracted from Bajpai (2016).	4
2.1	Power numbers of various impellers under turbulent conditions (Nienow, 1998). .	18
2.2	Dimensionless equations for $k_L a$	27
2.3	Bubble size measurements in stirred tank.	30
2.4	Summary of some researches about gas-liquid simulations published in the last decade.	38
2.5	Common variables used for determination of the turbulence length scale.	42
3.1	Characteristic dimensions of the tanks.	56
3.2	Rheological indexes for xanthan gum and carboxymethyl cellulose for the different concentrations. Both of the polymers were provided by <i>Sigma-Aldrich</i> , USA.	58
4.1	Regression coefficients for Eq. (4.1). For viscosity calculation, average shear rate was computed with Metzner & Otto (1957)'s equation.	84
4.2	Regression coefficients for Eq. (4.1) based on Pérez et al. (2006)'s correlation for average shear rate.	87
4.3	Summary of operating conditions for the experimental measurements.	93
5.1	Cell numbers of the numerical grids used in this study.	98
5.2	Effect of geometry and rotation model on some global quantities.	101

5.3	CFD average and maximum shear rates in s^{-1} for XG 0.25% at $N = 5 s^{-1}$. Values predicted with correlations in the literature are reported, as well as the apparent viscosity ($kg m^{-1} s^{-1}$) calculated respect to the average shear rate. . . .	103
5.4	Characteristic data in multiphase simulations of T_{60} at $N = 8.3 s^{-1}$, obtained with different drag coefficients. For each variable, relative errors respect to experimental data are reported in brackets.	110
6.1	Kinetics constants used in Equations (6.7) and (6.8).	127
6.2	Tank configurations used with the fermentation model.	129
6.3	Operating conditions and timescales for mixing, mass transfer, and substrate consumption in different configurations at $C_X = 20 g L^{-1}$. For confidentiality reasons, only an interval of the feed rates $q_{feed}/(g_S/g_X/h)$ was reported.	131
6.4	Average concentrations and kinetic rates for the simulations discussed in the chapter.	146

Chapter 1

Introduction

1.1 Production of biofuels and challenges to the replacement of fossil fuels

The increasing energy demand makes it necessary to find more sustainable alternatives to become independent from oil, coal and gas. Fuels derived from biomass are good candidates and can reduce the utilization of fossil fuels and so decrease the CO₂ production. In 2016, the global biofuel production was equal to 82.3 Mtoe¹, representing ca. 20% of the annual energy generated by renewable sources and accounting for about 4% of the global road transport fuel (IEA, 2017). The International Energy Agency (IEA) forecasted a continuous increase in the production of fuel from biomass feedstock that will account for up to 20% of the world transportation fuel by 2040 (IEA, 2014). According to the BP statistical review of World energy (BP, 2017), the major production of biofuel in 2017 was due to American countries, with a 45% share for North America and 27% for Central and South America. In these countries, the processes are mainly based on the production of ethanol, while in Europe and especially in Indonesia the production of biodiesel gives the main contribution to the total production of biofuels (figure 1.1). At the end of the 2016, ca. 12.3 Mtoe (15%) were produced in Europe, with Germany (3.9%), France (2.7%) and the Netherlands (2.0%) as the most productive countries.

The recent directives fixed the targets for the next few years in terms of production of biofuels and integration in the market of transportation fuels. For example, with the Energy Independence and Security Act of 2007, the US Government aims to increase the ethanol production to 36 billion of gallons annually by 2022. In Europe, the energy policy is established by the RED II (Renewable Energy Directive II); this directive replaced the previous RED

¹Tonne of oil equivalent (toe) is a unit of energy, defined as the energy that can be produced by 1 t of crude oil, approximately equal to 42 GJ. In accordance with international conventions, one toe is equivalent to 954 kg of gasoline.

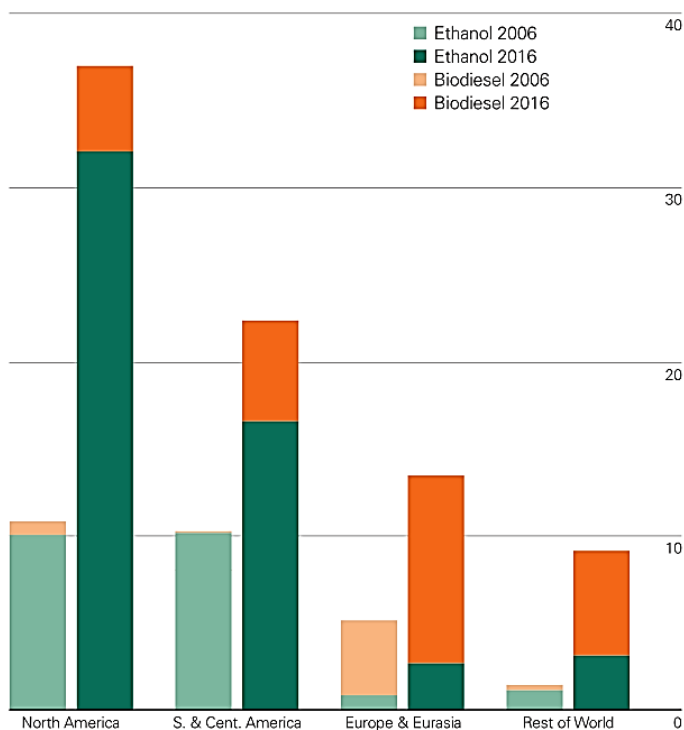


Figure 1.1: Production of ethanol and biodiesel (Mtoe) for countries in 2016 and 2006. Extracted from BP (2017).

(published in 2014) at the end of 2016, in order to live up to the commitments made by the EU countries during the UN climate change conference (COP 21) that was held in Paris in 2015. With the RED II, the European Commission purposes to build a collaboration network between the participant countries in order to fulfill the energy targets: by 2030, renewable energies will have to supply 27% of the total energy demand, with a share of 10% in transport fuels in all the EU countries. In this context, biofuels are then key element for achieving the international energy objectives.

1.2 Biofuels

The feedstocks used in the biofuel industry are very diversified, including edible plants and agricultural wastes as well. Depending on the nature of the raw materials, biofuels are generally classified in:

- First-generation biofuels, obtained from sugars, starch and triglycerides
- Second-generation biofuels, mainly derived from lignocellulosic materials

- Third-generation biofuels, that are algal-based fuels

For the last decades, first-generation biofuels have dominated the renewable fuels market, with more mature processing technologies, especially regarding the production of corn and sugar based ethanol (Azadi et al., 2017; Joshi et al., 2017). Bioethanol is produced by alcoholic fermentation of simple sugars, i.e. monosaccharides with low number of carbon atoms. These molecules can be directly obtained from sugar cane and byproduct of the sugar industry or from different amylaceous cereals, like wheat and corn. The conversion of starch contained in these cereals into glucose is made by means of an enzymatic saccharification. The main drawback in the bioethanol industry is the utilization of resources that would be destined to meet the food demand. In the last years, many researches have been addressed to quantify the role of first generation biofuels' production in the gradually increasing world commodity food prices (Sims et al., 2010). Problems regarding the transportation of the biomass are also present.

In this scenario, the ethico-economical dilemma of biofuel production based on edible crops can be solved by switching the production to second-generation biofuels, which have gained growing interest as a potential substitute to oil-derived fuels. Among the non-food competing biomasses, lignocellulosic materials are the most abundant renewable resource in the planet, with a homogenous distribution and easy availability all over the world (Bhutto et al., 2017). This feedstock comprises agricultural residues and byproducts, like cereal straw, forestry wastes, bagasse, and dedicated short rotation energy crops. Regarding energy crops, they still compete with food crops in terms of water and resources, but they are characterized by a higher energy field potential (defined in GJ ha^{-1}) and they can allow exploiting poor-quality lands. Furthermore, by displacing oil-based energy, second-generation bioethanol can drastically reduce the greenhouse gas (GHG) emissions: in their simulation, the United States Department of Energy (DOE) showed that corn ethanol reduces GHG emissions by 18% to 28% on a per-gallon basis in comparison to gasoline, while cellulosic ethanol offers an 87% reduction, reaching almost the 100% in the case if part of the biofuel so produced is used to provide the energy necessary in the plant site itself.

However, the production of more sustainable biofuels is still economically challenging. In fact, the production technology of cellulosic biofuels is complex, so capital costs are higher compared to the investment for a first-generation plant; in fact, while the capital cost for a corn-based plant is around 0.53 \$/l, the average investment for a cellulosic ethanol plant is almost seven-fold (Lynd et al., 2017). The fall of oil prices that had started in mid-2014 reached its low in 2016 (ca. 30 \$/barrel), hampering the investments in research and development of more cost-effective production plants of advanced biofuels (i.e. second- and third-generation biofuels). Nevertheless, countries keep investing on advanced biofuels because of their potential and importance in the world energy framework.

1.3 Production process of second-generation bioethanol

Fermentable sugars can be also produced from the enzymatic hydrolysis of lignocellulosic plants; the ethanol so-produced belongs to the biofuels of second generation. With respect to a first-generation plant, the production of cellulosic bioethanol is more complex because fermentable sugars contained in the vegetable matrix are less available in the case of woody biomass; a pretreatment is then necessary to achieve high production yield. In figure 1.2, the main steps that lead to bioethanol from different kind of biomass are illustrated. The different technologies differ for the upstream processes, which depend on the biomass.

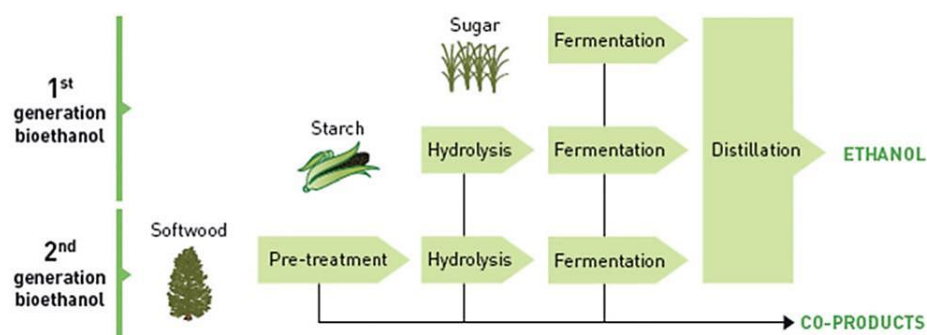


Figure 1.2: Production of bioethanol from biomass. Comparison between first and second generation process. From Brandt et al. (2013).

Pretreatments are necessary because of the different structure of lignocellulosic materials. The main components of this feedstock are: the cellulose, the hemicellulose and the lignin. These macromolecules constitute the cell wall of arboreal plants (figure 1.3) and their proportion can vary depending on the kind of biomass that is converted. As an example, the typical composition of some plants is presented in table 1.1.

Table 1.1: Fractional content of cellulose, hemicellulose and lignin in different lignocellulosic biomasses. The missing fraction is due to residual extractives (e.g. waxes and lipids) and ash. Extracted from Bajpai (2016).

Biomass	Cellulose	Hemicellulose	Lignin
Hardwoods	40–55	24–40	18–25
Softwoods	45–50	25–35	25–35
Wheat straw	30	50	15
Corn cobs	45	35	15
Grasses	25–40	35–50	10–30
Switchgrass	45	30	12

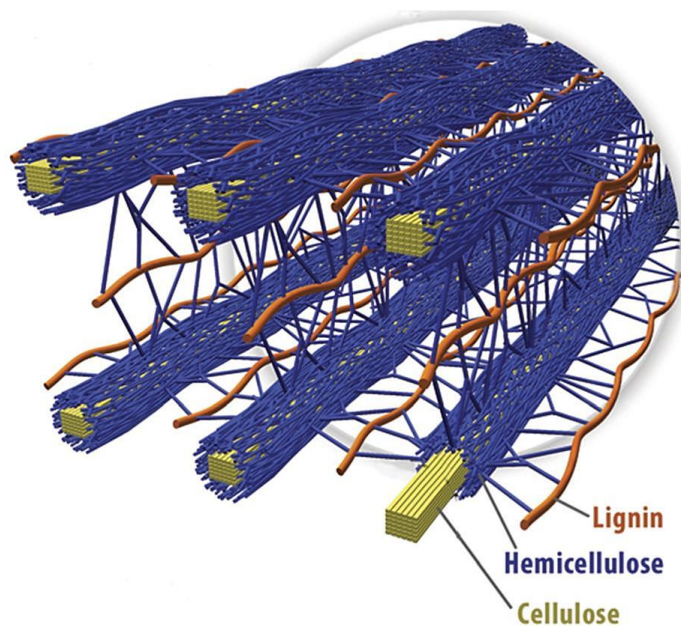


Figure 1.3: Structure of the cell walls of a lignocellulosic plant (Brandt et al., 2013).

Cellulose is a polymer of single beta-D-glucopyranose (i.e. glucose) units linked via β -(1,4) glycosidic bonds. Hydrogen bonds and van der Waals interactions between the different polymeric chains characterize the structure of the cellulose, which was proved being characterized by polymorphism. Crystalline form is the most present but amorphous arrangements are of vital importance because are more vulnerable to hydrolysis. The pretreatment prior to the saccharification process facilitates the hydrolysis of the cellulose and hemicellulose fractions by reducing the crystallinity of the cellulose and increasing the specific surface area. Several pretreatments exist, like biological, mechanical, chemical and physic-chemical processes, each one with its advantages and drawbacks. More information about the most recent pretreatment processes and their impact on the production of second-generation bioethanol can be found in the review of Bhutto et al. (2017).

Hemicellulose is a polymeric carbohydrate as well and it represents the second abundant substance in the plant fiber. It is made of five carbon atoms (xylose, arabinose) and six carbon atoms (galactose, glucose, mannose) carbohydrates. Hemicellulose has a lower polymerization degree than cellulose and it also shows a greater tendency to depolymerization due to its amorphous structure Brandt et al. (2013).

Lignin is an aromatic polymer and it provides rigid structure and protection to the plant from external factors. It presents a wide chemical composition depending on the kind of plant and also on which part of the plant is being considered. Lignin has a negative effect on the

efficiency of the entire process. In fact, it makes harder to extract the sugars from the cellulose and hemicellulose fractions and the phenolic monomers that are formed during the pretreatment act as inhibitors during the enzymatic fermentation (Chaabane & Marchal, 2013; Hardy, 2016). However, the ligninic fraction can be valorized and used as a fuel onsite.

The hydrolysis of cellulose is catalyzed by enzymes generically called cellulases, which are produced by many microorganisms in nature. However, the industrial production of cellulases is based on filamentous fungi, that are characterized by a high potential secretion of cellulolytic enzymes. *Aspergillus*, *Penicillium* and *Trichoderma* are the main genera used in the industrial production of bioethanol. Among these fungi, *Trichoderma reesei* is the species that has been employed the most (Gusakov, 2011). From the enzymatic saccharification simple sugars with six and five atoms of carbons are produced; among these, glucose represents the most abundant carbohydrate. Eventually, the last step of the process involves the purification of the ethanol so-produced by means of distillation.

Decreasing the production cost of the bioethanol is a key aspect. The main costs are due to the pretreatment of the lignocellulosic biomass and to the enzymatic hydrolysis (Lynd et al., 2017), so recent researches have been addressed to improve these steps of the process. The cost of cellulases represents a main fraction of the overall production cost of cellulosic ethanol, ranging from 10% to 30% depending on the production technology. An integrated production of the cellulase can decrease the cost per gallon up to 20% (Johnson, 2016). The enzymes' cost can be lowered by improving the activity of the enzyme cocktails — so less amount of cellulase per liter of ethanol is required — and/or by an optimization of the large-scale process. The latter approach requires a better understanding of the phenomena involved during the aerobic fermentation of the fungi, which leads to reliable scaling up procedures of the cellulase production process. However, this is not easy because of the complexity of the fermentation broth, which is linked to its rheology.

Filamentous organisms like *Trichoderma reesei* grow as filamentous macrostructure called hyphae (or mycelium). Two different morphological forms can be found: dispersed and pelleted, as shown in figure 1.4 (Amanullah et al., 2000; Paul & Thomas, 1998). The onset of one form with respect to the other depends on the fermentation time and the broth conditions. In general *Trichoderma reesei* is encountered in its dispersed form (Hardy, 2016).

The study of the morphology of a fermentative broth and its link between the conditions established inside the reactor is vital to assure the maximum growth of the microorganisms. In fact, the concentration of the biomass and the spatial arrangement of the mycelia is bonded with the rheology of the broth, which changes during the growth phase. The knowledge of the viscosity values during the fermentation is necessary to develop a scale-up procedure for aerated reactor. Hardy et al. (2015) developed specific tools to characterize the rheological

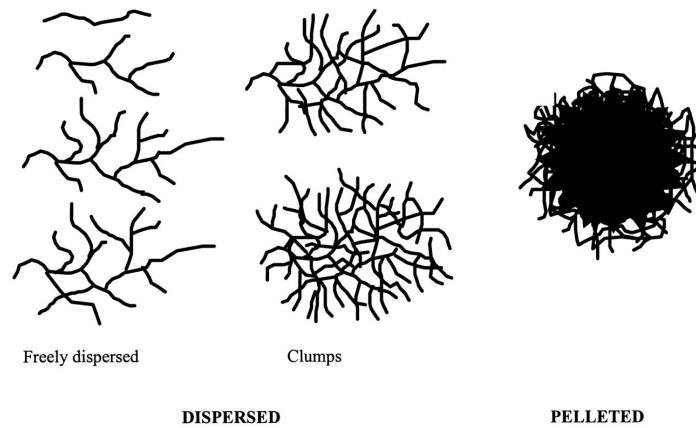


Figure 1.4: Morphological structures of filamentous fungi (Amanullah et al., 2000).

behavior of an industrial strain of *Trichoderma reesei*. To avoid the measurement bias due to a rearrangement of the filamentous structures, they devised a new impeller for a rotational rheometer. Figure 1.5 displays the ribbon helical propeller used in the study. Thanks to this new device, it was possible to better define the rheology of a suspension of *Trichoderma reesei*. Their main experimental results are summarized in figure 1.6.

It can be seen that during the fermentation, the media became more viscous with two different trends. First, an almost linear relationship exists between viscosity and concentration of the strain. At higher cell concentration, the viscosity exhibits a power relationship with the concentration. The first behavior can be attributed to interactions between the biomass

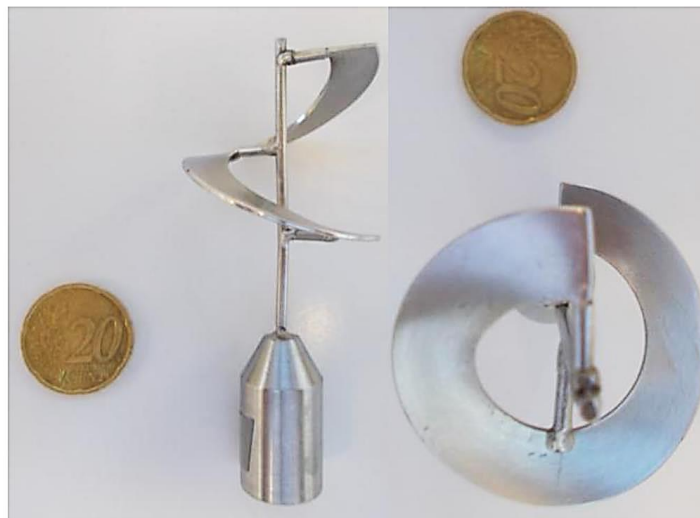


Figure 1.5: Lateral and top view of the impeller developed to measure the viscosity of filamentous suspensions (Hardy et al., 2015).

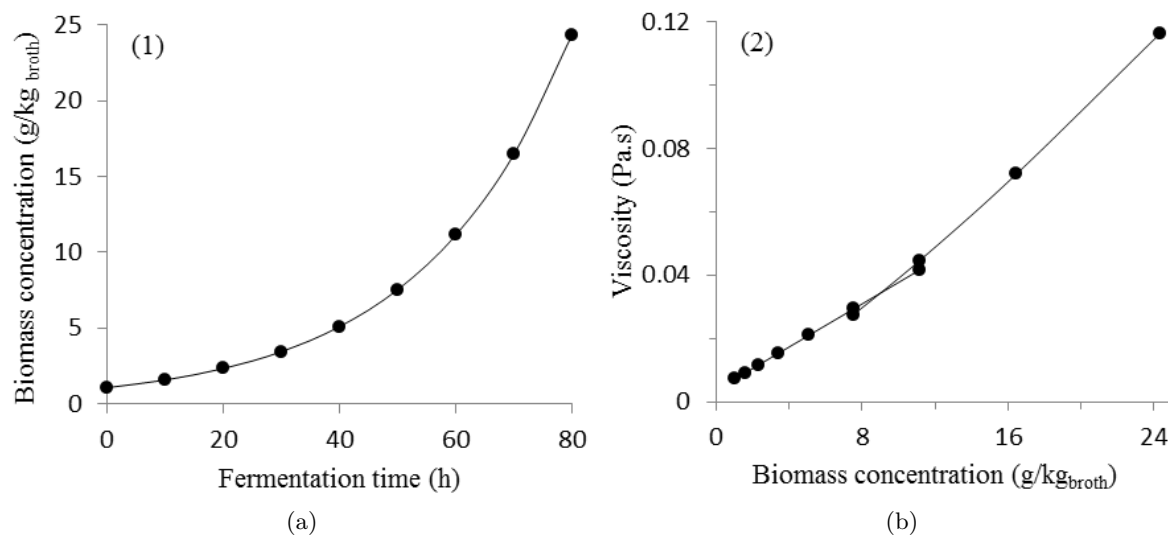


Figure 1.6: Evolution of the concentration of strain in the fermentative broth over time (1) and of apparent viscosity (at $\dot{\gamma} = 220 \text{ s}^{-1}$) as a function of the strain concentration (2) (Hardy et al., 2015).

particles and the culture broth. However, at concentration higher than 7 g kg^{-1} , the viscosity is more influenced by the quantity of biomass formed and interactions within the micela become more important (Hardy et al., 2015).

1.3.1 Production of cellulase from *Trichoderma reesei*: IFPEN procedure

IFPEN has developed an efficient dual-step process to produce cellulase from *Trichoderma reesei*. In the first phase, the growth of the cultured strain is carried out inside a batch reactor, where it is inoculated with an excess of nutrients. The substrate consists of glucose and/or steep corn liquor (Li et al., 2016). During the growing phase, the concentration of substrate decreases while the concentration of the mycotic biomass increases, reaching its maximum concentration ($15\text{--}40 \text{ g L}^{-1}$). Usually, this reaction takes place in a series of agitated reactors of increasing size. This phase is crucial to reach the maximum concentration of the microorganisms, but it is technologically challenging, because it is necessary to deal with the rise in viscosity during the growth of *Trichoderma reesei*, which is a strongly aerobic species. Therefore, it needs a constant supply of oxygen to grow. During the fermentation, the viscosity changes with the concentration, increasing oxygen demand while hindering the mass transfer.

The second step occurs in a fed-batch fermenter with a limiting concentration of substrates. Lactose is supplied at low and constant rate to induce the production of enzymes. The fermentative process is then followed by a filtration to recover the cellulase and the fungi. Both steps take place inside aerated stirred tank reactors, previously sterilized and equipped with

temperature control systems, in order to keep the temperature between 27–30 °C. Ammonia is used to alkalize the system and the pH is maintained in the optimum range 4–5. To prevent foaming during the fermentation, antifoams are added in the nutrients, which are mainly used in liquor form. More information about operating conditions and kinetics of the fermentation of different *Trichoderma* strains can be found in the thesis of Hardy (2016).

1.4 Objectives of the research

The production of fuels from ethical biomass has not reached yet the technological maturity to replace completely oil-based fuels. As presented in the previous paragraph, the process is challenging primarily because of the characteristics of the biomass. The need for pretreatments and enzymes to extract the fermentable sugars encumbers the commercialization of high-productivity ethanol plants. One of the routes for decreasing the total production cost goes through the pursuit of a more efficient process to produce the enzymes for the hydrolysis of the biomass. The expected result is to have, for large-scale reactors, the same yield that characterizes the study at the lab-scale. However, the scale-up of a bioprocess is not a straightforward procedure because of the complexity of the fermentative system, whose properties also vary in time.

In the case of *Trichoderma reesei*, for example, during the fermentation the rheology of the fluid changes and so the transport properties. The increase in viscosity during the growth of the microorganisms hinders the mass transfer, causing a decrease of the oxygen dissolved in the liquid with the consequent decay of the growth conditions of the fungi which, it is worth recalling, metabolize in aerobic conditions. Moreover, the shear-thinning behavior of the suspension can introduce heterogeneities because of the spatial distribution of shear rates, resulting in the development of strong concentration gradients of both the oxygen and the substrate. The existence of these heterogeneities can then lead to the formation of dead zones, which are parts of volume where no reaction occurs. This is a main problem recurring in the scale-up of a reactor because with the rise in size, difficulties to maintain the optimal conditions for the fermentation increase too (i.e. good gas dispersion inside the volume and the maintenance of acceptable shear stress).

The final goal of this research is to investigate fluid dynamics and mass transfer in non-Newtonian fluids in mechanically agitated reactors operating at industrial conditions (i.e. turbulent regime and high superficial gas velocity) and to develop a numerical model for the scale-up of bioreactors. The CFD software ANSYS Fluent was used throughout the work to perform the simulation of the system. However, the physical models upon which the simulation is based on needed to be validated, and this was done by comparing the CFD results with experimental data and empirical correlations. Unfortunately, when it comes to describe the

mixing of a fluid with complex rheology, literature data are not as available as those for simpler water-like systems.

This study can be placed inside a wide framework composed by other recent PhD theses, that have contributed to investigate some of the key aspects of the problem here delineated. In particular, the following aspects were studied during previous doctoral theses at IFPEN:

- Gabelle (2012) characterized the global characteristics of a fermenter in terms of mass transfer coefficient and mixing time, providing correlations for $K_L a$ and the power consumption in aerated conditions;
- The kinetics of the production of cellulase by *Trichoderma reesei* was modeled by Jourdier (2012);
- Alméras (2014) studied the scalar mixing in bubble columns, deriving a model for the turbulent dispersion in bubbly flows; Raimundo (2015) for measurements in bubble columns is used here to estimate the bubble size in stirred tank and non-Newtonian liquids;
- Hardy (2016) discussed the effect of shear on the cells, providing important information for the scale-up of *Trichoderma reesei* fermentation process;
- Gemello (2018) worked on bubble column reactors and his study on the population balance could be adapted also to describe the bubble size distribution inside a stirred tank;
- Roque (2020 forthcoming) will study the sensitivity of *Trichoderma reesei* metabolism to heterogeneities that are commonly found in large scale reactor.

Figure 1.7 shows all the elements that are needed in order to model an aerated fermenter, in terms of physical models and validation data. A comprehensive model requires the description of hydrodynamics, mass transport, and metabolic kinetics of the fermentative reaction; the CFD code is then used to numerically solve the resulting transport equations. As pointed out above, some models have been already developed: rheological behaviors of *Trichoderma reesei* strain (Hardy, 2016), kinetic model of the production of cellulase (Hardy, 2016; Jourdier, 2012), drag law in gas/liquid flow at high gas concentration (Raimundo, 2015), dispersion of a scalar in heterogeneous bubbly flow (Alméras et al., 2016).

What is missing is a model for the drag law and the mass transfer rate (K_L) in shear-thinning liquids, as well as experimental data on bubble size. To obtain these properties, measurements of bubble size have to be done; furthermore, these measurements have to take into account the effect of rheology and high gas flow rate. The CFD model is meant to describe the turbulent flow of a fluid with a complex rheological behavior, so the turbulence model with a non-Newtonian fluid needs to be validated as well. Fundamentally, the development of a robust model goes through the coupling of mass transfer and hydrodynamics.

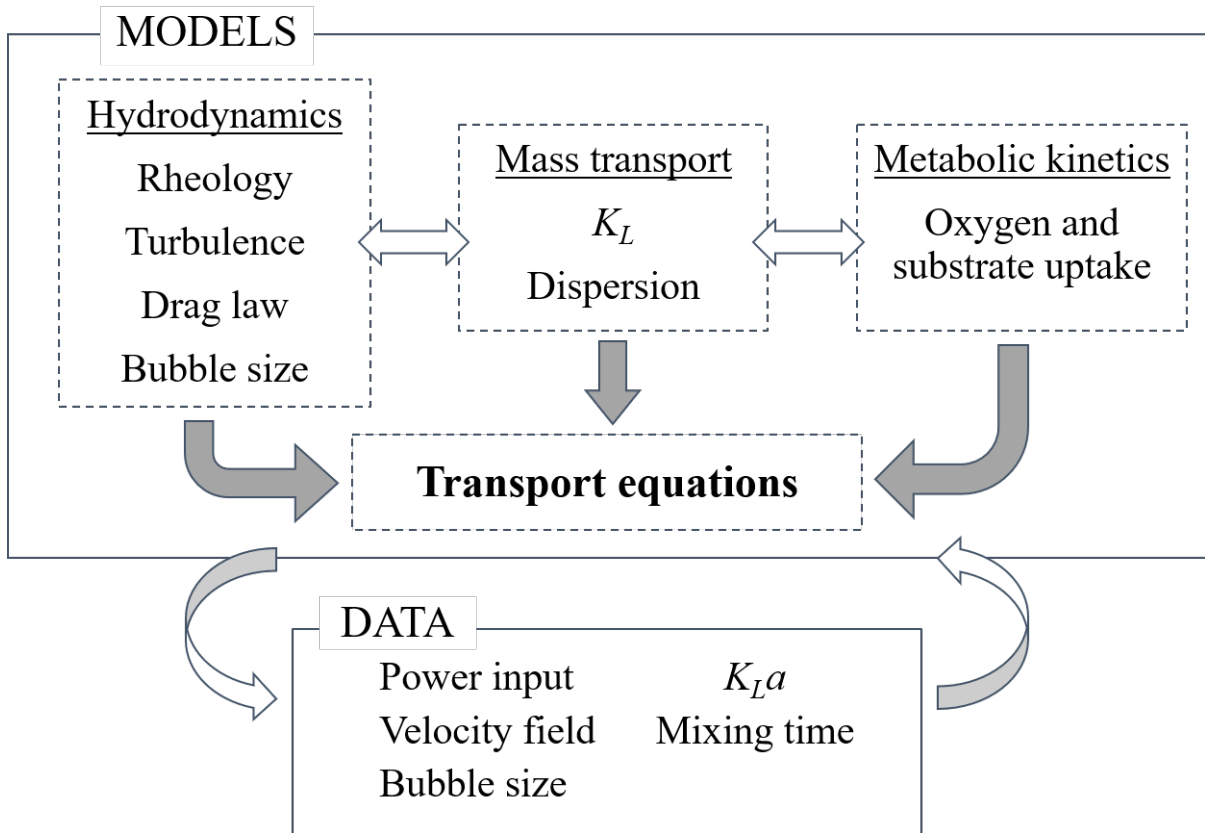


Figure 1.7: Logic chart showing the physical models necessary to characterize a bioreactor. The main experimental data used for the validation of the model are listed as well.

Concerning experimental data, the work on global and local reactor characterization conducted by Gabelle (2012) on complex liquids — that led to the development of correlations for $K_L a$, power consumption and gas hold up in aerated fermenters — was completed with novel data on bubble size and liquid-side mass transfer coefficient collected during the experimental stage of this study. Preliminary results on liquid velocity were also obtained at relatively low gas velocities.

For the determination of bubble size, the cross-correlation method with a dual optical probe (Raimundo et al., 2016) was tested, while the velocity of the liquid was measured using the Pavlov tube (Forret et al., 2006; Raimundo, 2015). The experiments were carried out in two reactors (40 L and 400 L) and two model fluids (xanthan gum and carboxymethyl cellulose solutions) replaced the fermentation broth; surfactants were also used to implement and to investigate the effect of antifoams that are generally used in the industrial fermentation of *Trichoderma reesei*.

Experimental data on bubble size and mass transfer coefficient were used as parameters in

the CFD simulations, whereas mixing time, power draw, and gas holdup served to validate the closure models. Among these, models for the liquid rheology and for the drag coefficient were of main interest. After the validation of the CFD model, its reliability to describe a large-scale fermenter was tested.

1.5 Structure of this manuscript

In this introductory chapter, the general background of the biofuels industry has been presented, with a highlight on the production of second-generation bioethanol from lignocellulosic feedstock. In addition, the strategy and the problematic linked to the CFD modeling of bioreactor have been described and placed within this context. Summarizing, the main objectives of this study are:

- Acquisition of experimental data that are necessary for the validation of the fermenter model;
- Integration and validation of closure models (drag law, rheology, turbulence, and K_L) in the CFD simulation of large-scale reactors, with coupling of hydrodynamics and mass transfer;
- Use of the CFD model to describe industrial fermenters, and provide useful information that might be used in other projects (e.g. design of scale-down models).

In the next chapter, the main notions about hydrodynamics and the mass transfer in stirred tank reactors are presented. This chapter is meant to provide the key concepts required to understand the contents presented throughout the document. The deepening of turbulent mixing and transport phenomena occurring inside an industrial reactor is beyond the scope of this study, so the reader will be referred to other works that cover the different topics in much more detail. In Chapter 3, the methodology that was applied in the experimental study in the first phase of research is described. There, the details of the reactors and the measuring tools that were used are reported. The experiments were conducted on model fluids (xanthan gum and carboxymethyl cellulose) that were used in place of the real fermentative culture media to analyze the effect of the rheology on the measuring techniques. Chapter 4 summarizes the results used for the validation of the optical probe and the Pavlov tube to measure the average bubble size and the liquid velocity, respectively. This set of data was used to validate the CDF model and to screen available closure models (Chapter 5); application of the numerical model to study industrial problems is then discussed in Chapter 6. At the end, a concluding chapter will summarize all the salient results and achievements of the research.

Chapter 2

Theoretical aspects of agitated reactors: hydrodynamics, mass transfer and numerical modeling

2.1 Introduction

The aim of this section is to provide the reader with theoretical aspects of agitated tanks, in order to explain the turbulent mixing and mass transfer in aerated shear-thinning liquid. Firstly, general considerations on hydrodynamics and mass transfer will be discussed. The key parameters used to describe an agitated reactor and its performance, as well as the physical quantities that can be used as scale-up criteria will be presented too. The second part of the chapter will focus on numerical characterization of bioreactors, presenting the general theory of computational fluid dynamics and the main modeling strategies that have been proposed to simulate these systems.

The common practice to deal with the scale-up of agitated reactors has been to adopt empirical correlations to describe mixing and mass transfer; however, this approach has intrinsic limitations: the correlations are valid only for a specific range of operating conditions and usually, they rely on geometric constraints, thus making difficult their use for multi-scale purposes. For example, while ideal mixing can be assumed for well-mixed lab-scale reactors, gradients of concentrations and other scalar quantities are normally encountered at the production scale. CFD analysis, on the contrary, is becoming an appealing alternative because it presents the advantage of providing also a local characterization of the reactor, which can help to find what might cause poor mixing and mass transfer, and to understand how to improve the design of the fermenter to tackle these problems (Bach et al., 2017). In recent years, some researchers

have tried to harness the potential of numerical simulations to design new scale-down models for biological systems (Haringa et al., 2018).

2.2 Hydrodynamics of aerated stirred tanks

Mixing is an essential process, in which the components of the system are blended between them in order to reduce gradients of concentration, temperature and other properties. In bioindustry, mixing is very important because it permits to create and maintain an optimal environment for microbial cultures (Doran, 2013). Mixing can be accomplished in different ways and kinds of equipment; one of the most common is the agitated or stirred tank, which can also be used as a chemical reactor. Conventionally, a stirred tank consists of a cylindrical vessel with a flat or curved bottom, equipped with one or more impellers and, if it is designed to work in the transitional or turbulent regime, with lateral baffles that are used to prevent the fluid from swirling at higher velocity. This flow pattern is achieved by deviating the tangential flow in two opposite axial flows; therefore, performance of the tank is obviously greater, because of the formation of secondary recirculation loops. Depending on the process, a reactor with different geometry might be needed, so squared and horizontal cylinder tanks can also be found, as well as taller tanks with multiple agitators. In figure 2.1, the scheme of a standard aerated tank equipped with a single Rushton turbine is presented.

To classify the hydrodynamic regime at which the reactor operates, the Reynolds number is used; this dimensionless group expresses the ratio between inertial and viscous forces. For a Newtonian fluid it can be defined as:

$$Re = \frac{\rho ND^2}{\mu_l} \quad (2.1)$$

where ρ and μ_l are the density and viscosity of the liquid phase, N is the impeller speed and D the diameter of the impeller. In stirred tanks, the regime is laminar at $Re < 10$, while at $Re > 10000$ the mixing regime is fully turbulent. Values within this range describe the transitional regime. In most of the industrial applications, reactors are designed to work in the turbulent regime, because turbulent phenomena enhance mass and energy transfer rates. In the case of a non-Newtonian fluid, Re is defined differently because the dynamic response of the fluid to shear is different. The rheological behavior of a shear-thinning fluid can be expressed with the Ostwald-de Waele's model, also known as power-law model:

$$\tau = K\dot{\gamma}^n \quad (2.2)$$

where τ is the shear stress, $\dot{\gamma}$ is the shear rate, and K and n are the consistency and flow

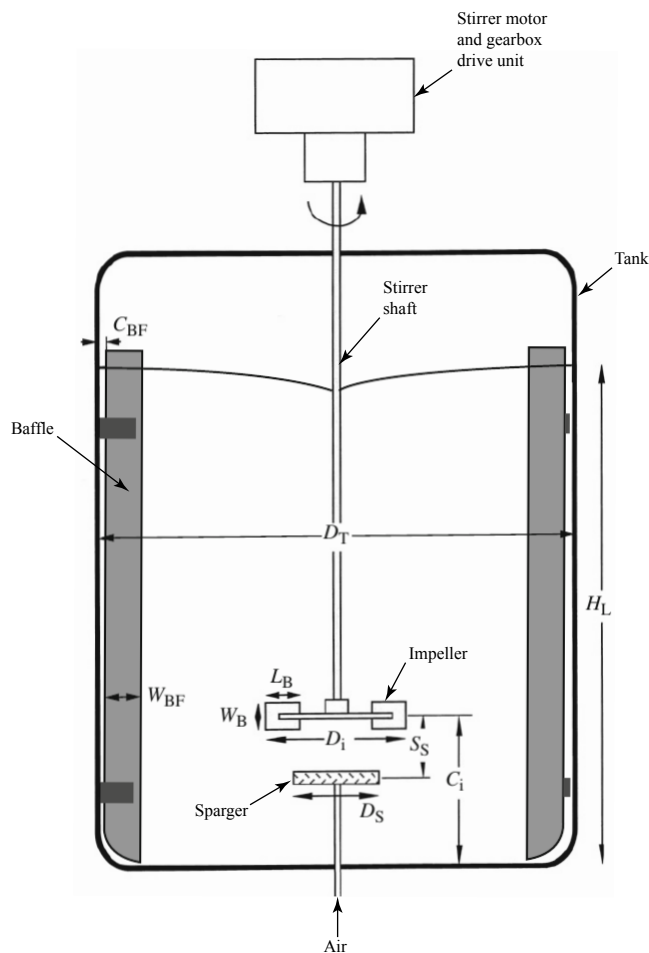


Figure 2.1: Typical configuration of an aerated stirred tank, with description of the main elements. Meaning of initials: D_T , tank diameter; H_L , liquid height; D_S , impeller diameter; C_i , impeller clearance; D_S , sparger diameter; S_S , distance between the sparger and impeller; L_B, W_B , blade length and width; W_{BF} , baffle width; C_{BF} , baffle distance from vessel's walls. Image adapted from Doran (2013).

behavior indexes, respectively. For a shear-thinning liquid, $n < 1$, meaning that viscosity decreases when the shear rate increases. An apparent viscosity μ_{app} can be defined as:

$$\mu_{app} = \frac{\tau}{\dot{\gamma}} = K\dot{\gamma}^{n-1} \quad (2.3)$$

Clearly, a wide range of shear rates can be expected inside a stirred tank, where higher values are encountered in the vicinity of the impeller blades; while far from agitator, velocity gradients are lower and so are the shear rates. Therefore, a distribution of apparent viscosity characterizes stirred non-Newtonian liquid, and at a fixed impeller speed, different hydrodynamic regimes might coexist in the reactor. For simplicity, a single value of Reynolds number is often used to classify the reactor regime even in the case of varying viscosity; thus, in most of the cases, the

average shear rate is considered to compute the apparent viscosity.

Researchers have proposed different ways to estimate the average shear rate. The most common approach is to use Metzner-Otto's relationship, that expresses the average shear rate as a function of the impeller speed:

$$\dot{\gamma}_{av} = k_S N \quad (2.4)$$

Here, k_S is a constant, which depends on the impeller geometry. For a Rushton turbine, the authors found the value $k_S = 12$ (Metzner & Otto, 1957). If this correlation is used, the impeller Reynolds number for a power-law fluid can be then expressed as:

$$Re = \frac{\rho N^{2-n} D^2}{K k_S^{n-1}} \quad (2.5)$$

Formally, the direct proportionality between the average shear rate and the impeller speed is valid only for a Newtonian fluid in the laminar regime, for which the constant gains a physical meaning. However, the extension of this method also for shear-thinning liquids and in the turbulent regime is a common practice (Ameur et al., 2016; Khapre & Munshi, 2014; Venneker et al., 2010; Zhang et al., 2017).

Equation (2.5) was derived empirically, by studying laminar flow in agitated tank with Newtonian fluids. Pérez et al. (2006) discussed Metzner-Otto's correlation through a theoretical analysis, extending the concept also to the turbulent flows of non-Newtonian liquids. According to their study, the average shear rate inside a stirred tank can be related to the rotation speed in the following ways:

$$\dot{\gamma}_{av} = qN \quad (2.6)$$

$$\dot{\gamma}_{av} = q' N^{3/(n+1)} \quad (2.7)$$

As further discussed in section 2.7.3, both relationships are based on Kolmogorov's theory of isotropic turbulence. The first equation is similar to Eq. (2.4) and valid for both Newtonian and non-Newtonian fluids in laminar systems; the value of the constant q depends on the impeller, because it contains the linear relationship between the impeller power number and the Reynolds number. Equation (2.7) defines the average shear rate inside a stirred tank at $Re > 10000$, and the constant q' depends on the rheological indexes for a power-law liquid. In the case of turbulent flow and Newtonian liquid, the exponent becomes 1.5, a result that agrees with empirical evidence. In Pérez et al. (2006) can also be found correlations for calculating the maximum shear rate close to the impeller.

To design a mechanically agitated reactor, some primary aspects have to be considered. It is then important to define:

- The power draw and the torque;
- The gas dispersion and how this will affect performance in terms of mixing;
- The mass transfer between the two phases;
- In biological systems, characteristic times of cell metabolism and substrate uptake.

Impeller power number

The power provided by the impeller is related to the mechanical torque with the following:

$$P = 2\pi N\Gamma \quad (2.8)$$

where Γ is the torque at the shaft of the impeller. The power draw can also be expressed in terms of power number N_P , that depends on the Reynolds number and on the impeller and tank geometries (Bujalski et al., 1987):

$$P = N_P \rho N^3 D^5 \quad (2.9)$$

Figure 2.2 depicts the power number dependency on Reynolds number. In the laminar regime, the power number strongly depends on the Reynolds number ($\propto Re^{-1}$), while in the turbulent regime, the power number reaches a constant value, different for each impeller geometry. For a standard configuration (i.e. $H : T = 1$), the turbulent power numbers of different kinds of impellers are listed in table 2.1. Rushton turbines are characterized by the highest N_P , which is in the range 5–6, depending on geometrical details (e.g. number of blades, blade and disk thickness, etc.) and on the presence of baffles. It follows that, compared to other agitators, radial turbines are capable to transmit more energy to the fluid. However, a high power number also means that for a specific value of impeller speed, the energy provided by the engine has to be high too, so will the operating costs.

For non-Newtonian fluids, the power number for Newtonian fluids can still be used; this is true especially at higher impeller speed, for which viscous effects are usually negligible if compared to turbulent phenomena.

Commonly, values of power number are provided by the manufacturers, but empirical correlations can be found, especially for the simpler designs. For instance, the correlation proposed by Bujalski et al. (1987) has become very common. Based on their correlation, the power number of disk turbines can be expressed in the following way:

$$N_P = 2.5 \left(\frac{s}{D}\right)^{-0.2} \left(\frac{T}{T_0}\right)^{0.065} \pm 3\% \quad (2.10)$$

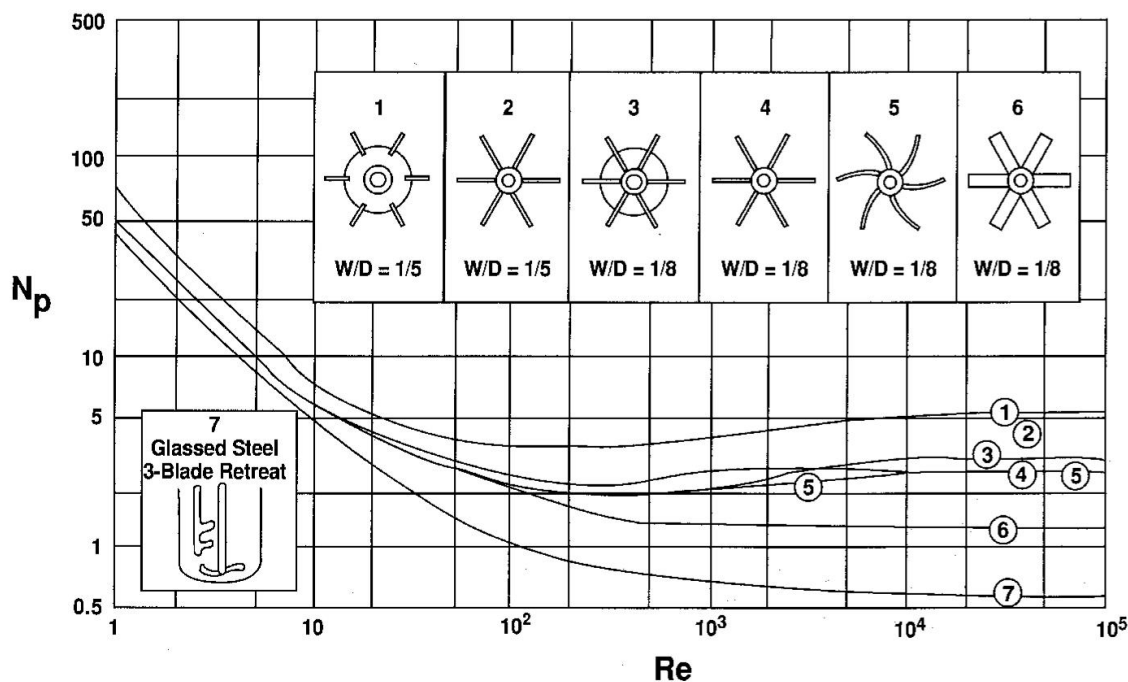


Figure 2.2: Power number as a function of Reynolds number for seven types of impellers. From Paul et al. (2004)

Table 2.1: Power numbers of various impellers under turbulent conditions (Nienow, 1998).

Impeller geometry	N_P
Six-blade Rushton	5.00
Scaba 6SRGT	0.45
4 blades inclined (45°)	1.27
6 blades inclined (45°)	1.70
Lightnin A315	0.84

where s is the disk thickness, D and T are the impeller and tank diameters, and T_0 is the reference diameter, equal to 1 m. The correlation led to a good prediction of the impeller power number when $0.01 \leq s/D \leq 0.05$ and in case of agitated vessels characterized by an impeller to vessel ratio in the range 0.25–0.70

2.2.1 Gas flow patterns

When gas is introduced in the tank, the interaction with the liquid phase can have a great impact on hydrodynamics of the system. The resulting flow pattern depends on the operating conditions and the geometry of the tank, and three different regimes based on the bubble

trajectories have been described in the literature. These regimes are: flooding, loading, and fully recirculated regimes. In figure 2.3, the transition between flow regimes by varying the gas flow rate or the impeller speed is shown. For a specific gas velocity, when the rotation speed is too low, the liquid velocity is not high enough to push the gas, and the impeller is flooded. In this condition, the gas forms ragged cavities behind the impeller blades and its flow pattern is essentially characterized by helical trajectories around the shaft with null dispersion of the gas phase in the vessel. As the rotation speed increases, bubbles start to occupy the top part of the tank and the regime goes from flooding to loading. A further increase in the impeller speed leads eventually to a fully dispersed regime, in which the gas phase is well distributed in every region of the tank, with gas bubbles present in both the recirculation loops above and below the impeller disk; when the impeller speed is very high, extra gas recirculating vortexes appear close to the free surfaces. The same passages described before are encountered in the opposite direction by decreasing the gas flow rate, while maintaining constant the rotation speed.

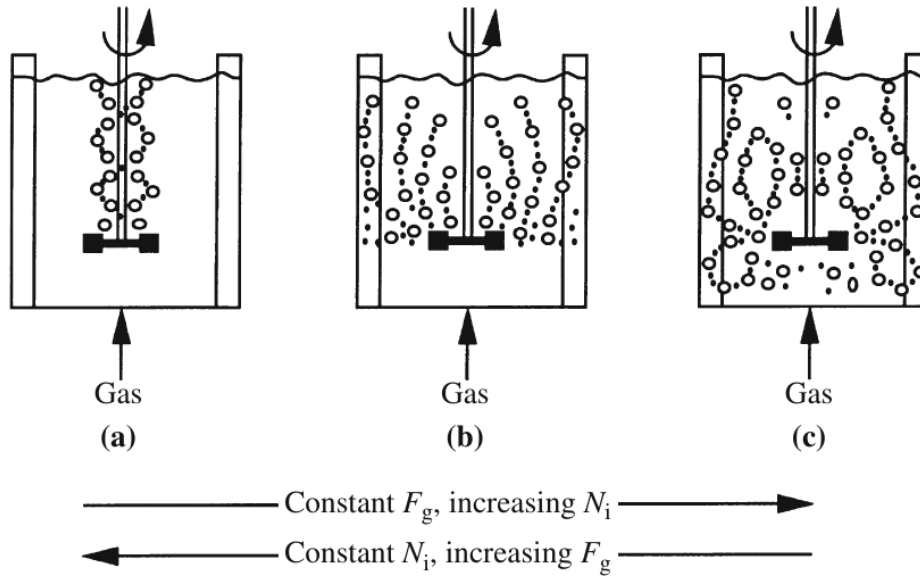


Figure 2.3: Flow regimes transition for a standard geometry; from left to right: (a) flooding, (b) loading, and (c) fully dispersed regimes. Diagram extracted from Doran (2013).

To better describe the transition between flow patterns, a flow map as in figure 2.4 can be used (Nienow, 1998). This graph is based on two dimensionless groups, namely the gas flow number Fl_g and the impeller Froude number Fr , whose definitions are presented below:

$$Fl_g = \frac{Q_g}{ND^3} \quad (2.11)$$

$$Fr = \frac{N^2 D}{g} \quad (2.12)$$

where Q_g is the gas flow rate from the sparger and g is the gravity acceleration. According to this map, the transition from flooding to loading regime occurs at N_F , or when:

$$(Fl_G)_F = 30 (Fr)_F \left(\frac{D}{T} \right)^{3.5} \quad (2.13)$$

The rotation speed above which the gas is well dispersed, namely N_R , can be calculated from:

$$(Fl_g)_R = 13 (Fr)_R^2 \left(\frac{D}{T} \right)^5 \quad (2.14)$$

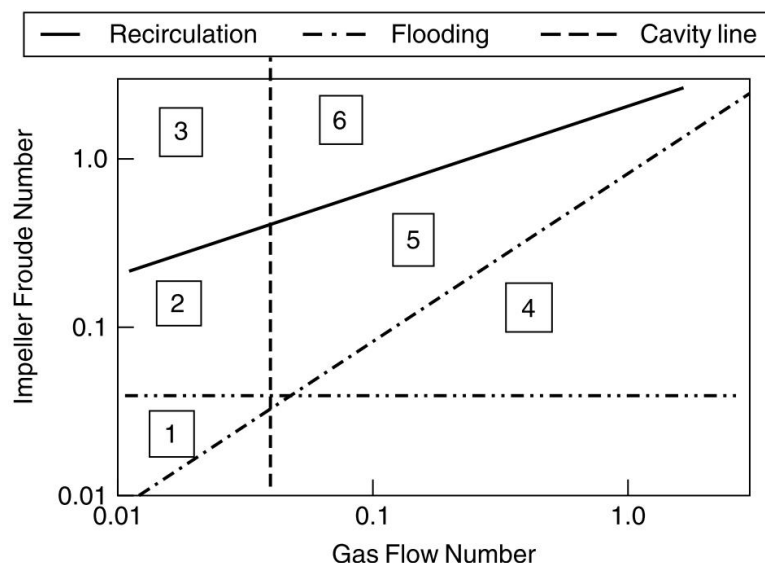


Figure 2.4: Flow map for a single Rushton turbine. (1) below minimum dispersion speed; (2) vortex cavities, no recirculation; (3) vortex cavities with recirculation; (4) flooded; (5) loaded with large cavities; (6) large cavities with recirculation. Extracted from Paul et al. (2004).

The gas tends to accumulate in low-pressure zones behind the blades, creating ventilated cavities. The presence of these cavities causes a decrease in the power drawn, so less energy is provided to the liquid by the impeller, and the bigger the cavities, the lower the power drawn. In figure 2.5, the shape and the size of these cavities formed behind the blades of a Rushton turbine are represented. Cavity formation is strongly related to the gas flow regime, and the structure of the cavities can be predicted thanks to empirical correlations (Nienow, 1998). Equations proposed in the literature for cavity transitions are complex relationships between gas flow number, Froude number, and the tank geometry.

In viscous shear-thinning broths, ventilated cavities are larger and more stable; even at relatively low aeration rate, large structures form behind the impeller blades, and their size is slightly affected by the gas rate. For this kind of liquids, it is more difficult to define the boundaries of the flooding condition.

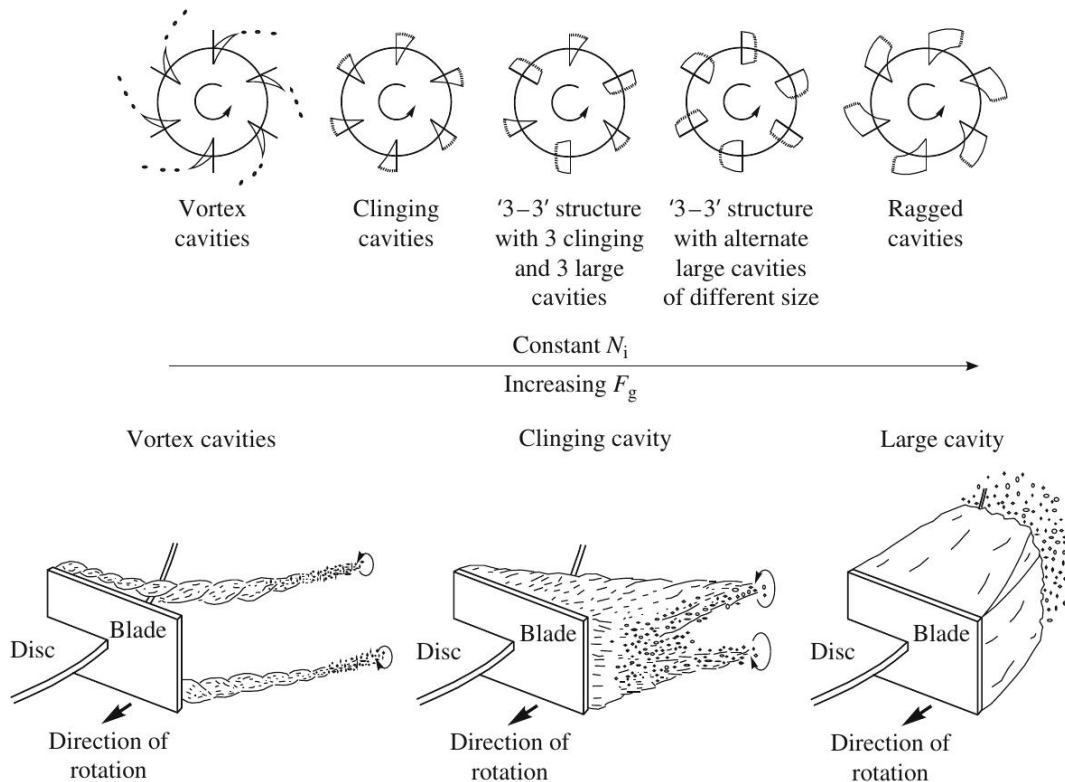


Figure 2.5: Evolution at increasing gas flow rate F_g of gas cavity structure behind the blades of a Rushton turbine. Original imagine from Nienow (1998), adapted by Doran (2013).

In gassed liquids, the power draw P_g is lower than in the case of the ungassed system. In general, the power drawn by the liquid decreases with the gas flow rate; in the light of the contents of the previous paragraph, it is correct to link the power loss with the variation of cavities shapes and patterns. For Rushton turbines, a great power loss is related to the passage from vortex to clinging cavities, and from these to the "3-3" structure, which are the transitions characterized by a variation of the gas cavities size. From this point and up to the formation of ragged cavities, the P_g remains almost constant. In fact, the last transitions are characterized by a change of shapes, with small variation of cavities size.

The power reduction due to aeration can be expressed in terms of relative power demand (RPD), as the ratio P_g/P . The suggested approach to obtain RPD is to first identify the cavity regime, and then to use one of the correlations for that specific regime (Paul et al., 2004). In the case of "3-3" cavities structure, Bruijn et al. (1974) proposed the following equation for

RPD:

$$\frac{P_g}{P_0} \approx 0.18Fl_g^{-0.20}Fr^{-0.25} \quad (2.15)$$

For the other regimes, constant values are usually reported; therefore, for vortex and clinging cavities, RPD is about 0.9, while it ranges between 0.4–0.5 when six large cavities form behind the blades.

More general correlations to estimate the power loss can be found in the literature (Bouaifi & Roustan, 2001; Gabelle et al., 2011). One of the most common is the one of Michel & Miller (1962), for which:

$$\frac{P_g}{P_0} = \left(P_0^2 N D^3 Q_g^{-0.56} \right)^{0.45} \quad (2.16)$$

Gabelle and coauthors proposed a different correlations that can be used for tanks with a diameter up to 0.6 m, and also for dual-impeller systems:

$$\frac{P_g}{P_0} = \max \left[\left(\frac{P_g}{P_0} \right)_{lim} ; \exp \left(-15.36 N_P^{0.16} Q_g^{0.62} T^{-1.7} \left(\frac{D}{T} \right)^{0.51} \right) \right] \quad (2.17)$$

Equation (2.17) expresses a strong influence of the tank diameter and gas flow rate on the relative power draw, and it led to an average error of 10%. Moreover, this equation is valid also when $Q_g = 0$ and for high gas flow rates, at which RPD reaches a constant value that depends on the impeller geometry (Paul et al., 2004). For standard Rushton turbines, Gabelle (2012) measured a value of $(P_g/P_0)_{lim} = 0.33$.

2.3 Key aspects of mass transfer

2.3.1 Mass transfer coefficient

In aerobic fermentations, the concentration of dissolved oxygen (DO) is a crucial parameter because microorganisms need oxygen and nutrients to live and proliferate. To guarantee the perfect growing conditions for the strain, the DO has to be maintained above a specific critical value, which depends on the microorganism. However, as shown in Section 1.3, the behavior and the viscosity of the system can change during the fermentation, directly affecting the transport of oxygen in the fermentative broth. Consequently, the efficiency of the mass transfer can gradually fall during the reaction; therefore, it becomes necessary to modify the operating conditions in order to improve the oxygen transfer. This performance adaptation can be managed by acting, within a certain range, on both the gas flow rate and the impeller speed.

The mass transfer between the gas and the liquid phase is usually described by considering the two-film theory of Lewis-Whitman. This model describes the exchange of a species A from

one phase to another, because of the presence of a concentration gradient. This driving force is concentrated at the interface, within the film of each phase (figure 2.6).

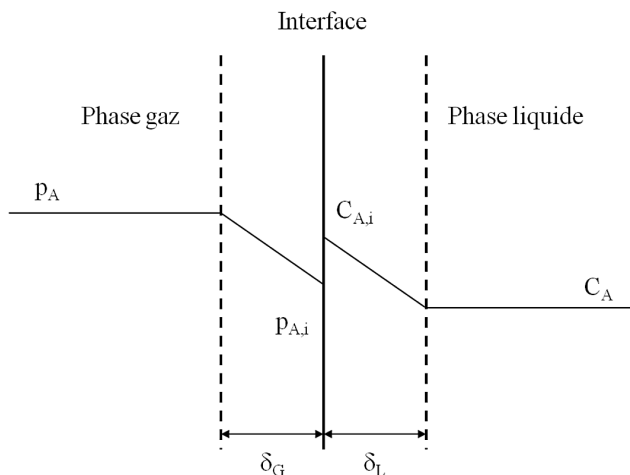


Figure 2.6: Representation of two-film theory of Lewis-Whitman.

Given the component A being transferred from the gas phase to the liquid phase, the flux for each phase can be written as:

$$J_{A,g} = k_G (p_A - p_{A,i}) \quad (2.18)$$

$$J_{A,l} = k_L (C_{A,i} - C_A) \quad (2.19)$$

where p_A and C_A are the partial pressure and the concentration of A in the gas and in the liquid, respectively. The subscript i stands for interface. At the interface, the thermodynamic equilibrium is reached and the partial pressure is related to the concentration through Henry's law:

$$p_{A,i} = H_A C_{A,i} \quad (2.20)$$

where H_A is the Henry constant for component A at a specific temperature and for the considered liquid. Introducing the equilibrium constant, Eq. (2.18) becomes:

$$J_{A,g} = H_A k_G (C_A^* - C_{A,i}) \quad (2.21)$$

here C_A^* is the equilibrium concentration in the liquid. Dealing with concentrations at the interface is not easy, so an overall mass transfer is usually introduced, so the flux can be expressed in terms of the overall driving force respect to the liquid concentration:

$$J_{A,l} = K_L (C_A^* - C_A) \quad (2.22)$$

Rearranging Eqs. (2.19), (2.21) and (2.22), and considering the equality of the fluxes through each phase at the steady state, the different mass transfer coefficients can be related as follows:

$$\frac{1}{K_L} = \frac{1}{k_L} + \frac{1}{H_A k_G} \approx \frac{1}{k_L} \quad (2.23)$$

The last approximation is valid in system like air-water, because the oxygen has a low solubility in water, so the Henry constant is high. Furthermore, k_G is usually much higher than k_L . In such a system, the limiting step is the diffusion of the species into the liquid phase and practically, $K_L \approx k_L$. Knowing the net flux through the interface, the oxygen transfer rate (OTR) can be finally obtained by multiplying the flux and the specific surface area:

$$OTR = J_{O_2} a = k_L a (C_{O_2}^* - C_{O_2}) \quad (2.24)$$

$k_L a$ is known as the volumetric mass transfer coefficient and is a property of great importance to characterize the mass transfer in aerated reactors. In general, it is difficult to measure the transfer rate k_L , and the specific interfacial area a ; therefore, $k_L a$ is frequently used to quantify the performance of aerated systems.

There are different models to express k_L , but the most common are based on the penetration theory of Higbie and the surface renewable model (Devi & Kumar, 2017). Based on Higbie's penetration model and Kolmogoroff's theory of isotropic turbulence, (Kawase et al., 1987) derived the following expression for the liquid-phase transfer coefficient of a bubble with a mobile surface:

$$k_L^{penetration} = \frac{2}{\sqrt{\pi}} \sqrt{D_l} \left(\frac{\varepsilon}{\nu} \right)^{0.25} \quad (2.25)$$

where D_l is the diffusivity of the gas in the liquid phase, ε and ν are the turbulent dissipation rate and the kinematic viscosity of the liquid phase. This model is based on the assumption that small liquid eddies have a constant exposure time. Danckwerts (1951) refined Higbie's penetration theory, by considering different exposure times at the gas-liquid interface. Based on this modification, Lamont & Scott (1970) expressed the mass transfer coefficient as:

$$k_L^{eddycell} = K \sqrt{D_l} \left(\frac{\varepsilon}{\nu} \right)^{0.25} \quad (2.26)$$

Here K is a model constant. Various authors have reported different values of this constant in the range 0.30–0.54; for air-water systems agitated by a single Rushton turbine, Laakkonen et al. (2007a) found a good agreement with experimental results for $K = 0.46$. Other authors theorized the surface renewal mechanism as a phenomenon being controlled mainly by the phase relative velocity (i.e. slip velocity) u_{slip} , which is defined as $u_{slip} = |u_l - u_g|$. Calderbank (1958)

defined the contact time in terms of average slip velocity and mean bubble diameter:

$$k_L^{slipvelocity} = \frac{2}{\sqrt{\pi}} \sqrt{\frac{D_l}{d_b/u_{slip}}} \quad (2.27)$$

The same approach was used by Frössling (1968), who applied it to describe the transfer at the interface of a rigid sphere. In this case, the dependency on the molecular diffusivity is different and the mass transfer coefficient is expressed as:

$$k_L^{rigid} = c \sqrt{\frac{u_{slip}}{d_b}} D_l^{2/3} \nu^{-1/6} \quad (2.28)$$

Depending on the theoretical approach that is used to explain the surface renewal at the gas-liquid interface, models for the liquid-side mass transfer coefficient can be then divided into eddy turbulence model and slip velocity models. In the literature, several studies in agreement with both the theories can be found, making it legitimate to think that both phenomena take part simultaneously in mass transfer mechanisms. For example, Devi & Kumar (2017) compared numerical results obtained with all the four models here presented, concluding that $k_L^{eddycell}$ and $k_L^{slipvelocity}$ were able to better predict the mass transfer coefficient in agitated bubbly flows.

Estimation of the liquid-side coefficient

The different definitions of k_L that were discussed in the previous chapter, have provided the theoretical base for dimensionless equations. However, empirical correlations are more common, as discussed in the exhaustive review of Garcia-Ochoa & Gomez (2009). Most of these correlations are based on Kolmogorov's theory of isotropic turbulence, and they have the following general formula:

$$k_L = C \sqrt{\frac{D_l}{\nu}} \left(\frac{P_g}{\rho V} \nu \right)^{1/4} \quad (2.29)$$

Several values of C can be found in the literature ranging from 0.3 to 1.13 (Kawase et al., 1987, 1992; Lamont & Scott, 1970; Linek et al., 2005; Prasher & Wills, 1973; Zhang & Thomas, 1995). Attempts were made by Kawase et al. (1992) to find the proportionality constant from physical parameters; from the analysis of hydrodynamics, they derived the following equation:

$$k_L = C'(n, K) \sqrt{D_l} \left(\frac{P_g}{V} \frac{1}{K} \right)^{1/2(1+n)} \quad (2.30)$$

where coefficient C' is a function of the rheological index. For water, the authors provided a value of $C' = 0.301$.

Correlation for the volumetric mass transfer coefficient

To estimate the volumetric mass transfer coefficient in stirred tanks, empirical correlations are common. These correlations express $k_L a$ as a function of operating conditions, and they present the general form:

$$k_L a = \left(\frac{P_g}{V} \right)^a U_g^b \mu^c \quad (2.31)$$

Many authors proposed different values of the exponents a , b , c by fitting of experimental results. This wide range of values can be explained by saying that all the authors did not use the same measuring technique and they conducted experiments at different gas velocities, tank diameter, and impeller configuration. Labík et al. (2017) reviewed some of the correlations that can be found in the literature.

Among the different correlations, the one proposed by Gabelle et al. (2011) was used to compare the experimental results that were obtained in this work. Gabelle's correlation was preferred over the other ones because the experimental setup and the operating conditions investigated in this research were the same as the ones used in their study.

$$k_L a = 0.023 \left(\frac{P_g}{V} \right)^{0.44} U_g^{0.47} \left(1 + \frac{\mu_{app}}{\mu_c} \right)^{-1} \quad (2.32)$$

With these values, the mass transfer coefficient was predicted with an average error of about 20%. The different formulation of the last term, by introducing a *critical* apparent viscosity μ_c , allowed them to better describe the effect of rheology on mass transfer in the aerated tank. By data fitting, they used the value of 0.018 Pa·s as the critical viscosity. Thus, when the apparent viscosity is lower than μ_c , its influence on the mass transfer is hidden by the other quantities. However, above this value, the rheology has a stronger influence on the mass transfer coefficient. In this correlation, Metzner-Otto's model was considered to calculate the apparent viscosity of the liquid.

Dimensionless correlations are less common, even though they can offer a deeper understanding of the phenomena behind the mass transfer coefficient. Among these, some of the most recent ones are listed in table 2.2.

2.4 Bubble size in aerated stirred tanks

The knowledge of the bubble size in a gas liquid reactor is very important because it permits to better understand gas dispersion mechanism and performance of the reactor. In fact, the

Table 2.2: Dimensionless equations for $k_L a$.

Author	Equation
Schlüter & Deckwer (1992)	$k_L a \left(\frac{\nu}{g^2}\right)^{1/3} = 7.94 \cdot 10^{-4} \left(\frac{P_g/V}{\rho(\nu g^4)^{1/3}}\right)^{0.62} \left[\frac{Q_g}{V} \left(\frac{\nu}{g^2}\right)^{1/3}\right]$
Garcia-Ochoa & Gomez (2009)	$k_L a \frac{D^2}{D_l} = 11.96 \left(\frac{D^2 N \rho}{\mu}\right)^{0.5} \left(\frac{ND}{U_g}\right)^{-0.5} \left(\frac{\rho D^2 N^3}{\sigma}\right)$
Moucha et al. (2012)	$k_L a \frac{D^2}{D_l} = 0.37 \left[\frac{ND}{(\varepsilon\nu)^{1/4}}\right] \left(\frac{U_g}{U_{tip}}\right)^{0.52} \left(\frac{ND}{U_{tip}}\right)^{0.52}$

Sauter mean diameter is directly related to the interfacial area a with the gas holdup α_g :

$$a = 6 \frac{\alpha_g}{d_{32}(1 - \alpha_g)} \quad (2.33)$$

Here a is expressed in terms of volume of liquid.

The bubble size distribution in an aerated vessel is hard to predict because of the complex hydrodynamic regime. In fact, different levels of turbulence can be encountered in a tank, especially in the case where the liquid has a complex rheology. The most common formula to estimate the mean bubble size inside a stirred tank was formulated by Calderbank (1958), and it is based on the expression originally derived for liquid drops by Hinze (1955):

$$d_{32} \propto \frac{\sigma^{0.6}}{\varepsilon^{2.5} \rho^{0.6}} \alpha_g^{0.5} \quad (2.34)$$

According to this expression, the Sauter mean diameter can be related to the maximum diameter, which depends on the ratio between the turbulent shear stresses and the interfacial forces: when the first overcome the second ones, the deformed bubble goes through breakage. Equation (2.34) is then based on turbulence theory, and it is valid when coalescence does not occur; Calderbank's correlation can be often find in the following simplified version:

$$d_{32} \propto \left(\frac{P_g}{V}\right)^{-0.4} \quad (2.35)$$

The exponent 0.4 follows from the assumptions that in turbulent flows bubble size is solely determined by the breakup probability. However, fitting of experimental data for coalescing systems led to smaller exponents (Alves et al., 2002). For coalescing systems, Alves and cowork-

ers proposed the empirical relationships:

$$d_{32B} = 0.0076 \left(\frac{P_g}{V} \right)^{-0.14} \quad (2.36)$$

$$d_{32T} = 8.5 \left(1 + 32.5 \frac{Q_g}{D^2} \right) \left(\frac{P_g}{V_I} \right)^{-0.24} \quad (2.37)$$

here the subscripts B and T indicate the mean diameter in the bulk and in the turbine region, respectively, whereas V_I represents the volume swept by the impeller. Effect of gas loading was expressed in terms of gas flow rate (Q_g).

In a mechanically agitated vessel, the impeller region is characterized by the highest shear rate; consequently, the majority of breakup events occur in this region (Alves et al., 2002; Bouaifi & Roustan, 1998). In the liquid volume close to the impeller, the highest values of turbulent kinetic energy were measured, with the maximum values found at the impeller tips. Recent studies on the breakup of single bubble in stirred tanks have described breakup of bubbles as a phenomenon mainly due to turbulent fluctuations of the momentum in the liquid phase; these, are generally referred to as eddy-bubble interactions. These interactions between a dispersed particle and one or more eddies can occur in four different ways, depending on the turbulent energy spectrum. Summarizing the review study of Hasan (2017), a bubble can be deformed and eventually broken-up by the interaction with several small eddies, with the outer edge of a big turbulent eddy, or by being transported inside a big eddy; interactions with two paired eddies can also be possible. These cases are represented in figure 2.7.

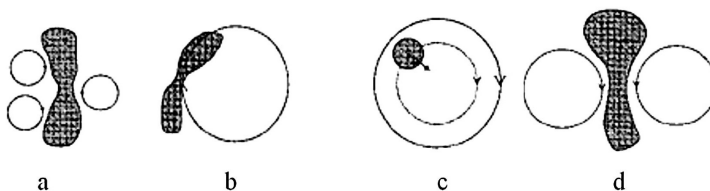


Figure 2.7: Eddy-bubble interactions: (a) interaction with several eddies, (b) interaction with the outer edge of an eddy, (c) transport within a big eddy, (d) collision with opposite eddies.

Other breakup mechanisms other than eddy-bubble interactions can be found in a stirred tank. For instance, also shear stresses generated by the relative motion of the phases can stretch and break the bubbles up. Laminar shear stress generated by the drag force is affected by the viscosity of the liquid phase, therefore this breaking mechanism is more recurrent in high viscosity liquids (Rueger & Calabrese, 2013). Moreover, high shear stresses are also present in the viscous boundary layer of the impeller blades, where the flow discharge pattern in front of the blade can cause the breakup of the dispersed phase. Lastly, a mother bubble can split in smaller bubbles even because of a clash with the impeller blade: the impact with a sharp solid can break the particles even without prior deformation.

Regardless of the mechanism involved, breakup occurs mainly in the impeller region, close to the impeller blades and in the region of impeller vortexes. Different experimental studies showed that the smallest bubbles were found close to the tip of the impeller blades, whereas bubble size started to increase at the end of the impeller discharge flow, close to the walls of the tank (Alves et al., 2002; Barigou & Greaves, 1992).

Coalescence occurs in the areas characterized by low turbulence like the region close to the walls, where a higher bubble density is normally present. When two bubbles get progressively close to each other, coalescence can happen, that is when the liquid film around them gets thin enough to break. Thus, collision between two bubbles is efficient only if the contact time between them is longer than the film drainage time; otherwise, bubbles will bounce and no coalescence will occur (Machon et al., 1997). A simplified coalescence scheme is represented in figure 2.8.

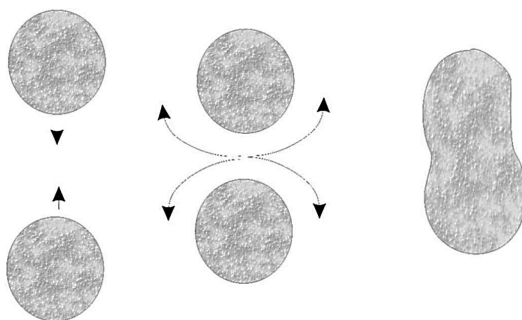


Figure 2.8: Liquid film drainage between two colliding bubbles and subsequent coalescence (Martín et al. 2010).

In viscous non-Newtonian fluids, rheology influences breakup and coalescence events. An increase in viscosity has an effect on the drainage time of the liquid film, which increases, slowing down the coalescence (Andrew & SPS, 1982; Chesters, 1991). Furthermore, the nonlinear dependency of viscosity on shear rate creates a wide distribution of shear stress, so coalescence and breakup rates are different with respect to an ideal media. That said, the region near the stirrer is always well mixed, whereas the rest of the tank can be characterized by lower Reynolds numbers. In a study on yield stress fluids, an extreme case was found and studied for the first time by Wichterle (1981). In fact, when the fluid is viscoelastic, the formation of a segregated zone around the impeller is very frequent. Several correlations were developed to estimate the size and the shape of these *caverns*; the main models available in the literature are listed and described in Ein-Mozaffari & Upreti (2010). The presence of these compartments inside the tank obviously has a negative effect on the global heat and mass transfer, thus affecting the performance of the reactor. Recently, CFD has been used to estimate the effect of the impeller geometry and its rotation speed on the size of the caverns, by monitoring the velocity contours

Table 2.3: Bubble size measurements in stirred tank.

Reference	System	U_g (mm s ⁻¹)	Technique
Bouaifi and Roustan (1998)	Water	0.10	Photographic
Alves et al. (2002)	Water, electrolytes	2.5–5	Capillar suction probe
Takahashi and Nienow (1998)	Water	0.1	Flash photographic
Barigou (1992)	Water, electrolytes	2.1–8.8	Capillary suction probe
Machon et al. (1997)	Water, electrolytes	2.8	Video microscope
Montante et al. (2010)	Water, glycerin	0.2–1.9	Photographic
Parthasarathy et al. (1994)	Water	0.25–1.25	Photographic
Laakkonen et al. (2007)	Water, n-butanol*	1.1–9.4	Photographic, capillary suction probe
Pinho et al. (2018)	Water	1.0–3.7	Photographic
Momiroski et al. (2018)	Water, CMC	0.7–3.5	Camera probe
Senouci-Bereski et al. (2018)	Water	0.9–2.7	Photographic
Kamiwano et al. (1998)	Water, CMC (up to 3%)	1.8	Photographic
Bao et al. (2010)	Water	23.4	Electric conductivity probe
Esmaili et al. (2016) [†]	Water, CMC, XG	40–200	Fiber optic probe

[†] Measurements in bubble column.

* In n-butanol, authors used CO₂ as the gas.

Ameur (2016); Pakzad et al. (2008); Sossa-Echeverria & Taghipour (2015).

Bubble size measurements

Some of the experimental studies on bubbly flows are summarized in table 2.3; the experimental technique used to measure bubble size, as well as the range of superficial gas velocity, are reported. Photographic methods are common and present the advantage of being non-intrusive measurements (Laakkonen et al., 2007; Montante et al., 2010; Pinho et al., 2018; Senouci-Bereksi et al., 2018). Bubble size distribution and mean diameter are obtained from image processing. Generally, viscous shear-thinning liquids are opaque, so photographic techniques cannot be used in these kind of systems.; for the same reason, this experimental method is not suitable at high superficial gas velocities.

Alves et al. (2002) and Barigou & Greaves (1992) measured bubble size distribution with a photoelectric suction probe. In this technique, bubbles are withdrawn by a calibrated capillary with a vacuum system and sampled. The slug of gas in the capillary is then measured and its length correlated with the original bubble diameter. The capillary probe method overcomes the limitations of the photographic analysis; nonetheless, it is characterized by greater errors when big bubbles are sampled, and the minimum detectable bubble diameter — which is related to the capillary diameter — might not be enough to sample most of the bubble size in aerated reactors.

Invasive phase-detective probes have been satisfactorily used in dense dispersed systems (Bao et al., 2010; Esmaili et al., 2016). Bao and colleagues used a dual conductive probe to

measure chord length distribution and Sauter mean diameter in air-water agitated tank. As the authors also explained, the technique is based on the measurement of the vertical bubble velocity component, and errors related to bubble trajectories were not quantified. Based on the same principle but with a single optic fiber probe, Esmaeili et al. (2016) obtained the bubble chord length in bubble columns and in shear-thinning solutions of carboxymethyl cellulose and xanthan gum. Optic and conductive probes are capable to obtain gas information even in systems characterized by high concentration of the gas phase, but the method's accuracy relies on strong hypothesis on bubble trajectory respect to the probe. Moreover, the probe needs to be as small as possible in order to reduce its impact on hydrodynamics.

Raimundo et al. (2016) developed a technique that allows one to obtain the Sauter mean diameter without any assumption on bubble trajectories. Their measurement method requires a dual optic probe; the signals of each probe are then treated in terms of bubbles' probability of being detected by the probes. The main drawback of the dual optic probe technique is that information about bubble size distribution are difficult to obtain in chaotic flows. Moreover, some hypothesis on bubble shape have to be made a priori.

Few experimental works have been conducted to characterize gas dispersion in a non-Newtonian liquid, because of the difficulties to perform reliable measurements at industrial operating conditions. In a study about gas dispersion in a fermenter equipped with different stirrers, Nienow (1990) pointed out the presence of a bimodal distribution in highly viscous shear-thinning liquids. The author reported the presence of numerous bubbles that were smaller than 1 mm, and few big bubbles, which constituted nevertheless the biggest fraction of the gas volume inside the reactor. Machon et al. (1980) reported the presence of two main bubble sizes in carboxymethyl cellulose solutions: very small pin-head bubbles and large spherical cap bubbles. They also observed a decrease in the gas holdup with the concentration of the polymer, due to the increase in bigger bubbles fraction. The latter are mainly pushed to the walls and their rising velocity is very high, while smaller bubbles are entrained by the recirculation loops above and below the impeller, so they have a higher residence time.

In a more recent study, Momiroski et al. (2018) used two in-situ camera probes to take pictures of bubbles in viscous solutions of glucose and carboxymethyl cellulose. They studied the effect of different impellers and of the liquid viscosity, by comparing the bubble size distribution, the Sauter mean diameter and the size of gas cavities. In the case of non-Newtonian liquid, the increase in viscosity caused the spread of BSD, so smaller bubbles were measured. At the same time, the authors visually noticed some big bubbles in the bulk of the vessel, confirming the presence of the bimodal distribution, as other researchers have already pointed out. Tiny bubbles were observed also in xanthan gum solutions Mohd Sauid et al. (2013). It has been reported that smaller bubbles are characterized by a lower k_L because of the rigidity of their interface and the absence of internal recirculation Clarke & Correia (2008); Garcia-Ochoa &

Gomez (2009).

Few authors have discussed the effect of liquid rheology on bubble size in bubble columns. Esmacili et al. (2016) used optical probes to obtain the average bubble chord length in different shear-thinning solutions. Bigger bubbles were found in more viscous systems, and the effect of viscoplasticity was also addressed.

2.5 Mixing time calculation in agitated tanks

Mixing time is an important quantity, because it provides useful information about mixing performance of the reactor. Globally, the shorter the mixing time, the faster is the homogenization of materials, and the timescales related to mass transfer and chemical reactions become more important. However, by considering the mixing time alone, it is difficult to study the presence and impact of poorly-mixed regions inside the vessel, which are indeed very important and can drastically decrease the yield of the process. For example, this is the case of biochemical reaction with aerobic microorganisms; these kinds of systems can be very sensitive to discontinuity in the environment, like a zone inside the vessel that is characterized by a scarce concentration of oxygen. In this case, the aerobic species can starve to death, causing a loss in the reaction yield. This is one of the various examples in which knowledge of local information about the mixing degree is vital to design a reactor, and it gives precious information for the scale-up.

Different techniques to calculate the mixing time exist, and they are all based on the variation of a liquid property after the addition of a certain tracer. Common monitored properties are: liquid pH, tracer concentration, conductivity, temperature, and color. The measurement output is usually normalized with respect to the final stable value, and the mixing time θ is then defined in terms of a specific degree of mixing. For example, the θ_{95} mixing time is defined as the time after which the normalized output will remain between 95% and 105% of the final value (Paul et al., 2004). In the context of the application of this research, the 95% mixing time is generally used, but tighter criteria are usually encountered in applications where a higher homogenization is required.

In some cases, authors reported the mixing time in terms of a dimensionless time, defined as $N\theta$, i.e. the number of impeller revolutions needed to obtain the required degree of homogeneity. In the literature, the correlation of Grenville & Nienow (2004) is frequently encountered. According to their correlation, the mixing time in stirred tanks equipped with a single turbine, can be estimated with the equation:

$$N\theta_{95}N_P^{1/3}\left(\frac{D}{T}\right)^2 = 5.20 \quad (2.38)$$

This correlation is valid in the turbulent regime, and when the liquid height is equal to the vessel diameter. At lower impeller speed or when the viscosity of the fluid is higher, the mixing regime can become transitional, so the power number is not constant with Re anymore; in this case, the mixing time is higher, and it can be predicted using a correlation like the following (Grenville & Nienow, 2004):

$$N\theta_{95}N_P^{2/3}Re\left(\frac{D}{T}\right)^2 = 183^2 \quad (2.39)$$

The constants presented in Eqs. (2.38) and (2.39) are characterized by a standard deviation of 10% and 17.4%, respectively. For configurations with more than one impeller and a ratio $H : T > 1$, the expression proposed by Cooke (1988) is well known. According to their correlation, mixing time can be estimated from:

$$N\theta_{95}N_P^{1/3}\left(\frac{H}{T}\right)^{2.43} = 3.3 \quad (2.40)$$

Another way to estimate the mixing time is from the mean circulation time θ_c . In fact, it is known that $\theta \approx 4 - 5$, depending on the required degree of homogeneity. Mean circulation time can be simply expressed with the following equation:

$$\theta_c = \frac{V}{Q} \quad (2.41)$$

where Q is the impeller pumping rate, that is equal to $Q = N_QND^3$. The pumping number (N_Q) depends on the impeller geometry, the mixing regime and the ratio D/T (Paul et al., 2004). For a Rushton turbine in the fully turbulent regime, $N_Q = 0.72$ is reported.

However, Middleton (1979) found that Eq. (2.41) was a too simplistic approach and inadequate for scale-up purposes, underestimating circulation time in big tanks. The researcher proposed a new expression from experiments of circulation time distribution at different tank sizes:

$$\theta_c = 0.5 V^{0.3} \frac{1}{N} \left(\frac{T}{D}\right)^3 \quad (2.42)$$

From the equations presented in this section, it can be seen that for a specific configuration of the reactor, mixing time varies linearly with the impeller speed. It follows that scaling-up of reactors is associated with an increase in mixing time, because lower rotation speeds are used at the large scale.

2.6 Scale-up of bioreactors

Scale-up is an important phase in the design of industrial processes. The principle is to predict the performance of an industrial-scale unit by extrapolating the results obtained during running tests at a benchmark scale in order to achieve the same yield. The main approach that has been used is to develop empirical and semi-empirical correlations whenever it was not possible to adopt a more rigorous, theoretically-based approach. The use of these correlations is appealing because of the direct link between unit performance and operating conditions or physical quantities, but their versatility is quite limited. In fact, empirical equations, keeping aside the physical phenomena that describe the system, rely on geometry constraints and their validity range depends on the conditions investigated during the experimental studies. Thus, usage of phenomenological relationships is still a common practice and further studies have been carrying out to find more precise correlations for the scale-up of complex industrial units.

In the biochemical industry, scale-up is a main issue because of the complex interrelationship between operating conditions and physical properties of the fermentative broths. In the case of filamentous fungi like *Trichoderma reesei*, the rheology of the broth can change during the cell growth phase. For *Trichoderma reesei*, the viscosity is affected by the concentration of the biomass and its morphology, that can change during the process modifying the oxygen demand. In fact, viscosity has in general a negative effect on transport phenomena. The power dissipated can be then increased to augment the mass transfer coefficient and promote the transfer of oxygen, but this will affect also the morphology of the strain because of its shear sensitivity. Damaging the filaments that are suspended in the broth will cause a loss in terms of the fermentation yield. Furthermore, mixing time at the lab scale are difficult to achieve at the large scale, because of the unrealistic energy demand at bigger scales. In addition to that, agitation in big fermenters is commonly provided by two or more impellers. In multi-impeller configurations, interaction between the flow patterns generated by every agitator causes an increase in the blending time, as reported in the literature Paul et al. (2004); therefore, in an industrial fermenter, mixing requires a time in the order of the minutes, causing the development of gradients (oxygen dissolved, substrate concentration, viscosity, ...) that have a significant effect on the growth of the biomass.

Several criteria have been used to attempt maintaining the performance of the process. Usually, a geometry similarity between the different scales is ensured, i.e. the ratios between the main sizes of the tank (D/T , H/T , ...). The geometrical constraints do not guarantee the same conditions at every scale, so the operating parameters have to be modified as well. Among these criteria, the most common are:

- The specific power dissipated;

- The velocity at the tip of the blades;
- The mass transfer coefficient;
- The energy dissipation/circulation function (EDCF)

These quantities are mutually related, so it is not possible to set all of them simultaneously. Fixing the volumetric power draw — usually together with the volume of gas in the fermenter — allows one to maintain a good mass transfer, but the velocity at the impeller tip increases as well. This leads to an increase of the mechanical stress and, eventually, to a deterioration of the cells. On the other hand, keeping constant the tip velocity V_{tip} has a negative effect on the $k_L a$ because it causes a reduction of the specific power input. A relatively recent approach was introduced by Smith et al. (1990), who correlated the effect of the agitation on the microorganisms with the passage frequency of the cells at the impeller height through the EDC function, which is given by:

$$EDCF = \frac{P}{kD^3} \frac{1}{\theta_c} \quad (2.43)$$

Here k is a dimensionless constant that depends on the impeller, and θ_c is the circulation time that can be obtained from:

$$\theta_c \approx \frac{V}{FIND^3} \quad (2.44)$$

The constant k is not easy to obtain, especially for reactors agitated by non-standard impellers. Hardy et al. (2017) proposed to use the maximum specific energy dissipation rate instead of the energy dissipated in the region of the impeller (P/kD^3). The new $EDCF$ definition becomes then:

$$EDCF_{\varepsilon_{max}} = \frac{\varepsilon_{max}}{\theta_c} \quad (2.45)$$

where ε_{max} can be estimated (Grenville et al., 2017):

$$\varepsilon_{max} = 1.04\rho N_P^{3/4} N^3 D^2 x \quad (2.46)$$

here x is the ratio between the impeller diameter and the trailing vortex diameter. For a Rushton turbine, Grenville et al. reported $x = 12$.

The use of the EDCF is a promising approach in the domain of bioprocess scale up. In their study about the scale-up of *Trichoderma reesei* fermentation, Hardy et al. (2017) obtained the best fit with their experimental data by using the $EDCF_{\varepsilon_{max}}$ approach.

2.7 Numerical simulations of stirred tanks

In this study, CFD was used to represent the behavior of bioreactors and analyze the effect of the liquid rheology, operating conditions and scale of the equipment on mixing and mass transfer efficiency.

The use of empirical correlations for scale-up purpose is uncertain because most of these correlations are based on geometry constraints and on certain hypothesis, like the assumption of ideal mixing. Furthermore, correlations provide characteristics at the global scale, thus cannot fully describe local spatial variations of properties inside the reactor. CFD models can then be used to overcome these limitations and provide more information about the process under examination. Thanks to the continuous advancement of technology that has led to increasingly powerful and more accessible calculators, the use of CFD solvers to investigate the behavior of mechanically agitated bioreactors has been growing in the last two decades.

However, one of the main issues in developing a CFD model is the validation of the closure models, that requires the need of reliable experimental data as a benchmark. Depending on what the primary goals of the simulation are, different information can be used for the validation. The most common are: the impeller power number, the mean velocity of the liquid, the turbulent kinetic energy and its dissipation rate, the mass transfer coefficient and the global gas holdup. It is also possible to validate the model by monitoring the variation of some quantities over time; for example, Kazemzadeh et al. (2016); Montante et al. (2005) measured the concentration of a tracer over time, from which the mixing time can be then defined and used to evaluate the accuracy of the model.

The main approach in industrial CFD is to use Reynolds-Averaged Navier-Stokes (RANS) equations to model turbulence and flow patterns. However, some studies based on LES techniques for turbulence can be found (Delafosse et al., 2008; Sungkorn et al., 2012; Zadghaffari & Moghaddas, 2010). The LES model is attractive because of its greater resolution in terms of time and length scales, but the grid requirements and the computational cost make it not suitable for the greatest part of the researches in the engineering field.

CFD has been widely employed to investigate turbulent mixing in stirred tanks with water, and a large amount of data has been produced for simple and multi-Rushton turbine configurations. For this reason, the case study of the single Rushton turbine has been used as a benchmark to evaluate the validity of turbulence models, discretization schemes and meshing strategies (Gradov et al., 2017; Huang & Li, 2013; Singh et al., 2011). However, as mentioned in the previous section, certain applications require radial and axial turbines that are characterized by a more complex geometry. In this case, CFD can also be used to predict mixing performance of new impeller designs (Devi & Kumar, 2017; Gimbun et al., 2009; Lane, 2017; Trad et al., 2017).

Classic turbulence models have been largely used to solve the main phenomena that occur in agitated tanks filled with water. Unfortunately, modeling of the same phenomena in non-Newtonian fluid has not reached yet the same maturity. A rigorous numerical approach was adopted by Gori & Boghi (2012), who proposed a turbulence model for a generalized Newtonian fluid. In their model, extra transport equations are solved for the instantaneous components of the rate-of-shear tensor and for the apparent viscosity. The study is indeed interesting, however, its implementation on current CFD solver is not trivial, because of the need of specific closure models. For this reason, a way simpler approach has been used by other researchers, who extended laminar models for non-Newtonian liquid to describe turbulent mixing in highly viscous and shear-thinning fluids (Ameur, 2016; Cortada-Garcia et al., 2017; Khapre & Munshi, 2015; Moilanen et al., 2006; Zhang et al., 2017).

Different methods are available to describe the relative motion between the rotating parts, i.e. the impeller, and the stationary elements in the tank, like baffles and the vessel walls. The Multiple Reference Frames model (MRF) has been found to give satisfying results (Haringa et al., 2017; Montante et al., 2005), and it has been often preferred over the more sophisticated Sliding Mesh model (SM) in which the grid surrounding the impeller region is rotated with the impeller and the shaft in small discrete steps. In the MRF model, however, a steady-state solution is calculated with respect to every part of the tank being in a static position. The equations are then solved in a moving framework for the impeller region, and in a steady framework for the other zones of the tank; information about momentum and pressure are exchanged through the interface between these two zones. More details about these and other impeller rotation models can be found in several books, for example Paul et al. (2004) and Ranade (2001). The SM model is more rigorous than the MRF model, allowing one to better simulate the physics inside a stirred tank and it is generally preferred when strong interactions between the impeller and the baffles are expected. However, it requires more computational resources. Deglon & Meyer (2006) demonstrated that the MRF model can give good results in terms of turbulent quantities if a very fine computation grid and a higher order discretization scheme are used to model the reactor.

As pointed out by Lane (2017), with more powerful hardware available in the last decade, several studies have been conducted to establish some guidelines about the mesh. The most interesting thing is that the prediction of the turbulence quantities is sensitive to the grid resolution and while about two thousand elements can predict very well the mean flow pattern, to obtain a good value of the turbulent dissipation rate, meshes made of more than $6 \cdot 10^6$ cells are required.

Concerning multiphase simulations, the Eulerian model is the most commonly used, but it requires closure models for interphase exchanged forces. A critical analysis of the most recent publications about simulations of bubbly flows in agitated tanks highlighted a variety

of approaches that have been used. In table 2.4, some of the newer studies based on the MRF Euler-Euler method are described; the list is not exhaustive, but it is however helpful to recognize recurrent models and numerical strategies. In most of the simulations, very low to low superficial gas velocities were used. Although in industrial applications these values are rarely encountered, low gassing rate are required to obtain the experimental data that are used for validation of the CFD model, namely the gas and liquid velocities (Montante et al., 2008; Shi & Rzehak, 2018). Shi and colleagues modeled all the interaction force terms, finding good agreement with experimental data from different sources. However, the majority of the researchers validated their results by considering the drag force only.

Drag correlations that takes into account the shape range of bubbles are in general preferred; among this family of drag laws, Tomiyama, Grace and the model of Ishii and Zuber are quite common in simulations of bubble columns and stirred tanks. Nevertheless, experiments in gassed tanks have been also validated by employing the Schiller and Naumann model for rigid single-sized particles. From table 2.4 it can be seen that in this case, to better fit experimental gas holdup and flow pattern, authors modified the drag coefficient by considering the contribution of turbulence, being the simple drag law model incapable to fully captured the gas-liquid interactions. From empirical observations, it has been reported that in turbulent bubbly flows, air bubbles have a lower terminal velocity. Turbulence dampening clearly has an effect on bubble rising velocity; however, its contribution seems to decrease with the gas flow rate, becoming negligible for gas rates that are normally encountered in industrial reactors.

Several authors claimed that, in order to obtain the correct global and local gas fraction, the gas phase should be model as a polydispersed phase (Amer et al., 2019; Liangchao et al., 2018; Wang et al., 2014). In this case, population balance equations are solved to obtain the bubble size distribution. It is clear that this approach is closer to the real physics that characterize bubble size variations due to coalescence and breakup phenomena, which occur in the tank.

Table 2.4: Summary of some researches about gas-liquid simulations published in the last decade.

Reference	U_g (mm s ⁻¹)	Turbulence model	Forces [†]	Drag model	Bubble size	Notes
Petitti et al. (2009)	0.2–1.0	$k - \epsilon$	D	Tomiyama	QMOM	Turbulent dampening*
Elqotbi et al. (2013)	5.0	$k - \epsilon$	D	Schiller-Naumann	Monodispersed	Biomass rheology
Gimbun et al. (2009)	3.0–7.4	realizable $k - \epsilon$	D, L	Ishii-Zuber	PBM (MUSIG)	
Wang et al. (2014)	2.6–5.2	$k - \epsilon$	D, L	Ishii-Zuber	QMOM	
Nauha et al. (2018)	7.0–50	realizable $k - \epsilon$	D	Tomiyama	Monodispersed	PBM in compartmental simulation
Yang et al. (2015)	3.2–4.8	$k - \epsilon$	D	Schiller-Naumann	Monodispersed	Turbulent dampening*
Haringa et al. (2017)	53	$k - \epsilon$	D	Universal	PBM	
Devi & Kumar (2017)	2.5–7.4	$k - \epsilon$	D	Schiller-Naumann	Monodispersed	Turbulent dampening*
Shi & Rzehak (2018)	0.08–2.1	SSG-RSM	D, L, WL, TD, VM	Schiller-Naumann	Monodispersed	Turbulent dampening**
Bach et al. (2017)	5.0–20	$k - \epsilon$	D	Grace	Monodispersed	T.reesei rheology
Amer et al. (2019)	0.1–0.7	$k - \epsilon$	D	Schiller-Naumann	PBM	
Liangchao et al. (2018)	5.0–37	RNG $k - \epsilon$	D, TD	Grace	PBM	

[†]See Eq. (2.77) for the meaning of initials.

*Modification of liquid viscosity.

**Correction of bubble terminal velocity (Lane et al., 2005).

However, it is less clear in which extend, a single bubble size can be enough to estimate the gas phase properties with sufficient precision. From the table, half of the publications showed good agreement with experimental by modeling a monodispersed gas phase; in these cases, mass transfer and gas holdup were well predicted by the solver (Bach et al., 2017; Devi & Kumar, 2017).

More consistent is the choice of the turbulence model. In fact, two-equations closures based on k and ε equations are widely used, and validated in both ungasged and multiphase flows. Most of the studies were done with standard or realizable model, the latter introducing several improvements in the case of rotating flows. A description of these models and turbulence modeling will be presented in the next section. Sophisticated turbulence model have been tested too (see Shi & Rzehak (2018)); however, for industrial applications were the main focus is on global behaviors, solidity of the simpler $k - \varepsilon$ models is usually preferred.

2.7.1 Governing equations and multiphase modeling

The governing equations upon which every model is based on are the Navier-Stokes equations, which represent the local conservation of mass and momentum, respectively (Bird et al., 2006):

$$\frac{\partial \rho}{\partial t} + \nabla \cdot (\rho \mathbf{u}) = 0 \quad (2.47)$$

$$\frac{\partial \rho \mathbf{u}}{\partial t} + \nabla \cdot (\rho \mathbf{u} \mathbf{u}) = -\nabla P + \nabla \cdot \boldsymbol{\tau} + \mathbf{g} \quad (2.48)$$

where $\boldsymbol{\tau}$ is the viscous stress tensor and \mathbf{g} is the vector of the body forces per unit of volume acting on the fluid (solely gravity, in most cases). The stress tensor is given by:

$$\boldsymbol{\tau} = \mu \left[\nabla \mathbf{u} + \nabla \mathbf{u}^T - \frac{2}{3} \nabla \cdot (\mathbf{u} \mathbf{I}) \right] \quad (2.49)$$

where \mathbf{I} is the identity matrix. It can be seen that the last term in Eq. (2.49) is zero for incompressible fluids. In this case, the stress tensor becomes:

$$\boldsymbol{\tau} = \mu \left(\nabla \mathbf{u} + \nabla \mathbf{u}^T \right) = \mu \mathbf{D} \quad (2.50)$$

here \mathbf{D} is the rate-of-deformation tensor.

2.7.2 Turbulence modeling

Navier-Stokes equations describe both laminar and turbulent flows; so, a way to simulate turbulent flows could be to resolve directly this equation without any need to model turbulence. This approach is called direct numerical simulation (DNS), but is still not possible in engineer-

ing applications due to the huge computational resources required. At high Reynolds number, very fine grids and short time steps are necessary to describe the variety of length and time scales that characterize high-Re turbulent flows. In turbulent flows, the smallest length scales are given by the Kolmogorov scale (Andersson et al., 2011).

$$\eta = \left(\frac{\nu^3}{\varepsilon} \right)^{1/4} \quad (2.51)$$

By dimensional analysis, it is also possible to state that:

$$\frac{\eta}{L} \sim Re^{-3/4} \quad (2.52)$$

The number of grid elements in each direction scales approximately as:

$$N \approx \frac{L}{\eta} \quad (2.53)$$

For its chaotic nature, turbulence is an intrinsic three-dimensional phenomenon, so number of cells should scale with N^3 . This assumption, together with Eqs. (2.52) and (2.53), give a total number of cells in the order of magnitude of $N \sim Re^{9/4}$. It is obvious that, even at moderate Reynolds number, too much computational effort is required because of the very fine mesh size.

Another way to solve turbulence could be to model with a subgrid stress model only the smallest scales of turbulence, which are encountered where the flow is mainly viscous, (e.g. near a wall), while momentum equation is directly solve only for the main flow, where largest eddies are in. This approach is called large-eddy simulation (LES) and allows one using coarser meshes than in DNS. Furthermore, intermediate-to-large turbulent eddies are hard to model in a universal way due to their anisotropy, whereas the smallest ones can be easily modeled with universal subgrid models.

However, the most common way to compute turbulence is averaging in time continuity and Navier-Stokes equations by Reynolds decomposition. The concept is to split instantaneous variables into a mean part — time independent — and a fluctuating part:

$$s(t) = \bar{s} + s'(t) \quad (2.54)$$

In other words, time-averaging over a reasonable time permits to describe separately fluctuations and non-turbulence (or statistically) quantities. Applying Reynolds decomposition to both

pressure and velocity in Eqs. (2.47) and (2.48) yields:

$$\frac{\partial \rho}{\partial t} + \nabla \cdot (\rho \bar{\mathbf{u}}) + \nabla \cdot (\rho \mathbf{u}') = 0 \quad (2.55)$$

$$\frac{\partial (\rho \bar{\mathbf{u}})}{\partial t} + \frac{\partial (\rho \mathbf{u}')}{\partial t} + \nabla \cdot [\rho (\bar{\mathbf{u}} + \mathbf{u}') (\bar{\mathbf{u}} + \mathbf{u}')] = -\nabla \bar{P} - \nabla P' + \mu (\nabla^2 \bar{\mathbf{u}} + \nabla^2 \mathbf{u}') + \mathbf{g} \quad (2.56)$$

where the strain-stress tensor is expressed for a Newtonian fluid. Time-averaging leads to a new set of PDE known as Reynolds-averaged Navier-Stokes (RANS), presented in Eqs. (2.57) and (2.58). The time average operation is done over a timescale larger than those of turbulence, but smaller than the timescale of mean quantities. This means that time derivative terms in these equations take into account a variation that takes place during a time larger than turbulence timescales:

$$\frac{\partial \rho}{\partial t} + \nabla \cdot (\rho \bar{\mathbf{u}}) = 0 \quad (2.57)$$

$$\frac{\partial (\rho \bar{\mathbf{u}})}{\partial t} + \nabla \cdot (\rho \bar{\mathbf{u}} \bar{\mathbf{u}}) = -\nabla \bar{P} + \mu \nabla^2 \bar{\mathbf{u}} + \mathbf{g} + \nabla \cdot \boldsymbol{\tau}' \quad (2.58)$$

The averaging generates a new term, $\boldsymbol{\tau}' = -\overline{\rho \mathbf{u}' \mathbf{u}'}$, also referred to as the Reynolds stress tensor (RST). It is an unknown symmetric second-order tensor which has to be modeled in order to close the problem. An approach to do so would be to derive a transport equation for the RST itself; unfortunately, this leads to a third-order tensor. Deriving an equation for this term would yield an equation that contains fourth-order moments of the velocity components. This goes on indefinitely and is noted as the closure problem. The Reynolds stress tensor is a symmetric matrix, this means that six components are unknown, and six equations are needed to close the problem. The Boussinesq approximation states that RST is proportional to the mean velocity gradients, describing turbulent transport of momentum as a diffusivity process: a turbulent viscosity is introduced and its modeling is the aim of the several turbulence models that are based on Boussinesq's hypothesis:

$$\boldsymbol{\tau}' = -\overline{\rho \mathbf{u}' \mathbf{u}'} = -\frac{2}{3} (\rho k + \mu_t \nabla \cdot \bar{\mathbf{u}}) \mathbf{I} + \mu_t (\nabla \bar{\mathbf{u}} + \nabla \bar{\mathbf{u}}^T) \quad (2.59)$$

Here, k is the turbulent kinetic energy, equal to $k = 1/2 (\overline{\mathbf{u}' \cdot \mathbf{u}'})$.

Turbulence models are referred to as zero-, one- and two-equation models, if they involve zero, one or two PDE to solve together with the RANS equations Eqs. (2.55) and (2.56). In this work, only two-equation models have been used; thus, only these will be described further. By dimensional analysis it can be seen that the turbulent viscosity μ_t is defined as follows:

$$\mu_t = C_{\mu_t} \rho u L \quad (2.60)$$

Thus, the turbulent kinematic viscosity ν_t is proportional to a turbulent velocity scale and a length scale, which are responsible for most of the turbulent transport. According to Kolmogorov and Prandtl's hypothesis, the characteristic turbulent velocity u can be expressed in terms of square root of the time-averaged turbulent kinetic energy, k . It follows that an extra PDE that describes transport of turbulent kinetic energy has to be solved. Concerning the characteristic length L , it can be defined algebraically (one-equation models, e.g. Prandtl's $k-l$ model and Spalart-Allmaras model) or determined from an additional transport equation (two-equation models). Generally, the second equation describes the transport of an arbitrary property χ , as a length-determining quantity. The correlation with the length scale can be expressed as:

$$\chi = k^\alpha l^\beta \quad (2.61)$$

Different values of α and β lead to a different meaning of the second turbulence variable χ . In table 2.5 characteristic values for $k-\varepsilon$ and $k-\omega$ models are presented.

Table 2.5: Common variables used for determination of the turbulence length scale.

α	β	γ	Interpretation of χ
0	1	l	Length scale, l
1/2	-1	$k^{1/2}/l$	Frequency scale, ω
3/2	-1	$k^{3/2}/l$	Dissipation rate, ε
-1/2	1	$k^{-1/2}l$	Timescale, θ

Standard and realizable $k-\varepsilon$ models

In $k-\varepsilon$ models, the turbulent length scale is defined in terms of turbulent dissipation rate ε . The standard formulation is then based on the two transport equations for k and ε ; for an isothermal and incompressible system, these read:

$$\frac{\partial(\rho k)}{\partial t} + \nabla \cdot (\rho k \mathbf{u}) = \nabla \cdot \left[\left(\mu + \frac{\mu_t}{\sigma_k} \right) \nabla k \right] + G_k - \rho \varepsilon \quad (2.62)$$

$$\frac{\partial(\rho \varepsilon)}{\partial t} + \nabla \cdot (\rho \varepsilon \mathbf{u}) = \nabla \cdot \left[\left(\mu + \frac{\mu_t}{\sigma_\varepsilon} \right) \nabla \varepsilon \right] + C_{1\varepsilon} \frac{\varepsilon}{k} G_k - C_{2\varepsilon} \rho \frac{\varepsilon^2}{k} \quad (2.63)$$

G_k is the production of turbulent kinetic energy due to mean velocity gradients, and μ_t is the turbulent viscosity; these quantities are defined as:

$$G_k = \left(-\overline{\rho \mathbf{u}' \mathbf{u}'} \right) : (\nabla \bar{\mathbf{u}}) \quad (2.64)$$

$$\mu_t = C_\mu \frac{\rho k^2}{\varepsilon} \quad (2.65)$$

In the model, there are five constants, the values of which are: $C_{1\varepsilon} = 1.44$, $C_{2\varepsilon} = 1.92$, $\sigma_k = 1.0$, $\sigma_\varepsilon = 1.3$, and $C_\mu = 0.09$.

The realizable $k - \varepsilon$ model, is based on a different transport equation for the turbulent dissipation rate. Moreover, C_μ is not a constant anymore, but a function of the turbulence quantities and the velocity field. The following equation is solved to obtain ε :

$$\frac{\partial(\rho\varepsilon)}{\partial t} + \nabla \cdot (\rho\varepsilon\mathbf{u}) = \nabla \cdot \left[\left(\mu + \frac{\mu_t}{\sigma_\varepsilon} \right) \nabla \varepsilon \right] + \rho C_{1\varepsilon} \dot{\gamma} \varepsilon - \rho C_{2\varepsilon} \frac{\varepsilon^2}{k + \sqrt{\nu\varepsilon}} \quad (2.66)$$

where $C_1 = \max [0.43, \eta(\eta + 5)^{-1}]$, $\eta = \dot{\gamma}k/\varepsilon$, and $\dot{\gamma} = \sqrt{2\mathbf{S}:\mathbf{S}}$. \mathbf{S} is the rate-of-strain tensor, which represents the symmetric part of the rate-of-deformation tensor \mathbf{D} (i.e. $\mathbf{S} = 1/2\mathbf{D}$). The model constants are: $C_2 = 1.9$, $\sigma_k = 1.0$, and $\sigma_\varepsilon = 1.2$.

2.7.3 Viscosity for non-Newtonian liquids

For a non-Newtonian liquid, Equation (2.50) can be written as:

$$\boldsymbol{\tau} = \mu_{app}(\mathbf{D}) \mathbf{D} \quad (2.67)$$

In general, apparent viscosity depends on all the three invariants of the rate-of-deformation tensor; however, for inelastic non-Newtonian fluids, the dependency on the third invariant can be neglected (Gori & Boghi, 2012). In this case, the viscosity is related to the second invariant only, and it can then be expressed in terms of shear rate:

$$\boldsymbol{\tau} = \mu_{app}(\dot{\gamma}) \mathbf{D} \quad (2.68)$$

where $\dot{\gamma} = \sqrt{1/2\mathbf{D}:\mathbf{D}}$. Due to Reynolds decomposition for turbulent flows, shear rate would be expressed in terms of fluctuating and mean shear rates, leading to more complex RANS equations. In particular, the appearance of non-linear terms are expected in the diffusive terms of each equation (Gori & Boghi, 2012); however, no closure models have been proposed yet. Current CFD solvers compute the non-Newtonian shear rate by simply considering the average velocity gradients (ANSYS Fluent Theory Guide).

In this study, a new approach based on Kolmogorov's theory of isotropic turbulence is proposed. Equations (2.6) and (2.7) are both obtained from the following relationship:

$$\dot{\gamma}_{av} = \left(\frac{1}{K} \frac{P}{V} \right)^{\frac{1}{n+1}} \quad (2.69)$$

Here, the average shear is related to the specific power draw and the rheological properties of the liquid phase. According to the isotropic turbulence theory, the power drawn by the liquid

goes through the energy cascade, down to the smallest eddy length scale, at which is dissipated; P can then be obtained from the integration over the total volume of turbulent dissipation rate:

$$P = \int_V \rho \varepsilon dV \quad (2.70)$$

The following hypothesis is made: that the shear rate can be expressed in terms of the local dissipated energy. Therefore, the shear rate can be computed from:

$$\dot{\gamma} = \left(\frac{\rho l \varepsilon}{K} \right)^{\frac{1}{n+1}} \quad (2.71)$$

It can be noticed that Eq. (2.71) relates the local shear rate to the Kolmogorov time scale τ_k :

$$\dot{\gamma} = \sqrt{\frac{\rho l \varepsilon}{\mu_{app}}} \equiv \tau_k^{-1} \quad (2.72)$$

2.7.4 Multiphase modeling

Multiphase flows are classified in dispersed and separated (or stratified). A schematic representation of these flows is shown in figure 2.9. Stirred vessels typically work in a dispersed flow regime, with bubble and/or solid particles that are dispersed in the continuous phase. If it is still possible to obtain good results when the dispersed phase is made of small particles (like bubbles or droplets), as either the volume fraction of the dispersed phase or the dimension of the particles increases, the dispersed phase heavily influences the behavior of the continuous phase, so the simulation becomes more difficult.

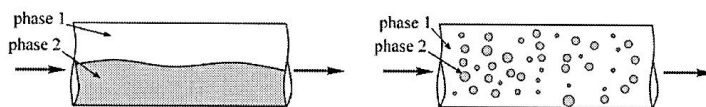


Figure 2.9: Main classification of multiphase flow: separated flow (left) and dispersed flow (right) (Andersson et al., 2011).

There are essentially two models for multiphase dispersed system: the Euler-Lagrange model and the Euler-Euler model. These formulations differ with respect to the frame in which the flow governing equations are formulated. The Euler-Lagrange framework describes the continuous medium in a Eulerian frame of reference (i.e. the point of view is stationary), whereas the dispersed phases are described in a Lagrangian frame of reference. This method gives very good results allowing one to describe the motion of each particles, but it is obviously unsuitable for systems characterized by high values of the gas holdup, due to the massive required computational cost. On the other hand, Euler-Euler formulation treats the phases as

interpenetrating continuous media, solving continuity and momentum equations for each phase. The drawback is that closure equations are needed in order to describe the interaction between the phases that constitute the system. In this work, high rates of gas are considered; therefore, only the Euler-Euler model will be further discussed.

The Euler-Euler model, also called the two-fluid model, is obtained by volume averaging the governing equations, considering the bulk properties of each fluid and introducing the local volume fraction α_k where the subscript k represents the k -th phase (e.g. $k = 1$ for liquid phase and $k = 2$ for bubbles). Thus, Eqs. (2.47) and (2.48) become:

$$\frac{\partial \alpha_k \rho_k}{\partial t} + \nabla \cdot (\alpha_k \rho_k \mathbf{u}_k) = 0 \quad (2.73)$$

$$\frac{\partial \alpha_k \rho_k \mathbf{u}_k}{\partial t} + \nabla \cdot (\alpha_k \rho_k \mathbf{u}_k \mathbf{u}_k) = -\nabla (\alpha_k P) + \nabla \cdot (\alpha_k \mathbf{T}_k) + \alpha_k \mathbf{g}_k + \mathbf{f}_k \quad (2.74)$$

where \mathbf{f}_k is the interaction force between the k -th phase and the others. Further equations are needed to solve the system.

$$\sum_k \alpha_k = 1 \quad (2.75)$$

$$\sum_k \mathbf{f}_k = 0 \quad (2.76)$$

In general, Eq. (2.73) is solved for the dispersed phases, whereas the volume fraction of the continuous phase is obtained from Eq. (2.75).

The difficulty of computing and resolving this set of equations arises, besides from the intrinsic complexity of the equations themselves, from the need of closure models to model the terms \mathbf{T}_k and \mathbf{f}_k . The tensor \mathbf{T}_k represents the rheology of the fluid and could be very complex if the phase is not a Newtonian fluid (Eq. (2.67)). The vector \mathbf{f}_k represents the momentum transfer between the fluids across the interface, and it can be expressed as a sum of different terms, each representing a different physical phenomenon. As suggested in the literature, these interaction forces have been highlighted (Ranade, 2001):

$$\mathbf{f}_k = \mathbf{f}_{D_k} + \mathbf{f}_{L_k} + \mathbf{f}_{VM_k} + \mathbf{f}_{WL_k} + \mathbf{f}_{TD_k} \quad (2.77)$$

- \mathbf{f}_D , drag force;
- \mathbf{f}_L , lift force;
- \mathbf{f}_{VM} , virtual mass force;
- \mathbf{f}_{WL} , wall lubrication force;
- \mathbf{f}_{TD} , turbulent dispersion force.

In stirred tanks and bubble columns, the drag force is the main force involved in the inter-phase interaction; so, it is often the only one used in the simulation. The last term in Eq. (2.77) is modeled in the case of turbulent gas-liquid flows.

For the two-equations turbulence models, ANSYS Fluent allows one to choose among three different class of turbulence models for multiphase flows: the mixture model, the dispersed model and the per-phase model, in which turbulent quantities are solved for each phase. In this research study, only the dispersed formulation was used, because of the high concentration of the dispersed phase and the density difference between gas and liquid phase. With the dispersed method, turbulence quantities for the continuous phase are predicted from transport equations (Eqs. (2.62)–(2.66)), properly modified for taking into account the phase fraction, while turbulence quantities for the dispersed phase are obtained using correlations from Tchen’s theory of homogeneous turbulence.

Mathematical models for drag coefficient

During its rising motion, the bubble is accelerated thanks to buoyancy, and decelerated due to the friction between the surface of the bubble and the surrounding fluid. In a system made of n different phases, the momentum transferred due to the friction between the k -th phase and the other n -th – 1 phases can be expressed as follows:

$$\mathbf{f}_{D,k} = \sum_{j=1}^n K_{jk} (\mathbf{u}_j - \mathbf{u}_k) \quad (2.78)$$

where the index j is for the generic phase and $j \neq k$. For the sake of simplicity, from now on, only two phases will be considered, i.e. $n = 2$, and the subscripts g and l will be used to indicate the dispersed phase and the continuous phase, respectively. K_{gl} is referred to as the interphase exchange coefficient and, when both of the phases are fluid, it is defined as:

$$K_{gl} = \frac{C_D Re_b a \mu_l}{8d_b} \quad (2.79)$$

Re_b is the bubble Reynolds number, defined with respect to the relative velocity between the bubble and the fluid, while a is the interfacial area concentration.

$$Re_b = \frac{\rho_l d_b |\mathbf{u}_g - \mathbf{u}_l|}{\mu_l} \quad (2.80)$$

a is defined as the interfacial area between phases per unit mixture volume. It is directly derived from the surface of the bubble and in the particle model is equal to:

$$a = \frac{6\alpha_g}{d_b} \quad (2.81)$$

Finally, by substituting Eqs. (2.79)–(2.81) in Eq. (2.78), the drag force can be expressed as following:

$$\mathbf{f}_D = \frac{3}{4}\alpha_g \frac{\rho_l C_D |\mathbf{u}_g - \mathbf{u}_l|}{d_b} (\mathbf{u}_g - \mathbf{u}_l) \quad (2.82)$$

Equation (2.82) was obtained by considering spherical bubbles. In the case of different shape, the Sauter mean diameter is considered, while the definition of the drag coefficient has to take into account the non-spherical effect. There are different models to calculate the drag force coefficient C_D . In a heterogeneous gas-liquid flow, the dispersed phase is rarely characterized by a single particle size, which clearly has an effect on the gas bubbles velocity and the flow field in general. Furthermore, only bubbles with small diameter have a spherical shape. The different bubble regimes are usually characterized by a different drag coefficient.

One of the simplest models is the one of Schiller and Naumann, which can be used to predict the bubble velocity of a spherical bubble in a stagnant liquid. Even though this model is mainly suitable for rigid spherical bubbles — which are characterized by a small diameter (ca. 1 mm in air-water system) — it has been frequently used in simulations with bubble diameters up to 5.3 mm (Amer et al., 2019; Devi & Kumar, 2017). However, the gas holdup was not always validated. Better results were usually obtained if contribution of turbulence is taken into account (Gradov et al., 2017).

More general drag coefficient models are the ones of Tomiyama, Grace, and Ishii and Zuber, in which, depending on the Reynolds number, several coefficients are used. The Ishii-Zuber's model presents also a correction term in the case of high gas concentration. In bubbly flows, at least three different regimes can be identified: viscous, distorted bubble, and spherical cap regimes. In the universal drag laws, each coefficient is expressed in the following forms:

$$C_{D_{visc}} = \frac{24}{Re_b} \left(1 + 0.1Re_b^{0.75}\right) \quad (2.83)$$

$$C_{D_{dis}} = \frac{2}{3}\sqrt{Eo} \left(\frac{1 + 17.67f^{*6/7}}{18.67f^*}\right); f^* = (1 - \alpha_g)^{1.5} \quad (2.84)$$

$$C_{D_{cap}} = \frac{8}{3}(1 - \alpha_g)^2 \quad (2.85)$$

Here, the Reynolds number is computed by considering a modified liquid viscosity. In fact, the

gas presence increases the viscosity of the continuous phase, leading to an effective viscosity:

$$\mu_e = \frac{\mu_l}{1 - \alpha_g} \quad (2.86)$$

The drag coefficient is then calculated based on the following relationship:

$$C_D = \begin{cases} C_{D_{visc}} & \text{if } C_{D_{visc}} \geq C_{D_{dis}} \\ \min(C_{D_{dis}}, C_{D_{cap}}) & \text{if } C_{D_{visc}} < C_{D_{dis}} \end{cases} \quad (2.87)$$

Another common drag coefficient formulation is the model of Grace. Several studies have used this model to predict the multiphase flows in bubble columns and agitated tanks. In this model, unlike the universal drag laws, no modification of the liquid phase properties due to the gas are taken into account; moreover (and like in Tomiyama's model) the bubbles shape regimes are defined in terms of two dimensionless groups: Eötvös number (Eo), and Morton number (Mo). The drag force coefficient is then calculated with the equation:

$$C_D = \max \left[\min \left(C_{D_{ellipse}}, C_{D_{cap}} \right), C_{D_{sphere}} \right] \quad (2.88)$$

The three drag coefficients are defined in the following way:

$$C_{D_{sphere}} = \begin{cases} 24/Re & \text{if } Re < 0.1 \\ 24(1 + 0.15Re^{0.687}) & \text{if } Re \geq 0.01 \end{cases} \quad (2.89)$$

$$C_{D_{cap}} = \frac{8}{3} \quad (2.90)$$

$$C_{D_{ellipse}} = \frac{4}{3} \frac{\rho_l - \rho_g}{\rho_l} \frac{g d_b}{U_t^2}; \quad U_t = \frac{\mu_l}{\rho_l d_b} Mo^{-0.149} (J - 0.857) \quad (2.91)$$

where J is a piecewise function of the numbers Mo and Eo. An alternative modeling approach for the drag force coefficient in stirred tanks was proposed by Scargiali et al. (2007), who obtained the coefficient from a balance of forces:

$$C_D = \frac{3}{4} \frac{(\rho_l - \rho_g) g d_b}{\rho_l U_t^2} \quad (2.92)$$

In this study, Scargiali et al. (2007) model was implemented via User Defined Functions, estimating the bubble terminal velocity with the equation of Mendelson (1967):

$$U_t = \left(\frac{2.14 \sigma}{\rho_l d_{32}} + 0.505 g d_{32} \right)^{0.5} \quad (2.93)$$

Here, σ is the surface tension, that was set to 0.072 N m^{-1} for all the simulations.

Bubble rising in non-Newtonian liquids have been described, but very few correlations have been obtained (Dewsbury & Karamanev, 2000; Margaritis et al., 1999; Tzounakos et al., 2004). Margaritis et al. (1999) measured the bubble terminal velocity in several shear-thinning solutions at different concentrations. They found that the drag curve was very similar to the characteristic one for contaminated Newtonian liquids, but with a three-fold decrease of C_D for a wide range of Re . Furthermore, no effect of polymer concentration was noticed. Based on their measurements of bubble terminal velocity as a function of the bubble volume, they proposed the following relationship:

$$C_D = \begin{cases} \frac{16}{Re} (1 + 0.173Re^{0.657}) + \frac{0.413}{1 + 16300Re^{-1.09}} & \text{if } Re < 60 \\ 0.95 & \text{if } Re \geq 60 \end{cases} \quad (2.94)$$

In the creeping flow, Eq. (2.94) yields $16/Re$, confirming that bubbles rising in power-law fluids do not follow Stokes model ($24/Re$) but rather the Hadamard-Rybczynski model for non-rigid spheres.

Few years later, Tzounakos et al. (2004) extended the analysis by correlating the effect of surfactant concentration on bubble shape and surface mobility in carboxymethyl cellulose and xanthan gum solutions. Comparison with free rising of solid particles highlighted the effect of surface mobility and bubble inner circulation on terminal velocity. For surfactant concentrations lower than the critical micelle concentration, bubble shape was not affected; at the contrary, surface mobility was, thus causing an increase in drag coefficient.

2.7.5 Use of CFD in bioreactors simulations

In order to understand and predict the performances of bioreactors, a solid knowledge of reactor fluid dynamics aspects and of the mass transfer, as well as the aspects related to the biological behaviors, are required. Unfortunately, the separately study of mixing and biological parameters is not enough to predict and thus improve the performance of industrial bioreactors (Nienow, 1998). So, the main objective has to be to explain the link between hydrodynamics and all the parameters that are specific to the biological system, such as shear rate sensitivity, oxygen demand, morphology variation, etc.

As hoped by Nienow, since 1998 and thanks to the continuous advancements in calculation technology and in models accuracy, CFD has been employed along classical methods to describe the connection between these two classes of phenomena.

Schmalzriedt et al. (2003) modeled a fed-batch culture in an aerobic fermenter. The authors described the abiotic phase by using physical properties of water; this assumption, allowed them to neglect the influence of mass transfer and kinetics on the stationary flow field. By doing so,

it was possible to separate fluid dynamics and material balances; the latter were solved for the substrate and the dissolved oxygen in fed-batch reactors, by using the predicted local flow field, which was coupled with a simple unstructured kinetic model. In the theory of bioprocessing and fermentation, unstructured models represent the microbial population as a single component system, whereas in structured models cells are described as multicomponent systems (González-Figueredo et al., 2018). The first approach is clearly simpler, because does not consider the inherent cell metabolism and modification of cell composition during fermentation. In the article of Schmalzriedt et al., an example of application of the model with a more complex structured kinetic model is also discussed, highlighting the potential of CFD tools also to describe intracellular concentrations. They concluded by discussing the importance of experimental data on metabolic response to spatial variation in the extra-cellular concentration field, which would allow researchers to ameliorate numerical models.

To better describe the interaction between mixing and microbial kinetics, Morchain et al. (2014) used a 3D Euler-Euler approach with a simple kinetic model, coupled with a population balance equation that helped describing the adaptation dynamics of the biotic phase. Their model showed the effect of different time scales on cells adaptation to spatial heterogeneities, that were simulated in a 70 m³ reactor. Precisely, dynamics with a characteristic time greater than the circulation time (e.g. the microbial growth) were not affected by the concentration gradients in the vessel; at the contrary, faster dynamics like the substrate uptake, that were characterized by a time scale comparable to the circulation time, were influenced by the gradients in the large scale fermenter.

A different approach for describing the effect of local substrate gradients in industrial fermentation was chosen by Haringa et al. (2017), who further elaborated the concept of lifetime analysis introduced in CFD models by Lapin et al. (2004). Haringa and colleagues used an Euler-Lagrange model to describe *Saccharomyces cerevisiae* fermentation in a multi-impeller reactor. Multiphase Euler-Euler simulations were done to firstly obtain liquid and gas flow field, and a simple Monod kinetics was implemented for the consumption of substrate. Finally, Lagrangian trajectories of massless particles simulated the microorganism lifetimes. This analysis provided interesting results in terms of extra-cellular fluctuations, residence time distributions for the different metabolic regimes (i.e. starvation, limitation, and excess respect to the substrate concentration), and nature of passage between two different regimes. In figure 2.10, an example of CFD post-processing of bioreactors is presented. The lifetime analysis can provide valuable information in terms of transition patterns between the different metabolic regimes, frequency of passage, and residence time distribution. Nevertheless, the culture broth was modeled as water-like material, thus the effect of complex rheology on mixing and mass transfer was not taken into account. This limitation in the numerical representation, could hide some important features in mixing of shear-thinning systems.

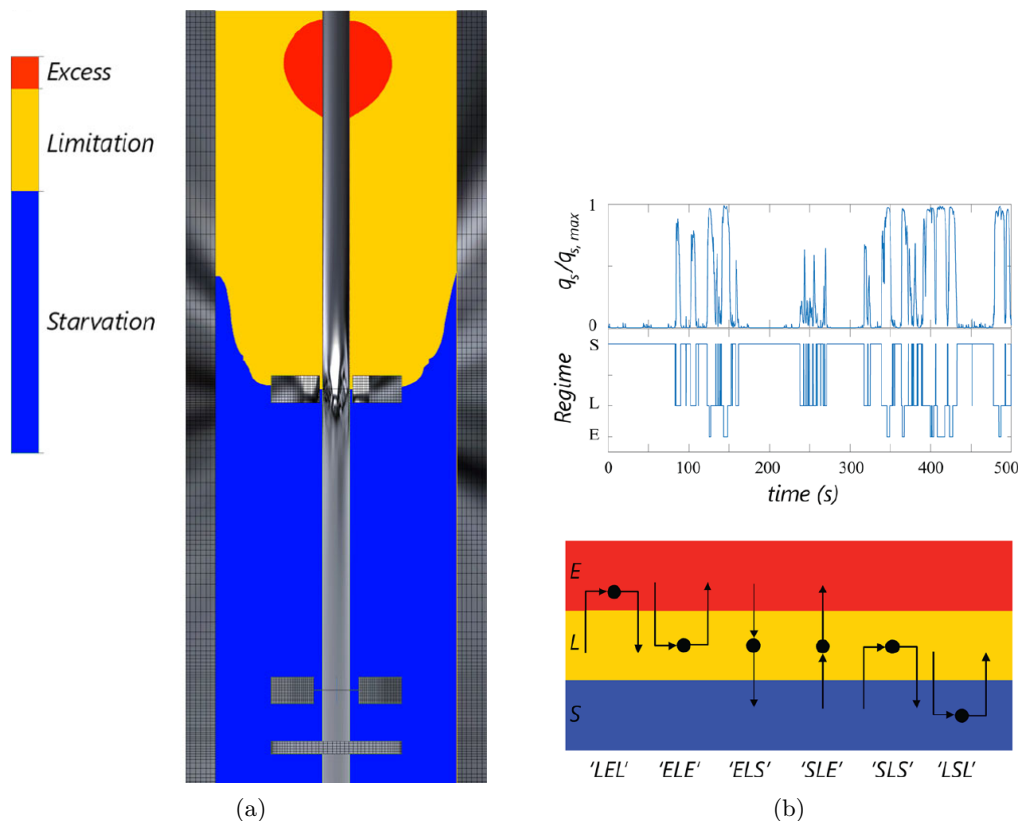


Figure 2.10: CFD analysis of *Saccharomyces cerevisiae* fermentation. (a) Distribution of substrate uptake; (b) from the top: signal of specific substrate uptake, regimes series, and regimes transition patterns. Images from Haringa et al. (2016).

From the examples aforementioned, it appears that even when simple kinetic models are used, CFD simulations can lead to very useful insights on local mixing on metabolic regimes, and can estimate the effect of hydrodynamics parameters on biological performances. It is important to remark that description of cell metabolism by using a kinetic model represents a strong simplification. In fact, microorganisms do not follow the same mechanisms as in a chemical reactions. Moreover, the environment can have an effect on the intra-cellular conditions; therefore, by using chemical kinetics, one would just neglect the adaptation dynamics of the cells. Modeling a biochemical reaction with a kinetic model has then some clear limitations and is a debatable approach. Nevertheless, it is possible to predict the scale of heterogeneities in the bioreactor, leading towards better reactors design and scale-down models. Furthermore, coupling between predicted fluid dynamics and microbial dynamics, is not limited to the use of simple kinetic models, but more complex mechanisms can also be implemented (Lapin et al., 2006; Schmalzriedt et al., 2003). More sophisticated models can be found in the research of Morchain (2000).

In the literature, recent papers that focus on turbulent mixing and mass transfer in non-

Newtonian liquid can be found. However, very few attempts have been done to couple microorganism kinetics and mixing in a system characterized by a complex rheology. Because of the distribution of shear rates in an agitated tank and the connection between rheology and mass transfer, modeling of the liquid rheology is necessary in the description of microbial fermentation that are characterized by a shear-thinning liquid. Research by Bach (2018) showed the capability of CFD simulations in predicting concentration gradients in large bioreactors. In particular, the author discussed the effect of different impeller geometries on oxygen gradients in *Trichoderma reesei* fermentation, in which the rheology of the liquid phase was taken into account through the power-law model.

2.7.6 Scale-down models from CFD

In previous sections, the role of CFD in predicting heterogeneities in large bioreactors was discussed, as the importance of interpretation of numerical results to aid the scale-up of aerobic reactors. In fact, it is important to study the effect of oxygen, nutrients, pH, and temperature gradients on the metabolism of the cells. The continuous exposure at different microenvironments can have an effect on the performance of microorganisms. Furthermore, kinetic models are usually developed from experiments at lab-scale, and the same model might not be accurate to describe the reactions in the large-scale fermenter.

In this context, the impact of fermenter heterogeneity on fermentation yield can be studied with a scale-down approach; this method, allows one to optimize the rate-limiting step in a specific fermentation process, in order to improve design of industrial units (Oosterhuis et al., 1985). Furthermore, lab-scale experiments can guide genetic engineers to work on the design of more resistant and well-performing microorganisms.

Substrate and oxygen inhomogeneities at the large scale have been studied at the lab scale by using mainly three setups: a well-mixed stirred tank (STR), and two-compartment models with either two stirred tanks (STR+STR) or with a well-mixed tank and a plug flow reactor (STR+PFR). For a single compartment configuration, fluctuating conditions can be achieved by imposing a pulsating feed with variable or fixed pulse variation; when oxygen fluctuations are studied, variation in dissolved oxygen can also be create by varying the head pressure. In configurations with two reactors, passage between rich and poor zones are modeled by changing the flow rates between the two compartments and the volume of the reactors; effects of substrate or oxygen gradients have been represented in STR+PFR models (Paul et al., 2004).

A successful scale-down model has to be capable to reproduce the conditions in the production process at which microorganisms are exposed, like temporal fluctuations in nutrients concentration and volumetric extent of poor and rich zones. This is not always easy to achieve, especially when very short time scales need to be reproduced. In fact, if well-mixed STR are

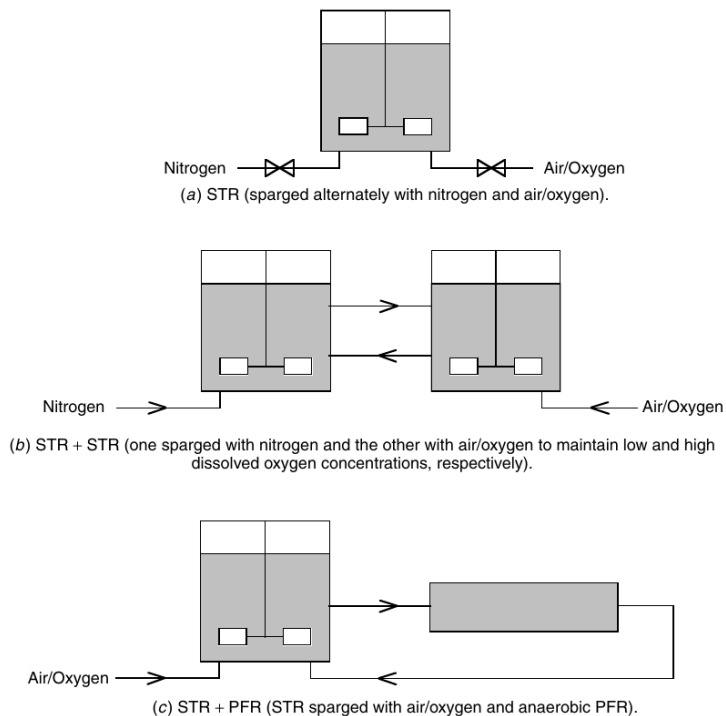


Figure 2.11: Scale-down configurations to recreate dissolved oxygen heterogeneities. Figure from Paul et al. (2004).

used, fast variation of substrate uptake would be achieved only by using high cells concentration, even greater than the ones inside industrial reactor ($dC_S/dt = -q_S C_X$)

Haringa et al. (2018) used CFD to design new scale-down models for the fermentation of *Saccharomyces cerevisiae*. The authors used the Lagrangian description of particles (as it was already mentioned in the previous section) to describe the fermenter heterogeneity in terms of substrate-uptake lifelines. Simulations provided microbial cell statistics such as residence times in the nutrient-rich zone and the maximum $q_S/q_{S,max}$ for every passage from the famine zone, to the feast one. These q_S -lifelines, were then used as a criterion to design scale-down models, by matching the lifetimes fluctuations between the two scales. Eventually, they found that a single STR with pulsating feed of substrate was able to reproduce numerical fluctuations in the big reactor. CFD was also used to validate the ideal mixing hypothesis for the scale-down lab-scale reactor. Nevertheless, the effect of aeration in viscous non-Newtonian fluids on mixing and mass transfer was not taken into account, because of limitations in the CFD turbulence models. As it was pointed out at the end of the previous section, rheology should be modeled because of its effect on the reactor's performance (e.g. decrease in mass transfer, see Section 4.3.4).

2.8 Conclusions

This chapter introduced the main theoretical elements that characterize mixing and mass transfer in agitated reactors. Furthermore, the potential of using CFD for design and scale-up of bioreactors was justified by discussing the most recent publications on the topic.

Hydrodynamics and mass transfer characterizing stirred tanks reactors have been deeply studied in the scientific community. The majority of the results were obtained for system like air-water, whereas in the case of non-Newtonian liquids, less data are in general available. In particular, because of technological limitations, correlations to predict bubble size and liquid-side mass transfer coefficient in shear-thinning liquids are scarce; however, these data are needed in order to develop a predictive CFD model for bioreactors.

The interaction with a dispersed phase, can change greatly the liquid hydrodynamics; among the different interphase force terms, the drag force is the predominant one, so it is the only one that is commonly described in CFD models. In the literature, the MRF model has been widely used to solve the rotating parts in the reactors, along with the multiphase Eulerian model. Furthermore, RANS equations represents the main choice to model turbulent multiphase flows, even though closure models for non-Newtonian rheology are still missing. This is an important challenge to take up in the forthcoming years, because it would enhance CFD usability for the design of fermentation process, as most of cell cultures have complex rheology.

Different approaches have been already applied to couple the predicted flow field with the microbial kinetics — mainly defined in terms of simple unstructured models — showing the capabilities of CFD codes to analyze the influence of spatial heterogeneities in terms of nutrients concentrations; analysis of microorganisms lifelines, for example, can be extended to the design of more reliable scale-down simulators, which can then be used for a "rational" design optimization (Haringa et al., 2018). However, the effect of complex rheology in coupled mixing-microbial simulations, needs to be further investigated.

Chapter 3

Experimental setup

In this chapter, the equipment and experimental techniques used throughout the study are presented. As discussed in Chapter 2, data about bubble characteristics in dense bubbly flows are scarce, especially in the case of shear-thinning liquids; this information is necessary because it allows one to obtain the liquid-side mass transfer coefficient from indirect measurements. Knowledge of k_L and its influence on operating conditions (rheology, power draw, gas flow rate) are required to accurately simulate oxygen transfer between the two phases.

Validation of the cross-correlation techniques (or CC) and the subsequent measurement of bubble diameters were the main objectives of the experimental campaigns, which also included the estimation of volumetric mass transfer coefficient, gas holdup, and mixing time. Furthermore, an attempt was made to obtain the liquid velocity inside the stirred tanks by using a Pavlov tube (modified Pitot tube), but as it is discussed later in the text, the technique needed some improvement prior to extend its use to more industrially-relevant operating conditions. For each technique, details of the equipment and its working principle are provided in the text.

Measurements were done at the laboratories of IFPEN in Solaize, where two transparent tanks were used to validate the new techniques and to collect data¹. These tanks were built during the PhD thesis of Gabelle (2012), who used these units to characterize the hydrodynamics and the mass transfer of shear-thinning liquids in aerated conditions.

¹During the experimental part of the study, some interns helped the author to put in place and use the different techniques that were used to characterize the aerated stirred tanks. In order, these interns were: Bastien Barthet (contribution on first measurements with oxygen probes), Dimitri Oyone Nguema (bubble sampling with photographic method), and Yanis Nadri (mixing time measurements).

3.1 The stirred tanks

Two agitated vessels of different size were used during the experiments: one made of temperate glass with a maximum volume of about 40 L and a Plexiglas one of 400 L (T_{30} and T_{60} respectively). Both tanks were equipped with four lateral baffles. The main geometrical details for both the tanks are shown in table 3.1. All the experiments were run in the standard configuration, by respecting geometrical constraints, so all the main sizes and clearances can be expressed as a multiple of the tank diameter. The height of the liquid H , for example, was set to $H/T = 1$ which led to a volume of 21 L in T_{30} and of 170 L in the bigger tank (figure 3.1). With this configuration, only an impeller can be used, and the choice has fallen upon the Rushton turbine. In fact, as already stated in the previous chapter, disk turbines represent a good choice when the gas is injected from the bottom of tank below the impeller because of its capacity to disperse efficiently the gas. Furthermore, more data are available for the Rushton turbine in the literature.

Table 3.1: Characteristic dimensions of the tanks.

Tank Size (m)	T_{30}	T_{60}
T	0.3	0.6
D	0.1	0.2
H	0.3	0.6
h_D	0.1	0.2
h_S	0.05	0.1
B	0.02	0.04

Air at 2 bar was injected by means of a ring sparger, placed below the turbine disk and slightly smaller than this. The sparger installed in T_{30} and T_{60} had, respectively, 25 and 120 evenly spaced holes of a diameter of 1 mm, through which the flow rate was varied between $0.5 \text{ Nm}^3 \text{ h}^{-1}$ and $20 \text{ Nm}^3 \text{ h}^{-1}$; with this interval of flow rates, the available superficial gas velocities were within the range $0.5\text{--}40 \text{ mm s}^{-1}$.

The top of the tank T_{30} was too small to accommodate the moving supports for the probes, so only one radial position was accessible for measurement with the optical probe. For this reason, only the bigger vessel was used to obtain bubble size and gas fraction at different positions in the liquid. In order to adapt the optical probes and the Pavlov tube and to have access to different zones in the tank T_{60} , a preliminary modification on the vessel was made. The support consists of a shaft that can slide axially, and which is bolted on two plates (figure 3.2) that can move along the radial direction. By coupling the two allowed movements, it was possible to investigate a wide area inside the tank, placed in a midplane between two adjacent baffles.

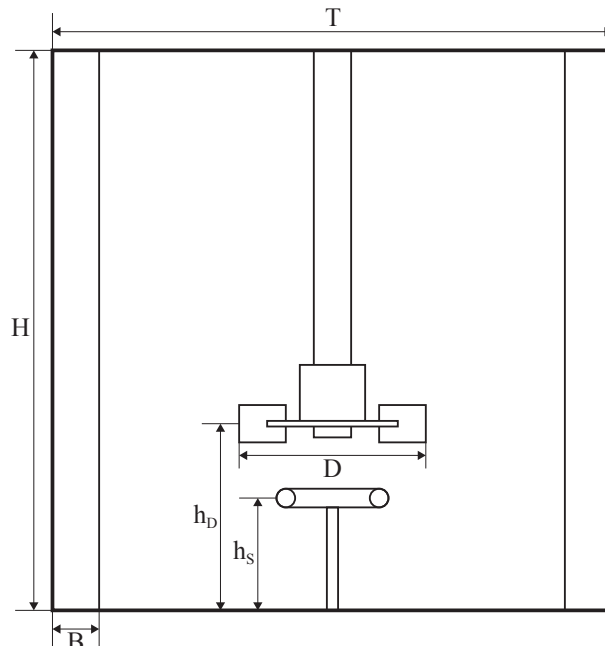


Figure 3.1: Geometrical details of the tank.

3.2 Model fluids

At the end of fermentation, the liquid phase of *Trichoderma reesei* contains a considerable amount of proteins — mainly cellulase but also hydrophobins that act as surfactants (Cox et al., 2009; Tchuenbou-Magaia et al., 2009) — and additives (pH regulator, antifoam agents, etc.), which have an impact on the mass transfer rate because of their effect on bubbles coalescence and interface phenomena. However, because of its irregular composition, the fermentation broth is scarcely reproducible, and a model fluid is more suitable to quantify the effects of rheology and surfactants. In the case of filamentous fungi, rheology is strictly linked to the concentration of the microorganisms, which changes during fermentation.

The presence of this solid suspension in the liquid prevented the use of the cross-correlation technique in the fermentative medium, due to the probe's fragility. Filtration of the culture broth made the measurement possible, but at the expenses of the rheological properties; the filtered broth was, in fact, characterized by a water-like rheology, with a high content in proteins. Gabelle et al. (2012) measured the viscosity of the system during the fermentation of *Trichoderma reesei*, showing that xanthan gum (XG) solutions at different concentrations can be used to reproduce the rheological behavior of the broth during its fermentation. Two mass concentrations of the polymer were used in this study: 0.25% and 0.50%. The latter had a rheology very similar to the broth's at the end of the fermentation process. When dissolved



Figure 3.2: Detail of the moving trail support that was mounted in the tank T_{60} .

in water, XG creates an opaque solution, so it could not be used to validate the bubble size measurement technique using visualization. During the first part of this study, carboxymethyl cellulose (CMC) at concentrations 0.25% and 0.50% was used instead.

The aqueous solutions of these polymers exhibit shear-thinning properties (i.e. the viscosity decreases with the shear rate). The apparent viscosity of the solutions was expressed with the Ostwald-de Waele relationship:

$$\mu_{app} = K\dot{\gamma}^{n-1} \quad (3.1)$$

where K is the consistency index (Pa s^n), n the flow index, and $\dot{\gamma}$ the average shear rate (s^{-1}). Rheological properties for the model fluids at varying concentrations are reported in table 3.2. At higher polymer concentration — because of appearance of viscoplastic effects — a more complex model would have to be used to express the apparent viscosity.

Table 3.2: Rheological indexes for xanthan gum and carboxymethyl cellulose for the different concentrations. Both of the polymers were provided by *Sigma-Aldrich*, USA.

Fluid	Concentration %	K (Pa s^n)	n (-)	Use
CMC	0.25	0.05	0.82	Validation of CC
	0.50	0.44	0.65	
XG	0.25	0.70	0.38	Influence of rheology
	0.50	2.77	0.24	

In their recent study, Gemello et al. (2018) investigated the effect of ethanol on bubble coalescence in water and showed that even at a very low concentration, the alcohol reduced the bubble size in the bubble column. To modify the coalescence of the system, ethanol at a concentration of 0.05%_{vol} was dissolved in the tested solutions. Rheological characterization

showed that at this concentration, ethanol had no effect on the rheology of xanthan gum solutions. As a consequence, adding a small amount of ethanol was considered a potential solution to mimic the influence of all the additives that are dissolved in the fermentation broths, and which are suspected to partially block coalescence. However, other possibilities, as the addition of surfactant, will also be presented.

3.3 Bubble size measurement

The Sauter mean diameter was obtained with a dual fiber optic probe manufactured by *A2 Photonic Sensor*, France. It consists of two phase-detective glass probes vertically aligned, connected to an optoelectronic module. As said before, this measurement technique was already validated in bubble columns, at high gas fraction. The acquisitions were done at 1 MHz and the repeatability error was found to be $< 3\%$. The characteristics of the probe were chosen based on the expected bubble size and gas fraction in the tank; the most important specification is the clearance d between the two detective tips. In fact, the smallest detectable bubble diameter is equal to the tips' gap. In figure 3.3, the dual probe and its characteristic signal are shown. Once outside its protection cap, the diameter of the sensor's body was only 3 mm, while the inter-probe distance was $d = 730 \mu\text{m}$.

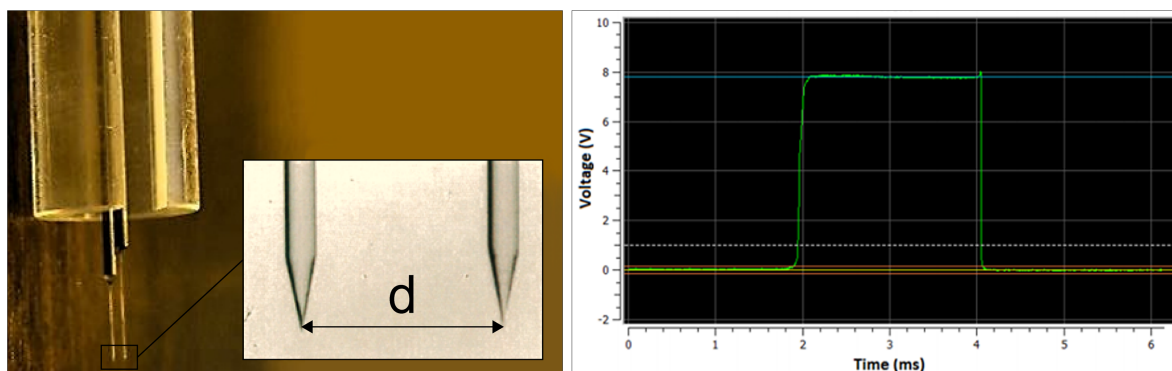


Figure 3.3: Detail of the optical probe and its plastic protection (left) and shape of the signal when a bubble is detected by the sensor (right).

The two probes simultaneously carry two signals, which can be cross-correlated in terms of the Eulerian spatial correlation coefficient $R_g(d)$:

$$R_g(d) = \frac{\int_{t_0}^{t_{exp}} S_A(t)S_B(t)dt}{\int_{t_0}^{t_{exp}} S_A(t)dt} \quad (3.2)$$

$S_i(t)$ is the instantaneous signal of the probe i and t_{exp} is the total time of the measurements.

The latter has to be long enough to ensure convergence, i.e. when at least 5000 bubbles were detected by the sensor. Raw signals were normalized in order to have $S_i(t) = 0$ or 1, depending on whether the probe's tip was in the liquid or in the gas phase respectively. The correlation coefficient is then obtained statistically, by considering the events where both probes' tips are inside a bubble simultaneously ($S_A(t) = S_B(t) = 1$). Unlike classical techniques based on the use of intrusive phase-detective probes, the de-wetting time — used to obtain the bubble diameter from the measurements of the bubble velocity — is not taken into account with the cross-correlation method, so no hypothesis about bubble trajectory were needed. However, the only issue related to bubble trajectory remained the possible interaction with the support of the probe.

Raimundo et al. (2016) derived a model for $R_g(d)$ by performing Monte Carlo simulations in which they considered different inter-probe distances, bubbles' shapes and their orientation with respect to the sensor, finding a unique relationship between the cross-correlation coefficient and the ratio $d/d_{h,32}$:

$$d_{h,32} = a_{shape} \frac{d}{R_g(d) - 1} \pm 10\% \quad (3.3)$$

where a_{shape} is a regression coefficient that depends on the bubble's shape. Raimundo et al. (2016) provided $a_{shape} = -1.4720$ for spherical bubbles and $a_{shape} = -1.5978$ in the case of oblate bubbles. Normally, in air-water systems, bubbles larger than 2 mm deviate from the spherical shape. At the studied operating conditions, bubbles can be described as oblate spheroids; therefore, the *horizontal* diameter measured with the optical sensor (with $a_{shape} = -1.5978$) was converted using the following equation:

$$d_{32} = \sqrt[3]{d_{h,32}^2 d_{v,32}} = \sqrt[3]{d_{h,32}^3 E} \quad (3.4)$$

where E is the height-to-width ratio of the bubble. Equation (3.4) was found to be a very good approximation (error < 2%) of the more rigorous calculation based on conservation of the surface/volume ratio. The bubble's aspect ratio was calculated with the equation of Weltek et al. (1966), originally derived for liquid-liquid dispersion but also validated in gas dispersed systems (Clift et al. (2005)):

$$E = \left(1 + 0.163 Eo^{0.757}\right)^{-1} \quad (3.5)$$

where Eo is the Eötvös number.

The optical probe was inserted from an opening at the top of the tank T_{30} in between two adjacent baffles. Due to geometrical constraints, it was not possible to move the probe along the radial direction, so the only accessible position was at a distance $T/3$ from the center of the tank (i.e. the location midway between the impeller blade tip and the vessel wall). The validity of using a single measurement to describe the distribution of mean bubble diameters is

discussed in Section 4.3.1.

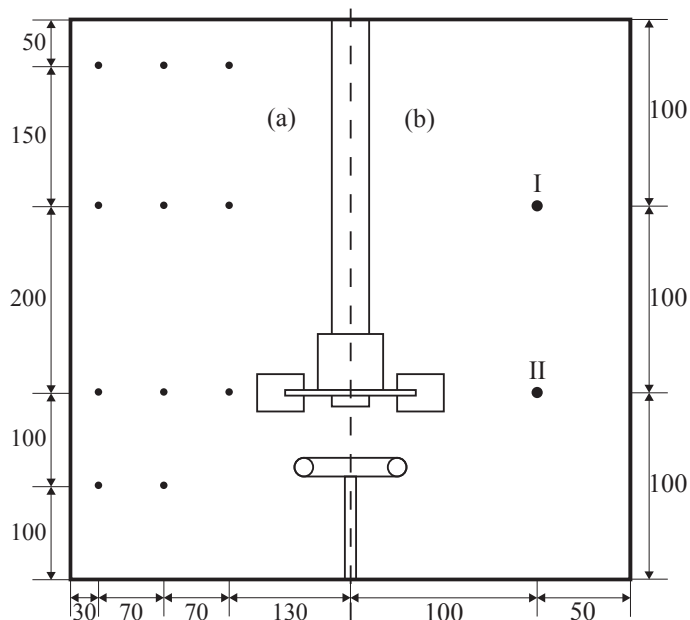


Figure 3.4: Locations investigated with the optical probes inside the tanks T_{60} (a) and T_{30} (b). In the small tank, the point II was also used for mass transfer coefficient measurement.

To check the accuracy of the technique in stirred tanks and in non-Newtonian fluids, data obtained with the probe were compared to Sauter diameters calculated from photographic analysis at *low gas fraction* and in CMC solutions. Pictures were taken with a Nikon D300S placed 1 m away from the tank, and two LED panels were installed behind the vessel to enhance the visibility inside the liquid. The camera mounted a 105 mm lens with a focal ratio $f/2.8$ and a shutter speed of $1/1600$ s was used. Finally, the pictures were manually analyzed with the open source software *ImageJ*, and each bubble was considered oblate ellipsoid (i.e. surface and volume were obtained by measuring the major and minor axis). The Sauter mean diameter was then calculated from the surface and volume of every ellipsoid:

$$d_{32} = \frac{\sum_{i=1}^{400} V_i}{\sum_{i=1}^{400} A_i} \quad (3.6)$$

where S_i and V_i are the surface and the volume of each bubble. For each condition, pictures were shot at different instants and convergence for d_{32} was obtained by sampling 400 bubbles (Gabelle (2012)). An example of image used for the photographic analysis is represented in figure 3.5.

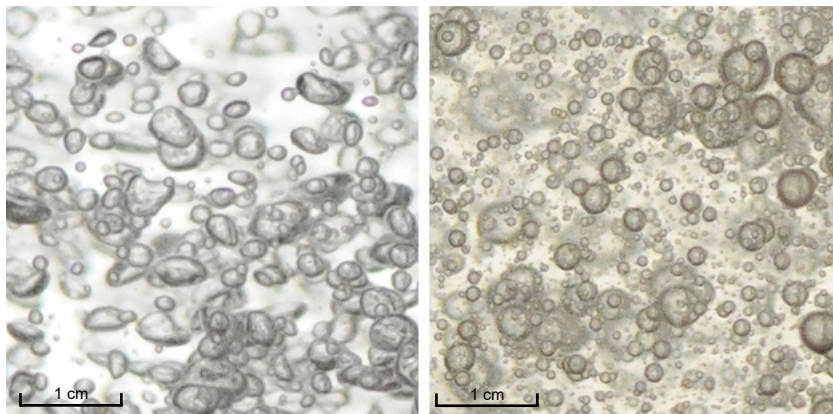


Figure 3.5: Frames acquired in water (left) and in a solution of CMC 0.50% (right) at the same operating conditions. Only bubbles with a sharp outline were measured.

Frames had a resolution of about $4\text{ cm} \times 4\text{ cm}$ and were centered with respect to the position of the optical probe. Moreover, the focus plane was placed at about the same location of the probe's tips; consequently, bubbles close to the wall were not taken into account. Results from image analysis also verified the assumptions on the bubbles' shapes, and average aspect ratio in water and CMC was in the range 0.75–0.90, in agreement with Eq. (3.5).

3.4 Gas holdup

The global gas holdup was obtained visually by measuring the increase in liquid height due to the gas dispersed in the solution. The fraction of the gas volume was then defined as:

$$\alpha_g = 1 - \frac{H_0}{H_g} \quad (3.7)$$

where H_0 is the initial height prior to inject air and H_g is the average height of the free surface in the aerated system. The global gas holdup was also compared to the local gas fraction measured with the dual-probe in a larger tank (see Section 4.2) and integrated over the section of the tank.

3.5 Volumetric mass transfer coefficient

The global mass transfer coefficient was calculated by a dynamic technique as previously described by other authors (Devi & Kumar, 2017; Gabelle et al., 2012; Garcia-Ochoa & Gomez, 2009; Labík et al., 2017). The oxygen present in the liquid is initially stripped by injecting nitrogen. Then, the feed is turned off and gas bubbles can leave the liquid. Finally, the agita-

tion of the tank is restored, and the air is injected at the desired flow rate until the dissolved oxygen has reached the saturation concentration. Clark-type oxygen probe (*fast OX-100*, manufactured by *Unisense*, Denmark) was used to measure the concentration of dissolved oxygen in the liquid. The probe was placed in the midplane between two adjacent baffles and in the impeller discharge region in order to minimize the influence of liquid film renewal at the probe tip, which can affect the reading, especially in highly viscous media (figure 3.4). The dynamic method was used to obtain the value of the volumetric mass transfer coefficient. The concentration curves were then analyzed by considering the liquid as if perfectly mixed and the gas phase as if moving in a plug flow reactor (Gabelle et al. (2011)); $k_L a$ was obtained by solving the following set of differential equations of oxygen balance in both phases:

$$\frac{dC_l}{dt} = \frac{k_L a}{1 - \alpha_g} \left(\frac{\bar{C}_g}{m} - C_l \right) \quad (3.8)$$

$$\frac{\partial C_g}{\partial t} = -\frac{Q_g}{S\alpha_g} \frac{\partial C_g}{\partial x} - \frac{k_L a}{\alpha_g} \left(\frac{C_g}{m} - C_l \right) \quad (3.9)$$

The system is solved with MATLAB 8.6 and the initial values of $k_L a$ and t_0 (i.e. the time at which oxygen enters in the system) have to be provided. The concentration profile obtained is then compared to the experimental one and the error between these two curves is minimized with the method of least squares. The values of $k_L a$ and initial time are modified until the difference of the two profiles is acceptable.

The probe response time was measured in water and polymeric solutions, and it was found to be <0.6 s, which was also more than five times less than the characteristic transfer time ($1/k_L a$). Therefore, the probe dynamics was found negligible and not taken into account (Al-Rubeai et al. (2015)). From a repeatability analysis, the precision of the measure was assessed at 7%. However, according to Pinelli et al. (2010), when the accuracy of the physical models was also accounted for, a minimum uncertainty of 20% had to be considered.

3.6 Mixing time

The mixing time was measured in the small tank T_{30} , in water and xanthan gum solutions. Mixing time was calculated by using a colorimetry technique: a dye was injected in the liquid, and its variation over time was recorded with the same camera that was described in Section 3.3. Two LED panels were placed behind the vessel to increase the visibility inside the vessel, and the lights of the room were turned off to reduce the influence of unwanted reflections. The video so captured was divided in several frames, which were then analyzed with the utility *plug im!*, a freeware in-house image processing platform. Thanks to one of the software algorithms, the concentration of the dye was associated to the color intensity in each image; the tracer

color level was done at different zones of the vessel, by mean of a mask, like the one showed in figure 3.6b. Finally, the software ignored the black zones, while recorded the color intensity inside the tank where the white regions of the mask were located.

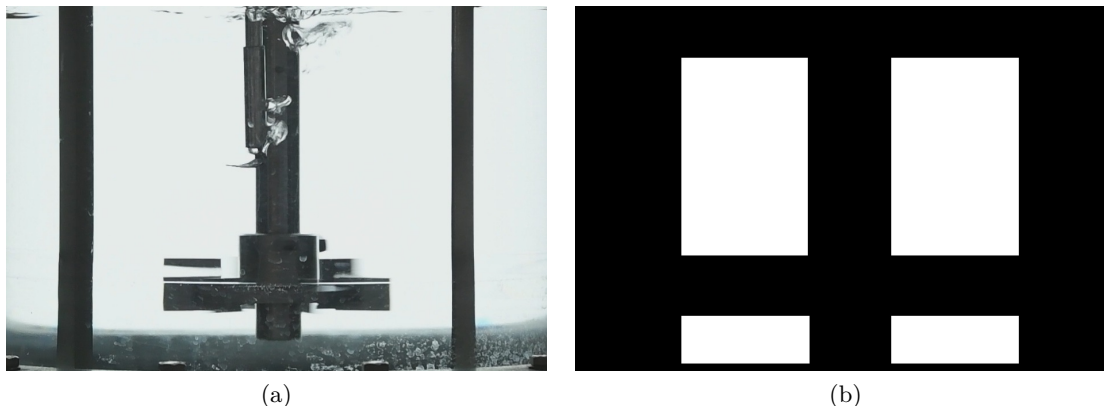


Figure 3.6: Mask creation for image treatment from the first frame of the video (a). The software registered pixels' brightness in each of the white zones (b).

The dye was a dilute solution of Drimaren violet R-2RL, which is a dye used in the textile industry. The injection system has a great influence on the measure, especially when the mixing time is of the order of seconds. After injecting 10 ml of tracer, a second syringe filled with water helped to have a quick injection of the dye (Gabelle, 2012).

The algorithm analyses the brightness of every pixel inside the windows of the mask, in terms of grey level. For each region, the algorithm computes the mean value of brightness S (that normally ranged between 0 and 255), which has to be normalized between the final value S_∞ when a complete mixing is reached, and the initial non-zero value, S_0 (Paul et al., 2004):

$$S'(t) = \frac{S(t) - S_0}{S_\infty - S_0} \quad (3.10)$$

For a better reading of the data, the logarithm of the variance was considered, and the contribution of every zone was taken into account by considering the RMS of the variance (figure 3.7):

$$\log \sigma^2 = \log \left\{ \frac{1}{4} \left[(1 - S'_1)^2 + (1 - S'_2)^2 + (1 - S'_3)^2 + (1 - S'_4)^2 \right] \right\} \quad (3.11)$$

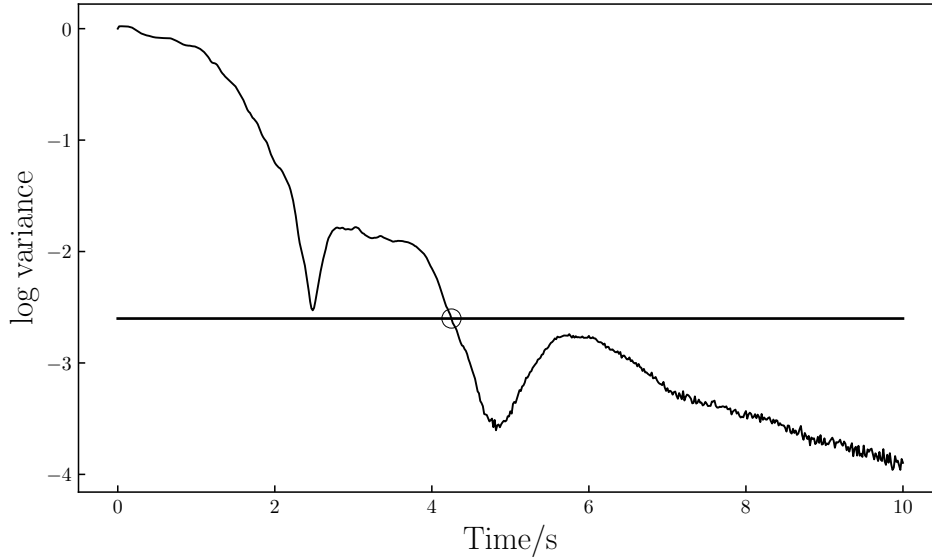


Figure 3.7: Log variance versus time plot. The horizontal line represents a level of mixedness of 95%.

3.7 Liquid velocity

In the range of operating conditions investigated, the volume gas fraction is too high to make usable techniques like PIV or LDA (Boyer et al., 2002). The modified Pitot tube, or Pavlov tube, is an intrusive technique that has been used in the case of dense bubbly flows (Cheng et al., 2017). Velocity measurement is done by measuring the differential pressure between two perpendicular tubes. Thus, according to Bernoulli's equation, the mean local velocity can be obtained by averaging the instantaneous velocities:

$$V_l = \frac{\sum_{i=1}^N u_i}{N} \text{ with } u_i = \begin{cases} \left(\frac{2\Delta P_i}{\rho_l}\right)^{0.5} & \text{if } \Delta P_i \geq 0 \\ -\left(\frac{-2\Delta P_i}{\rho_l}\right)^{0.5} & \text{if } \Delta P_i < 0 \end{cases} \quad (3.12)$$

where u_i is the instantaneous velocity calculated from the kinetic energy balance, ΔP_i is the differential pressure captured at the instant i and N is the total number of acquisitions.

Gemello (2018), Raimundo (2015), and Forret et al. (2006) successfully used a two-dimensional Pavlov tube to measure the mean velocity and velocity fluctuations inside a bubble column operating with superficial gas velocity up to 35 cm s^{-1} . The advantage of using a four-tubes Pavlov tube is that two velocity components can be simultaneously measured. In this configuration, two opposing tubes are connected to the same manometer (figure 3.8).

The Pavlov tube that was used in this study was made of four stainless L-shape 5 mm diameter tubes that were arranged inside a stainless supporting tube with a diameter of 40 mm.

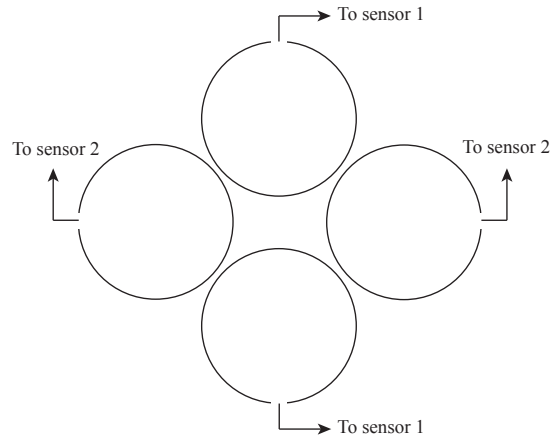


Figure 3.8: Working scheme of the two-dimensional Pavlov tube.

Figure 3.9 shows the measuring probe of the Pavlov tube.

The equipment was introduced inside the tank T_{60} by using the same moving support as for the optical probe (figure 3.2). A blowback system helped getting rid off bubbles that were gradually entrained inside the tubes, decreasing the sensitivity of the pressure measurement. The four tubes were filled with water in order to transmit the local pressure up to the pressure sensors. The differential pressure was measured by means of a pressure transmitter of the PD-33 X series (Keller, Winterthur, Switzerland) and the acquisition time was two minutes at a frequency of 400 Hz.

The presence of vibrations generated by the rotating part of the tank, did not allow to measure the velocity fluctuations. However, the analysis of these vibrations pointed out that



Figure 3.9: Detail of the measuring tip of the Pavlov tube.

their mean contributions on the mean velocity was null, so they should not affect its calculation (figure 3.10).

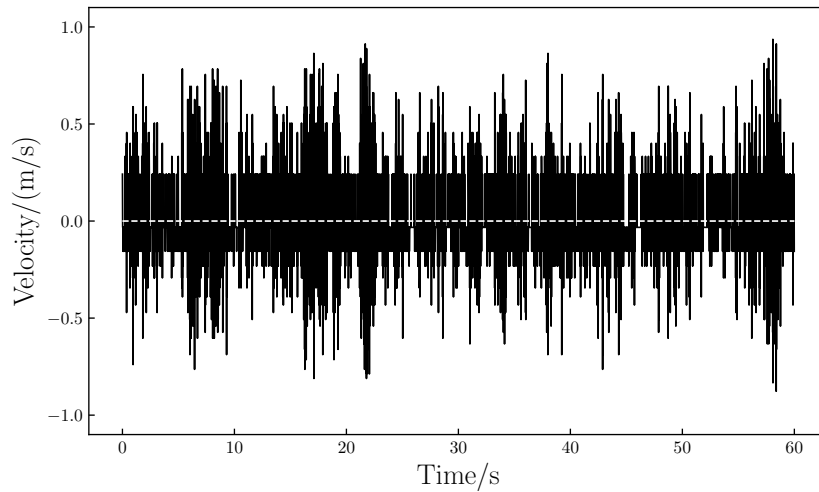


Figure 3.10: Quantification of vibrations. In black continuous line, the instantaneous velocity, whereas the mean value is represented with the white dashed line.

Some authors discussed the limitations of this technique for the case of non-Newtonian fluids (Escudier & Presti, 1996; Smith et al., 1967). In particular, Smith and colleagues, measured the velocity of a polymeric solution with viscoplastic behavior flowing in a pipe. The researchers showed the influence of Pitot tube diameter and polymer concentration on the velocity measurement. The anomalous behavior of the Pitot tube was explained by considering the drag reduction phenomenon that had already been observed in turbulent pipe flows of non-Newtonian liquids (Virk, 1975).

Etemad et al. (2003) used numerical simulations to verify the range of applicability of Bernoulli's equation in the case of power-law fluids, introducing a correction factor for the equation. In their study, the effect of the flow behavior index, Reynolds number, and distance between the static and impact tubes was addressed. In turbulent flows and in the case of small pitot tubes (i.e. the two ports are close to each other) the correction factor was very close to unity, so the velocity could be computed directly from classical equation. Furthermore, shear-thinning liquids behaved almost like water, while shear-thickening liquids ($n > 1$) showed the greatest differences.

In this study, the Pavlov tube was used to measure liquid velocity close to the impeller blade; therefore, a high Reynolds number was obtained even for non-Newtonian liquids. Moreover, only shear-thinning fluids were considered, so Eq. (3.12) was used.

Chapter 4

Characterization of hydrodynamics and mass transfer in aerated non-Newtonian liquids

This chapter contains results and discussion of the experiments that were carried out throughout the research thesis. As it was pointed out in the introductory chapter, the strategy of this study was to achieve a deeper comprehension of non-Newtonian liquids, prior to use CFD to simulate performance of bioreactors.

In Chapter 2, it was already highlighted the lack of information about bubble size in shear-thinning liquid, and the role that this data has in the development of more reliable CFD solvers. In fact, by measuring the Sauter mean diameter and the volumetric mass transfer coefficient, k_L can be estimated and used to model the mass transfer. For this reason, the main part of the experimental research was aimed to the validation of a new technique able to measure mean bubble diameter in gassed shear-thinning liquids. The knowledge of this property, together with measurement of gas holdup and volumetric mass transfer coefficient, led to the estimation of k_L in such systems. Moreover, the role of liquid viscosity, as well as the presence of surfactant were studied and empirical correlations for the quantities of interested were proposed. These results were published in a scientific journal (Cappello et al., 2020). At the end of the chapter, attempts of the local liquid velocity measurements at high gas fraction are presented; some mixing time measurements are also reported.

4.1 Validation of the optical probe measurement

The cross-correlation technique was originally developed to measure average bubble diameter in bubble columns in the turbulent regime with a gas holdup of up to 40% (Raimundo et al., 2016). However, in order to maintain the uncertainty of the measurement below 10%, the global gas holdup should not be greater than 23%. In our study, this condition was always respected, even at high gas velocity. Despite working with a lower gas content, the more chaotic gas flow pattern in a stirred tank, as well as the high viscosity of the model fluids, could affect the reliability of the technique. The outcome of the validation phase is presented in figure 4.1, where it can be seen that the relative standard deviation (RSD) between the diameter obtained with the dual-probe and the diameter from the image analysis was about 11%, regardless of the rheology of the liquid. The optical probe can also provide local values of the gas fraction; from the integration of these values over the volume of the liquid, the global gas holdup can be obtained. This measurement was done in a large vessel, and the comparison with the global gas holdup obtained with the visual method led to a RSD of less than 9%.

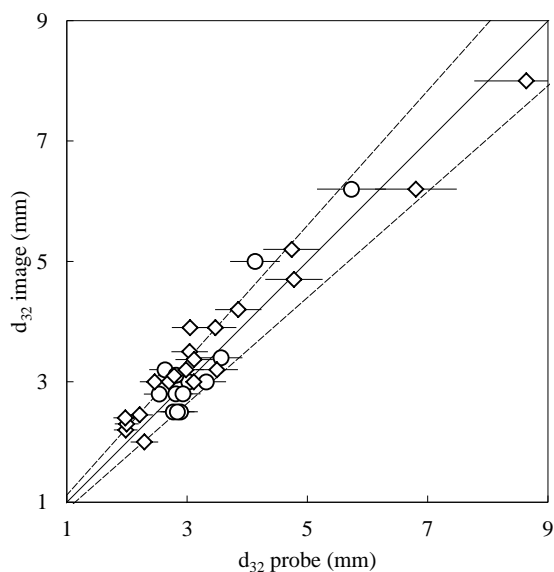


Figure 4.1: Mean Sauter diameter measured with the optical probe and from image analysis. Data refers to: water (\circ), CMC 0.25% and 0.50% (\diamond), $\pm 12\%$ (---), parity line (—).

These findings suggest that the accuracy of the optical probe technique is neither affected by the viscosity of the fluid nor by the hydrodynamics of the mixing tank. Moreover, it is reasonable to also extend the results obtained in CMC to XG solutions, as the two polymeric solutions have similar viscosities under the operating conditions investigated in the validation study. Furthermore, this proved that the volume fraction of bubbles smaller than the distance between probes remained small enough not to impact the calculation of d_{32} . This result is

consistent with that reported by Gabelle et al. (2011), who found that the volume fraction of small bubbles trapped in CMC and XG solutions was lower than 0.4%.

4.2 Spatial distribution of gas holdup and bubble size and effect of the tank size

Firstly, the spatial distribution of the local Sauter mean diameter and gas holdup were addressed. During this phase of the study, the optical probe was inserted inside a larger tank in which more locations were accessible for measurement. Figure 4.2 shows the spatial distribution of the Sauter mean diameter measured in the large tank at two different gas flow rates. Outside the impeller discharge zone, the Sauter mean diameter was almost constant, in accordance with what had been found by other researchers (Alves et al., 2002; Barigou & Greaves, 1992; Bombač et al., 1997). A slightly increase in the bubble size with the liquid height could be noticed. Nevertheless, the standard deviation of the diameters was less than 7%; hence, the definition of a bulk diameter to represent the entire gas phase seems to be valid. The region close to the impeller is not the main focus of this study, so it was decided to not investigate it further in order to avoid an excessive tearing of the optical probe.

Measurements made in both tanks at constant dissipated power and superficial gas velocity showed that d_{32} was practically the same for both vessel sizes. Consequently, the majority of experiments were done in the small tank (T_{30}) in order to investigate a wider range of gas velocities and power draw. In this configuration, the value at the center position between the blades and the wall was used as the representative Sauter mean diameter.

4.3 Effect of rheology and additives on bubble size and mass transfer

The correlations presented in this work are based on the following formalism, which has been widely used in similar studies to describe the volumetric mass transfer coefficient, the gas holdup, and the bubble size (Bach et al., 2017; Gabelle et al., 2011; Garcia-Ochoa & Gomez, 2009; Linek et al., 2004):

$$X (\equiv d_{32}, \alpha_g, k_L a, k_L) = c_1 \left(\frac{P_g}{V} \right)^{c_2} U_g^{c_3} \mu_a^{c_4} \quad (4.1)$$

The regression coefficients c_i were obtained with the least squares method.

Different criticisms can be made on the chosen formalism. For instance, it is a dimensional expression, and the involved quantities are not fully independent from each other. Nevertheless,

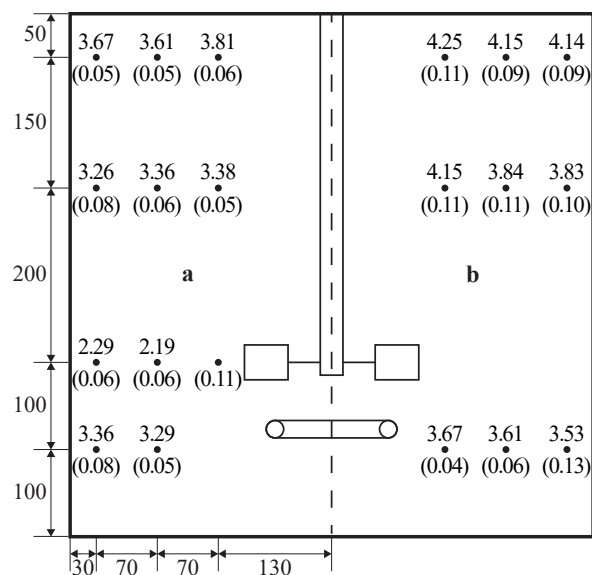


Figure 4.2: Sauter mean diameter in mm and gas holdup (in brackets) in the large tank. Data were collected for $N = 8.3 \text{ s}^{-1}$ and for $U_g = 8 \text{ mm s}^{-1}$ (a) and $U_g = 20 \text{ mm s}^{-1}$ (b). The probe locations are also indicated.

alternative dimensionless expressions — as the ones suggested by Akita & Yoshida (1974) — lead to very complex equations where physical variables can be involved in many independent groups following opposite effects. For this reason, despite its flaws the simple expression Eq. (4.1) stands popular in similar studies.

4.3.1 Sauter mean diameter

The Sauter mean diameter for the studied fluids is presented in figure 4.3. Regardless of the rheology of the liquid, the average bubble size decreased when the power input increased, while it increased with the air flow rate. For a fixed superficial gas velocity, more energy is provided to the liquid by increasing the impeller rotation speed, so breakage phenomena are promoted. The effect of the gas flow rate, on the other hand, is the opposite. In fact, when more gas enters in the system, gas cavities behind the Rushton blades change shape and become bigger, directly affecting the energy transferred by the impeller (Paul et al., 2004). In addition to this phenomenon, bubble coalescence is favoured at higher gas concentration. This effect explains the increase in bubble size at constant dissipated power for different gas velocities.

From the results obtained in demineralized and in tap water, it is clear that the effect of contaminants in tap water was overshadowed by the influence of gas flow rate and dissipated power. The concentration of the polymer had a major effect, especially at relatively low impeller

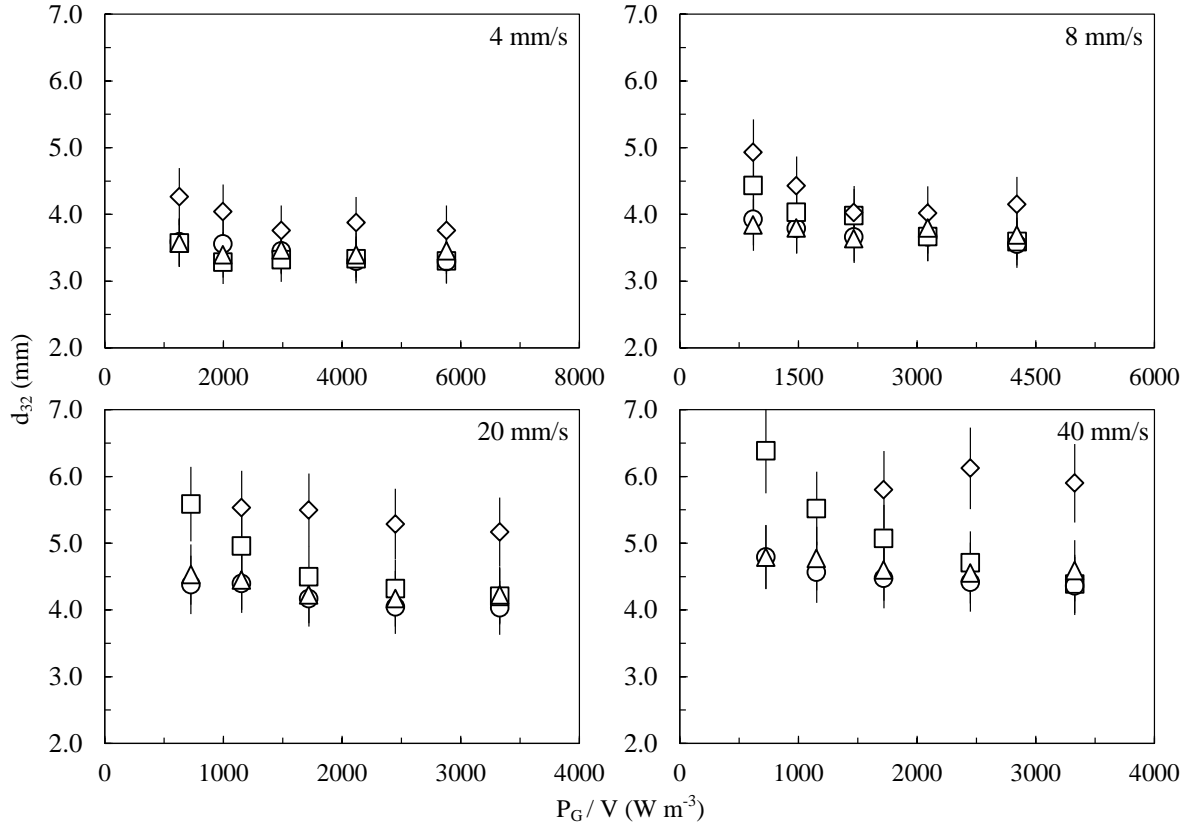


Figure 4.3: Sauter mean diameter at several superficial gas velocities in: tap water (\circ), demineralized water (\triangle), XG 0.25% (\square) and XG 0.50% (\diamond).

speed and high gas flow rate. For example, at $U_g = 4 \text{ mm s}^{-1}$, gas dispersion in XG 0.25% was characterized by the same average diameter as measured in water; while at higher gas velocity, bigger bubbles were measured in the polymeric solution. The Sauter mean diameter approached the values in water only at the maximum rotation speed. In the solution XG 0.50%, the measured bubble diameter was always higher (+22% on average) than the one measured in water at the same conditions even at the maximum impeller speed.

Due to the presence of surfactants and additives, the surface tension of the fermentation broth is different from that of water and polymeric solutions. The surface tension in the filtered broth was found to be 0.032 N m^{-1} ; additionally, xanthan gum did not have any effect on the surface tension. As a consequence, the coalescence mechanisms are drastically affected and the bubble size was expected to be smaller. Measurements with the optical probe confirmed this assumption (figure 4.4).

An image of the fermentation broth during bubble diameter acquisition is shown in figure 4.5. Visually, the gas inside the filtered broth was finely dispersed in the liquid phase with micro-bubbles smaller than the distance between the glass tips of the probe, so they could not be

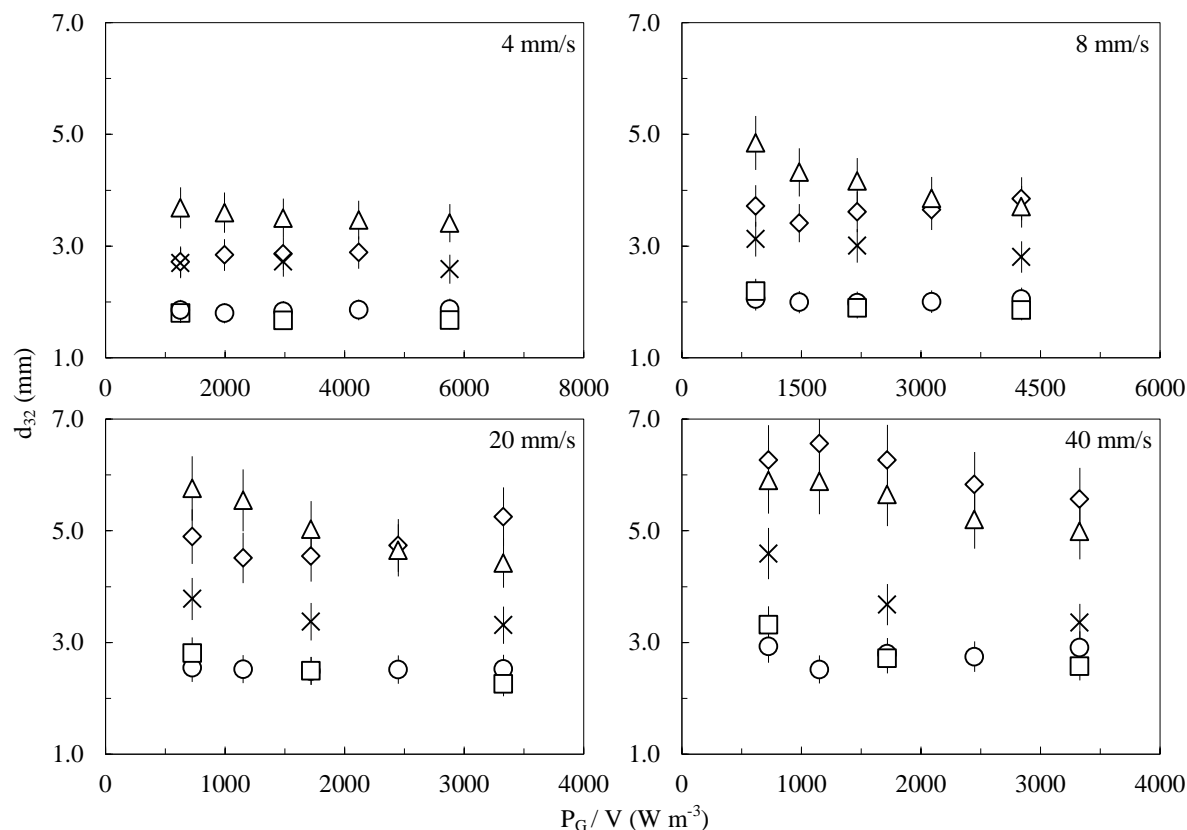


Figure 4.4: Effect of additives on the bubble Sauter mean diameter. Data collected at several superficial gas velocities in: broth (\circ), water + ethanol (\square), broth + XG 0.50% (\diamond), XG 0.50% + ethanol (\triangle), and XG 0.25% + ethanol (\times).

detected. However, the Sauter mean diameter, by definition, should not be affected excessively because of the greater contribution of the bigger bubbles.

For the biological media (i.e. filtered broth and filtered broth + XG 0.50%), the effect of the dissipated power was negligible. Some influence of power input could be noticed only at $U_g = 40 \text{ mm s}^{-1}$ for both of the systems. In the filtered broth, bubble diameter was in the range 1.5–2.6 mm, where the bigger bubbles were measured at high gas flow rate. The same bubble size range was measured in water after the addition of pure ethanol. In fact, the bubble size measured in solutions with ethanol was found to be smaller, as already reported by other authors (Gemello et al., 2018; Machon et al., 1997).

With a concentration of alcohol of 0.05%_{vol}, a reduction in the average diameter of around 50% was measured in water; while in xanthan gum solutions, the reduction was less significant. In XG 0.25% and XG 0.50%, the bubble diameter decreased after the dissolution of ethanol, on average by 25% and 5% respectively. These results indicate that both additives and viscosity affected the mean bubble size, but the latter had a greater impact on the measured d_{32} . After



Figure 4.5: Presence of microbubbles in aerated broth.

adding ethanol, the relative difference between the bubble diameter measured in XG 0.50% and in filtered broth + XG 0.50% was only 6%. Via ethanol dissolution, it was possible to modify the coalescence of air bubbles, thus reducing the bubble size. However, the effect of the alcohol on the bubble surface phenomena is not easy to predict. Machon et al. (1997) studied the effect of electrolytes and alcohols on bubble diameter, concluding that the bubble size cannot be simply correlated to the surface tension of the solution. In fact, at the alcohol concentration used in this study, the surface tension of the solution can be considered constant and equal to the one of water (Gemello et al., 2018; Vazquez et al., 1995).

Figure 4.6 shows the comparison between the correlation proposed in this study and others available in the literature. Alves et al. (2002) correlated their data only in terms of dissipated power only in non-viscous solutions. Furthermore, they investigated superficial gas velocities up to 5 mm s^{-1} . Their correlation reads as:

$$d_{32}/\text{m} = 0.0076 \left(\frac{P_g}{V} \right)^{-0.14} \quad (4.2)$$

Even though the influence of the power dissipated was almost the same, their correlation was not able to predict the experimental data of this work, with an average error of about 30%. Among the few correlations where the viscosity is considered, the correlation proposed

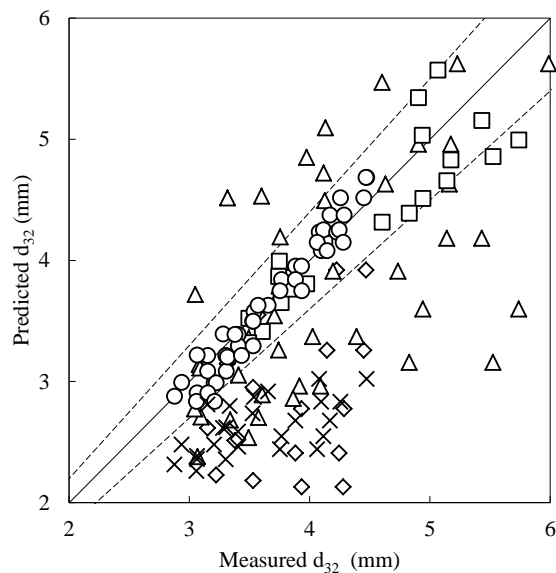


Figure 4.6: Comparison between different correlations to measure the mean bubble size. This work: water (\circ), XG (\square); Bhavaraju et al. (1978): water (\diamond), XG (\triangle); Alves et al. (2002): water (\times); $\pm 10\%$ (---), parity line (—).

by Bhavaraju et al. (1978) led to a similar error (26%). Bhavaraju et al. defined the mean bubble diameter as:

$$d_{32}/m = 0.7 \sigma^{0.6} \left(\frac{P_g}{V} \right)^{-0.4} \rho_l^{-0.2} \left(\frac{\mu_{app}}{\mu_g} \right)^{0.1} \quad (4.3)$$

They derived their equation from theoretical considerations, so the dissipated power appears with the power -0.4 . The correlation proposed in this work (Eq. (4.1), table 4.1) predicted the experimental data with a RSD of 7%. The scatter of the points with other authors' correlations is not surprising because of the different operating conditions investigated (gas flow rate, gas sparger design).

The diameter measurements performed in CMC 0.5% solutions have also been compared with predictions from Eq. (4.1), leading to an error in the value of the bubble diameter below 13%. As CMC and XG solutions exhibited similar behaviours, it could be concluded that the measurement method is well-adapted to both systems.

Decrease in bubble size via proteins dissolution

Surface active agents are naturally produced during the fermentation of *Trichoderma reesei*. These surfactants were identified as class II hydrophobins (HFBII); these fungal proteins present a very high surface activity, reducing the surface tension of the liquid phase up to $30\text{--}35 \text{ mN m}^{-1}$ (Cox et al., 2007). In order to accurately describe the fermentative system, the effect of these

proteins has to be taken into account.

Prior to choose ethanol to hinder bubble coalescence, preliminary tests to study the effect of different protein surfactants were carried out. These measurements were done in a glass-made tank of 25 L. The vessel diameter was 0.23 m and a single Rushton turbine ($T/D = 3$) provided energy to the liquid; four baffles and a ring sparger constituted the rest of the internals. The optical probe was inserted from an opening at the top of the vessel, midway in between two baffles; the probe's tips were submerged up to 14 cm from the rounded bottom of the tank (i.e. about 6 cm above the impeller disk). Two types of proteins were considered: class II hydrophobin (HFBII) and bovine serum albumin (BSA).

Bubbles size was measured in filtered *Trichoderma reesei* batch and in water, after addition of HFBII. The effect of the surfactant concentration is presented in figure 4.7. As it was

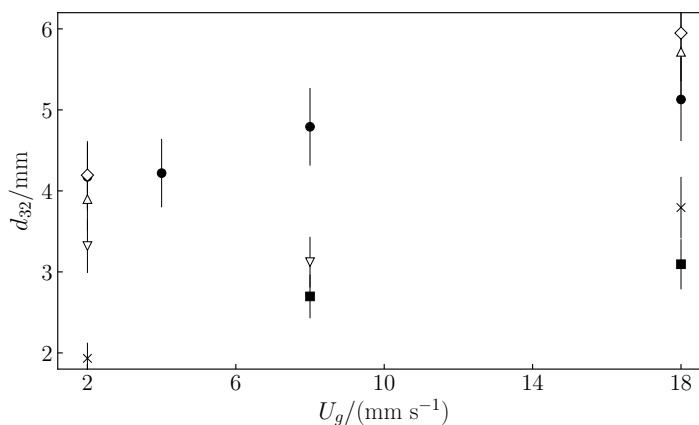


Figure 4.7: Effect of HFBII concentration on the Sauter mean bubble diameter for $N = 11.7 \text{ s}^{-1}$. Water (●), filtered broth (■), water + HFBII 1 mg L^{-1} (◇), water + HFBII 5 mg L^{-1} (△), water + HFBII 20 mg L^{-1} (×), water + HFBII 50 mg L^{-1} (▽).

expected, smaller bubbles were found in the filtered broth, which contained high concentration of proteins. Surface tension for this batch was measured and its equilibrium value was about 37 mN m^{-1} . For HFBII concentration lower than 20 mg L^{-1} , the Sauter mean diameter was comparable to the one measured in water without the addition of surfactant. However, by increasing the protein concentration, bubbles were stabilized to smaller diameters; furthermore, the formation of a stable foam was observed. At a concentration of 50 mg L^{-1} , the foam reached a volume of about 30% of the total liquid volume.

Due to its high cost, pure hydrophobin is not well suited for experimentation at large scale. As a valid alternative, bovine serum albumin proteins were selected by engineers at IFPEN department of *Physical chemistry and Materials*. Foam produced in samples with BSA was comparable to the one generated in by hydrophobins; however, BSA foam was somehow less stable (figure 4.8).

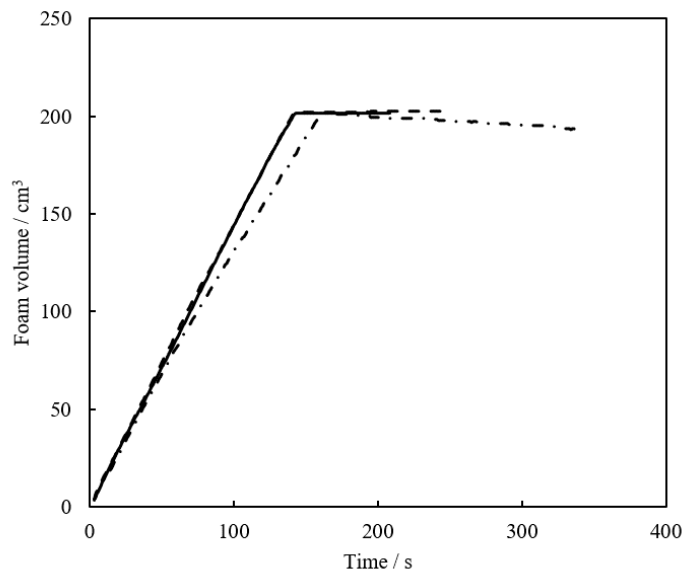


Figure 4.8: Foam stability over time for *Trichoderma reesei* sample (—), water + HFBII (----), and water + BSA (-·-·).

Bovine serum albumin fraction V was provided by *Sigma-Aldrich*, USA. In figure 4.9, the Sauter mean diameter at different BSA concentration is reported. The serum albumin protein

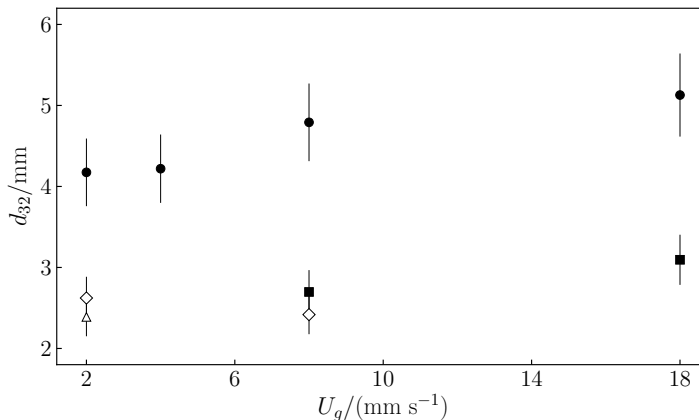


Figure 4.9: Effect of BSA concentration on the Sauter mean bubble diameter for $N = 11.7 \text{ s}^{-1}$. Water (●), filtered (■), water + BSA 25 mg L^{-1} (◇), water + BSA 50 mg L^{-1} (△).

had a similar effect on bubble size, causing a decrease in d_{32} . A concentration of 25 mg L^{-1} was enough to block coalescence in water and form bubbles with a mean diameter of the ones measured in the fermentation broth.

From a physicochemical point of view, surface active proteins such as HFBII and BSA, could be used to reproduce the gas/liquid interface phenomena that take place in a fungal

fermentation broth. However, formation of the foam made their use unpractical for bubble size and $k_L a$ measurements, causing liquid overflowing. Thus, foaming prevented from having reliable experiments, especially in shear-thinning liquids; in fact, viscosity has in general a positive effect on foam stability, decreasing liquid drainage from the foam. Ethanol was therefore used to hinder bubble coalescence in the liquid phase, in order to have in model fluids similar bubble size and gas holdup ranges as in the fermentation broth.

4.3.2 Gas holdup

The global gas holdup in water and xanthan gum solutions at different gas velocities is represented in figure 4.10. By increasing the impeller speed and the power dissipated, more bubbles were "trapped" in the recirculation flow. This caused an increase in the global gas holdup regardless of the liquid studied. The same outcome was found by increasing the air flow rate because of the greater volume of gas dispersed in the liquid phase. As previously discussed, air bubbles are bigger in polymeric solutions where their rise velocity is higher, explaining the lower holdups compared to water. It was only for $U_g = 40 \text{ mm s}^{-1}$ that some differences between tap water and demineralized water were recorded, probably because of the greater importance of bubble coalescence at high gas flow rate, where the presence of contaminants in water has a more important effect. Regression coefficients for Eq. (4.1) are listed in table 4.1 together with the relative error.

Measurements in the fermentation broth (figure 4.11) showed a considerable increase in the gas holdup, consistent with the results on bubble size discussed previously. As expected, adding ethanol to water and polymeric solutions had the same effect, with an average increase in the holdup by 13%. Even though the addition of ethanol into water led to similar values of the Sauter mean diameter in the broth, the gas holdup data were notably different. This outcome could be explained by the presence of micro-bubbles in the fermentation media where they constituted an important fraction of the gas phase, thereby causing an increase in the gas holdup. Therefore, a significant fraction of bubble in the broth were not detected by the optical probe; bubbles smaller than the probes gap cannot be measured, so mean bubble diameters in the broth presented in section 4.3.2 might have been overestimated.

The volume of gas retained in the filtered broth with XG 0.50% was about 30% higher than the values obtained in XG 0.50% aqueous solutions. However, by adding ethanol it was possible to reduce this difference to 15%.

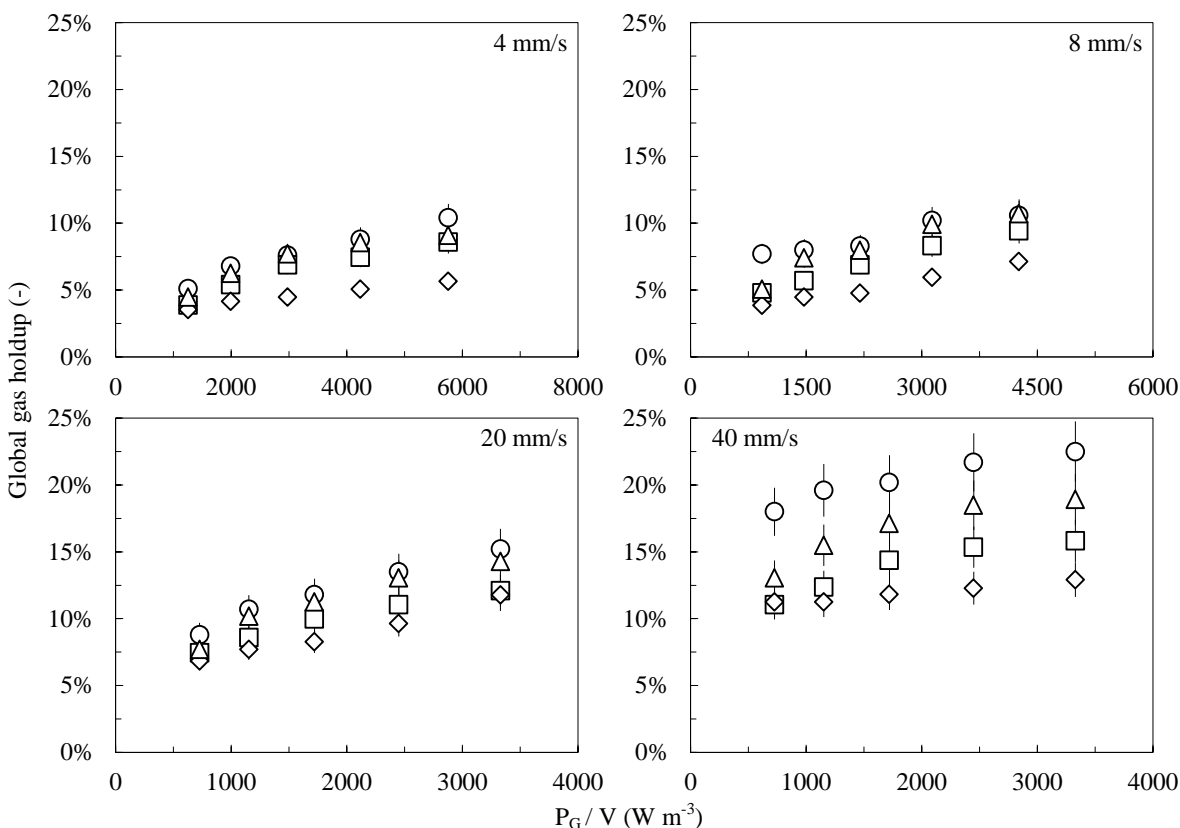


Figure 4.10: Global gas holdup at different superficial gas velocities measured in: tap water (\circ), demineralized water (\triangle), XG 0.25% (\square), and XG 0.50% (\diamond).

4.3.3 Volumetric mass transfer coefficient

The findings presented above point to the conclusion that rheology and contaminants drastically modify the interfacial area. Consequently, they have a certain influence on the mass transfer phenomena. It is widely known that viscosity negatively affects the volumetric mass transfer coefficient in agitated reactors (Gabelle et al., 2012; Garcia-Ochoa & Gomez, 2009). In figure 4.12, $k_L a$ values are reported for all the media analysed except for the filtered broth. In fact, as stated previously, a considerable fraction of gas consists of bubbles smaller than 0.5 mm. It has been reported that under these conditions, the dynamic method to estimate the mass transfer coefficient does not provide reliable results (Pinelli et al., 2010). Small bubbles give a different contribution to the $k_L a$, so different techniques and models have to be used in this case. Compared to water, a loss of 64% and 85% was found for XG 0.25% and XG 0.50%, respectively. If there was any difference between demineralized water and tap water, it was less than the measurement error. The regression coefficients (table 4.1) were found to be in agreement with the values that are normally encountered in the literature (Gabelle et al., 2011;

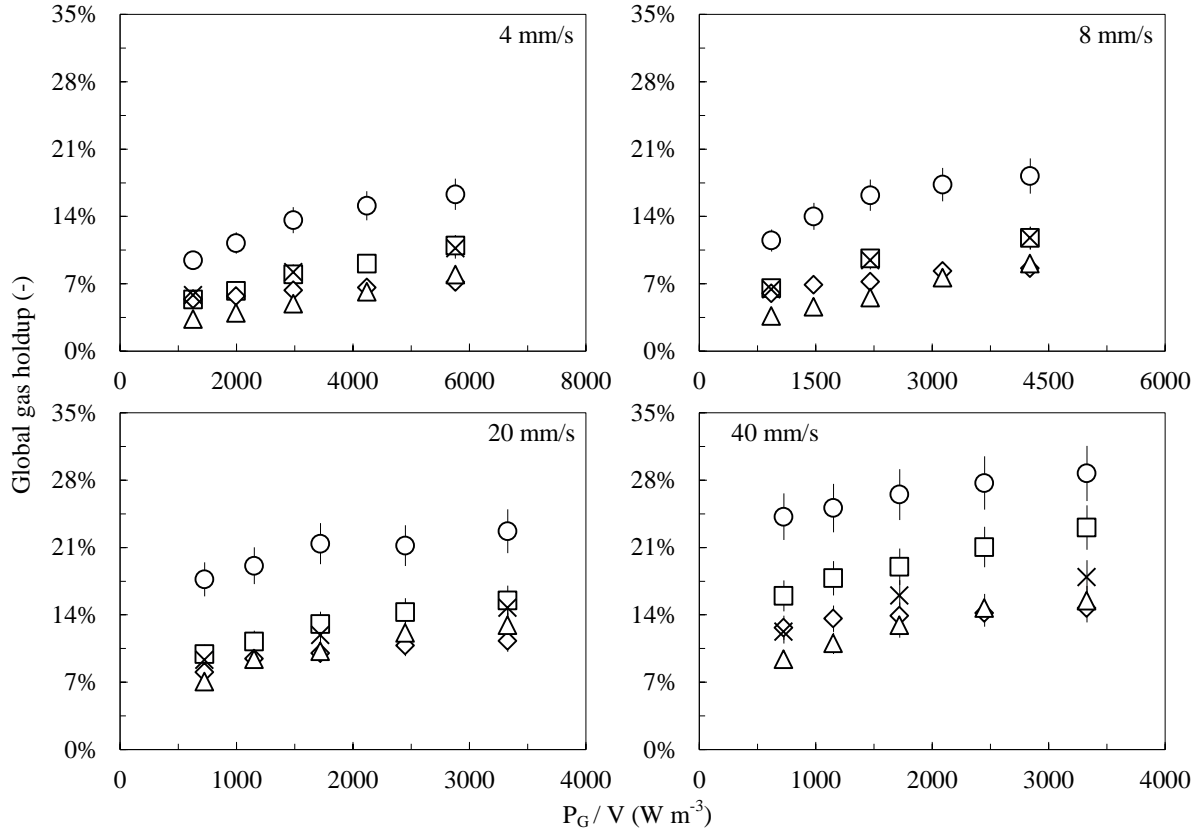


Figure 4.11: Global gas holdup at different superficial gas velocities in: broth (\circ), water + ethanol (\square), broth + XG 0.50% (\diamond), XG 0.50% + ethanol (\triangle), and XG 0.25% + ethanol (\times).

Garcia-Ochoa & Gomez, 2009; Van't Riet, 1979).

The $k_L a$ increased after adding ethanol, the magnitude of its effect depending on the rheology of the liquid. In the case of water, a two-fold increase was observed; while in XG, the effect of the ethanol was dampened by the viscosity, and $k_L a$ values were 50% higher than the ones measured in XG solutions without ethanol.

4.3.4 Liquid-side mass transfer coefficient

With regards to the results presented in Section 4.2, quasi-homogeneous bubble sizes and gas holdups were measured in the tanks (except at the vicinity of the impeller), so it is reasonable to define an average k_L from the measurement of Sauter mean diameter, gas holdup and volumetric mass transfer coefficient:

$$k_L = k_L a \left(\frac{6}{d_{32}} \frac{\alpha_g}{1 - \alpha_g} \right)^{-1} \quad (4.4)$$

Values of k_L for fluids at different rheology are reported in figure 4.13. Although k_L calculations

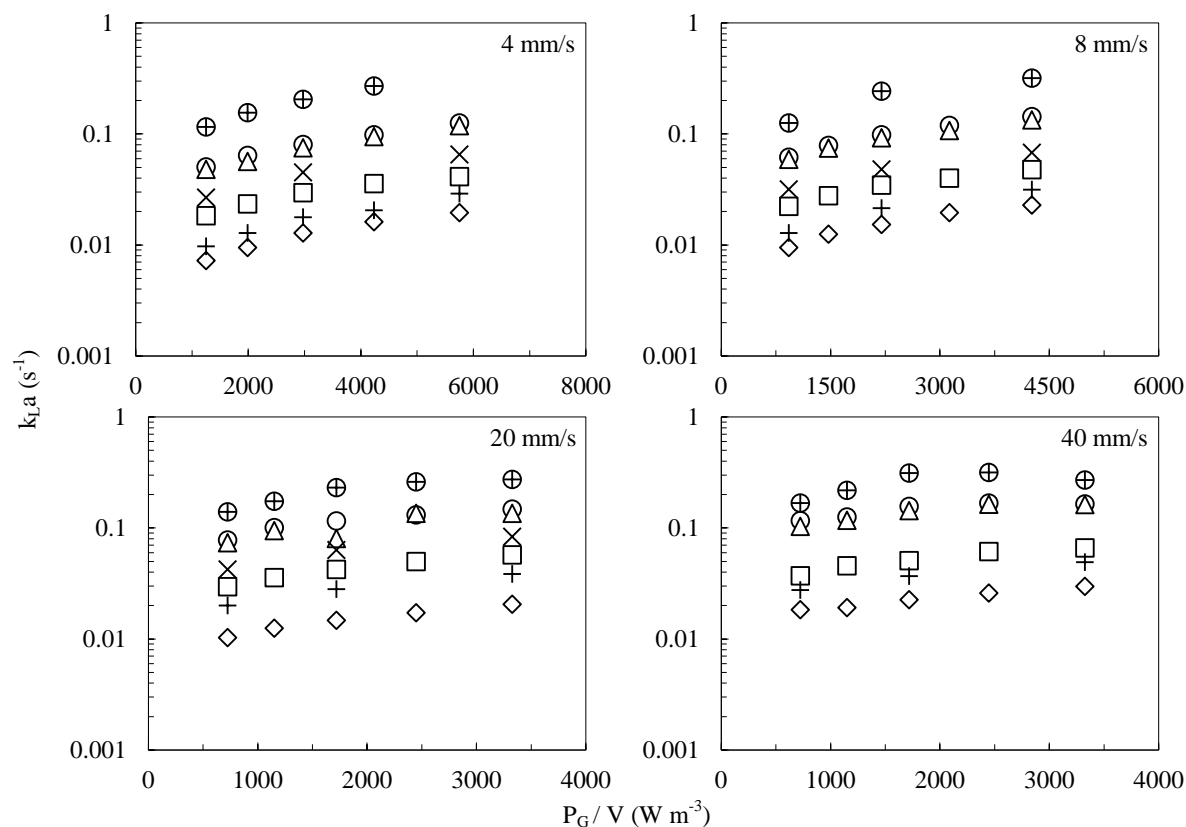


Figure 4.12: Influence of dissipated power and gas flow rate on the volumetric mass transfer coefficient. Data obtained in: tap water (\circ), demineralized water (\triangle), water + ethanol (\oplus), XG 0.25% (\square), XG 0.25% + ethanol (\times), XG 0.50% (\diamond), and XG 0.50% + ethanol ($+$).

were quite dispersed around their respective average values, they did not follow a clear trend with the power input, so data dispersion was attributed to the accumulation of experimental imprecision. The average k_L in water was twice the value in XG 0.25% and more than three times that of the one in XG 0.50%, confirming that the rheology of the system has an important effect on the mass transfer at the gas-liquid interface. By taking into consideration the results discussed in Section 4.3.3, it can be deduced that viscosity hinders the mass transfer because it negatively affects both the interfacial area and k_L . It is important to mention that at the concentration of xanthan gum used in this study, the oxygen diffusion coefficient (\mathcal{D}_l) is the same as in water (Ho et al., 1988); therefore, if Danckwerts's theory is used to describe the mass transfer mechanism, one could assume that rheology influences the surface renewal rate at the bubble's interface (Danckwerts, 1951; Garcia-Ochoa & Gomez, 2009). After adding ethanol, no variations of the k_L values were noticed in water.

As a consequence, the increase of $k_L a$ due to the addition of ethanol in the solutions (figure 4.12) is linked only to the modification of interfacial area. The addition of ethanol in XG

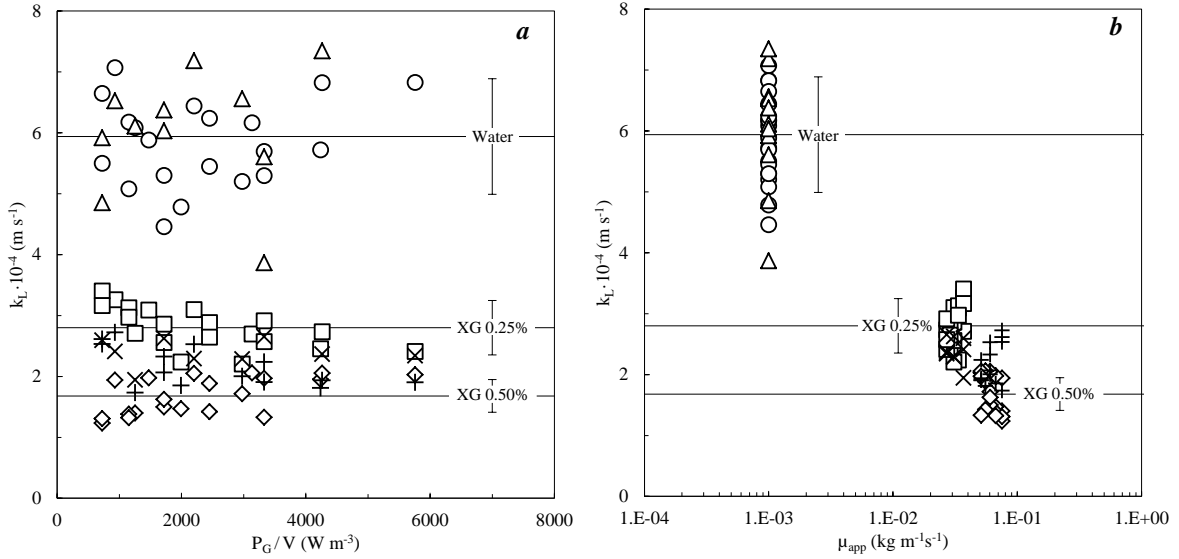


Figure 4.13: Liquid-side mass transfer coefficient as a function of the dissipated power (a) and the apparent viscosity (b). Data obtained in: water (\circ), water + ethanol (\triangle), XG 0.25% (\square), XG 0.25% + ethanol (\times), XG 0.50% (\diamond), and XG 0.50% + ethanol ($+$). For every fluid, error bars ($\pm 16\%$) around the mean value are also reported.

0.25% and 0.50% led to opposite effects on the average k_L : -15% and $+19\%$ respectively. These apparently contradictory outcomes were considered to be solely the result of the inaccuracy of calculation, as they stand close to the associated standard error. Moreover, contrary to most of the findings available in the literature, neither any effect of the dissipated power nor any of the gas flow rate was observed (table 4.1).

Equation (4.1) for k_L can be rewritten in the following form:

$$k_L = 2.56 \cdot 10^{-3} \left(\frac{\rho \mathcal{D}_l}{\mu_{app}} \right)^{0.25} \quad (4.5)$$

To obtain a dimensionless correlation, liquid density and diffusion coefficient were added, but for all of the systems studied, their values were considered to be, in fact, constant.

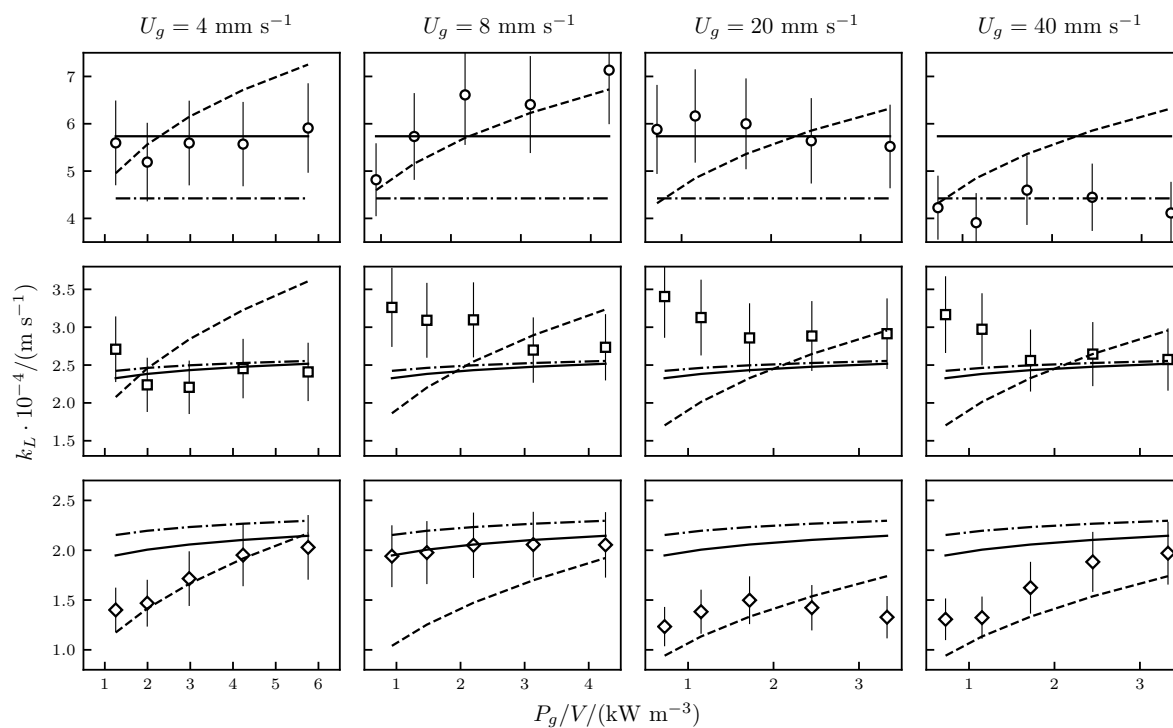
Figure 4.14 shows the comparison between Eq. (4.5) and experimental results for water and xanthan gum solutions; two of the correlations from the literature that exhibited the best agreement are also reported. The graphs emphasized the scarce influence of power draw on k_L .

Most of the correlations proposed in other studies are based on Kolmogorov's theory of

Table 4.1: Regression coefficients for Eq. (4.1). For viscosity calculation, average shear rate was computed with Metzner & Otto (1957)'s equation.

	system	c_1	c_2	c_3	c_4	RSD %
d_{32} m	W, XG	$1.76 \cdot 10^{-2}$	-0.08	0.15	0.04	6.6
	W+EtOH, XG+EtOH	$2.88 \cdot 10^{-2}$	-0.08	0.17	0.17	11.6
	B, B _{XG}	$2.41 \cdot 10^{-2}$	-	0.30	0.16	7.5
α_g (-)	W, XG	$4.68 \cdot 10^{-2}$	0.30	0.45	-0.07	10.8
	W+EtOH, XG+EtOH	$4.20 \cdot 10^{-2}$	0.32	0.44	-0.07	10.8
	B, B _{XG}	$7.50 \cdot 10^{-2}$	0.17	0.35	-0.16	5.8
k_{La} (s^{-1})	W, XG	$1.54 \cdot 10^{-3}$	0.41	0.31	-0.36	14.4
	W+EtOH, XG+EtOH	$5.86 \cdot 10^{-4}$	0.45	0.18	-0.48	17.7
k_L ($m s^{-1}$)	W, XG	$1.01 \cdot 10^{-4}$	-	-	-0.25	16.6
	W+EtOH, XG+EtOH					

W = water, XG = xanthan gum, B = filtered broth, B_{XG} = filtered broth with xanthan gum
 0.50%_w, EtOH = ethanol at a concentration of 0.05%_{vol}.


 Figure 4.14: Liquid-side mass transfer coefficient at different gas velocities. Data for: water (\circ), XG 0.25% (\square), XG 0.50% (\diamond), Equation (4.5) (—), Kawase et al. (1992) (---), Calderbank & Moo-Young (1961) (-.-.).

isotropic turbulence, and they have the following general formula:

$$k_L = C \sqrt{\frac{\mathcal{D}_l}{\nu}} \left(\frac{P_g}{\rho V \nu} \right)^{1/4} \quad (4.6)$$

Several values of C can be found in the literature ranging from 0.3 to 1.13 (Kawase et al., 1992; Lamont & Scott, 1970; Linek et al., 2005; Prasher & Wills, 1973; Zhang & Thomas, 1995). Attempts were made by Kawase et al. (1992) to find the proportionality constant from physical parameters. From the analysis of hydrodynamics, they derived the following equation:

$$k_L = C'(n, K) \sqrt{\mathcal{D}_l} \left(\frac{P_g}{V} \frac{1}{K} \right)^{1/2(1+n)} \quad (4.7)$$

where coefficient C' is a function of the rheological index. For water, the authors provided a value of $C' = 0.301$; C' values for model fluids were obtained from fitting of experimental data. In general, their correlation was able to predict data from this work within an average error of 23%. In both Eq. (4.5) and Eq. (4.7), the viscosity of the liquid phase appears with the same exponent. The correlation of Kawase et al. (1992) shows k_L 's dependence on dissipated power with an exponent equal to 0.25 for water and 0.36–0.40 for model fluids. However, Eq. (4.5) — and more generally the fact that power supply does not explicitly affect k_L — agrees with other correlations from the literature. For example, the correlation proposed by Calderbank & Moo-Young (1961) expresses a liquid-side mass transfer coefficient that depends neither on the bubble slip velocity nor on the dissipated power, but only on physical properties:

$$k_L = 0.42 \left(\frac{\Delta \rho \nu g}{\rho_l} \right)^{1/3} \left(\frac{\mathcal{D}_l}{\nu} \right)^{1/2} \quad (4.8)$$

This relationship depends on the viscosity of the phases, and it is valid for bubbles larger than 2.5 mm. Prediction of our data with Eq. (4.8) led to an average error of 24%. In figure 4.15 the totality of the deduced k_L values are compared with the correlations previously discussed. The total uncertainty of liquid-side mass transfer coefficient was estimated from the error of the experimental techniques used throughout the study, and it was found to be around 16%. However, if the maximum error relative to $k_L a$ data is considered (i.e. 20%, Pinelli et al. (2010)), the uncertainty of k_L rises to 24% that is comparable to the average error of the correlation proposed. It was therefore difficult to precisely quantify the effect of input power on the mass transfer rate.

Beyond the choice of the correlation to estimate k_L , one important question that arose was the definition of average shear rate to calculate the apparent viscosity in the tank (Eq. (3.1)). In the present study, Metzner-Otto's model was considered, but other calculations can be found in the literature, as reported by Pérez et al. (2006) According to Pérez and colleagues,

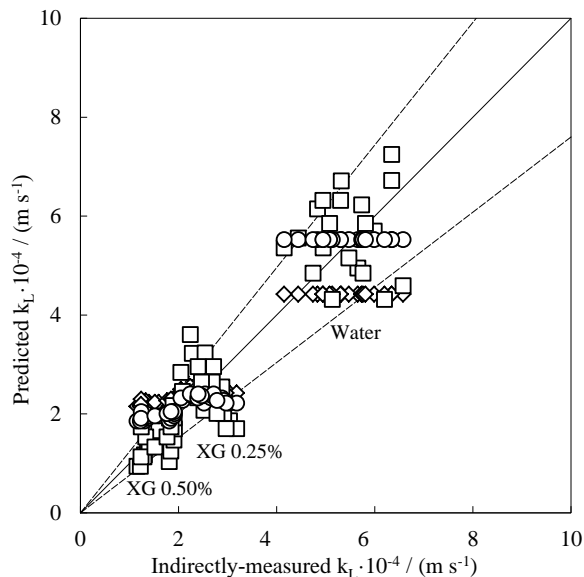


Figure 4.15: Comparison between different correlations to estimate the oxygen transfer rate. Equation (4.5) (\circ), Kawase et al. (1992) (\square), Calderbank & Moo-Young (1961) (\diamond), $\pm 10\%$ (----), parity line (—).

average shear rate in turbulent non-Newtonian fluids depends on rheological indexes, so that $\dot{\gamma} = \left(\frac{1}{K} \frac{P_g}{V}\right)^{1/(n+1)}$. Alternatively, considering that the shear rate in the vicinity of bubbles is governed by the slip between gas and liquid, one could define $\dot{\gamma} \approx \frac{U_g/\alpha_g}{d_{32}}$ (Amirnia et al., 2013). However, when these alternative definitions of the average shear rate were used to estimate the apparent viscosity, very similar regression coefficients for Eq. (4.1) were obtained. In table 4.2, regression coefficients and RSD error are reported in the case where Pérez et al. (2006) was used to compute average shear rate for power-law liquids.

Equation (4.1) for the liquid-side mass transfer coefficient was used to estimate the volumetric mass transfer coefficient, and the comparison with some experimental data is shown in figure 4.16.

In conclusion, in this study it was found that viscosity has a primary role in the mass transfer in stirred tanks, affecting mainly the mass transfer rate. Gas flow rate and impeller rotation speed influenced the measured $k_L a$ as well, but their effect was due to modification of the interfacial area only. In particular, the dissipated power had a negligible effect on the liquid-side mass transfer rate; however, because of the accuracy of k_L data, the influence of power input could have been underestimated.

Table 4.2: Regression coefficients for Eq. (4.1) based on Pérez et al. (2006)'s correlation for average shear rate.

system		c_1	c_2	c_3	c_4	RSD %
d_{32} m	W, XG	$1.94 \cdot 10^{-2}$	-0.08	0.15	0.05	6.5
	W+EtOH, XG+EtOH	$2.00 \cdot 10^{-2}$	-0.04	0.16	0.19	9.5
	B, B _{XG}	$2.16 \cdot 10^{-2}$	-	0.29	0.15	8.0
α_g (-)	W, XG	$4.98 \cdot 10^{-2}$	0.28	0.45	-0.08	10.5
	W+EtOH, XG+EtOH	$4.47 \cdot 10^{-2}$	0.31	0.44	-0.08	9.9
	B, B _{XG}	$8.12 \cdot 10^{-2}$	0.16	0.36	-0.16	6.6
k_{La} (s^{-1})	W, XG	$1.22 \cdot 10^{-3}$	0.40	0.31	-0.40	16.5
	W+EtOH, XG+EtOH	$3.83 \cdot 10^{-4}$	0.44	0.18	-0.55	18.3
k_L ($m s^{-1}$)	W, XG	$9.19 \cdot 10^{-5}$	-	-	-0.26	16.0
	W+EtOH, XG+EtOH					

W = water, XG = xanthan gum, B = filtered broth, B_{XG} = filtered broth with xanthan gum 0.50%_w, EtOH = ethanol at a concentration of 0.05%_{vol}.

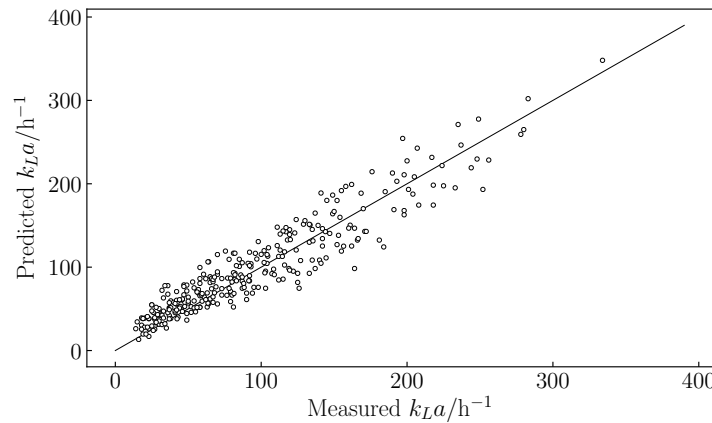


Figure 4.16: Predicted volumetric coefficient versus experimental values. Values obtained in this thesis were integrated by measurements with different impeller configurations and fluids reported in Gabelle (2012). Symbols: k_{La} (\circ), parity line ($—$).

4.4 Mixing time measurement

Measurements of mixing time were done in the small tank, in both aerated and unaerated solutions. In figure 4.17, a sequence of images shows the blending of the tracer after injecting it in the liquid. In the case of the vessel with single impeller, the mixing time is usually relatively short; at this scale and impeller speeds, measured blending times were in the order of seconds.

In figure 4.18, mixing time for water and xanthan gum solutions with and without aeration

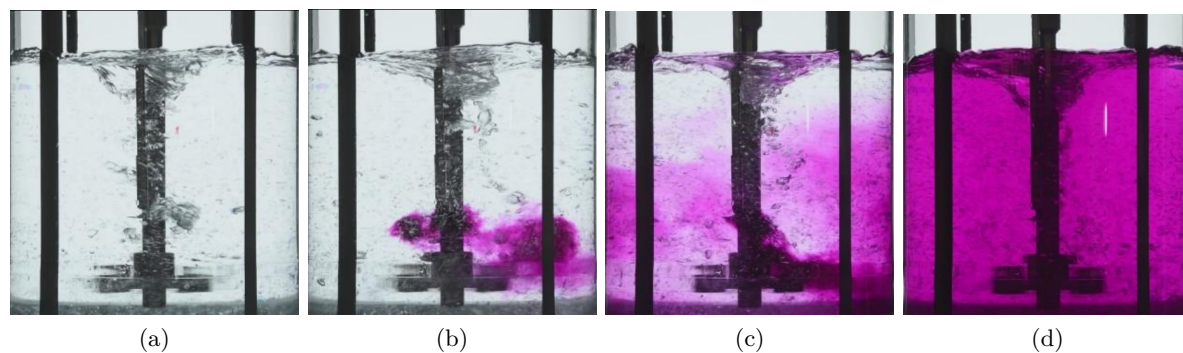


Figure 4.17: Image sequence of the mixing phenomenon in water captured by the camera, from the initial time at which the tracer is being injected (a) to the complete mixing of the tracer (d).

are presented. At higher impeller speed and without air injection, mixing times in water were found comparable to values predicted with the correlation of Grenville (Eq. (2.38)). As already reported in the literature, the effect of gas flow rate was different depending on the impeller speed (Montante & Paglianti, 2015). For example, at $U_g = 40 \text{ mm s}^{-1}$ and low N , the 95% homogeneity in water was reached in a shorter time in comparison to the unaerated mixing; the opposite was found at higher agitation rate.

Compared to water, a longer blending time was measured in solutions of xanthan gum, and the more concentrated the solutions, the longer the mixing time.

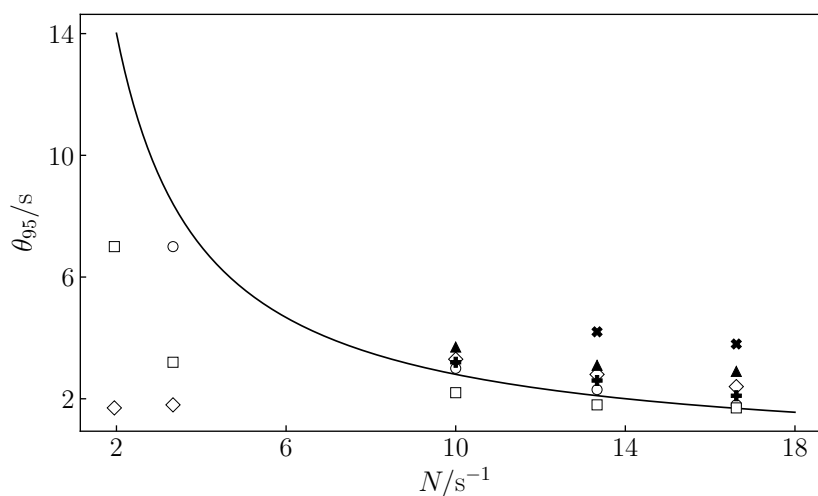


Figure 4.18: Mixing time calculated inside T_{30} for water and 0.25% xanthan gum, at different gas flow rates. Without aeration: water (○), XG 0.25% (▲); $U_g = 8 \text{ mm s}^{-1}$: water (□), XG 0.25% (+); $U_g = 40 \text{ mm s}^{-1}$: water (◇), XG 0.50% (×).

4.5 Liquid velocity measurement

Measurements of the liquid velocity were conducted only in the bigger tank. In this work, two Pavlov tubes with different hole sizes were tested. The two tubes had measuring tips with four holes, of 0.5 mm for the first one and 1.0 mm for the second. Preliminary tests suggested that no remarkable differences were found based on the holes diameters (figure 4.19), so the smaller Pavlov tube was used for the validation part because of its smaller global size.

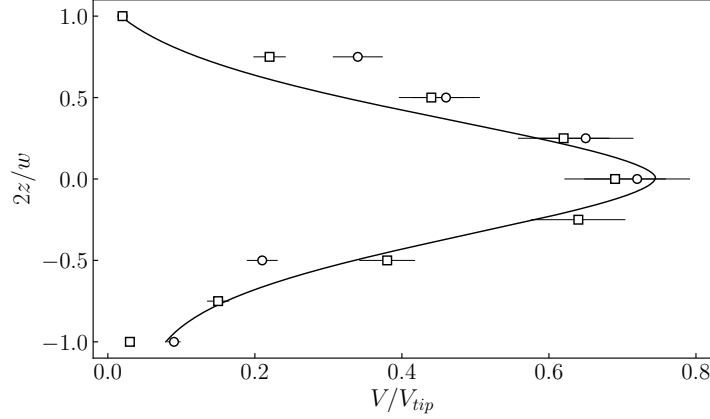


Figure 4.19: Impeller discharge profile of the radial component in water for $N = 1.3 \text{ s}^{-1}$. Holes diameter: 0.5 mm (●), 1.0 mm (■), Venneker et al. (2010) (—).

To assess accuracy of the technique, the set of correlations proposed by Venneker et al. (2010) were used for comparison. For the radial profiles at the disk height:

Axial velocity

$$\frac{U}{V_{tip}} = U_{wall} + (U_1 - U_{wall}) \left(\frac{r}{R}\right)^{-m_U} \tanh^2 \left[C_U \left(\frac{T}{D} - \frac{r}{D} \right) \right] \quad (4.9)$$

Radial velocity

$$\frac{V}{V_{tip}} = V_1 \left(\frac{r}{R}\right)^{-m_V} \tanh \left[C_V \left(\frac{T}{D} - \frac{r}{R} \right) \right] \quad (4.10)$$

Tangential velocity

$$\frac{W}{V_{tip}} = \left[\frac{1}{W_1} + C_W \ln^2 \left(\frac{r}{R} \right) \right]^{-1} \quad (4.11)$$

Here, U , V , and W are the axial, radial, and tangential components, which are normalized respect to the impeller velocity at the blade tip; r is the radial coordinate, whereas R is the impeller radius.

Furthermore, the radial velocity along the height of the impeller's blade was compared to

the values obtained with the following equation:

$$\frac{V}{V_{tip}} = \frac{V_1}{1.048} \exp\left(-C\left|\frac{2z}{w} - 0.01\right|^m\right) - 0.033\frac{2z}{w} \quad (4.12)$$

where z is the axial coordinate from the center of the disk, and w is the blade height. The reader can find the meaning and values of the other variables in the article of Venneker et al. (2010).

The Pavlov tube allows one to measure two velocity components at the same time. However, the best results were obtained for the radial component of the velocity, while for the axial and the tangential the device gave incoherent and non-reproducible results. In figure 4.20 experimental data in water in the range $1.3\text{--}4.2\text{ s}^{-1}$ are presented. The radial velocities were in good agreement with the results available in the literature, and the normalized values were independent on the impeller speed (Venneker et al., 2010). Data for the axial velocity were more scattered and they did not provide reproducible results; the same was found for the tangential velocity (not shown in the graph).

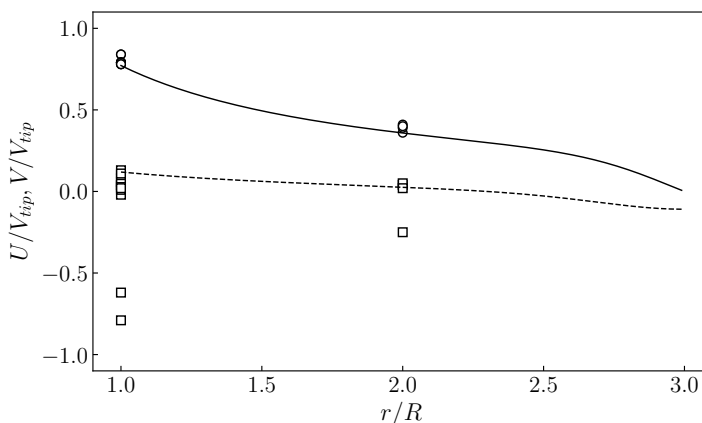


Figure 4.20: Radial profile of the mean velocities in water at the impeller disk level. Normalized radial velocity: experimental (\circ), Venneker et al. (2010) (—); normalized axial velocity: experimental (\square), Venneker et al. (2010) (---).

The axial profile of the liquid velocity at the impeller discharge was then analyzed. The profiles for three impeller speeds are shown in figure 4.21. The radial velocity was found to be close to the one calculated with the correlation proposed by Venneker et al. For each velocity, the measured radial velocity values are in good agreement with the theoretical values, especially close to $z^* = 0$, where the average error did not exceed 20%. Far from the impeller disk, the discrepancy between experimental data and correlation was larger, maybe because of the interaction between the discharge flow and the recirculation loop developed below the impeller. In this zone, in fact, the flow is three-dimensional and the measuring tool was less

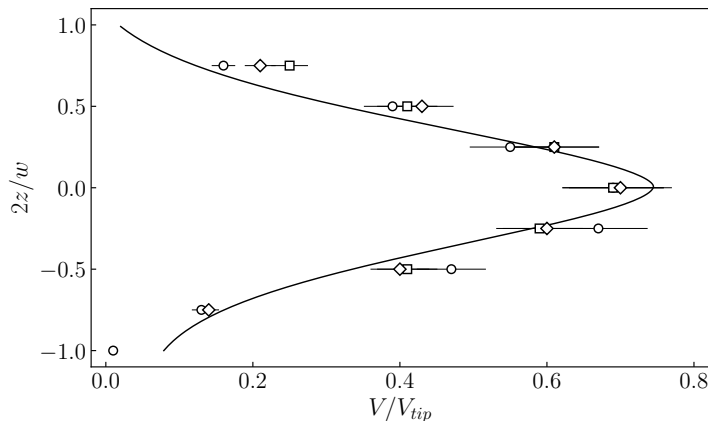


Figure 4.21: Impeller discharge profile of the radial component in water at different rotation speed. 2.5 s^{-1} (\circ), 5.0 s^{-1} (\square), 5.8 s^{-1} (\diamond), Venneker et al. (2010) (—).

precise. The pressure resolution of the sensor used with the Pavlov tube was 0.2 mbar, which corresponds to a velocity resolution of 0.2 m s^{-1} , a value of the same order of magnitude of the liquid velocity for $|z^*| \geq 1$. For every case, the integration of the velocity profile led to a flow number Fl_l in the range 0.76–0.80, comparable to the value 0.78 that is expected for Newtonian fluids at high Reynolds number (Venneker et al., 2010). One of the advantages of the Pavlov tube is that it can be used also in gassed conditions with high values of the superficial gas velocity (Raimundo, 2015).

In Chapter 2 it is written that the presence of gas in the liquid could affect the mixer hydrodynamics in several ways. Some liquid can be trailed by the bubble wakes, so the axial velocity may increase or decrease depending on the initial direction of the liquid flow. Also, the presence of gas cavities behind the impeller blades lowers the energy provided to the liquid, so the pumping in the impeller region and the radial velocity (Venneker, 1999). The effect of the gas dispersion was investigated for $U_g = 1 \text{ mm s}^{-1}$ and the results are presented in figure 4.22. Measured liquid velocity in aerated conditions was compared to the correlation developed by Rousar & Van den Akker (1994), which reads as:

$$\frac{V}{V_{tip}} = 0.7 RPD^{0.34} \exp \left[\frac{-(2z/w)^2}{0.309} \right] \quad (4.13)$$

The radial velocity seemed to be influenced by the presence of the gas even at this relatively low gas velocity, for which the P_g/P_0 was equal to 0.8. A decrease in the liquid velocity could be noticed for the first half of the blade, with a diminution of about 12% at the impeller disk height. However, in the bottom half of the blade, the liquid velocity in the gassed conditions was higher.

In figure 4.23 the radial liquid velocity along the blade tip is presented for a solution of XG

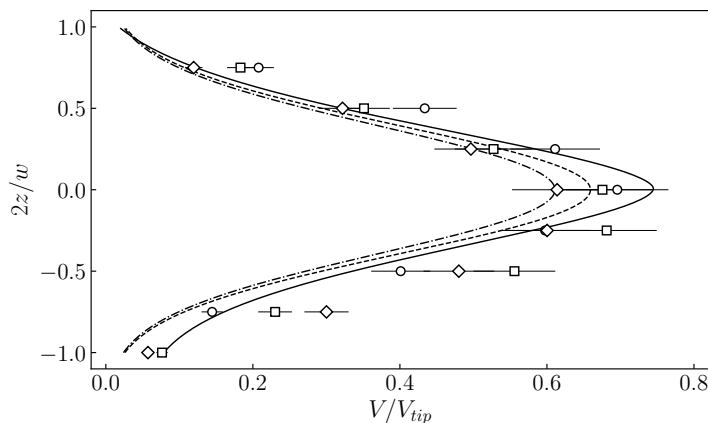


Figure 4.22: Influence of the gas dispersion on radial velocity at the impeller discharge region in water, for $N = 5.8 \text{ s}^{-1}$. Single phase flow (\circ), $U_g = 1 \text{ mm s}^{-1}$ (\square), $U_g = 4 \text{ mm s}^{-1}$ (\diamond), Venneker et al. (2010) (—), Rousar & Van den Akker (1994) ($U_g = 1 \text{ mm s}^{-1}$) (---), Rousar & Van den Akker (1994) ($U_g = 4 \text{ mm s}^{-1}$) (-.-.).

0.1% and water, at $N = 5.8 \text{ s}^{-1}$ and for both gassed and ungassed conditions. As expected,

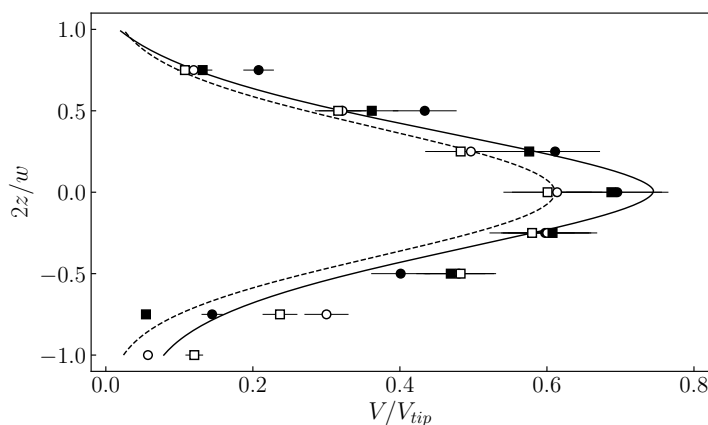


Figure 4.23: Effect of viscosity on radial velocity in gassed conditions at $N = 5.8 \text{ s}^{-1}$. Without gas: water (\bullet), XG 0.1% (\blacksquare), Venneker et al. (2010) (—); $U_g = 4 \text{ mm s}^{-1}$: water (\circ), XG 0.1% (\square), Rousar & Van den Akker (1994) (---).

no big differences were found among the two fluids, and the velocity profile measured in the presence of gas followed the same trend as already seen for water. Thus, compared to the unaerated system, a decrease in the radial velocity could be observed below the disk level, while along the upper half of the impeller blades, the velocity was slight higher. The absence of an influence of the rheology on the radial velocity in this zone of the tank is not surprising. In fact, close to the impeller — where the highest shear rate can be found — XG 0.1% presents an apparent viscosity of the same order of magnitude of the water viscosity, and the molecular mechanisms of momentum transfer are then covered by the turbulent transfer.

The Pavlov tube could be used also at higher gas flow rates and rotation speed, provided one uses a proper supporting and/or tube design. In the configuration used in this study, the tube was inserted from the top opening; the Pavlov tube was then bolted only from the upper part. In this way, the structural support was not enough to avoid excessive vibrations of the tube at higher gas velocity and impeller speed. Nevertheless, the Pavlov tube could be one of the few techniques to measure liquid velocity in dense bubbly flows, but further study on the geometry of the tube and its insertion in the vessel are needed to extend the use of the tube for more relevant operating conditions.

4.6 Conclusions

An innovative technique was validated to estimate bubble size in turbulent systems based on a dual optical probe and then used in a stirred tank reactor. Gas holdup and volumetric mass transfer coefficient were measured as well. The experiments were done in water, in non-Newtonian shear-thinning solutions of xanthan gum, and in a filtered broth from the fermentation of *Trichoderma reesei*. In addition, ethanol was used to modify the coalescence of air bubbles in water and in model fluids. Compared to proteins as a surfactant, ethanol presented the advantage of not creating a stable foam, thus not affecting the reliability of the measuring techniques. Measured quantities and the relative operating conditions are summarized in table 4.3.

The blockage of coalescence by proteins in the fermentation broth severely impacted bubble sizes and mass transfer. To reproduce this effect, different attempts were made by adding small amount of surfactants (BSA) and ethanol. In both cases, the decrease in bubble size was qualitatively well reproduced, although it was not possible to conclude that added compounds had the same influence on bubble-liquid interface as the one of additives in the fermentation broths. Ethanol was preferred over BSA because it did not create a stable foam, thus facilitating mass transfer measurements; ethanol was considered a good (although not perfect) solution to mimic the effect of broth's surfactants on interface phenomena.

Table 4.3: Summary of operating conditions for the experimental measurements.

Quantity	Tank	System	P_g/V W m^{-3}	U_g mm s^{-1}
Sauter mean diameter	T_{30}, T_{60}	W, XG, +EtOH	700–6000	4–40
Gas holdup	T_{30}, T_{60}	W, XG, +EtOH	700–6000	4–40
$k_L a$	T_{30}, T_{60}	W, XG, +EtOH	700–6000	4–40
Mixing time	T_{30}	W, XG	200–6000	0–40
Radial liquid velocity	T_{60}	W, XG	500–4000	0–4

A preliminary analysis showed that outside the impeller region, the bubble Sauter mean diameter was almost independent from the probe location. This outcome made it possible to estimate k_L from the average values of d_{32} , α_g and $k_L a$. Experimental data were fitted to empirical correlations, which estimated the effect of gas velocity, power input per volume unit, and viscosity of the media. The analysis pointed out different results concerning the role of each parameter on mass transfer:

- The effect of power input on $k_L a$ is mainly due to its effect on α_g , and this effect is strengthened by the simultaneous decrease in d_{32} with the dissipated power.
- Similarly, the superficial gas velocity causes an increase in $k_L a$ because of the increase in α_g . However, this effect is partly restrained by the simultaneous increase in d_{32} with the gas flow rate.
- The effect of viscosity on $k_L a$ is primarily due to its effect on k_L , and this effect is strengthened by the simultaneous increase in d_{32} and decrease in α_g .
- k_L 's dependence on dissipated power and superficial gas velocity was negligible or below the overall accuracy of the correlation.
- Adding ethanol was a valid method to mimic the effect of surfactants in viscous *Trichoderma reesei* broths. Additives increased $k_L a$, and this phenomenon is explained by the decrease in d_{32} and the increase in α_g . In fact, no influence on k_L was observed, and this result can probably be extended to protein surfactants in the broth.

Data collected in this study and the correlations proposed can provide a valuable contribution to the design and scale-up of agitated fermenters. Bubble size measurements in viscous non-Newtonian fluids can be used, for example, to validate coalescence and drag law models implemented in CFD solvers. Furthermore, mixing hydrodynamics were studied by measuring mixing time and liquid velocity. For the latter, the Pavlov tube was used, showing its potential in velocity measurement in dense bubbly flows. However, with the current design it was not possible to extent its use to high impeller and gas flow rates, because of the presence of strong vibrations.

Finally, experimental results and proposed correlations also provided input parameters, subgrid models, and test cases for validation of CFD simulations, which will be discussed in the next chapter.

Chapter 5

Validation of multiphase CFD models

The numerical characterization of stirred tank reactors will be presented in this chapter, and the main findings will be also published in an upcoming volume of *Chemical Engineering Science*. The goal of this study is to predict mass transfer and hydrodynamics of industrial-scale units, focusing on the application of CFD to study transient behaviors of microorganisms. The analysis of lifetime pioneered by Lapin et al. (2004), and recently the studies of Haringa et al. (2016, 2018) showed the potential of Eulerian-Lagrangian approach to obtain valuable information for the design and optimization of aerobic bioreactors. The present study wants to focus on the effect of rheology on substrate gradients. Due to scarcity of data on turbulent mixing in complex fluids, every aspect of the numerical model (e.g. turbulence model, drag law, rheology definition, etc.) needs to be validated. However, in the light of the scope of this work, some simplifying assumptions were done; these, are justified along the chapter.

Firstly, details of the simulations setup are presented, and the validation of the mesh is assessed. The choice of turbulence model and approach to simulate the rotating parts in un-aerated systems are justified; the best way to model the complex rheology is also discussed. Power number, mixing time and liquid flow pattern were used to validate the model. Then, aerated reactors are described, with a focus on available drag law models, for both Newtonian and non-Newtonian fluids. Depending on the operating conditions, the experimental d_{32} or its predicted value (table 4.1) were used to define the gas bubble size in the multiphase simulations.

5.1 Numerical setup

5.1.1 Solver configuration

Simulations were run with ANSYS Fluent 2019 R2 (v.19.4). Equations for momentum and continuity were solved by using the pressure-based coupled algorithm, which gave more stable simulations compared to the segregated algorithm, especially in the case of multiphase simulations. The coupled solver requires more memory, because momentum and pressure-based equations are solved simultaneously at the same step; nevertheless, CFD robustness benefits from it and less iterations are usually necessary to achieve convergence (Keating, 2011).

Second-order schemes were used for the discretization of velocity, pressure, and turbulent quantities equations, whereas the volume fraction equation was discretized with a first-order scheme. The use of high-order schemes for convection terms has been advised by different authors (Aubin et al., 2004; Deglon & Meyer, 2006); in fact, together with the mesh resolution, the discretization scheme greatly affects the computation of turbulent quantities; underestimation of turbulent kinetic energy and its dissipation rate in agitated tanks simulations is a known issue (Lane, 2017; Singh et al., 2011).

Turbulence was modeled with the realizable k - ε model, and its *dispersed* formulation was used for multiphase cases. Equations for turbulent quantities were then solved only for the liquid phase and used to derive the ones for the gas phase.

Moreover, the MRF approach was employed to describe the impeller rotation. Unlike the sliding mesh method, mesh of rotating parts is stationary, while equations are solved in a moving framework for the impeller region and in a steady framework for the other zone of the tank; information about momentum and pressure are exchanged through the interface between these two zones. For estimation of global hydrodynamics in standard tank configurations, the MRF model has been found computationally more efficient (Aubin et al., 2004; Shi & Rzehak, 2018).

Cases were solved with steady state formulation, and the pseudo-transient method was used to further improve stability. The pseudo-transient formulation introduces implicit under-relaxation factors, that are based on a pseudo-time step ANSYS Fluent Theory Guide (2019).

Finally, the simulation was considered converged when the following criteria were simultaneously verified:

- All the variables' residuals, normalized to the highest value during the first five iterations, dropped to $\sim 10^{-6}$ (liquid-only case) or $\sim 10^{-4}$ (multiphase case);
- Torque on the shaft, liquid average velocity, turbulent dissipation rate, and average gas fraction were constant within $\pm 3\%$ of their final values.

5.1.2 Computational grid and boundary conditions

The computational grid was created via meshing tools included in the ANSYS suite. Figure 5.1 shows the mesh that was used. All the walls were designed as zero-thickness bodies, and the

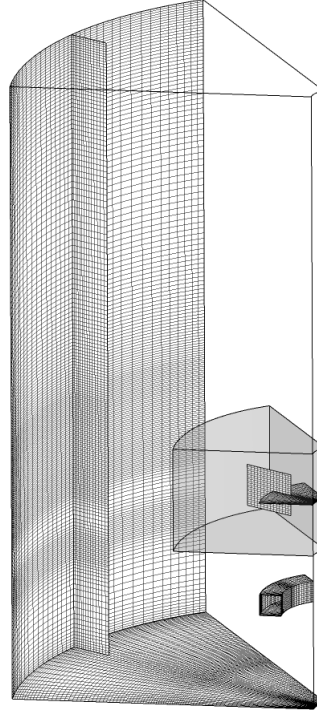


Figure 5.1: View of the mesh #2 (see table 5.1) used in most part of the simulations. Refinement of the mesh in the rotating zone and along the sparger walls can be noticed. The MRF volume is also highlighted.

shaft was extended down to the vessel bottom. By doing so, it was possible to simplify the mesh creation and to increase the quality of the computational grid, because only hexahedral elements were used. Moreover, by treating the lateral surfaces as periodic boundaries, only a sixth of the tank was modeled; this simplification has been already used in several studies, where only half or a sixth of the actual geometry were simulated (Haringa et al., 2018; Lane et al., 2005; Liangchao et al., 2018). Some simulations were run to check the influence of the periodicity condition, confirming that this approach led to good estimation of the global liquid and gas characteristics.

The top free surface was defined with a degassing boundary condition, that acts as a free-slip wall for the liquid phase and an outlet for the dispersed phase, which leaves the domain.

Except for the impeller and the shaft, all the other walls were defined as no-slip walls for the continuous phase and as free-slip walls for the dispersed one. To take into account the accumulation of gas in the impeller region, impeller and shaft were modeled with a no-

slip conditions for both phases instead. The scalable wall function was adopted to deal with turbulence in the regions close to walls. This wall treatment is based on the standard wall function (Launder & Spalding, 1974), but it performs better for grids where y^+ is lower than 10. In fact, by using only hexahedral elements, the use of inflation layers to locally refine the mesh was not possible, so zones with a low y^+ were unavoidable.

Gas injection was modeled with a velocity inlet boundary condition at the top surface of the sparger. To avoid unnecessary complications, the injection surface was meshed as a flat surface, rather than considering the real pierced rounded sparger. The inlet volume fraction of the dispersed phase was set to unity.

5.2 Un aerated tank simulations

5.2.1 Mesh sensitivity

Mesh sensitivity was done by considering four different meshes, whose cell numbers are reported in table 5.1. The condition $y_{max}^+ \sim 300$ was respected for all the grid resolutions. For data validation, tank T_{60} was considered, and power number and liquid velocity were used to compare mesh's accuracy.

Table 5.1: Cell numbers of the numerical grids used in this study.

Mesh id.	Cells number
1	77600
2	621200
3	131600
4	4970000

Power number

Power number obtained from the integral turbulent dissipation rate (N_{P_ε}) was compared to the value obtained by considering the torque at the shaft and impeller (N_{P_T}), and the percentage difference was used to judge the quality of the mesh. The two quantities are so defined:

$$N_{P_T} = \frac{6}{\rho_l N^3 D^5} \sum_i 2\pi N \Gamma_i \quad (5.1)$$

$$N_{P_\varepsilon} = \frac{6}{\rho_l N^3 D^5} \int \rho_l \varepsilon dV \quad (5.2)$$

The factor 6 was added because only a sixth of the reactor was modeled; summation of the torque was done considering all the rotating surfaces.

In figure 5.2 the effect of mesh resolution and numerical scheme on power number can be seen. As written in the introduction, the choice of the discretization scheme for convection

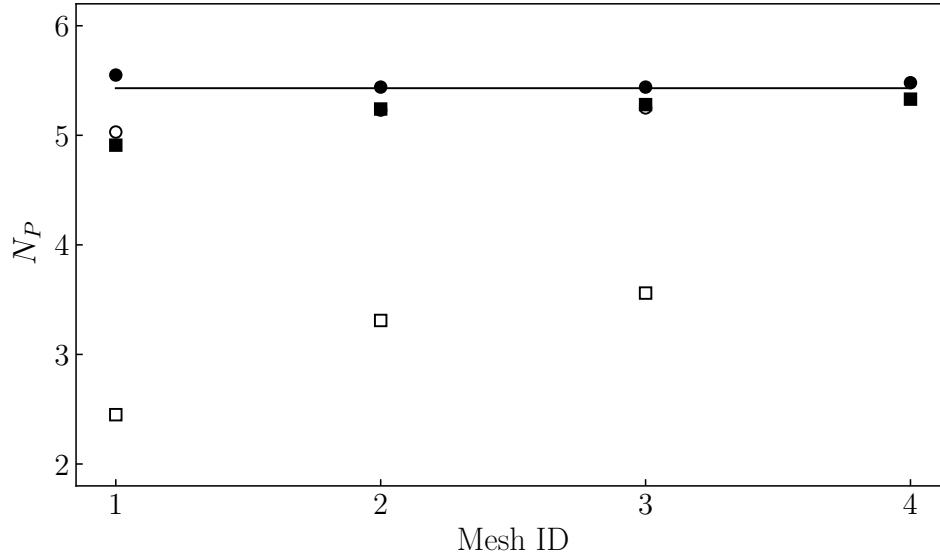


Figure 5.2: Impeller power number computed with different grids and definitions. Symbols: N_{P_T} 1st order (○), N_{P_ϵ} 1st order (□), N_{P_T} 2nd order (●), N_{P_ϵ} 2nd order (■), Bujalski et al. (—).

terms had a great impact on the computation of turbulent quantities. In particular, it was found that the discretization method for the momentum equation played the main role, whereas the discretization scheme for κ and ε equations slightly improved the predicted power number. With the first-order scheme, the power number from turbulent dissipation rate was heavily underestimated; increasing the mesh resolution partially solved the problem. In fact, for mesh #3, a difference of about 40% was still found between numerical and expected values. On the other hand, the torque was slightly influenced by the choice of discretization method.

Even with the coarsest mesh, power number from torque was close to the expected value. Going from mesh #1 to mesh #2, the discard between N_{P_ϵ} and N_{P_T} computed with the second order scheme went down from 12% to 4%. Further increasing in the mesh density lowered the discrepancy only to 3%, so mesh #2 was considered fine enough to describe the global hydrodynamics of the reactor. By using a very refined mesh, turbulent quantities can be satisfactorily computed, however the discretization domain cannot be too fine, and a compromise with the computation time has to be reached.

Liquid velocity

It is important to well predict the liquid flow characteristics at the discharge zone, where the energy is being transferred from the impeller to the liquid. Accuracy of predicted liquid velocity was assessed by comparing numerical results with set of correlations proposed by Venneker et al. (2010), already presented in Section 4.5 (Eqs. (4.9)–(4.12)), and with experimental data, whenever available.

In the CFD analysis of liquid velocity profiles, averaging within different angular position is very important. In fact, as Shi & Rzehak (2018) explained: "If however the measurement point falls within the rotating zone simple time-averaging will not provide the impeller-angle average implied by the experimental data. Hence, in this case the simulation data are in addition averaged also over the impeller angle." Therefore, results presented in this study were averaged at three different angular positions: 15°, 30° and 45°. In the chosen system of reference, the two periodic boundaries were located at 0° and 60°.

In figure 5.3 simulated values of liquid velocity components are reported for water along with theoretical profiles, as calculated by Venneker et al. (2010). The mean flow was well captured with all mesh resolutions, and a good agreement with the theoretical correlations was obtained. Major discrepancies were found in the case of the axial velocity profile in the vicinity of the impeller blade (figure 5.3a). A possible explanation is the effect of blade thickness, which could not be taken into account in the simulations. However, this effect was judged negligible, considering that all the other profiles were well predicted.

Regardless of the mesh size, good agreement with expected values was found for both tangential and radial components of liquid velocity in the discharge region of the tank (figure 5.3b,c), as well as for the radial velocity close to the impeller tip ($r/R = 1.05$) (figure 5.3d). For the velocity in front of the blade, experimental results obtained with Pavlov tube at similar conditions are reported for completeness.

In the light of the above-discussed results, mesh #2 was judged fine enough to describe the turbulent mixing in the tank.

Accuracy of MRF approach and partial domain

In figure 5.4, the gas fraction at the impeller plane for both MRF and SM models is shown. At the considered operating conditions, the tank was characterized by $Fl_g = 0.04$ and $Fr = 1.81$; for these set of values, the 3 – 3 cavity structure was expected. Obviously, due to the periodic boundary conditions, such a structure could not be obtained with a partial domain (figure 5.4a). However, the simulation of the entire geometry figure 5.4b was capable to reproduce the alternating pattern of the gas cavities, with three clinging cavities and three large

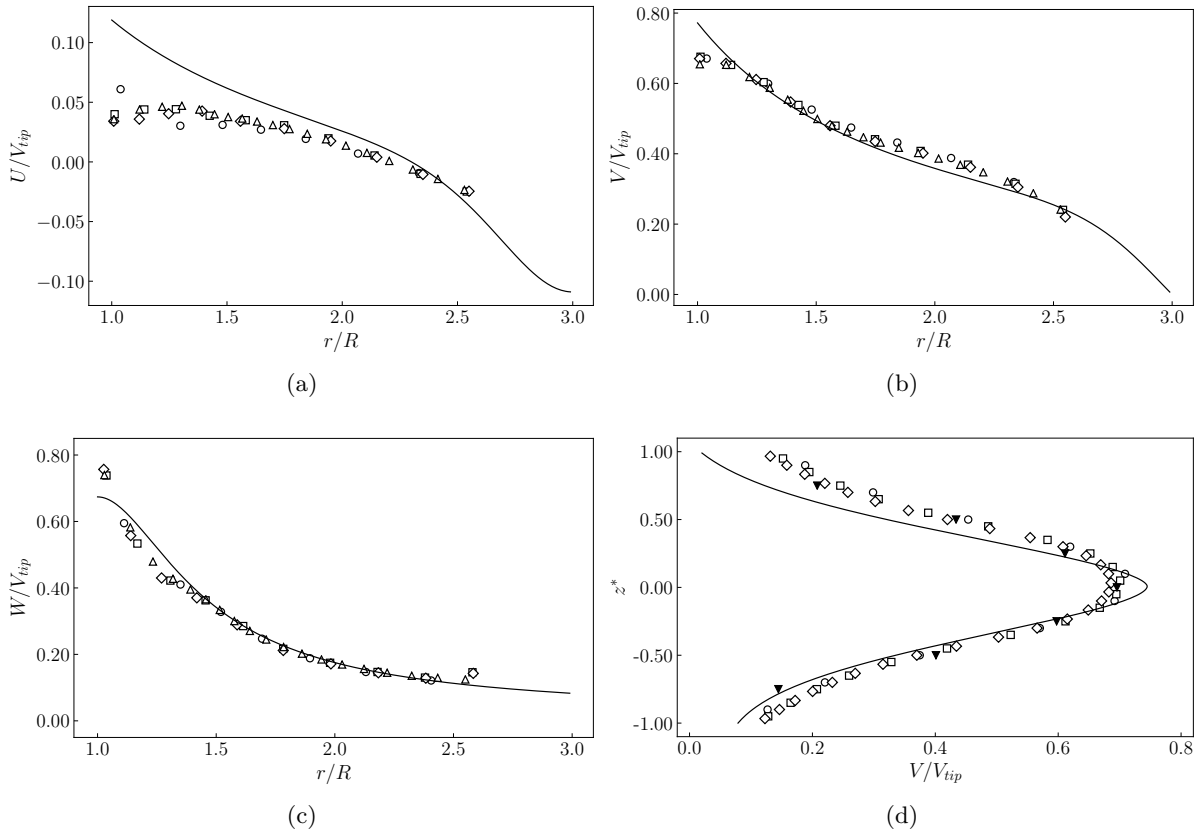


Figure 5.3: Effect of mesh resolution on normalized velocity profiles in T_{60} at $N = 8.33 \text{ s}^{-1}$ ($Re = 3 \cdot 10^5$). Radial profiles at the impeller disk height of: axial velocity (a), radial velocity (b), tangential velocity (c); radial velocity along the impeller blade (d). Legend: mesh 1 (○), mesh 2 (□), mesh 3 (◇), mesh 4 (△), Venneker et al. (2010) (—), experimental (▼).

cavities. Interestingly, in the case of the partial geometry, it seemed that the size and shape of aerated cavities were in between the ones of the full geometry.

Additionally, the rotation model did not have a strong impact on the global hydrodynamics, as it can be seen in table 5.2. Comparable errors were in fact obtained with both models. The

Table 5.2: Effect of geometry and rotation model on some global quantities.

Case	RPD	Gas holdup	$k_L a / \text{h}^{-1}$
Partial, MRF	0.49	0.068	229
Full, SM	0.45	0.075	277
Experimental	0.41*	0.072	237

* Extracted from Gabelle (2012).

Relative Power Draw was better predicted with the full geometry and sliding mesh model,

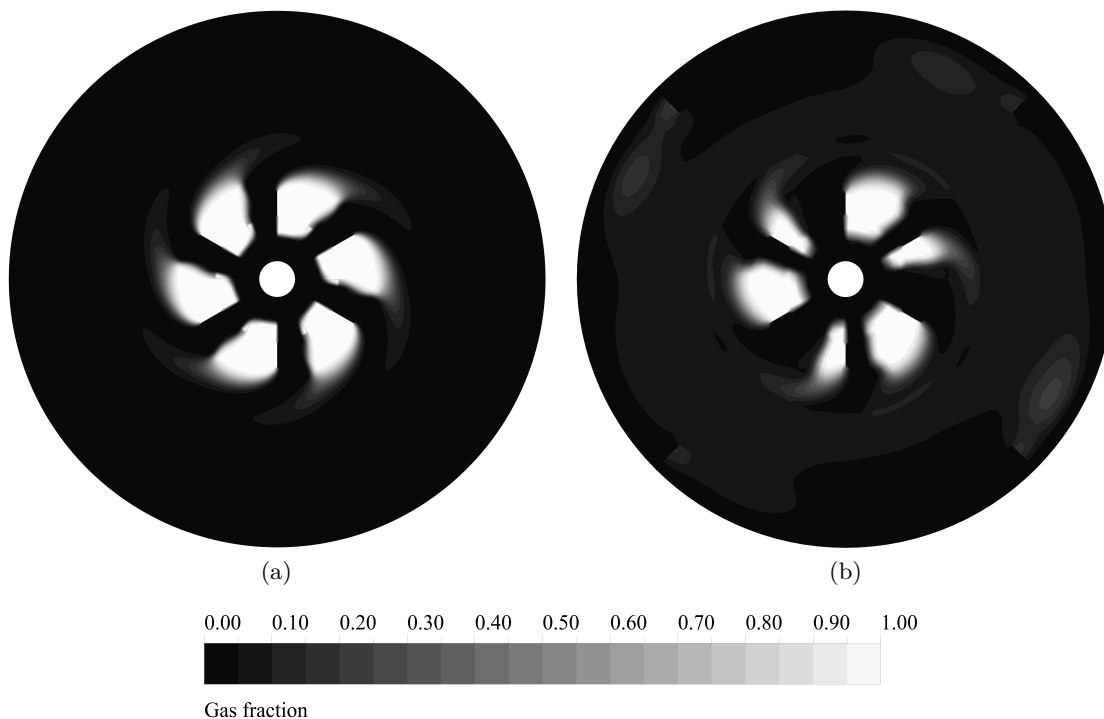


Figure 5.4: Gas cavity structures in T_{30} at $U_g = 8 \text{ mm s}^{-1}$ and $N = 13.3 \text{ s}^{-1}$ by using MRF (a) and SM models (b). A sixth of the domain was simulated in the case of the MRF approach; to facilitate the comparison, the partial geometry was repeated in post-processing to represent the full tank.

probably because of the more accurate representation of the aerated cavities. Nevertheless, in the perspective of industrial scale simulations, the simpler MRF approach with the periodic geometry was retained, as it was capable to provide accurate results with an acceptable error. A full geometry is however recommended in the case in which gas structures behind the impellers need to be accurately predicted, for example to study transition between the different aerated regimes (Section 2.2).

5.2.2 Rheology modeling: definition of shear rate

To model a power-law liquid, the shear rate has to be defined (Section 2.7.3). In ANSYS Fluent, the model for turbulent non-Newtonian flows is just an adaptation of the formulation for laminar flows, where molecular viscosity is simply replaced by the apparent one, calculated from the gradient of mean velocity:

$$\dot{\gamma} = \sqrt{\frac{1}{2} \mathbf{D} : \mathbf{D}} \quad (5.3)$$

where \mathbf{D} is the deformation rate tensor (ANSYS Fluent Theory Guide). In Section 2.7.3, the reader was exposed to the challenges of a more rigorous approach in shear rate modeling in

turbulent flows; in this study, a simplistic approach based on turbulence theory was preferred. Assuming that the shear is maximum at the Kolmogorov scale and not governed by the mean flow, Eq. (2.71) was used to compute the local shear rate (Pérez et al., 2006):

$$\dot{\gamma} = \left(\frac{\rho l \varepsilon}{K} \right)^{\frac{1}{n+1}}$$

Mixing case of a 0.25% XG solution was used to compare shear rate computed by using Eq. (2.71) and via average velocity gradients. In table 5.3, values of the average shear rate and the maximum one are reported for both models. The laminar model implemented in Fluent was

Table 5.3: CFD average and maximum shear rates in s^{-1} for XG 0.25% at $N = 5 \text{ s}^{-1}$. Values predicted with correlations in the literature are reported, as well as the apparent viscosity ($\text{kg m}^{-1} \text{ s}^{-1}$) calculated respect to the average shear rate.

	$\dot{\gamma}_{av}$	$\mu_{app}(\dot{\gamma}_{av})$	$\dot{\gamma}_{max}$
<u>CFD</u>			
Velocity gradient	14	0.137	$9.35 \cdot 10^2$
Kolmogorov	219	0.025	$1.45 \cdot 10^4$
<u>Correlation</u>			
Metzner & Otto	58	0.057	
Pérez et al.	237	0.024	
Wichterle et al.			$1.13 \cdot 10^4$

found inadequate in the case of turbulent flows, being the average apparent viscosity more than twice the values obtained from correlations; also the maximum shear rate at the impeller zone was very unrealistic. On the other hand, the computation of molecular viscosity by considering the local dissipation rate led to more significant results, with average shear rate, maximum shear rate and apparent viscosity closer to the values obtained with correlations. For this reason, the local model was preferred over the one based on mean velocity gradients.

The local apparent and turbulent viscosities with both models are shown in figure 5.5. Comparable viscosity values were found in the discharge region, where there were also high velocity gradients. However, in the rest of the tank, viscosity from velocity gradients was probably overestimated. In the case of the default Fluent definition, the average apparent viscosity was $0.20 \text{ kg m}^{-1} \text{ s}^{-1}$, while the value $0.06 \text{ kg m}^{-1} \text{ s}^{-1}$ was obtained when the dissipation rate was used to define the shear rate. In any case, even if the molecular viscosity was found to vary by one order of magnitude depending on the shear rate model, the eddy viscosity was barely affected by it.

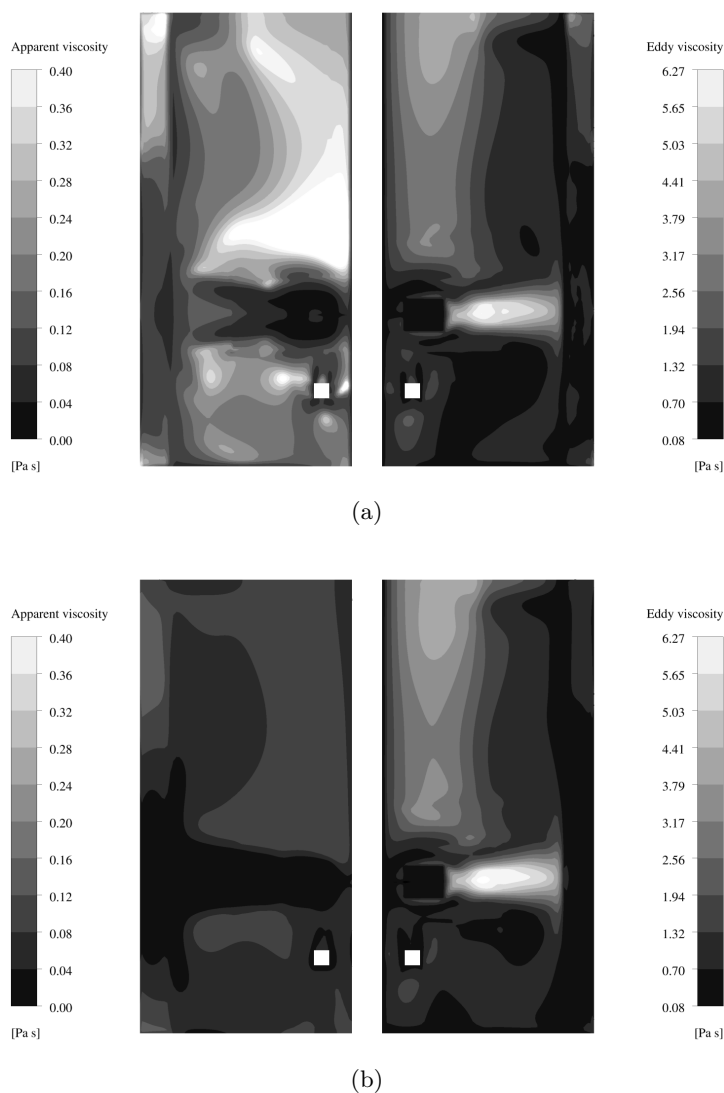


Figure 5.5: Apparent and turbulent viscosity for XG 0.25% at $N = 5 \text{ s}^{-1}$ computed with different shear rate models: from velocity gradients (a) and from turbulent dissipation rate (b).

5.2.3 Mixing time in ungasged reactor: rheology effect

As evolution of a scalar species over time and space can provide important information about mixing in the reactor, it can also be used to validate numerical model. Mixing time was computed by considering the injection of an inert species, which had the same physical properties of the bulk phase, namely viscosity and density. Species model as implemented by Fluent was preferred over the resolution of a custom scalar equation, because the latter presents some numerical difficulties concerning the conservation of the quantity, which might affect mixing time calculation.

Initial tests showed that the amount of tracer injected did not have any effect on the mixing time, as long as it was introduced at the same location. In all the simulations, the tracer was introduced from the top, by patching a unity value of its concentration in a computational cell right below the liquid level. Giving the predominantly axial development of the flow field in an agitated tank, the use of a periodic domain should not affect the calculation (Haringa et al., 2017).

Mixing time was obtained by exporting the standard deviation of the tracer's concentration at each time step, computed by considering all the cells of the computational domain and according to the following definitions:

$$\sigma(t) = \sqrt{\frac{1}{n} \sum_{i=1}^n (C_i(t) - \langle C \rangle)^2} \quad (5.4)$$

$$\langle C \rangle = \frac{1}{n} \sum_{i=1}^n C_i \quad (5.5)$$

where n is the total number of facets and $\langle C \rangle$ is the average concentration of the tracer. Mixing time is computed by considering the logarithm of the variance and level of homogeneity of 95%, therefore:

$$\log \left(\frac{\sigma(\theta_{95})}{\langle C \rangle} \right)^2 = -2.60 \quad (5.6)$$

By considering every cell as a detection probe, calculation of mixing time is supposedly more precise, because more poorly-mixed regions of the tank are taken into account.

Only the species transport equation was solved during the transient analysis and it was discretized with a second order scheme. Moreover, a bounded second order scheme was used for the time-derivative term, which was solve by considering a fixed time step size of 0.01 s.

In figure 5.6, mixing times for water and xanthan gum at concentration of 0.25% and 0.50% are reported, together with data from the broadly used correlation of Grenville (1992) which, for vessels where the liquid height is equal to the tank diameter, reads:

$$N\theta_{95} = (5.2 \pm 0.52) \left(\frac{T}{D} \right)^{-2} N_P^{-1/3} \quad (5.7)$$

Equation (5.7) is valid for turbulent flows, for which gives an average error of 10%. In laminar and transitional flows, mixing time is usually longer; Grenville & Nienow (2004) proposed the following equation for relatively low Reynolds number:

$$N\theta_{95} = (183 \pm 31.8)^2 \left(\frac{T}{D} \right)^{-2} N_P^{-2/3} Re^{-1} \quad Re < Re_{trans} \quad (5.8)$$

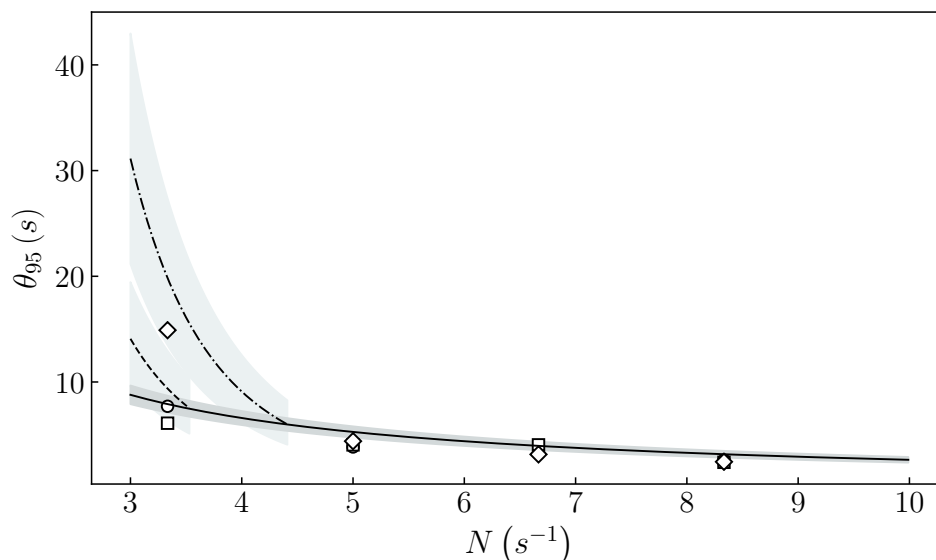


Figure 5.6: CFD mixing time in T_{60} without aeration. Data: water (○), XG 0.25% (□), XG 0.50% (◇), Grenville (—), Grenville & Nienow (XG 0.25%) (---), Grenville & Nienow (XG 0.50%) (-.-).

The transition between transitional and turbulent regime was defined by considering the following equation (Grenville & Nienow, 2004):

$$Re_{trans} = 6370N_P^{-1/3} \quad (5.9)$$

The CFD model was able to predict a reasonable mixing time for almost all the conditions, especially at high impeller speed; the mean relative error was 14% for water, whereas it was around 35% for xanthan gum simulations. Furthermore, at intense agitation rates, rheology had a negligible effect on the blending time (Gabelle et al., 2011). At lower rotation speed, weakness of the turbulence model shows up, and the computed mixing time in XG was way shorter than the expected value. At this condition, the correlation proposed for transitional regimes was used (Grenville & Nienow, 2004), with Re_{trans} as threshold value; this correlation presents a greater uncertainty, so points in the transitional regime were less reliable for validation of the model. It was also assumed that the power number was constant and equal to the value at high Re . Moreover, operating conditions at higher impeller rotational speed are more relevant for this study, because of the higher interest for industrial applications. That said, it is not surprising that far from conditions where the flow is fully turbulent, predictions were less reliable. However, mixing times here presented fell within a reasonable range, and the overall trend was predicted.

5.3 Air-water simulations

Industrial aerobic fermenters operate at high superficial gas velocity, which leads to gas holdup up to 20%. Simulation of systems characterized by high concentration of the dispersed phase can be computationally demanding, so only the Euler-Euler approach model provides a good compromise between precision and performance. Mathematically, Eulerian phases are treated as interpenetrating media, and they are described by their volume fraction. Among the three Euler-Euler multiphase models implemented in ANSYS Fluent, namely *VOF* model, *Mixture* model and *Eulerian* model, the latter is the more complex, but gives better results when the dispersed phase is characterized by a range of size; this condition is common in dense bubbly flows. For these reasons, the Eulerian model was used in this study.

To reduce computational time and numerical instabilities, multiphase simulations were initialized from monophasic solutions, and a value of gas fraction close to the experimental value (when available) was patched to all the fluid zone of the domain.

5.3.1 Drag model screening for the air-water case

Inclusion of interaction forces between continuous and dispersed phase is very important for obtaining a good prediction of the flow. As it was discussed in Section 2.7, in these type of gas-liquid systems, the resulting hydrodynamics is mainly due to drag force. In this study, several closure models for the drag term were tested.

Initial simulations were run by also considering virtual mass force and lift force along with drag interaction. These test cases showed the little impact of these extra terms on the gas-liquid flow; moreover, simulations became more unstable. Consequently, extra interaction terms were not included in the model.

Despite its limitations, the Schiller-Naumann model can be often found in researches with similar equipment; however, in the light of the measured bubble size (Chapter 4), it was decided to ignore this model for small rigid bubbles and to study models that are more suitable for dense bubbly flows. Therefore, the following drag models were used: Grace (Clift et al., 2005), the universal drag laws (Kolev, 2005), and the one based on bubble terminal velocity (Scargiali et al., 2007). The latter is not present in Fluent, so it was implemented by means of *User Defined Functions*.

All the aforementioned drag models were originally developed to describe the rising of single bubbles in stagnant liquids. However, in a heterogeneous flow, the velocity field of each bubble is influenced by the presence of other bubbles. The presence of a swarm of bubbles can thus have an impact on the interphase drag, causing bubbles acceleration or deceleration. Recently, Gemello et al. (2018) improved hydrodynamics prediction in bubble columns at high gas fraction

(> 15%) by employing a modified swarm-factor equation.

Furthermore, turbulence can also have an impact on the bubble terminal velocity. In the literature, it has been proved that in turbulent two-phase flows, turbulence in the continuous phase slows down the dispersed phase. In contexts similar to this study, turbulent dampening has been included in different ways: by increasing the effective viscosity of continuous phase (Bakker & Van den Akker, 1994; Petitti et al., 2009), by modifying directly the bubble terminal velocity (Montante et al., 2007; Petitti et al., 2009; Zadghaffari & Moghaddas, 2010), or by introducing a correction factor linked to turbulent eddies length (Brucato et al., 1998; Lane et al., 2005). The literature review presented in Section 2.7, showed that turbulence dampening is doubtless necessary in the case of low gas fraction and if Schiller-Naumann drag model is adopted. Nevertheless, all of the different ways to include turbulence dampening were tested, by leading to either nonphysical gas recirculation in the lower loop or increase in the global gas holdup.

In figure 5.7, contours of gas fraction at the mid-plane at 45° obtained with different drag models are displayed. The gas fraction predicted with all the models was practically the same, with some differences for the simulation where the universal drag law was used (figure 5.7a). Models of Grace and Scargiali et al. (2007) led to the same air fraction distribution, which is not surprising, as they are both based on the characterization of the drag coefficient in terms of bubble terminal velocity. Regardless of the drag coefficient model, multiphase simulations were characterized by an accumulation of gas holdup in the recirculation loops, where pressure decreases. Also, gas accumulated behind the impeller blade; as it is discussed in the next section, prediction of gas cavities is vital to estimate the power demand in ungasged simulations. Additionally, the gas phase was dispersed inside the tank, with the gas coming from the ring sparger that was then radially redistributed by the impeller.

In figure 5.8, gas fraction at the impeller plane is showed. The shape of gas cavity is visible, and it can be seen that the gas accumulation behind the impeller blade had a comparable size between all the three models. A slightly bigger cavity was obtained with universal drag laws (figure 5.8 a), while no difference was noticed among the other two models (figure 5.8 b,c). In any case, the computed gas flow number ranged between 0.29 (universal laws) and 0.38 (Grace, Scargiali et al. (2007)), being reasonably close to the theoretical value 0.35. Moreover, according to Eqs. (2.13) and (2.14), all the simulations described a completely dispersed condition, with clinging cavities.

Data obtained with the cross-correlation technique (Section 4.2) were used to better evaluate drag models' accuracy. Results in terms of local gas fraction profiles are shown in figure 5.9. Once again, very similar results were obtained with all the drag laws. The numerical models performed well in describing the impeller discharge region (figure 5.9c). However, simulations

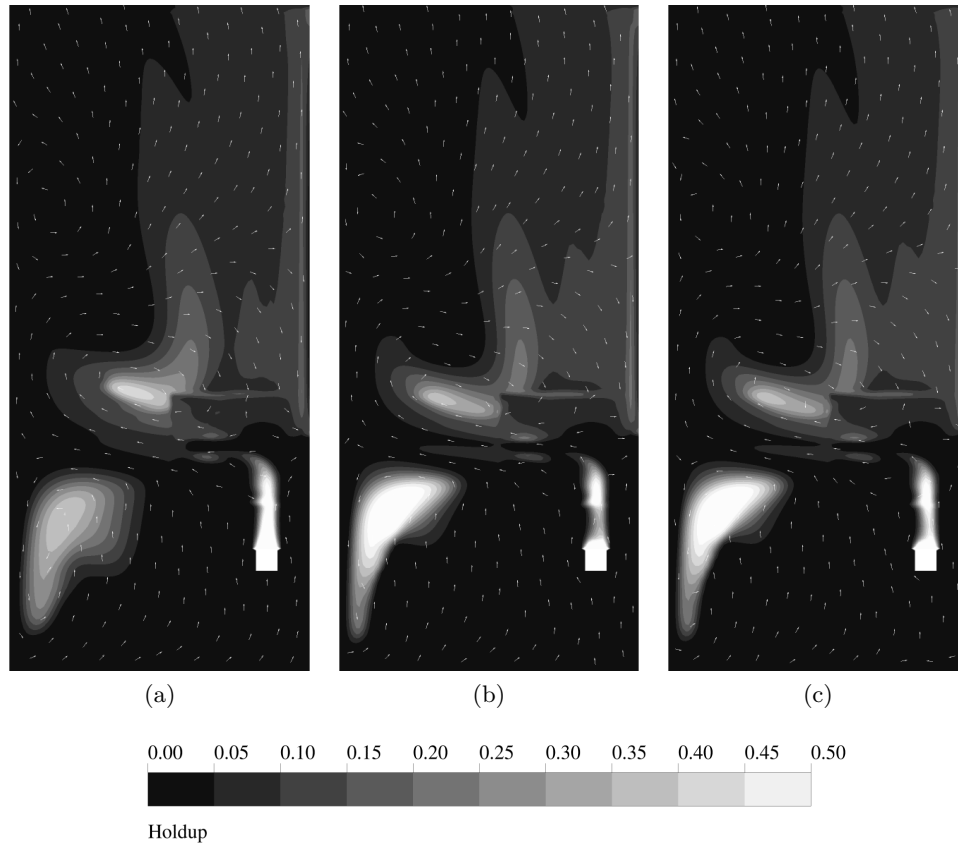


Figure 5.7: Gas volume fraction in the plane between the baffle and the periodic plane at $N = 8.3 \text{ s}^{-1}$ and $U_g = 8 \text{ mm s}^{-1}$. The contours were obtained by using: universal drag law (a), Grace (b), and Scargiali et al. (c). Vectors of air velocity in standard reference of frame are also represented.

were less accurate to reproduce the sampled gas fractions at higher axial locations. In fact, the gas fraction close to the walls was underpredicted by the CFD models. In contrast to experimental findings, predicted profiles of the gas volume fraction decayed very fast when moving towards the vessel walls. Therefore, numerical data were characterized by a mean error of 38%. These findings seem to suggest that simulations at this gas rate might be characterized by the underestimation of the gas dispersion in the tank. In figure 5.10, the gas distribution computed with the universal drag laws is compared to experimental results of Bombáč et al. (1997). The comparison is intended to be qualitative, because of the different operating conditions considered by Bombáč et al.. However, in both cases, impeller speed and gas flow rate were such that hydrodynamics was characterized by the vortex-clinging structure, so a similar gas distribution was expected. As can be seen in the figure, accumulation of the gas in the recirculation loops was reproduced, even though the amount of gas inside the loops was probably overestimated.

Nevertheless, global characteristics such as the Relative Power Demand (RPD), the global

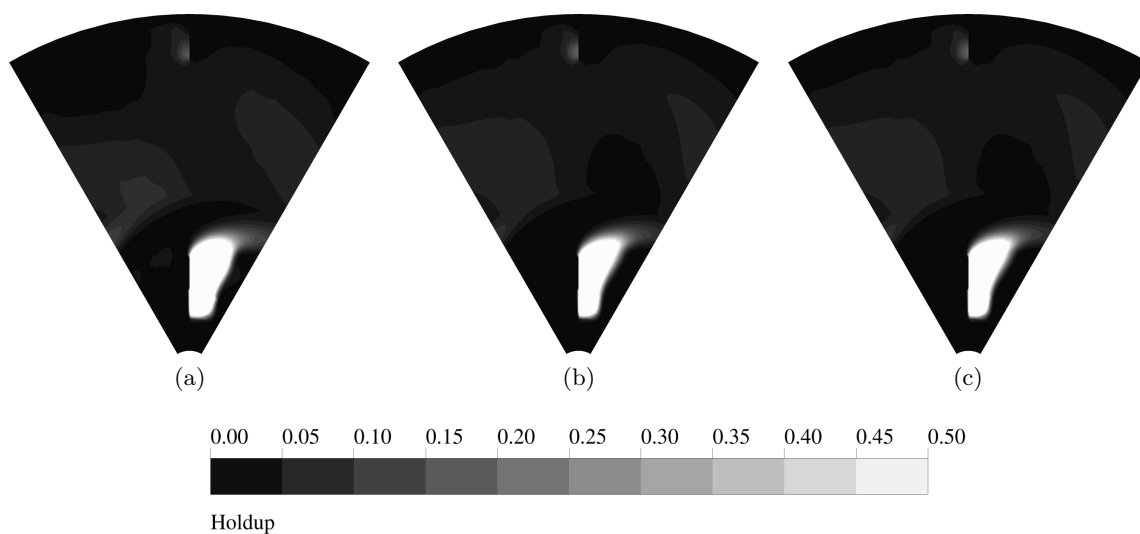


Figure 5.8: Gas volume fraction at the impeller height. The contours were obtained at $N = 8.3 \text{ s}^{-1}$ and $U_g = 8 \text{ mm s}^{-1}$ by using: universal drag laws (a), Grace (b), and Scargiali et al. (2007) (c).

gas holdup and the volumetric mass transfer coefficient were satisfactorily predicted. In table 5.4, values of these global quantities obtained by using different drag coefficient models are listed.

Table 5.4: Characteristic data in multiphase simulations of T_{60} at $N = 8.3 \text{ s}^{-1}$, obtained with different drag coefficients. For each variable, relative errors respect to experimental data are reported in brackets.

Drag model	$U_g \text{ mm s}^{-1}$	$d_B \text{ mm}$	RPD_{torque}^\dagger	RPD_ε^\dagger	Gas holdup	$k_{La} \text{ h}^{-1}$
Grace	4	3.1	0.56 (-15.2%)	0.64 (-3.0%)	$5.74 \cdot 10^{-2}$ (10.4%)	220 (11.1%)
Universal			0.55 (-16.7%)	0.67 (1.5%)	$5.74 \cdot 10^{-2}$ (1.9%)	202 (2.0%)
Grace	8	3.5	0.54 (3.8%)	0.61 (17.3%)	$6.92 \cdot 10^{-2}$ (12.0%)	266 (13.2%)
Universal			0.51 (-1.9%)	0.60 (15.4%)	$6.27 \cdot 10^{-2}$ (1.5%)	238 (1.3%)
Scargiali et al.			0.54 (3.8%)	0.60 (15.4%)	$6.74 \cdot 10^{-2}$ (9.1%)	259 (10.2%)
Grace	20	4.1	0.47 (42.4%)	0.55 (66.7%)	$9.75 \cdot 10^{-2}$ (6.6%)	295 (-1.7%)
Universal			0.37 (12.1%)	0.55 (66.7%)	$9.43 \cdot 10^{-2}$ (3.1%)	280 (-6.7%)

[†]Relative error respect to Eq. (2.17).

In general, the RPD calculated from the torque power number, was satisfactorily computed in all the cases, especially at lower gas flow rate. Comparable errors between the different models were found also regarding the RPD obtained with the integral dissipation rate; however, the loss in power input so calculated was systematically overpredicted. Contrary to single-phase simulations, the impeller power number computed from the turbulent dissipation rate was greater than the expected one. Reasons for this inaccuracy should be looked for in the multiphase turbulence model, probably focusing on improvement in the modeling of bubble

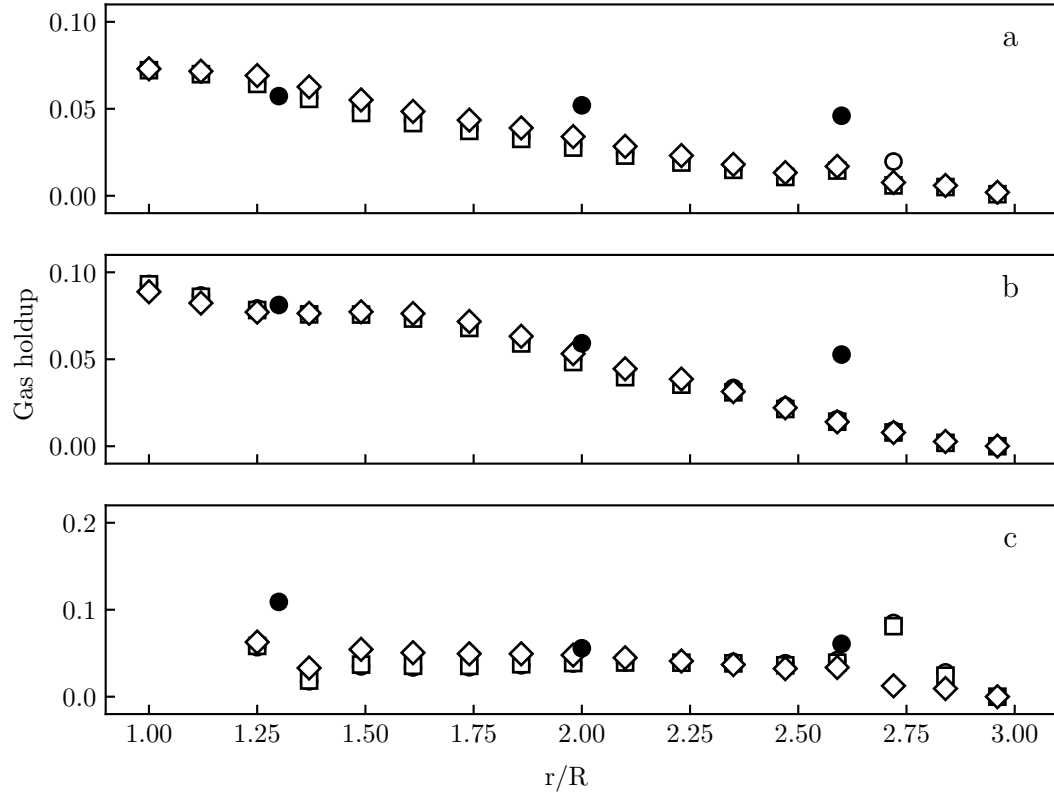


Figure 5.9: CFD and experimental gas fraction in water at $N = 8.3 \text{ s}^{-1}$ and $U_g = 8 \text{ mm s}^{-1}$; data were taken in T_{60} at different heights: impeller height (a), 200 mm (b) and 350 mm above the impeller disk (c). Symbols: experimental (\bullet), Grace (\circ), Scargiali et al. (2007) (\square), universal (\diamond).

contribution to turbulence.

By using the universal drag laws, it was possible to obtain a very good prediction of the global gas holdup and of the mass transfer coefficient. The latter was calculated by considering the volume average of $k_L a$, where k_L was obtained from the correlation presented in Chapter 4, while a was calculated locally as $6\alpha_g/d_B$ ¹.

In conclusion, screening of the drag coefficient model showed that universal drag laws gave better results in terms of global gas holdup and mass transfer coefficient. A better prediction of the relative power demand was also obtained, although prediction of turbulent quantities remains uncertain. Therefore, all the results concerning air-water systems presented in the following section, were obtained by using this drag model.

¹In Section 4.3, the interfacial area was defined respect to the volume of liquid ($a = 6\alpha_g/d_B(1 - \alpha_g)$) coherently with the $k_L a$ measurement. Instead, in this chapter the interfacial area was defined in terms of volume of reactor, in order to avoid the singularity at cells where $\alpha_g = 1$. Prior to compare numerical and experimental mass transfer coefficients, the latter was then converted into a reactor-volume basis.

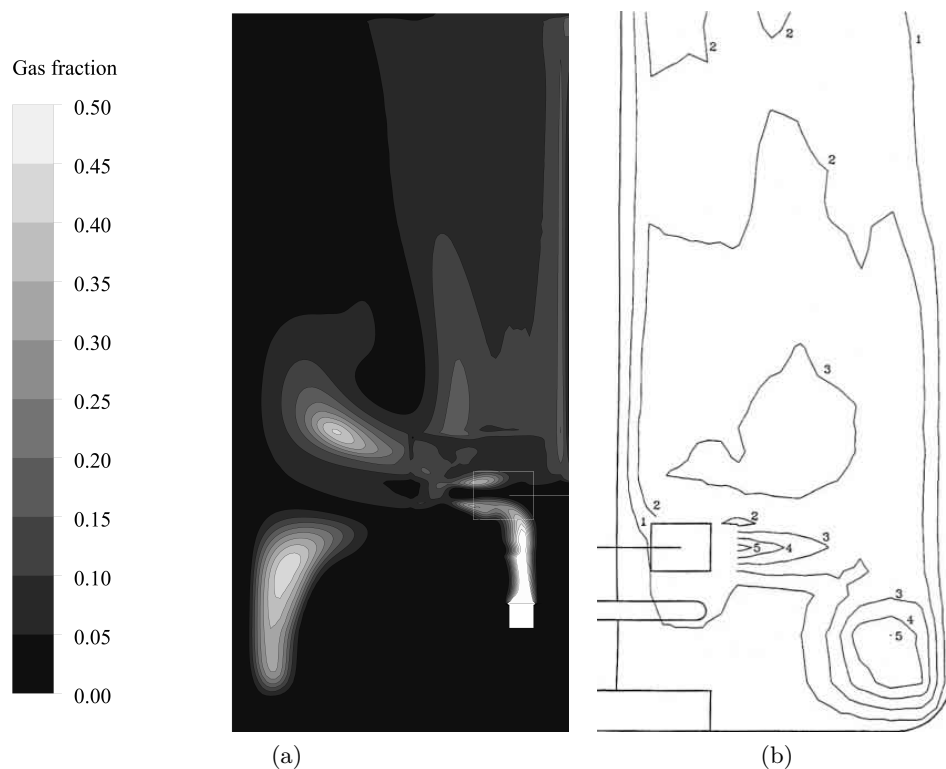


Figure 5.10: Contours of gas fraction in the VC regime based on CFD simulation (a) and measured by Bombač et al. (1997) (b).

5.3.2 Mixing in air-water: effect of gas rate and tank scale

Global gas holdup

In figure 5.11, the global gas fraction is presented for both tanks T_{30} and T_{60} at $N = 13.3 \text{ s}^{-1}$ and $N = 8.3 \text{ s}^{-1}$, respectively. Numerical data were compared with holdup measurements performed in this study. Gradual increase in gas holdup with the injection rate is expected, and simulated cases showed this trend. From the graph, it can be seen that numerical data for both tanks diameters were practically the same, as in the case of experimental findings. Errors of numerical values were $\approx 10\%$, that is in the same order of magnitude of the measurement precision.

Gassed power number and liquid velocity

Formation of gas cavities behind the impeller's blades causes modification on the energy supplied to the liquid, and has an impact on the reactor hydrodynamics. In fact, the decrease in power input in gas-liquid reactors depends on the shape and pattern of these cavities (Section 2.2).

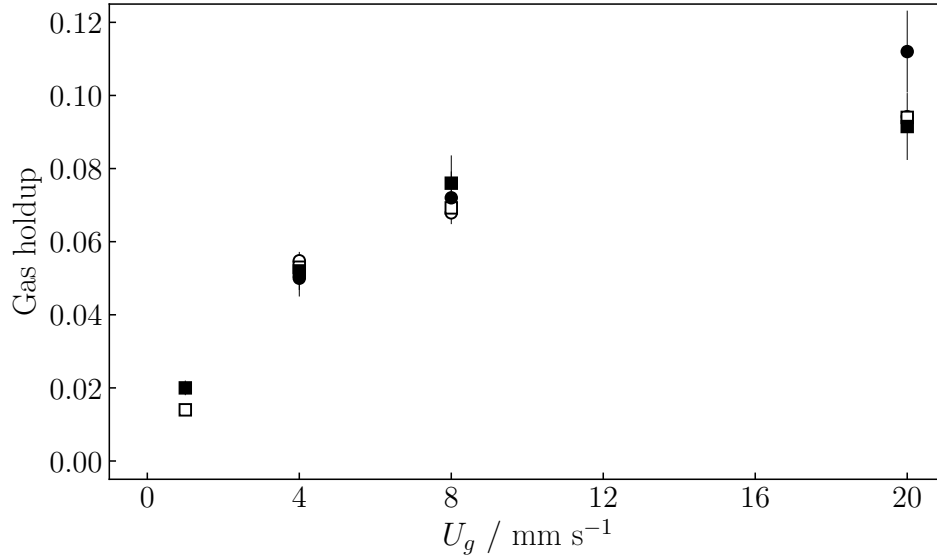


Figure 5.11: Numerical and measured gas holdup against superficial gas velocity for two tanks with different diameters. T_{30} , $N = 13.3 \text{ s}^{-1}$: CFD (●), experimental (○); T_{60} , $N = 8.3 \text{ s}^{-1}$: CFD (■), experimental (□).

In figure 5.12, RPD at different superficial gas velocities is shown for two tank sizes, and computational results are compared to experimental ones. As expected, simulated cases were

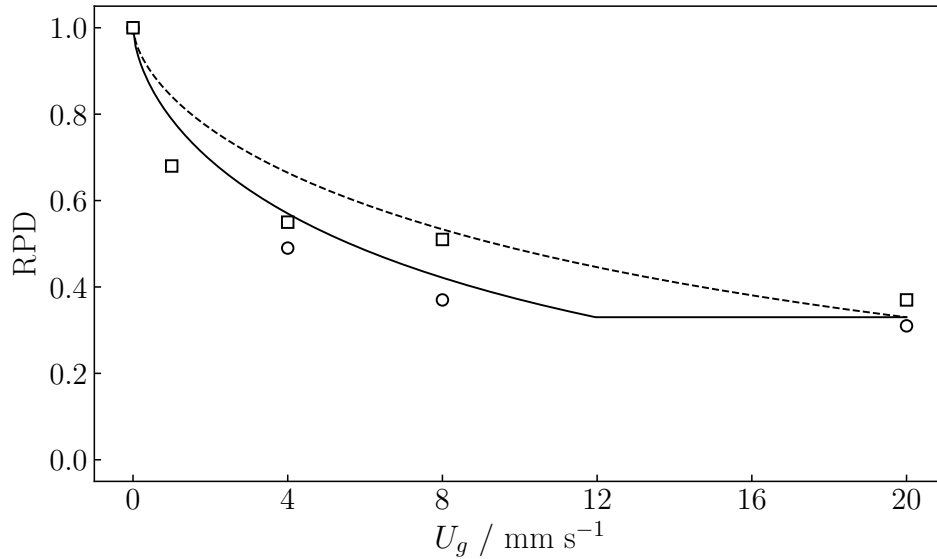


Figure 5.12: Relative power demand for two tank diameters at several gas velocities. CFD data: T_{30} , $N = 13.3 \text{ s}^{-1}$ (○), T_{60} , $N = 8.3 \text{ s}^{-1}$ (□); Eq. (2.17): T_{30} (—), T_{60} (----).

characterized by a decrease in RPD with the gas superficial velocity. For both tank diameters, the mean error was $\approx 14\%$, while the maximum error was $< 25\%$. Moreover, the maximum

error was obtained at lower gas flow rate; interestingly, the relative error decreased with the gas fraction. However, the average error was judged acceptable, in the light of the computational convenience by using a periodic approach.

Explanations for the discrepancy at lower gas rates can be found by investigating the gas accumulation behind the impeller blade. In figure 5.13, the shape of the aerated cavity is highlighted (isosurface for $\alpha_g = 0.5$). Both simulations were characterized by the formation of a clinging cavity. However, for the considered operating conditions, gas should form a vortex cavity (figure 5.14).

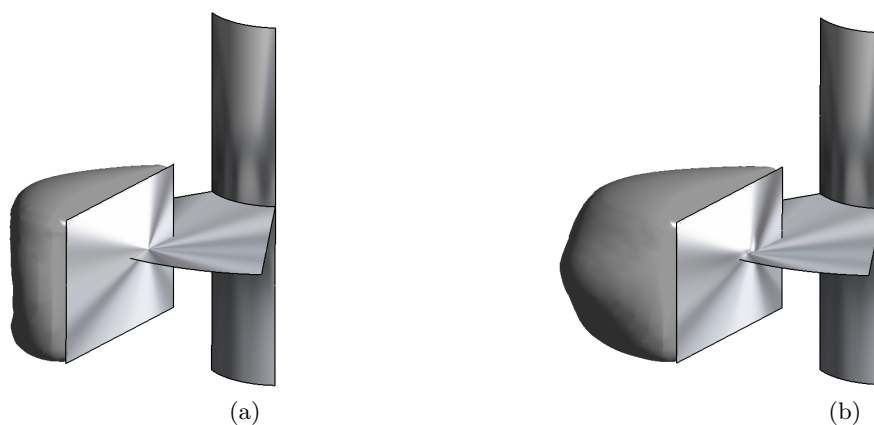


Figure 5.13: Isosurface of gas fraction at $U_g = 1 \text{ mm s}^{-1}$ (a) and $U_g = 4 \text{ mm s}^{-1}$ (b) in the tank T_{60} at $N = 8.3 \text{ s}^{-1}$.

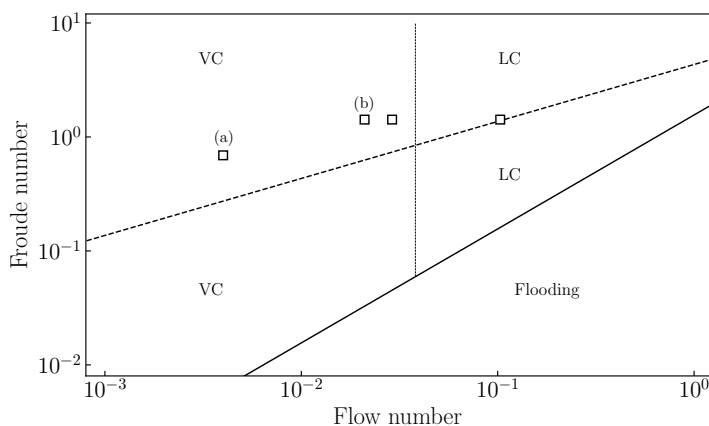


Figure 5.14: Regime flow map for T_{60} cases already reported in figure 5.12 (\square). Expected cavity shapes (vortex cavity, VC; larger cavity, LC) are highlighted, as well as the transitions from flooding to loading (—), and from partial to fully recirculated regime (----).

In figure 5.15, the profile of the liquid radial velocity along the impeller blade is displayed. Simulated data at different gas flow rates were compared to measurements made with the Pavlov

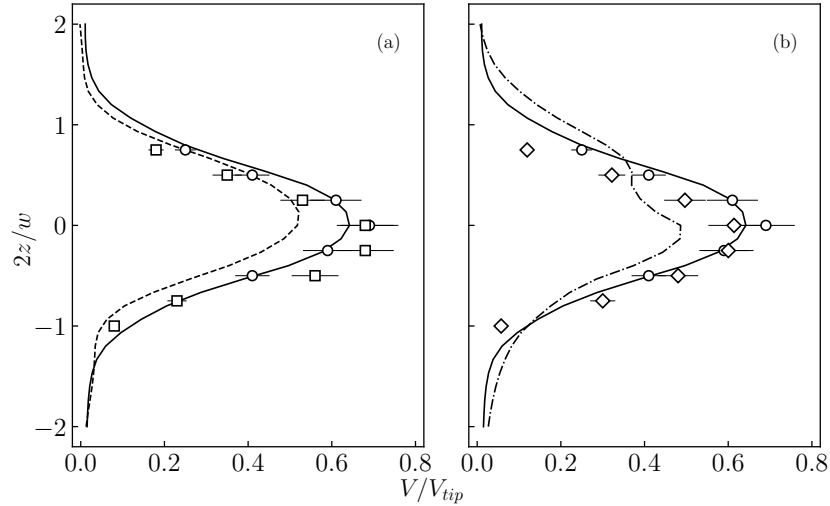


Figure 5.15: Profile of radial velocity for T_{60} at the impeller tip in air-water system at $N = 5.8 \text{ s}^{-1}$. Experimental data: $U_g = 0$ (\circ), $U_g = 1 \text{ mm s}^{-1}$ (\square), $U_g = 4 \text{ mm s}^{-1}$ (\diamond); simulation: $U_g = 0$ (—), $U_g = 1 \text{ mm s}^{-1}$ (---), $U_g = 4 \text{ mm s}^{-1}$ (-·-·-).

tube; the liquid velocity for the single phase flow was reported as a reference. At $U_g = 1 \text{ mm s}^{-1}$, the CFD profile followed qualitatively the experimental parabolic trend, with good agreement with measurements far from the center of the disk. Here, numerical V/V_{tip} was approximately 20% lower than the experimental value. Increase in gas flow rate caused a further decrease in the velocity at $z = 0$; the relative error with the measured value was again $\approx 20\%$.

Mixing time prediction

For the modeling of mixing time in aerated vessels, it was necessary to modify the turbulent Schmidt number Sc_t in order to have a better prediction of the mixing in the tank (figure 5.16). In fact, when the default value of 0.7 was used, the mixing time obtained with CFD was higher than the one measured in the tank: on average, numerical mixing time was almost three times longer. The best accuracy was found with the value $Sc_t = 0.1$. It follows that bubbles have a relevant effect on mixing inside the agitator: chaotic movement of the dispersed phase can increase the turbulence in the liquid phase, promoting the mixing of a passive scalar (Almérás et al., 2016). Almérás and colleagues proposed a model for the turbulent mixing in bubble columns operating at relatively low gas rate. Their model was tested in this study but, unfortunately, it was not capable to quantify the contribution of bubbles to the mixing of the tracer.

However, from the numerical results here presented, it seems clear that this contribution should be included in the model to improve its performance. This was not the main goal of this

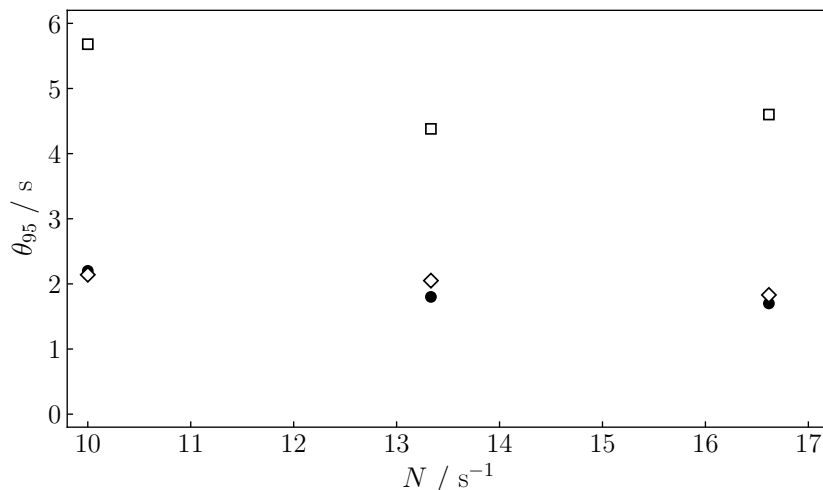


Figure 5.16: Effect of turbulent Schmidt number on computed mixing time for T_{30} at $U_g = 8 \text{ mm s}^{-1}$. Comparison with experimental data in T_{30} (Section 4.4). Symbols: experimental (●), $Sc_t = 0.7$ (□), $Sc_t = 0.1$ (◇).

thesis, so the approach based on tweaking of turbulent Schmidt number was retained. Although this strategy is commonly adopted in the scientific community (Gualtieri et al., 2017; Montante et al., 2005), it clearly affects the predictivity potential of the model; therefore, a more rigorous model based on physical interpretation should be developed.

5.4 Multiphase simulations of non-Newtonian liquids

5.4.1 Drag models for shear-thinning liquids

In modeling of multiphase flows with complex rheology, the universal drag laws did not give physical results. In fact, air-xanthan simulations were characterized by accumulation of gas in regions of the vessel where the liquid had a very low velocity (figure 5.17). Far from the impeller, due to the high value of viscosity, the liquid velocity was almost zero and, consequently, the Reynolds number was very small. In this condition, the drag coefficient used by the model was the one of a bubble rising in the Stokes regime; and its value increasing linearly with the decrease of Re . In this conditions, the drag coefficient of rigid bubbles rising in the Stokes regime was applied, leading to very high values of air concentration because of the high drag coefficient.

Therefore, in the case of viscous non-Newtonian fluids, the drag model proposed by Scargiali et al. (2007) was preferred, because it only depends on the bubble terminal velocity and the viscosity of the liquid is not explicitly taken into account. More effort must be taken to

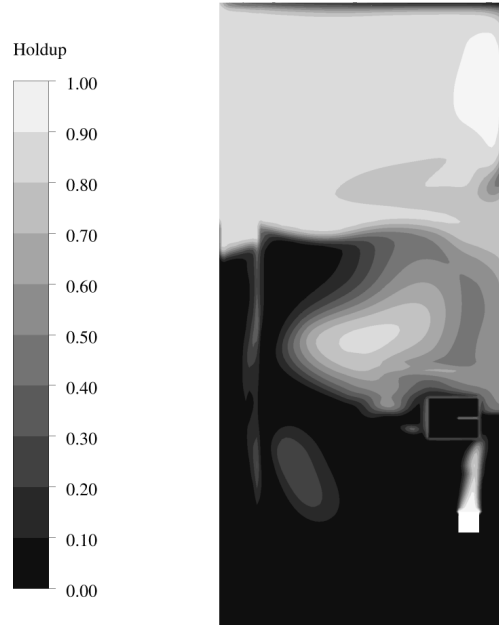


Figure 5.17: Contour of gas volume fraction in XG 0.50% at $U_g = 8 \text{ mm s}^{-1}$

extrapolate the correlations of bubble rising velocity and drag coefficient in stagnant liquid characterized by a complex rheology.

5.4.2 Hydrodynamics in air-xanthan cases

Global gas holdup

Figure 5.18 describes the mean holdup in xanthan gum solutions. In the case of XG 0.25%, an increase in gas holdup with the superficial gas velocity followed experimental findings. Except at the lowest gas rate, relative errors were below 3%. However, cases at higher concentration of xanthan gum were characterized by a greater mean error (25%). At $U_g = 40 \text{ mm s}^{-1}$, case for xanthan gum 0.50% did not reach convergence. In fact, the monitored quantities oscillated within $\pm 10\%$ respect to their final value.

Gassed power number

The power loss due to aeration is reported for XG in figure 5.19. No differences were noticed between the two concentrations. With an average error of 12%, it was found that the RPD was well predicted also in shear-thinning liquids.

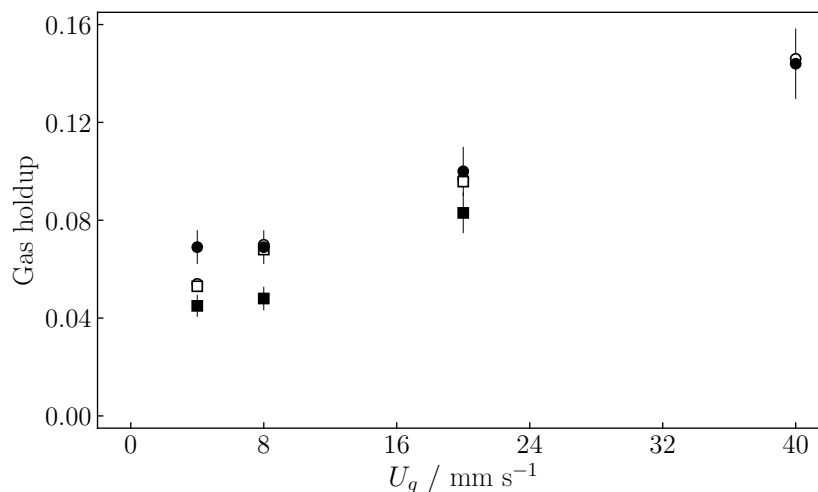


Figure 5.18: Numerical and measured gas holdup in XG against superficial gas velocity for T_{30} at $N = 13.3 \text{ s}^{-1}$. XG 0.25%: CFD (○), experimental (●); XG 0.50%: CFD (□), experimental (■).

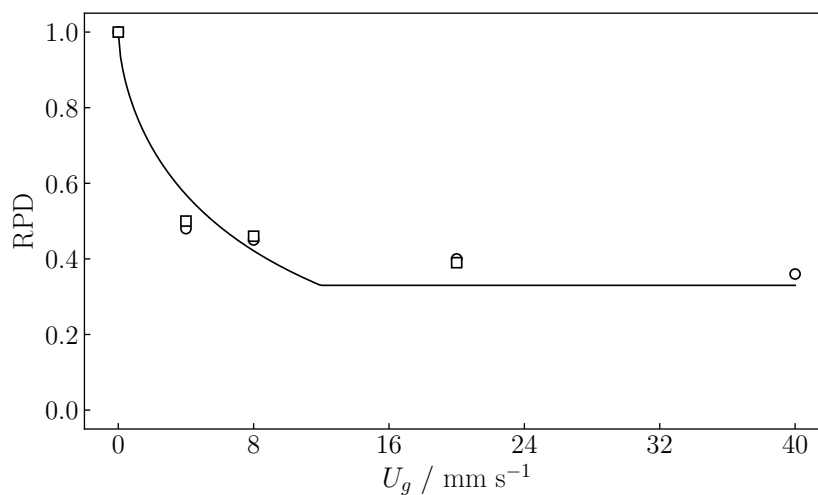


Figure 5.19: Relative power demand in T_{30} at $N = 13.3 \text{ s}^{-1}$ for XG solutions. XG 0.25% (○), XG 0.50% (□), Eq. (2.17) (—).

Mixing time prediction: xanthan gum case

Tweaking of the turbulent Schmidt number was necessary also for multiphase simulations of model fluids. In figure 5.20, numerical θ_{95} values at $U_g = 8 \text{ mm s}^{-1}$ are presented at different rotation speeds, and the effect of Sc is shown. Typical value of the turbulent Schmidt number (0.7) led to overestimation of mixing time. To decrease the relative error up to 15%, a low value of Schmidt number had to be used.

Tuning of the Sc with experimental data did not address the problem, represented by the

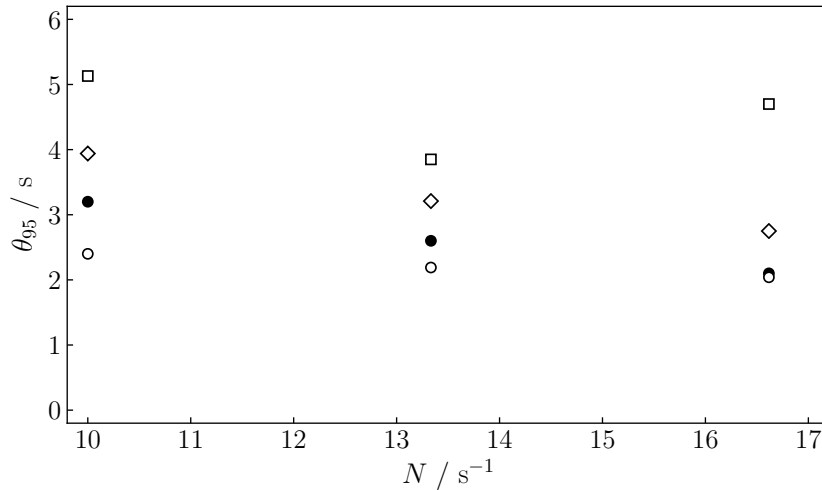


Figure 5.20: Mixing time in XG 0.25% at $U_g = 8 \text{ mm s}^{-1}$ with different Schmidt numbers. Experimental (\bullet), $Sc = 0.7$ (\square), $Sc = 0.2$ (\diamond), $Sc = 0.1$ (\circ).

weakness of multiphase turbulence model. Although useful, this approach only bypassed the poor representation of turbulent mixing in aerated media. However, by doing so, one can improve performance of the model, which applicability can be extended to cases with similar operating conditions (Gualtieri et al., 2017).

5.5 Conclusions

This chapter has outlined the validation of the CFD model for aerated reactors at high gas flow rate. Main points are summarized below:

- Global hydrodynamics well predicted with RANS equations and realizable k - ε turbulence model.
- For power-law fluids, extension of laminar models to turbulent mixing led underestimation of shear rate; better results in terms of average and maximum shear rates were obtained via a local turbulent approach.
- Among drag models for gas-liquid flows, universal drag laws gave the best agreement with experimental data in water. For aerated xanthan gum solutions, the model of Montante et al. (2008) based on bubble terminal velocity was preferred instead.
- Turbulent contribution of dispersed phase was not modeled explicitly; therefore, tuning of turbulent Schmidt number was required. Although not fully satisfying, this solution allows one to predict mixing times within an acceptable agreement.

The global numerical model was proven to be predictive enough for most of the operating conditions that were investigated in this study. Global quantities representative of hydrodynamics of the gas-liquid reactor were satisfactorily obtained. However, different limitations remain, such as: turbulent mixing in gassed conditions, a more descriptive drag model for bubbles in shear-thinning liquids, and a more rigorous turbulence model for complex fluids. In addition, the accurate description of aerated cavities structure might not be possible by using a periodic partial domain.

In order to move towards a more predictive CFD model for aerated reactors with rheologically complex fluids, a more detailed comparison of local gas fraction should be considered. For example, experimental data obtained via tomography (Sardeshpande et al., 2017) could be employed to investigate local gas distribution and the regimes transition in terms of gas flow number. Evidently, more efforts have to be done to develop a drag model to take into account the effect of liquid rheology. Finally, measurements of liquid and gas velocities at high gas content are eagerly awaited, thanks to whom the development and validation of closure models will surely benefit from; in particular, a better description of gas-liquid flows could accelerate the integration of the most recent models for turbulence in shear-thinning fluids (e.g. Gori & Boghi (2012)).

Chapter 6

Coupling of hydrodynamics, mass transfer, and kinetics: applications to bioreactors simulations

6.1 Prediction of mass transfer coefficient

A reliable description of the aerated reactor goes through a strong model for the mass transfer. In the case of aerobic fermentations, oxygen takes part in the reaction and the flux between gas and liquid phase has to be modeled. An erroneous estimation of the dissolved oxygen content can, in fact, mislead the interpretation of the rates of the substrate and oxygen conversions.

The mass transfer was modeled by solving two extra equations: one for the oxygen concentration in the gas phase, and the other for the dissolved oxygen. The gas phase was defined as a mixture of nitrogen and oxygen; the feeding composition was set in terms of oxygen mass fraction, which was equal to 0.23. Concerning the mass transfer mechanism, concentration at the interface was defined in terms of mass concentration ratio $m = C_{O_2}^{gas}/C_{O_2}^{liq}$. It was decided to have a saturation concentration of oxygen in the liquid of 0.008 g L^{-1} , therefore $m = 34$.

Last parameter required by the solver was the mass transfer coefficient. This quantity was expressed in terms of liquid-side coefficient k_L , considering the transport at the interface without any resistance in the gas phase. The model discussed in Section 4.3.4 was implemented in Fluent by means of an User Defined Function; for clarity, the correlation for k_L is reported again here:

$$k_L = 9.2 \cdot 10^{-5} \mu_{app}^{-0.26} \quad (6.1)$$

The coefficient so defined depended on the computed local μ_{app} , that is the local turbulent

energy dissipation (see section 2.7.3, Eq. (2.71)). However, Eq. (6.1) was originally obtained by fitting experimental data in terms of average dissipated power; therefore, by extending its use with local quantities, a linearization bias could be introduced and predictions in complex media being less accurate.

Prior to extending the use of the mass transfer model to the simulation of fermenters, the accuracy in terms of volumetric mass transfer coefficient was assessed. Firstly, a common basis for the comparison had to be defined. As mentioned in the previous chapter (section 5.3.2, p.112), to avoid nonphysical values of $k_L a$ at the cells characterized by a high gas volume fraction, the interfacial area was defined in terms of reactor volume. Therefore, experimental data — which were expressed respect to the liquid volume — were referred to the same volume basis by considering the average gas holdup. In addition, the average mass transfer coefficient was computed by using the mean values of both k_L and α_g ; the numerical $k_L a$ was then defined as:

$$k_L a = \langle k_L \rangle 6 \frac{\langle \alpha_g \rangle}{d_{32}} \quad (6.2)$$

Here, the averaging is intended as a volume average extended to the number of cells.

The numerical volumetric mass transfer coefficient was compared to measured values (section 4.3.3); this comparison is shown in figures 6.1 and 6.2. In the case of water, the computed

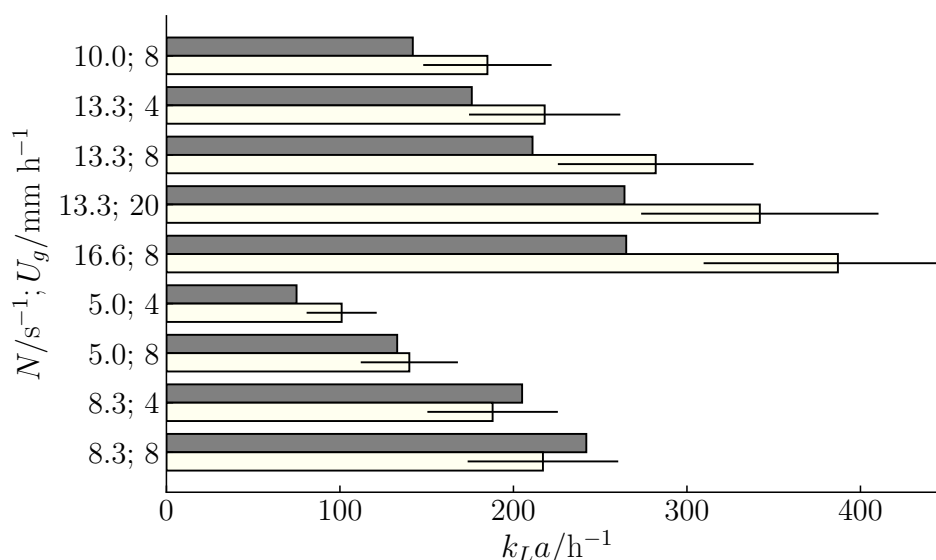
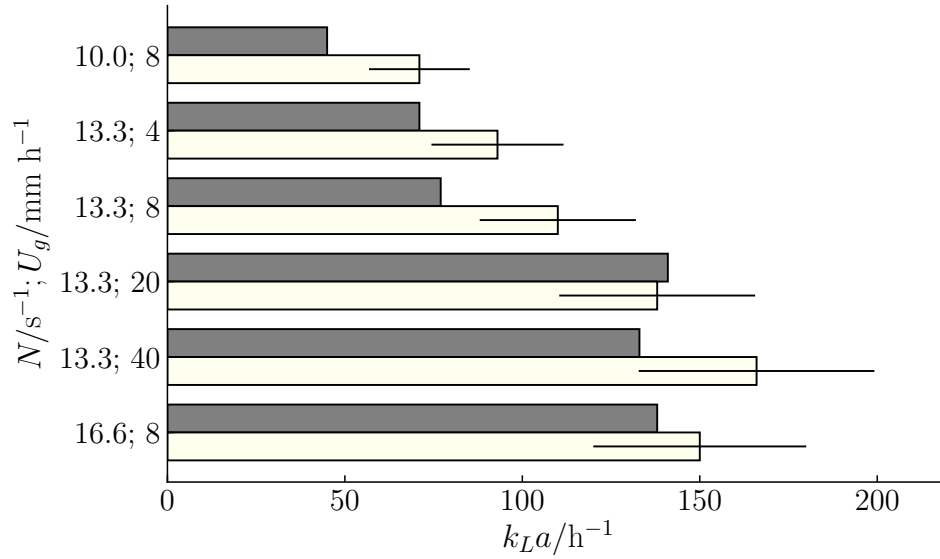


Figure 6.1: Average mass transfer coefficient in water at several operating conditions. Data are reported for CFD (dark bar) and experiments (light bar). For the experimental results, $\pm 20\%$ error bar is displayed.

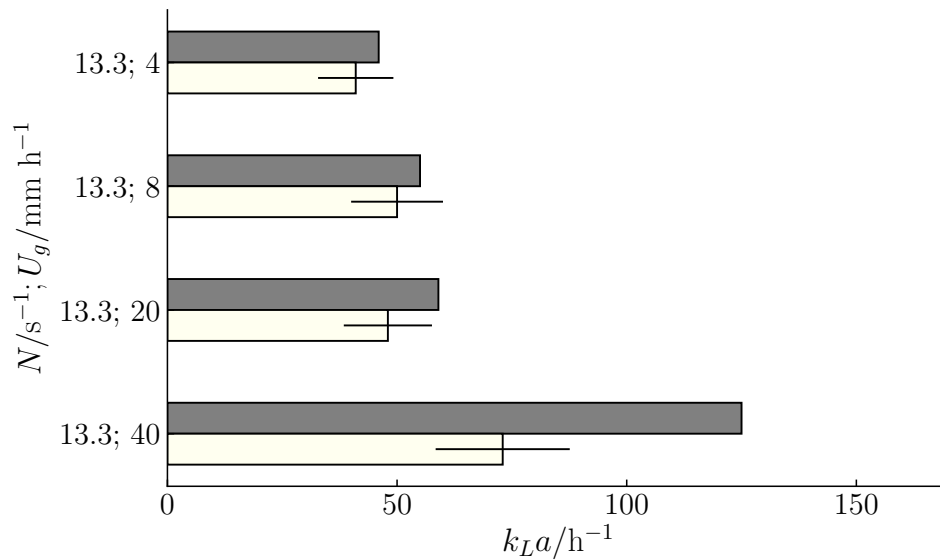
mass transfer coefficient was underpredicted in almost all cases. Nevertheless, the average discard with the experimental values was less than 20%. This difference may be partially explained

by an underestimation of the interfacial area, which is maybe linked to the presence of area with a very low gas concentration. Moreover, it was difficult to correlate the error in terms of operating conditions, as the discrepancy did not increase neither with the gas flow rate, nor with the impeller rotation speed.

In figure 6.2, similar plots are reported for the two xanthan gum solutions. The average



(a)



(b)

Figure 6.2: Average mass transfer coefficient in solutions of xanthan gum 0.25% (a) and 0.50% (b) at several operating conditions. Data are reported for CFD (dark bar) and experiments (light bar). For the experimental results, $\pm 20\%$ error bar is displayed.

error was slightly higher than before (24%), if one considers also the remarkable difference of 50% for the case referring to xanthan gum 0.50% at $N = 13.3\text{ s}^{-1}$ and $U_g = 40\text{ mm s}^{-1}$; at these conditions, the experimental average bubble size used for the simulation was 5.8 mm. It is worth to analyze the gas distribution for this specific case, which is displayed in figure 6.3. It

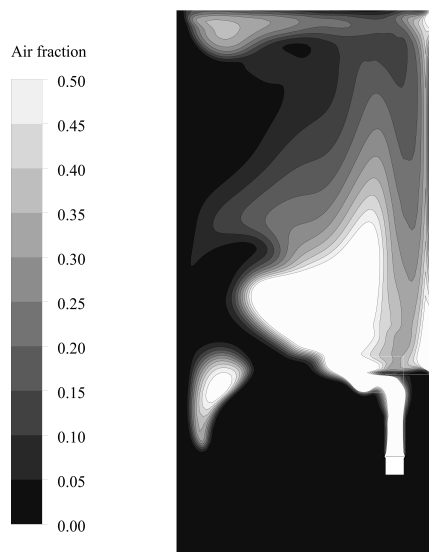


Figure 6.3: Contours of gas fraction in xanthan gum 0.50% at $N = 13.3\text{ s}^{-1}$ and $U_g = 40\text{ mm s}^{-1}$

can be seen that gas accumulated in a wide area above the impeller, in which the gas reached a concentration higher than 0.50. Note that in order to obtain a reasonable result in this specific case, the average $k_L a$ was computed by considering only the tank volume where $\alpha_g < 0.5$; in this occasion, the value of the mass transfer coefficient was equal to 70 h^{-1} and the average error went down to 17%. This brief example illustrated the need for a more representative drag law for non-Newtonian fluids, which would be based on experiments at higher gas fraction. However, despite its obvious limitations and taking into account its computational stability, the simple approach (based on the bubble terminal velocity) that have been used in this study was proven to be good enough in most of the studied conditions.

So, in this section of the chapter, the volumetric mass transfer coefficient was reported for water and xanthan gum solutions. Computed values were often found lower than the experimental ones (especially for simulations of air-water systems), even though the average error was of the same order of magnitude of the measuring technique.

6.2 CFD analysis of *Trichoderma reesei* fermentation

Before discussing results obtained with the CFD solver, the kinetic model is presented. Studies carried out by IFPEN researchers of the *Catalysis, biocatalysis and separation* department showed the pertinence of describing the fermentation process of *Trichoderma reesei* via a Monod-like kinetic model. As already reported in section 1.3.1, *Trichoderma reesei* presents two metabolisms depending on the environment; the increase in cells concentration is favoured at high substrate concentration, whereas production of enzymes occurs when the substrate is lower than a certain threshold concentration.

Therefore, in order to optimize both the growth of microorganisms and the production of valuable proteins, the fermentation is run in a fed-batch process: the growth phase, in which cells are nourished with mainly glucose, is followed by the enzyme production phase, where a mix of lactose and glucose constitutes the nutrients. In the latter, the substrate is constantly introduced in the system at a very low rate, to avoid the accumulation of sugar that would cause a decrease in the productivity.

In this study, the biological aspect was not investigated, and the formerly developed kinetic model was used without any modifications.

Trichoderma reesei kinetic model

Growth of microorganisms and proteins production were modeled via a Monod-type kinetic model. Rate of cell (X) growth, rates of substrate (S), oxygen (O₂) consumption, and rate of products (P) formation were expressed by the following equations:

$$\frac{dC_X}{dt} = \mu_X C_X \quad (6.3)$$

$$\frac{dC_P}{dt} = q_P C_X \quad (6.4)$$

$$\frac{dC_S}{dt} = -q_S C_X + Q_{feed} \quad (6.5)$$

$$\frac{dC_{O_2}}{dt} = -q_O C_X + k_{La} (C_{O_2}^* - C_{O_2}) \quad (6.6)$$

Here, μ_X is the specific growth rate, expressed in s^{-1} , whereas q_P represents the specific protein production rate ($g_P/g_X/h$); these kinetics variables are defined as:

$$\mu_X = \mu_{max} \frac{C_S^{n_\mu}}{K_{\mu_S} + C_S^{n_\mu}} \frac{C_{O_2}}{K_{\mu_O} + C_{O_2}} \quad (6.7a)$$

$$q_P = \left[\frac{q_{P_{max}} - q_{P_{min}}}{1 + \left(\frac{C_S}{K_{in.}}\right)^{n_{in.}}} + q_{P_{min}} \right] \frac{C_S}{K_{P_S} + C_S} \frac{C_{O_2}}{K_{P_O} + C_{O_2}} \quad (6.7b)$$

The values and the definition of each parameter are reported in table 6.1.

Figure 6.4 shows $q_P/q_{P_{max}}$ and μ_X/μ_{max} without oxygen limitations. Two regimes can be

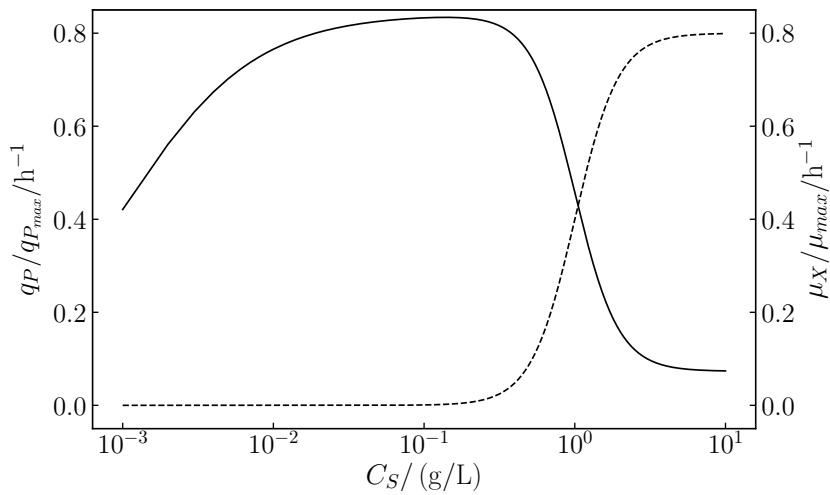


Figure 6.4: Influence of the substrate concentration on the specific production rate q_P (—) and specific growth rate μ_X (----) at $C_{O_2} = 0.008 \text{ g L}^{-1}$.

identified depending on the substrate concentration. At $C_S < 0.01 \text{ g L}^{-1}$, the substrate concentration is too low to favor the cell growth; in this environment, the biomass can then secrete proteins. The production rate is maximum in the concentration range $\sim 0.01\text{--}0.1 \text{ g L}^{-1}$. Increasing nutrient concentrations has a negative effect on the protein yield, because the substrate is mainly consumed by the microorganisms to growth.

Finally, the oxygen uptake q_O and the substrate consumption rate q_S are defined as follows:

$$q_O = \frac{\mu_X}{Y_{X,O}} + \frac{q_P}{Y_{P,O}} \quad (6.8a)$$

$$q_S = \frac{\mu_X}{Y_{X,S}} + \frac{q_P}{Y_{P,S}} \quad (6.8b)$$

where $Y_{X,O}$, $Y_{P,O}$, $Y_{X,S}$, and $Y_{P,S}$ are conversion yields (table 6.1).

The kinetic model based on Eqs. (6.7) and (6.8) is capable to describe the transition between the growth regime and the production regime. Prediction of instantaneous cells and protein concentrations is displayed in figure 6.5. The fermentation was carried out in a 2L reactor.

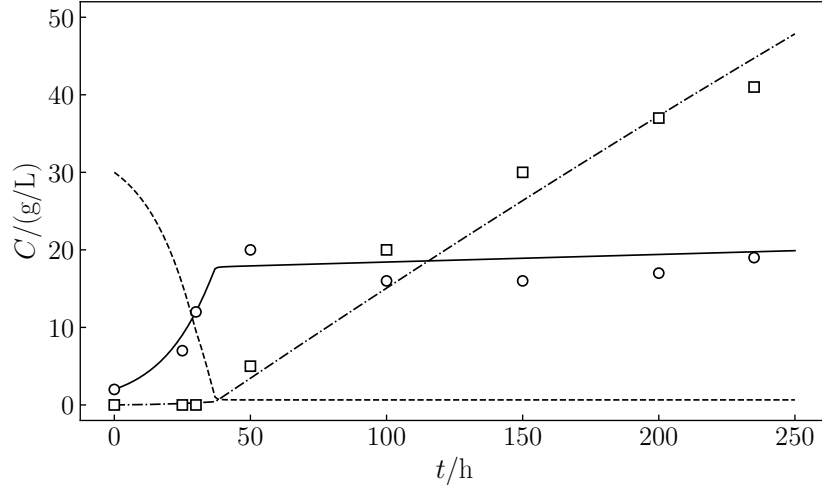


Figure 6.5: Concentration of species over time during lab-scale fermentation of *Trichoderma reesei*. The fed-batch started after 30 h, at a constant $Q_{feed} = 0.03 \text{ g}_S/\text{g}_X/\text{h}$. Experimental concentrations: biomass (\circ), protein (\square); model: biomass (—), protein (---), substrate (----).

Due to data confidentiality, detail on the culture strain could not be provided.

Fermentation started in batch mode, at a substrate concentration of 30 g L^{-1} and an initial

Table 6.1: Kinetics constants used in Equations (6.7) and (6.8).

Parameter	Value	Description
$\mu_{max} / (\text{h}^{-1})^\dagger$	0.05–0.15	Maximum growth rate
$K_{\mu_S} / (\text{g}_S/\text{L})^{n_\mu}$	1	Substrate affinity to biomass
$K_{\mu_O} / (\text{g}_O/\text{L})$	0.002	Oxygen affinity to biomass
$q_{P_{max}} / (\text{g}_P/\text{g}_X/\text{h})^\dagger$	0.015–0.030	Maximum production rate
$q_{P_{min}} / (\text{g}_P/\text{g}_X/\text{h})$	0.002	Minimum production rate
$K_{in.} / (\text{g}_S/\text{L})$	1	Growth/production threshold
$K_{P_S} / (\text{g}_S/\text{L})$	0.001	Substrate affinity to substrate
$K_{P_O} / (\text{g}_O/\text{L})$	0.002	Oxygen affinity to substrate
n_μ	3	
$n_{in.}$	3	
$Y_{X,O} / (\text{g}_X/\text{g}_O)$	0.98	Conversion yield to biomass
$Y_{P,O} / (\text{g}_P/\text{g}_O)$	1.03	Conversion yield to substrate
$Y_{X,S} / (\text{g}_X/\text{g}_S)$	0.5	Conversion yield to biomass
$Y_{P,S} / (\text{g}_P/\text{g}_S)$	0.5	Conversion yield to substrate

[†] For confidentiality, only a range was provided.

biomass concentration of 0.02 g L^{-1} . After 30 h, and at a residual substrate concentration of about 10 g L^{-1} , a constant flow rate of substrate was introduced in the system, and production of protein took place; in this phase, a mix of glucose and lactose constituted the nutrient. Moreover, the gas flow rate was high enough to have a sufficient concentration of dissolved oxygen during the entire process.

An important aspect to consider is the viscosity variation of the culture broth during the fermentation. In figure 6.6, the apparent viscosity of the broth at different cell concentrations is shown. The most concentrated xanthan gum solution showed a rheological behavior similar

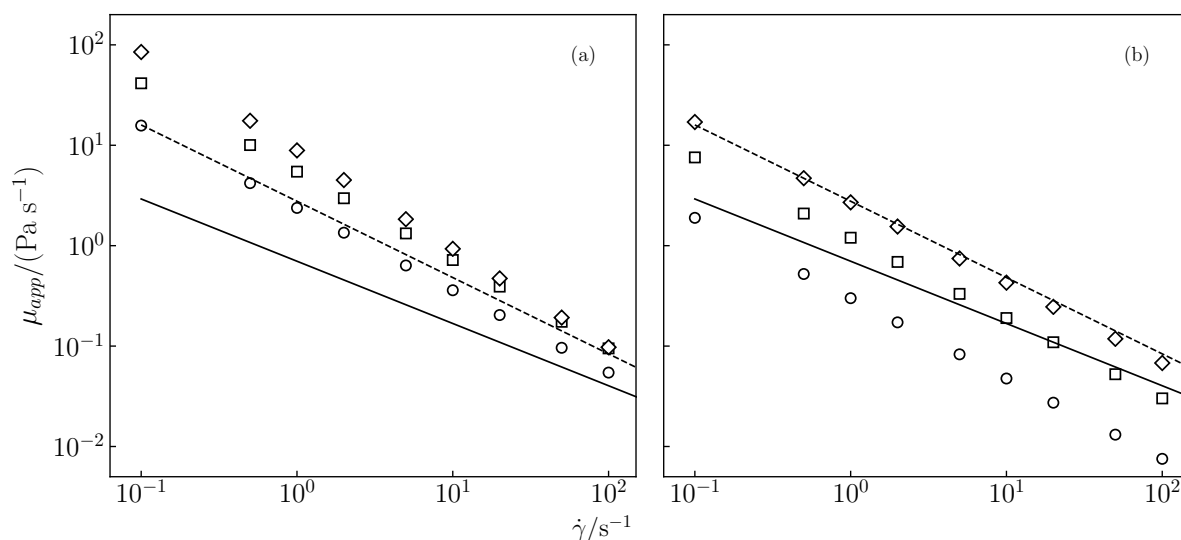


Figure 6.6: Rheology of fermentative broth at different biomass concentrations and during the growth phase (a) and the production phase (b). Data: $C_X = 10 \text{ g L}^{-1}$ (\circ), $C_X = 20 \text{ g L}^{-1}$ (\square), $C_X = 30 \text{ g L}^{-1}$ (\diamond), xanthan gum 0.25% (—), and xanthan gum 0.50% (----).

to the one of the broth in the growth phase at biomass concentration in the range 10–30 g L. Moreover, it can be noticed a decrease in apparent viscosity in the transition between the two regimes, due to the change in cells morphology (Hardy et al., 2015). In the production phase, broth rheology at $C_X = 20 \text{ g L}^{-1}$ and $C_X = 30 \text{ g L}^{-1}$ can be reproduced with XG 0.25% and 0.50% respectively.

6.2.1 Coupling of hydrodynamics and bio-kinetics

Solver settings

The kinetic model discussed in the previous section was implemented in Fluent via *User Defined Functions*. Equations for dissolved oxygen (DO) and substrate concentrations, as well as for the oxygen fraction in the gas phase were simultaneously solved. The CFD model described an

Table 6.2: Tank configurations used with the fermentation model.

Case	Tank diameter, T/m	H:T	Volume, V/m ³
1S	0.3	1	$2 \cdot 10^{-2}$
1B	5.0	1	98
4R	2.1	3	22

instantaneous condition of the real fed-batch fermentation, at the beginning of the production phase. Therefore, a constant concentration of biomass C_X was considered, and only Eqs. (6.5) and (6.6) were solved in steady state. After reaching a converged gas-liquid mixing simulation, equations of momentum, turbulence, and volume fraction were deactivated, while the species equations for the nutrients were activated. These equations were discretized using a second-order scheme. Only the production phase of the process was modeled; therefore, a constant concentration of biomass was considered. Even if at a low flow rate, the nutrient solution is provided continuously for hundreds of hours, causing an increase in the liquid volume and a dilution of the species concentrations; however, in all the simulated cases, the computational volume was kept constant. In this approach, simulations represented an instantaneous condition of the real fermentation, at the beginning of the production phase.

The main goal of the numerical study was to address the problem of large-scale fermenters design. In that configuration, the role of substrate gradients in the productivity of the system has to be considered. In order to recreate these gradients, bigger tanks were simulated, as the mixing time scales with the impeller speed. Therefore, besides the tank T_{30} that was used for the validation of the closure models, two other tanks were simulated; these had a volume of about 100 and 20 m³. In table 6.2, the details of each configuration are reported. The case 4R refers to a four-impeller configuration, which was used to extend the CFD model to a more practical problem. In the industrial scale, in fact, when high volume of liquid is processed, units with $H:T > 1$ are usually more convenient. In figure 6.7, the diagram of the multi-stage reactor is shown.

For the configurations 1B and 4R, tweaking of the Schmidt number was judged unnecessary due to a better prediction of the gas dispersion in the bigger tanks. Figure 6.8 shows the gas fraction for 1S and 1B at the same operating conditions (...); at the bigger scale, the turbulent viscosity could be high enough to mask the contribution of other forces to disperse gas bubbles; in fact, for the same dissipated power, the Reynolds number for the reactor 1B was more than thirty times higher than the one for 1S, while the turbulent viscosity ratio was even greater.

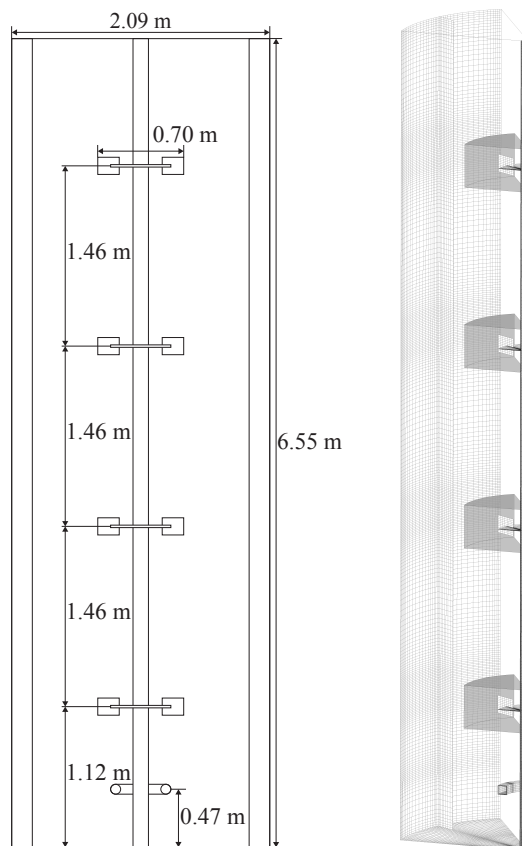


Figure 6.7: Scheme of the reactor with four Rushton turbines. On the right, details on the mesh used to model a sixth section of the tank.

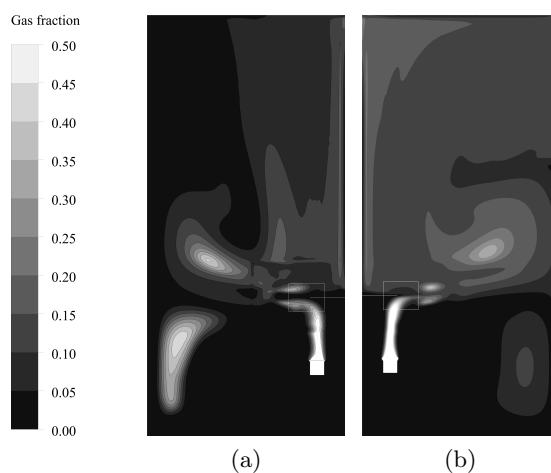


Figure 6.8: Contours of gas fraction in water in the VC regime based on CFD simulation for T_{30} (a) and for 1B (b). In order to compare the different cases, the same Froude and Flow numbers were considered.

6.2.2 Influence of hydrodynamics on substrate distribution

By comparing the characteristic times of the process, one can predict the formation of spatial gradients. In particular, one can define a Damköhler number, Da as:

$$Da = \frac{\theta_c}{\theta_S} \quad (6.9)$$

Here, θ_c is the characteristic flow time, usually taken as the circulation time ($\theta_c \approx \theta_{95}/4$ in stirred tanks), whereas θ_S is the reaction time. In this study, the substrate was the limiting reactant; therefore, the reaction time scale was defined in terms of average substrate consumption:

$$\theta_S = \frac{\langle C_S \rangle}{C_X q_S} \quad (6.10)$$

When Da is greater than one, reaction timescale is lower than the mixing one. In this scenario, the substrate gets consumed quickly before getting uniformly mixed inside the reactor, leading to the formation of concentration gradients. Finally, the characteristic mass transfer timescale ($k_L a^{-1}$) was considered as well. In table 6.3 different timescales are listed for the three configurations described above. For all the three simulation cases, the rotation speed and gas flow rate were chosen in order to have $P_g/V_l = 2300 \text{ W m}^{-3}$ and a superficial gas velocity of 8.3 mm s^{-1} , which correspond to common operating conditions for an industrial fermentation; the same average bubble diameter equal to 4.1 mm — experimentally measured for the configuration 1S — was adopted for the 1B and 4R cases. For the circulation time computation, the experimental mixing time was used in the case of 1S; for the configurations 1B and 4R, the values were predicted by using the correlations of Grenville (1992) and Cooke (1988), respectively.

The predicted performance of each configuration was evaluated in terms of normalized protein production rate, q_P^* , and normalized growth rate, μ^* :

$$q_P^* = \frac{q_P}{q_{P_{max}}} \quad (6.11)$$

$$\mu^* = \frac{\mu}{\mu_{max}} \quad (6.12)$$

Table 6.3: Operating conditions and timescales for mixing, mass transfer, and substrate consumption in different configurations at $C_X = 20 \text{ g L}^{-1}$. For confidentiality reasons, only an interval of the feed rates $q_{feed}/(\text{gS/gX/h})$ was reported.

Configuration	N / s^{-1}	Q_g / vvm	θ_c / s	$k_L a^{-1} / \text{s}$	$q_{feed}^I = 0.015\text{--}0.020$ θ_S / s	$q_{feed}^{II} = 1.5q_{feed}^I$ θ_S / s	$q_{feed}^{III} = 1.7q_{feed}^I$ θ_S / s	$q_{feed}^{IV} = 2q_{feed}^I$ θ_S / s
1S	13.3	1.7	1	40	10	26	100	1950
1B	1.6	0.1	5	63	10	26	100	1950
4R	2.7	$7.6 \cdot 10^{-2}$	27	60	10	26	100	1950

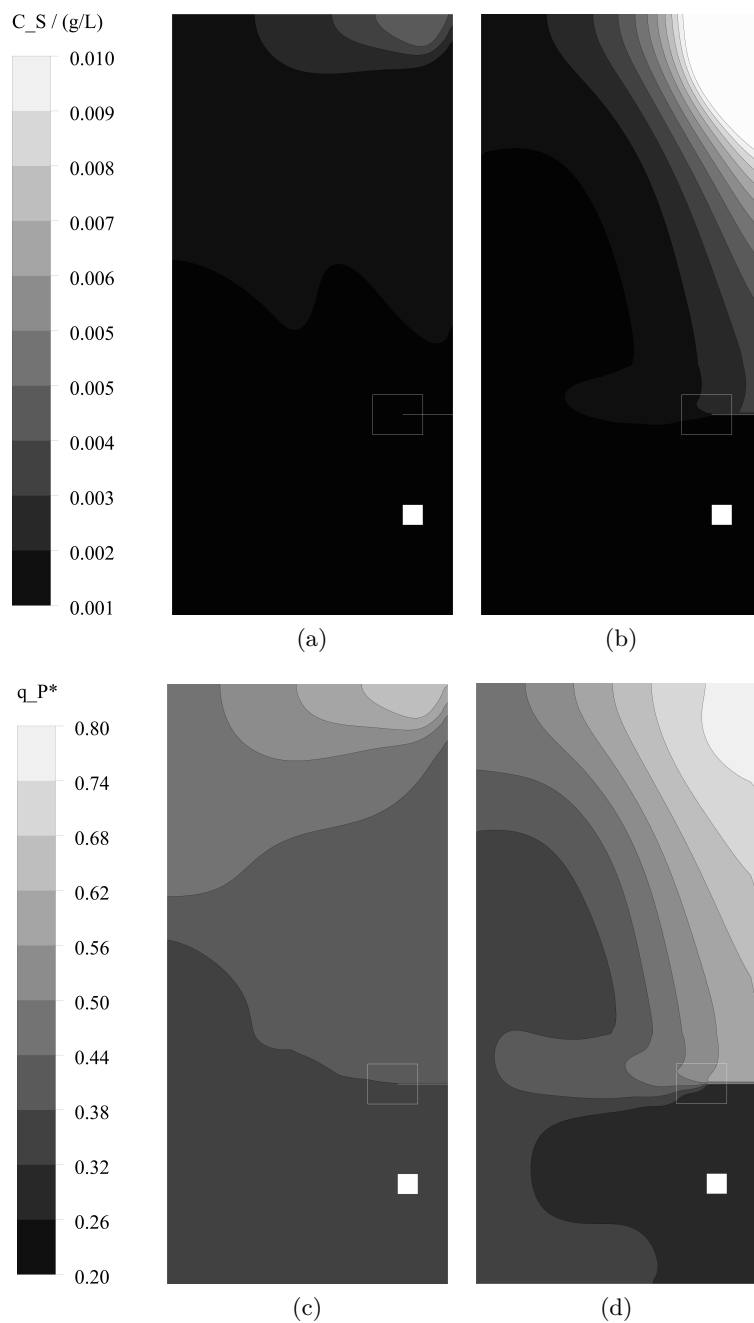


Figure 6.9: Substrate concentration distribution for the cases 1S (a) and 1B (b). A broader distribution of substrate was obtained in the big tank, which led to formation of a low-productivity area under the impeller (d).

Case at q_{feed}^I

In figure 6.9, contours for the substrate concentration and for q_P^* are displayed. For the small

tank (figure 6.9a), the circulation time was very short compared to the characteristic time of substrate consumption, and a homogeneous concentration of the sugar was obtained in the liquid. In fact, except for a small area close to the injection point, C_S varied between $0.0001\text{--}0.002\text{ g L}^{-1}$, with an average concentration of about 0.001 g L^{-1} in the rest of the tank. On the other hand, a clear gradient of C_S was obtained for the case 1B (figure 6.9b); the characteristic time to consume the substrate was shorter than the circulation time, so the reactant accumulated in the region close to the feed point, where it reached a concentration in the order of $1 \cdot 10^{-2}\text{ g L}^{-1}$. Moreover, the average concentration was equal to 0.002 g L^{-1} ; computation of the coefficient of variation for both the tanks read 0.3 for the small one, whereas $\text{CoV} = 3$ for the tank of 98 m^3 . The dissolved oxygen was homogeneous in both cases, and its average concentration was $5.97 \cdot 10^{-3}$ and $5.90 \cdot 10^{-3}\text{ g L}^{-1}$ for 1S and 1B, respectively.

The presence of a substrate gradient had consequences on the protein production rate. As it can be seen in figures 6.9c and 6.9d, the minimum and the maximum value of q_P^* was different between the two scales. Furthermore, because of the accumulation of substrate, in the tank 1B a broader volume was characterized by a higher q_P^* ; in the same configuration, the specific productivity below the impeller dropped to 20% of the maximum value.

A clearer representation of these results is presented in figure 6.10, where the substrate distribution is compared to the expected qp^* and μ^* for the same range of concentration. The substrate content was too low to favor cells growth; however, the maximum productivity was not yet reached, being the flow rate of nutrient relatively low. Moreover, the average C_S in 1S was equal to the one predicted by solving Eqs. (6.5) and (6.6). Compared to the ideal mixing case, the average substrate concentration in 1B was however higher.

In figure 6.11, the volume distribution of q_P^* for 1S and 1B is shown. The bigger tank was characterized by a broader distribution, with a certain fraction of cells in which the normalized production rate was very high (≈ 0.7). This high-productivity area was however limited to the volume close to the injection point, where the highest substrate concentration was reached. The specific production rate was the same in both cases (table 6.4); at this substrate feed rate, the growth rate was practically null, so the substrate would be consumed to only produce proteins.

Although the presence of a substrate gradient had in general a positive effect at this nutrient feed rate, one should also consider the dynamics of the process. In fact, in this analysis any cell adaptation dynamics was not considered, saying that microorganisms would instantaneously react solely based on the properties of the liquid phase (Bach, 2018; Morchain et al., 2014). Additionally, microorganisms could be permanently affected by exposure to poor zones, decreasing the protein yield. Therefore, in the case of the real process, the presence of a zone in the tank in which the productivity is high, could not entirely counterbalance those regions at low q_P due to the heterogeneous distribution of the nutrients.

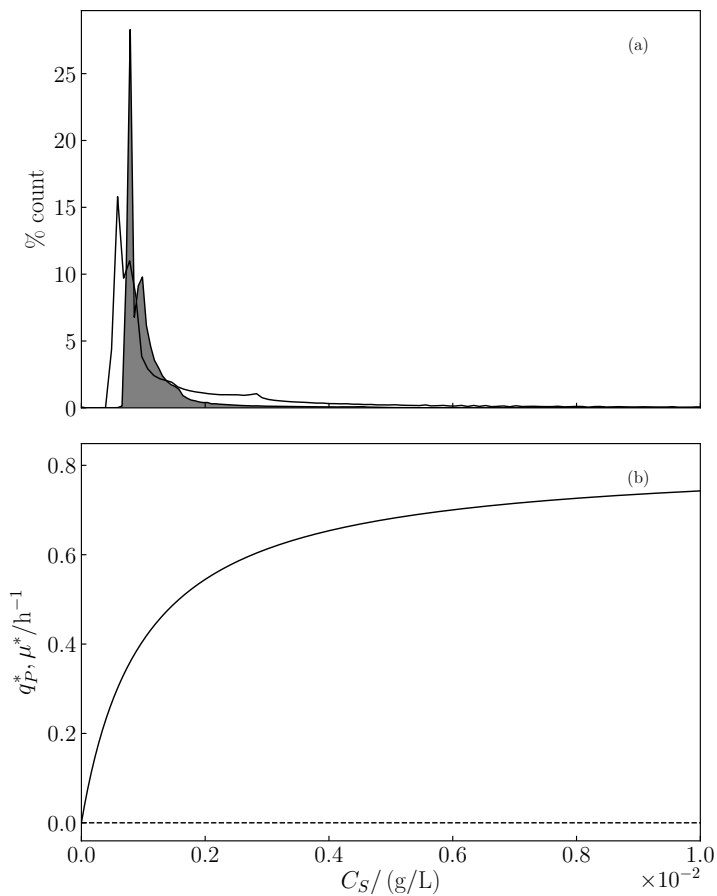


Figure 6.10: Substrate distribution (a) for the cases 1S (dark area) and 1B (empty area). In the graph at the bottom, q_P^* (—) and μ^* (----) are represented.

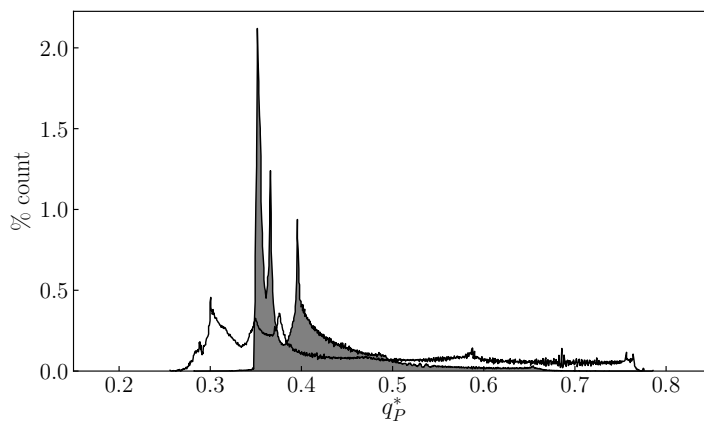


Figure 6.11: Density distribution of normalized production rate. The area in black represents the data for the small tank, whereas data for the big tank are represented by the empty area.

Hydrodynamics in multi-impeller reactors is more complex, due to the superimposed flows originated by every turbine. In the case of radial-flow turbines, axial mixing through the radial discharge is hindered, causing the formation of compartments. Although the mixing in each compartment can be fast, the global homogenization is slow. Figure 6.12 shows the effect of said increase in mixing time for the configuration 4R.

In this case, the mixing time was ten times longer than the reaction timescale, and strong gradients were obtained. Rapid consumption of the carbon source in the upper part of the tank, caused a depletion of nutrients in the bottom half, that is below the second impeller from the bottom. Here, the average concentration was about ten times lower than in the highest recirculation loop. Due to the pressure gradient, oxygen solubility increased from the top to the bottom of the tank; therefore, despite the higher substrate content, the oxygen concentration was higher in 4R configuration.

The complete distribution of C_S is reported in figure 6.13. In 4R, a very broad C_S distribution was found; half of the tank was at $C_S < 0.001 \text{ g L}^{-1}$, whereas concentrations in the order of 0.1 g L^{-1} were obtained above the first impeller. Peaks corresponding to the average concentration in each loop can also be noticed.

Substrate heterogeneities caused a wide distribution of the production rate, as reported in figure 6.14. The average specific production rate was practically equal in all three cases, because the same feed rate was considered and, due to the low C_S , no microbial growth was promoted. However, in the case 4R, a wide portion of the reactor was characterized by $q_P^* < 0.2$; quantification of these zones that are poor in nutrient is important to estimate the exposure time of microbial cells in drastic conditions.

Cases at q_{feed}^{II} and q_{feed}^{III}

By increasing the nutrient feed rate, the average substrate concentration increased as well. Figure 6.15 shows C_S , the production and growth rates for all the three configurations. Once again, mixing in the smaller tank was faster than the dynamics of substrate consumption; substrate concentration was almost constant inside the reactor and its value equal to the ideal-mixing case (0.004 g L^{-1}). In the bigger tanks, $\langle C_S \rangle$ was higher than the reported value: 0.006 g L^{-1} and 0.008 g L^{-1} for 1B and 4R, respectively (figure 6.15a).

Results at q_{feed}^{III} are reported in figure 6.15c,d. For simulations at this feed flow rate, only the comparison between the case 1S and 4R will be discussed. In fact, at this condition, the mixing time in 1B was lower than the reaction timescale (see table 6.3); therefore, no substantial difference existed between 1S and 1B. The 0.02 m^3 reactor kept following the behavior of an ideal-mixing case, with $\langle C_S \rangle = 0.017 \text{ g L}^{-1}$. On the other hand, 4R case showed an increase in $\langle C_S \rangle$, which was almost four times higher than in 1S. Moreover, with a coefficient of variation

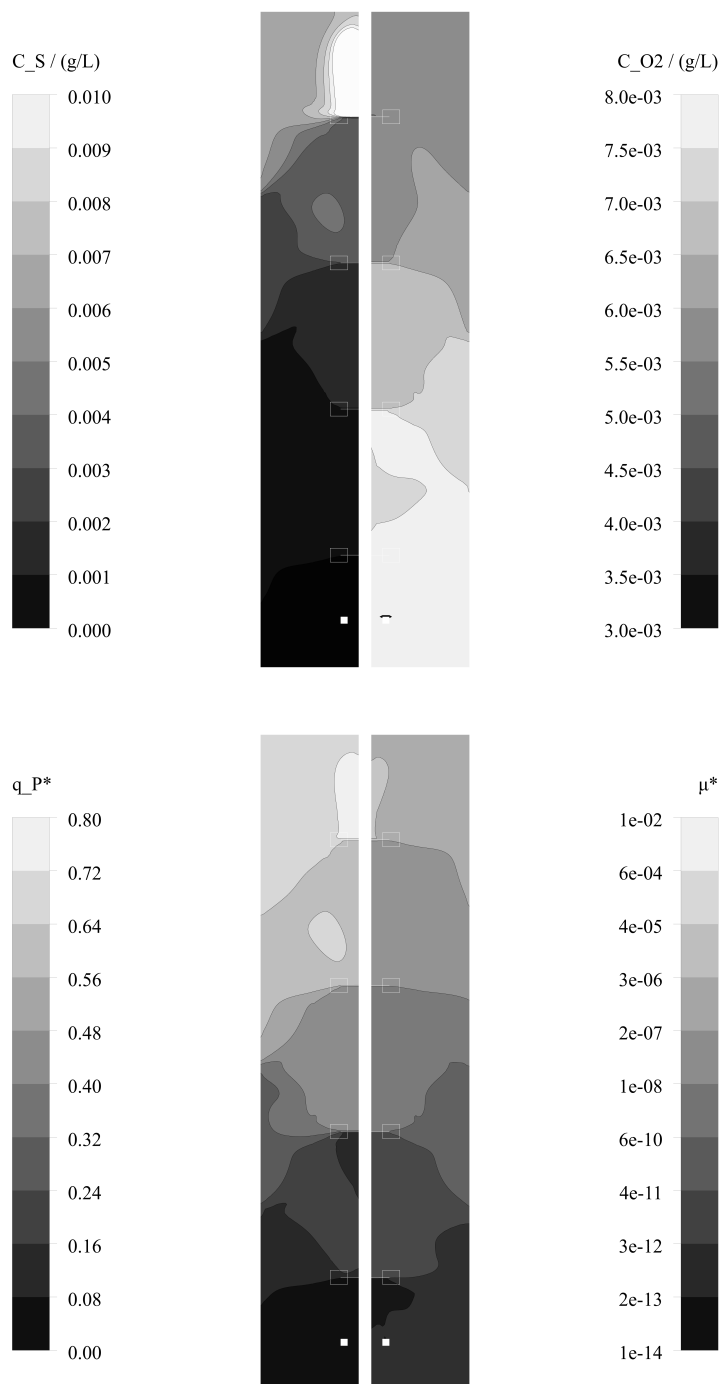


Figure 6.12: Species concentrations, normalized production and growth rates for the 4R.

of $C_S = 13.5\%$, the substrate distribution in 4R was more dispersed.

The normalized protein production rate at q_{feed}^{II} and q_{feed}^{III} is reported in figure 6.16. In

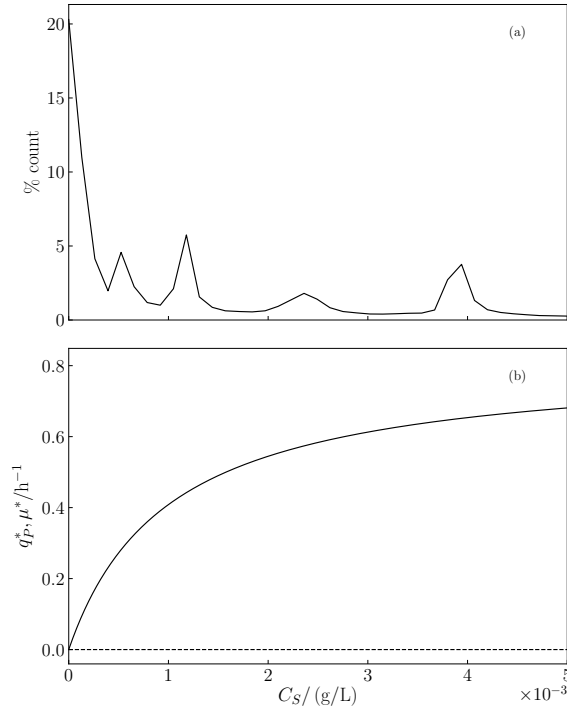


Figure 6.13: Substrate distribution for the configuration 4R (a). At the bottom, q_P^* (—) and μ^* (---) are reported.

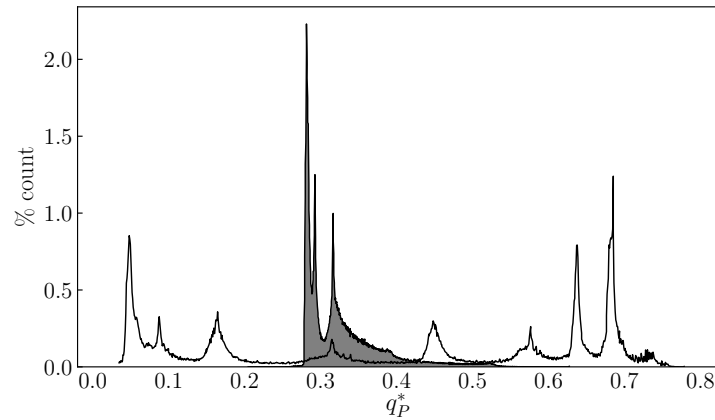


Figure 6.14: Density distribution of the normalized production rate. The dark area represents data for 1S, while the empty area is used for 1B.

contrast with the cases 1S and 1B, a bigger portion of the liquid volume with high q_P^* was found in 4R (figure 6.16a).

At q_{feed}^{III} , $q_P^* > 0.7$ for both the configurations 1S and 4R, but the latter was less uniform. At the bottom of the tank, a lower substrate concentration was present, causing a slight decrease in the specific productivity. Up to this feed rate, all the simulations described systems in which,

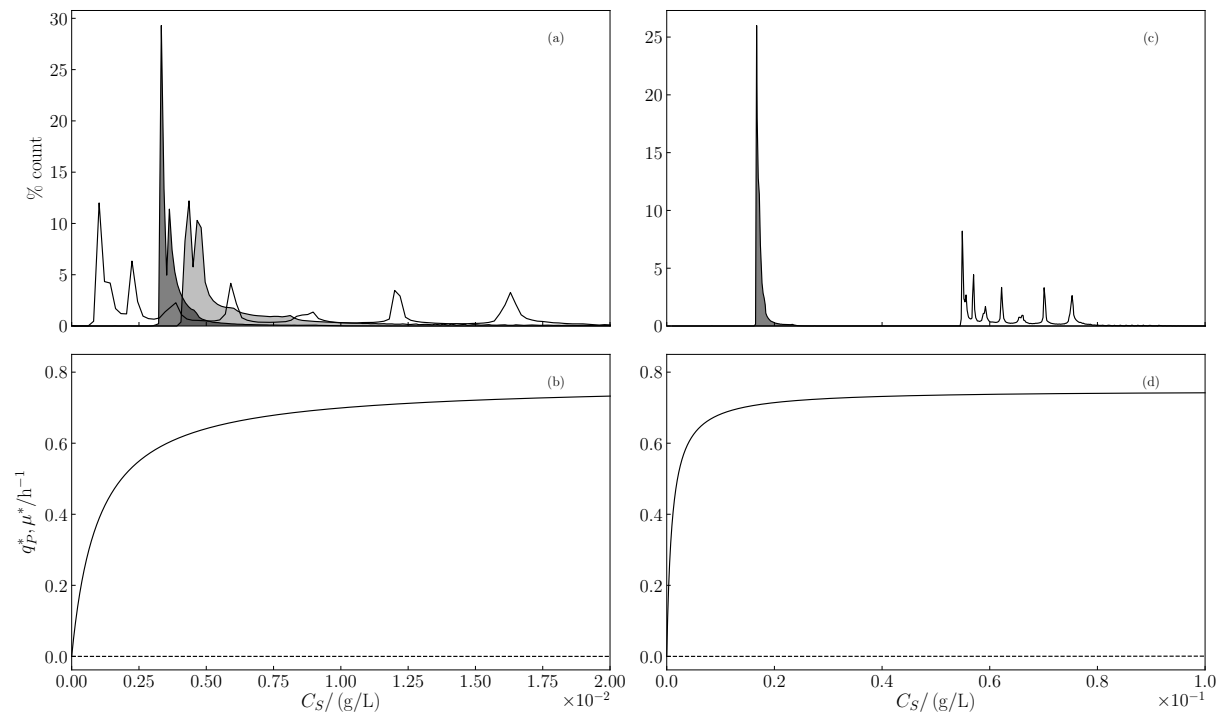


Figure 6.15: Substrate concentration at q_{feed}^{II} (a) and at q_{feed}^{III} (c). From the darker to the white area, data refer to 1S, 1B, and 4R, respectively; q_P^* (—) and μ^* (----) are also reported (b,d).

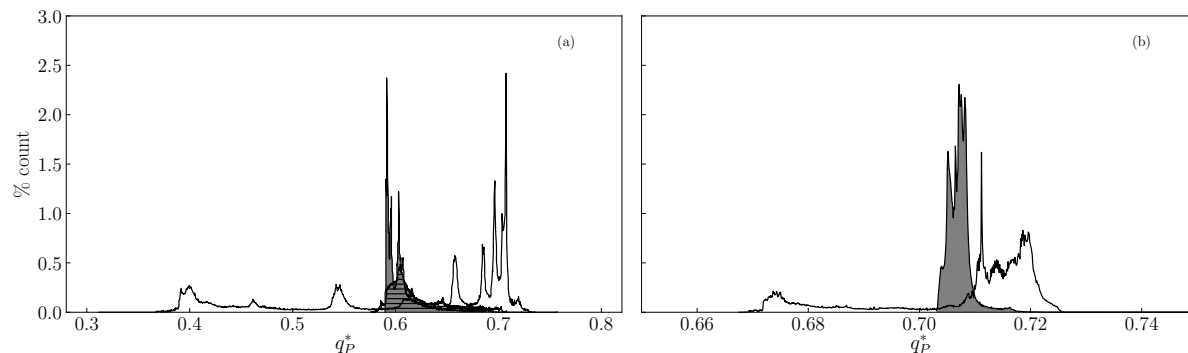


Figure 6.16: q_P^* at q_{feed}^{II} (a) and at q_{feed}^{III} (b) is represented for cases 1S (black area), 1B (gray area with horizontal lines), and 4R (empty area).

from an extra-cellular point of view, only production would happen. Therefore, the accumulation of substrate did not cause a decrease in the average specific productivity. Nevertheless, a protein yield loss could be noticed in the real process if substrate gradient was present.

Case at q_{feed}^{IV}

This condition described an extreme case, in which the average substrate concentration was higher than 0.1 g L^{-1} . At this value, growth of the microorganisms became competitive with the production of enzyme, causing a decrease in the protein yield. Referring to table 6.3, the reaction time at this q_{feed} was an order of magnitude higher than the mixing time computed for the configuration 4R; therefore, even at this scale, homogenization of the nutrient species was foreseen.

In figure 6.17, the concentration distribution for 1S and 4R is displayed. The very narrow

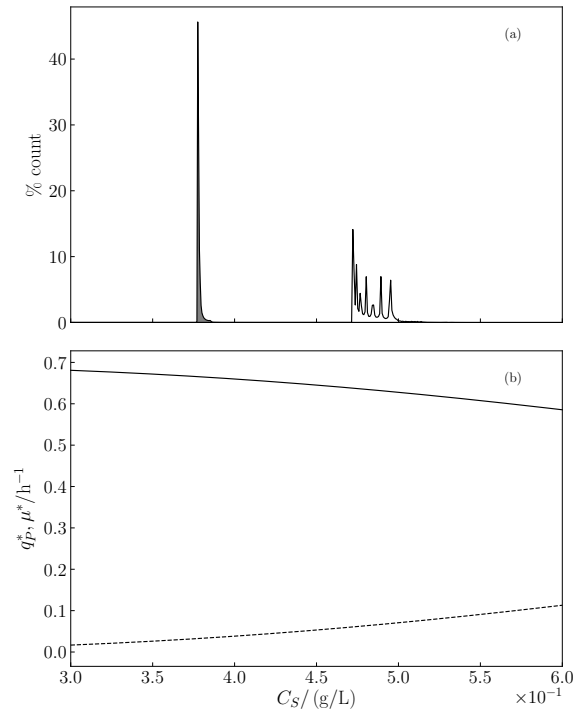


Figure 6.17: Substrate distribution (a) in the configurations 1S (dark area) and 4R (empty area). At the bottom, q_P^* (—) and μ^* (----) are represented.

profile for the smaller tank is not surprising; for this case, the coefficient of variation for C_S was less than 0.5%. More interesting is, however, the profile obtained for 4R. As already mentioned in the text, when several Rushton turbines are mounted, the axial mixing is hindered and this caused a minor heterogenization of the nutrient along the height of the reactor. Even if the coefficient of variation was $\approx 2\%$, a noticeable decrease in the specific production rate was found in 4R; a 13% decrease in q_P^* respect to the single-impeller configuration was computed. Reasons for this outcome can be explained by taking into account the cell growth rate.

Figure 6.18 shows q_P^* and μ^* values for 1S and 4R at the highest feed rate that was considered in this study; the variable μ^* was defined similarly as in Eq. (6.11). The case 1R had a similar

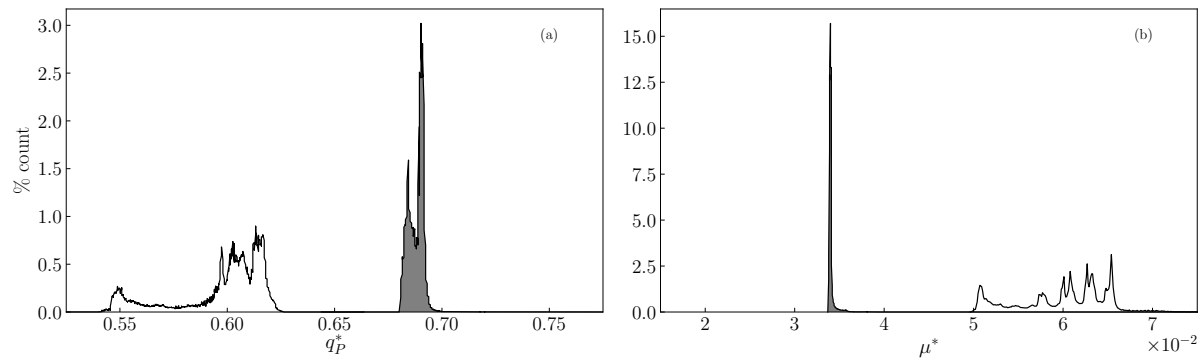


Figure 6.18: Density distributions of normalized production rate (a) and growth rate (b). Areas filled in black refer to 1S, whereas the empty areas represent data for 4R.

profile as the one found in figure 6.16b. In fact, in both cases, the average C_S was such that the system reached its maximum productivity. Nevertheless, at this substrate concentration, cellular growth rate started to increase. In 1S, an average value of $\mu^* = 0.034$ was found, which was four-to-nine order of magnitudes higher than in all the other simulations at lower q_{feed} . A greater loss in the specific protein yield was found in the 4R system. In this case, the average μ^* was three times higher than in the single-impeller configuration. Moreover, the normalized growth rate varied inside the reactor, due to the nutrient axial distribution.

Figure 6.19 displays the distribution of μ^* and C_S at the same plane. Although the average substrate concentration decreased of about 10% from the top to the bottom of the vessel, a greater increase in the growth rate would be experienced by cells moving inside the fermenter. In fact, a difference of almost 50% existed between the superior and inferior parts of the tank.

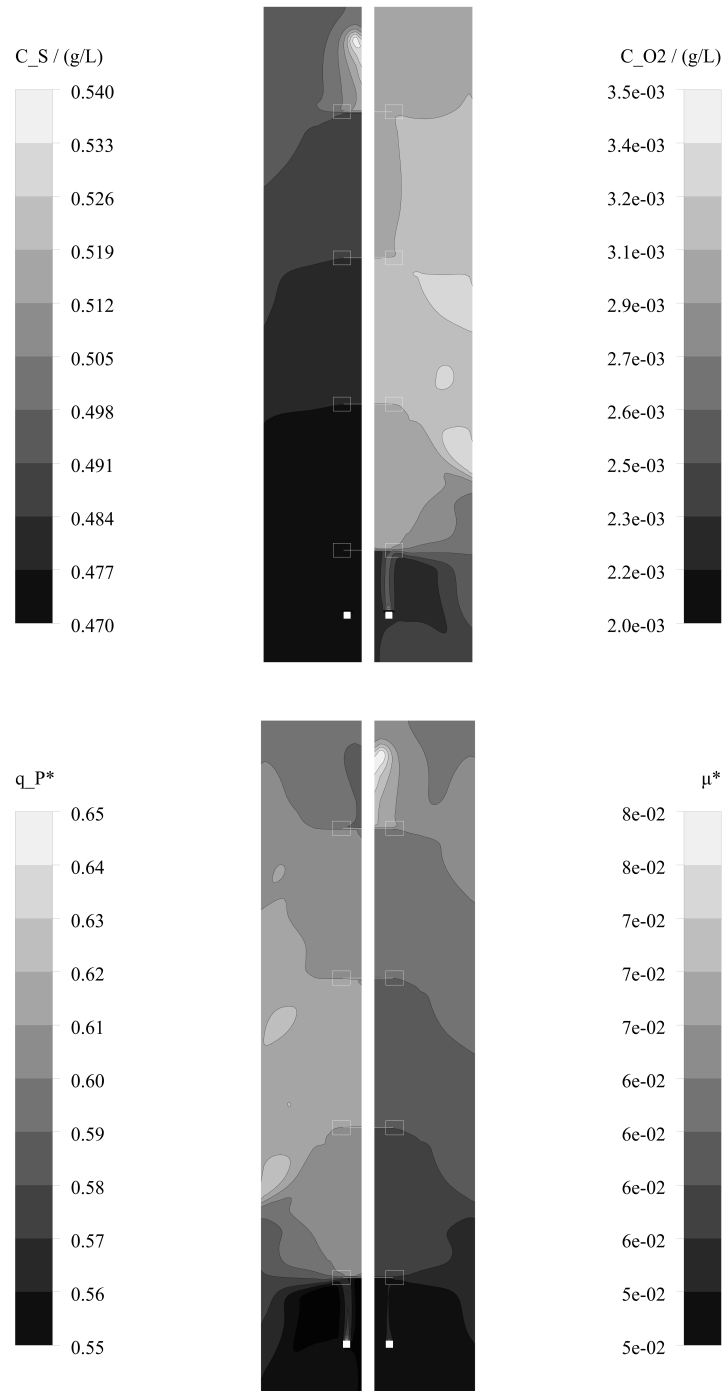


Figure 6.19: Isovalues contours of species concentrations, q_P^* , and μ^* for 4R case.

The average final concentrations of substrate, oxygen, and the average production and growth rates are shown in figure 6.20. Numerical values were compared to average results obtained by solving Eq. (6.5) and Eq. (6.6) for the ideal-mixing case and for two different $k_L a$ values; one solution of the equations was obtained for the same $k_L a$ that characterized the simulations, while for the other $k_L a$ a value of 200 h^{-1} was used. The latter was chosen high enough to guarantee a high dissolved oxygen concentration. The comparison with these two ideal-mixing cases allowed one to dissociate the effects of the non-ideal mixing and of oxygen limitation. Simulation of the case 1S led to results very similar to the ideal-mixing

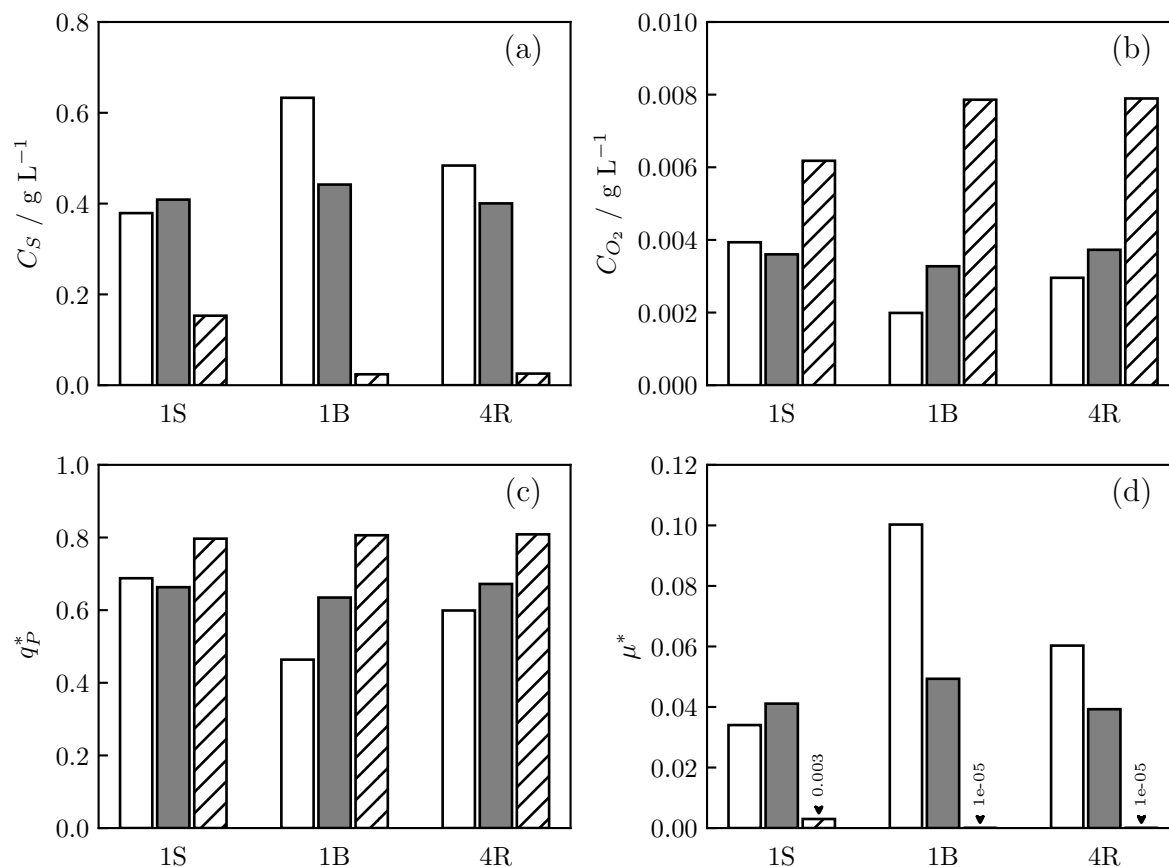


Figure 6.20: Nutrients concentration (a,b) and normalized production (c) and growth (d) rates for the case q_{feed}^{IV} . CFD and perfect-mixing values are reported in white and gray, respectively. The hatched bars represent estimated values at $k_L a = 200 \text{ h}^{-1}$.

case, as expected from the analysis of the Damköhler number. However, the average substrate concentration in the configurations 1B and 4R was higher (figure 6.20). This increase generated a greater oxygen demand in the bigger reactors, leading to a residual oxygen concentration lower than the one of the perfectly-mixed reactor (figure 6.20b).

Liquid viscosity: influence on oxygen transfer

The simulations discussed previously described a system at a cell concentration $C_X = 20 \text{ g L}^{-1}$. In section 6.2, the influence of the biomass concentration and the broth viscosity was highlighted. So, in order to analyze the effect of the system's viscosity, cases at $C_X = 30 \text{ g L}^{-1}$ were considered; data for this cell concentration were compared to the results presented in section 6.2.2 at q_{feed}^I and q_{feed}^{II} for the 4R geometry, and at the same operating conditions. However, due to the different rheology a d_{32} equal to 5 mm, in according to the correlation presented in Section 4.3.1. The concentrations distributions at the lowest feed rate are displayed in figure 6.21. The substrate concentration at $C_X = 30 \text{ g L}^{-1}$ was, on average, two times

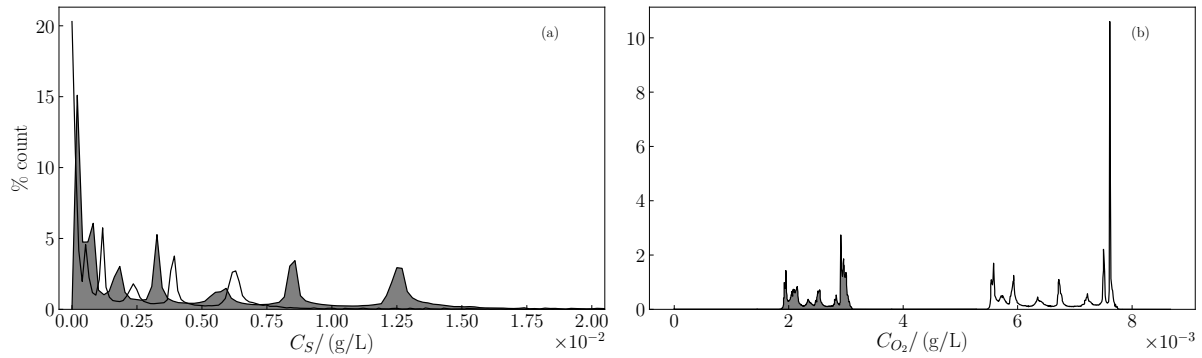


Figure 6.21: Substrate (a) and dissolved oxygen distributions (b) for the case at $C_X = 20 \text{ g L}^{-1}$ (empty area) and at $C_X = 30 \text{ g L}^{-1}$ (dark area).

higher than in the case at $C_X = 20 \text{ g L}^{-1}$. The higher viscosity caused a decrease in $k_L a$, so the dissolved oxygen content dropped around the average value of $2.55 \cdot 10^{-6} \text{ g L}^{-1}$, way lower than the one found for the system at $C_X = 20 \text{ g L}^{-1}$.

The decrease in the oxygen concentration led to a narrower distribution of q_P^* (figure 6.22); in fact, because of the lower oxygen concentration at the top of the reactor, substrate consumption in this area was slowed down; consequently, C_S in the other regions of the tank was higher. Due to the relatively low $\langle C_S \rangle$, microorganism would still be able to consume all the fed substrate, avoiding an excessive accumulation of nutrients. Nevertheless, decrease in the mass transfer capability caused a localized decrease in q_P^* , which could lead to productivity loss in the case of fermentation at higher substrate content.

In figure 6.23, the values of oxygen and substrate concentrations, and specific rates at $C_X = 30 \text{ g L}^{-1}$ are displayed. Compared to figure 6.12, no q_P^* values lower than 0.1 were established, but the area close to the injection point was characterized by $q_P^* < 0.6$, in agreement with the profile of the substrate concentration. In addition, similar profiles of the dissolved oxygen were found at both biomass concentrations; as discussed above, the oxygen content was almost three times lower in the case of the more viscous system.

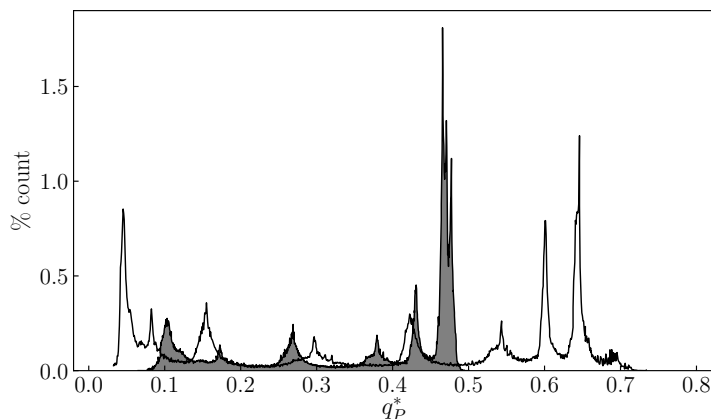


Figure 6.22: Density distribution of normalized production rate. The area in black represents the data at $C_X = 30 \text{ g L}^{-1}$, whereas data at $C_X = 20 \text{ g L}^{-1}$ are represented by the empty area.

The effect of viscosity on the substrate uptake was also studied at higher feed rate (q_{feed}^{II}). However, due to the strong decrease in the dissolved oxygen concentration, the substrate could not be consumed by the microorganisms, causing a continuous accumulation of the reactant. The simulation could not reach a steady state solution, because the equation for the biomass concentration (Eq. (6.3)) was not solved. Modeling also the dynamics of the biomass fermentation would have required the simulation of a very long physical time. Therefore, in the light of the scope of this study, it was decided to consider only the partial results without solving the equation for the microbial growth; nevertheless, it was possible to state that the limitation of oxygen was accompanied by an accumulation of substrate, coherently with experimental observations. In fact, if the oxygen content in the system became too low, cells would not be able to secrete proteins anymore, causing the substrate to accumulate. Eventually, cells growth would become the prevalent metabolic regime, leading to an unwanted situation.

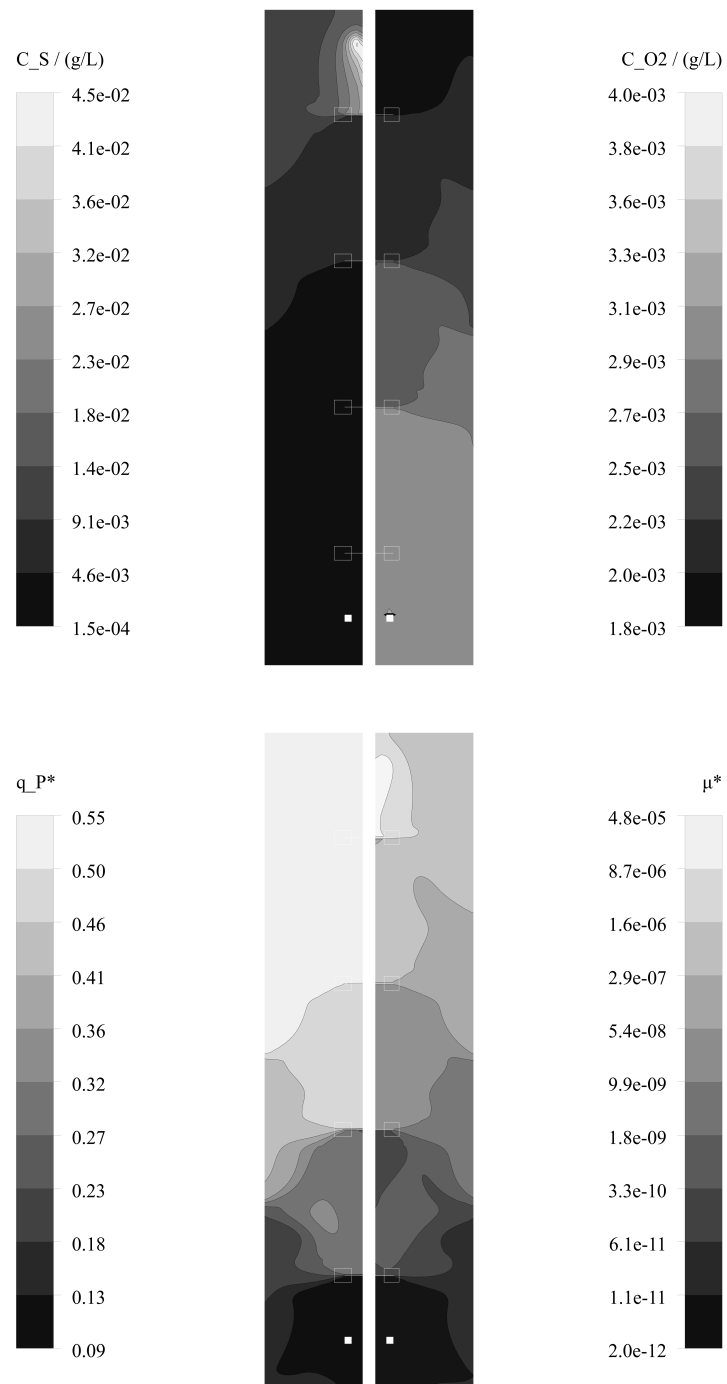


Figure 6.23: Isovalues contours of species concentrations, q_P^* , and μ^* at $C_X = 30 \text{ g L}^{-1}$.

Summary of the results

To facilitate the comparison between the different configurations and operating conditions, data presented in the previous section are collected in table 6.4. As expected, by increasing the

Table 6.4: Average concentrations and kinetic rates for the simulations discussed in the chapter.

Case	$C_X/\text{g L}^{-1}$	$\langle C_S \rangle/\text{g L}^{-1}$	$\langle C_{O_2} \rangle/\text{g L}^{-1}$	$\langle q_P^* \rangle$	$\langle \mu^* \rangle$
q_{feed}^I					
1S	20	$1.09 \cdot 10^{-3}$	$5.97 \cdot 10^{-3}$	$4.04 \cdot 10^{-1}$	$2.00 \cdot 10^{-9}$
1B	20	$1.55 \cdot 10^{-3}$	$5.90 \cdot 10^{-3}$	$4.08 \cdot 10^{-1}$	$1.63 \cdot 10^{-7}$
4R	20	$2.66 \cdot 10^{-3}$	$6.73 \cdot 10^{-3}$	$4.09 \cdot 10^{-1}$	$8.83 \cdot 10^{-8}$
4R	30	$5.38 \cdot 10^{-3}$	$2.55 \cdot 10^{-3}$	$4.06 \cdot 10^{-1}$	$4.14 \cdot 10^{-7}$
q_{feed}^{II}					
1S	20	$3.98 \cdot 10^{-3}$	$4.94 \cdot 10^{-3}$	$6.04 \cdot 10^{-1}$	$4.58 \cdot 10^{-8}$
1B	20	$5.95 \cdot 10^{-3}$	$4.02 \cdot 10^{-3}$	$6.13 \cdot 10^{-1}$	$7.16 \cdot 10^{-7}$
4R	20	$7.87 \cdot 10^{-3}$	$4.85 \cdot 10^{-3}$	$6.09 \cdot 10^{-1}$	$1.14 \cdot 10^{-6}$
4R [†]	30	> 1	$< 10^{-5}$	$\sim 10^{-7}$	$\sim 10^{-7}$
q_{feed}^{III}					
1S	20	$1.74 \cdot 10^{-2}$	$4.46 \cdot 10^{-3}$	$7.07 \cdot 10^{-1}$	$3.62 \cdot 10^{-6}$
4R	20	$6.47 \cdot 10^{-2}$	$3.89 \cdot 10^{-3}$	$7.09 \cdot 10^{-1}$	$1.84 \cdot 10^{-4}$
q_{feed}^{IV}					
1S	20	$3.79 \cdot 10^{-1}$	$3.94 \cdot 10^{-3}$	$6.88 \cdot 10^{-1}$	$5.13 \cdot 10^{-2}$
4R	20	$3.40 \cdot 10^{-2}$	$2.96 \cdot 10^{-3}$	$5.99 \cdot 10^{-1}$	$6.03 \cdot 10^{-2}$

[†] Partial results (the simulation did not converge).

feed rate, the substrate concentration in any reactor became higher. Moreover, hydrodynamics impacted the substrate distribution; due to the high mixing time, substrate gradients were found in the cases 4R, which were all characterized by a higher $\langle C_S \rangle$ compared to the simpler 1S and 1B configurations. Additionally, the multi-impeller reactor was interested by the presence of compartments between the impellers. This behavior caused the formation of gradients even at the highest feed rate, at which the reaction timescale was ten times higher than the mixing time. In that case, productivity loss was noticed in comparison to the single-Rushton reactor.

Influence of the liquid rheology and the mass transfer coefficient were highlighted by simulating two cases at $C_X = 30 \text{ g L}^{-1}$. At the lowest feed rate and under oxygen limitations, the nutrient content increased but, because of its low average concentration, cells growth conditions were not reached; therefore, the specific production rate remained relatively high. However, when the carbon-source feed rate was increased, the dissolved oxygen was all consumed causing accumulation of the substrate. In this scenario, the environmental conditions favored the microbial cell growth rather than the product formation.

6.3 Conclusions

The main focus of the chapter was the applications of the proposed CFD model to describe the mass transfer and the microbial kinetics in aerated reactors at different scales. The steady Eulerian MRF approach validated in chapter 5 proved to be accurate enough to predict the mass transfer in water and rheologically complex media. However, for the latter, some limitations of the model were highlighted. In fact, the simple drag coefficient based on the bubble terminal velocity, could not efficiently describe all the operating conditions considered in the study.

The second part of the chapter was devoted to the coupling of hydrodynamics and kinetics in the case of *Trichoderma reesei* fermentation. Specifically, enzyme production in fed-batch was modeled. Starting from simulations in which the multiphase flow field had been solved, equations for the oxygen mass transfer and the species reactions were solved at different feed rates and for three tank geometries. The scale-up influence on the substrate distribution was discussed; moreover, simulations of a four-impeller reactor highlighted the complex role of hydrodynamics on product formation. In particular, it emerged how even smaller variation of the nutrient concentrations, can have a strong impact on the extra-cellular environment.

In taking into account other studies in the literature, the novelty of this study is the implementation of the rheology in coupled simulations. The effect of the mass transfer coefficient on the substrate distribution was discussed, showing that a lower oxygen content could hinder the microorganisms substrate uptake, potentially causing a protein yield loss.

Even though, the microbial kinetic model that was used in the study was based on some rigid hypothesis, like the null cellular adaptation time, the obtained results are a strong basis tool for fermenters scale-up and design. An interesting but very complex improvement could also be to consider, microorganisms reaction to the environmental conditions, depending on their intra-cellular concentration Haringa et al. (2018); Schmalzriedt et al. (2003).

Nevertheless, the modeling approach adopted in the study could be extended to describe more complex system, providing a more sophisticated kinetic model. Finally, population balance equations could also be solved to implement the influence of a system made of cells at different conditions (Morchain et al., 2014).

General conclusions and perspectives

Biofuel technologies will play an important role in the ongoing energy transition. In particular, ethanol from ligno-cellulosic waste can reduce the consumption of fossil fuels while decreasing greenhouse gas emissions. To cut the final cost of ethanol from biomass, researchers can work on two fronts: improving the pre-treatments technologies and the optimization of the enzymes production process.

In the latter approach, one of the main challenges is constituted by the scale-up of the fermenters in order to minimize their production cost. This research study was placed within this framework; the main objectives were the experimental analysis to assess the effect of rheology on local mass transfer (bubble size, holdup, and k_L), and the numerical prediction of rheology effect on fermentation. Experiments were carried out on shear-thinning solutions to have a better understanding of the mass transfer phenomena in such systems, and Computational Fluid Dynamics was used to describe mixing, mass transfer and local reaction kinetics of in a gas-liquid reactor.

The main outcomes that were achieved are summarized in the next sections. Finally, some perspectives for future works are discussed at the end of the chapter.

Conclusions

Experimental characterization of shear-thinning liquids

One of the goals outlined in this study was the characterization of aerated shear-thinning liquids. Due to the liquid properties, the use of common measuring techniques for bubble size and liquid velocity is limited to low gas concentration. Therefore, the validation of novel methods was accomplished.

Bubble size and mass transfer coefficient

Taking into account the operating conditions of interest, bubble size was measured using the cross-correlation technique. This method, is based on a dual optical probe and allows one to estimate the average Sauter mean diameter by measuring the bubble detection probability (Gemello et al., 2018; Raimundo et al., 2016). After having validated the measuring technique, bubble size data was collected at several power draw values and gas flow rates. Experiments were carried out in water and xanthan gum solutions at different concentrations, to assess the influence of the liquid viscosity; additionally, the fermentation broth of *Trichoderma reesei* was studied.

It was seen that the average d_{32} increased with superficial gas velocity and with the apparent viscosity; the opposite effect was found for power input. Interestingly, the viscosity influence was less marked, as it had already been found in other studies on bubble columns (Esmaili et al., 2016). Moreover, the effect of surfactant proteins dissolved in the culture broth was partially reproduced by dissolving ethanol into water and polymeric model fluids. The addition of ethanol caused a decrease in the bubble size, and its effect was dampened by the liquid rheology. Moreover, measurements in filtered fermentation broth showed that ethanol can represent the effect of proteins (hydrophobins) normally present in some fermentation broths.

Together with gas holdup and $k_L a$ measurements, data on bubble size was used to estimate the liquid-side mass transfer coefficient. It was seen that the power draw had a minor effect on k_L , which was however largely influenced by the apparent viscosity. The mass transfer coefficient measured in xanthan gum solutions was two-to-three times lower than values in water, depending on the polymer concentration. In addition to that, the dissolved ethanol had negligible effect on the liquid-side mass transfer coefficient.

From the experimental study, a set of dimensional correlations for d_{32} , α_g , $k_L a$, and k_L were proposed (Section 4.3).

Liquid velocity in aerated conditions

Liquid velocity was measured thanks to a Pavlov tube. This equipment is a modified Pitot tube, which can be used for velocity acquisition at high gas fraction (Forret et al., 2006).

An attempt to measure the radial liquid velocity in water and xanthan gum solutions was made, and data so-collected was found in agreement with correlations in the literature (Rousar & Van den Akker, 1994; Venneker et al., 2010). However, the technique was not suitable for measurement at high impeller speed, because of the bias due to the vibrations induced by the rotating parts. Therefore, more sophisticated techniques should be used to characterize the local gas-liquid flow field in viscous shear-thinning liquids (e.g. Magnetic resonance velocimetry).

The velocity values obtained in this study, were nonetheless helpful for the CFD model validation.

Numerical applications to aerated fermenters

As can be seen in the recent literature, CFD has been continuously adopted to study hydrodynamics of agitated reactors and its impact on mass transfer and reaction yields (Bach et al., 2017; Haringa et al., 2017; Schmalzriedt et al., 2003).

Differently from similar studies, and thanks to the novel dataset built during the research, a comprehensive tool for the design of industrial fermenters was developed. To do so, an accurate description of the gas-liquid mixing, as well as the mass transfer had to be obtained.

By taking into account the future use of the model for simulation of reactors at large-scale, whenever possible, it was opted for the simplest configuration in terms of computation resources.

General aspects of the CFD model

The turbulent flow was solved with a two-equation RANS approach. The realizable $k - \varepsilon$ gave overall accurate results in terms of global mixing time, power draw, and liquid velocity, in both single- and multi-phase flows. Moreover, the use of periodic boundary conditions together with the MRF model, did not affect the accuracy of the model while keeping the computational cost bearable.

Simulations of gas-liquid systems were accomplished by using the Eulerian model; the interaction between the phases was described in terms of drag coefficient only. In complex liquid simulations, the simplified drag model based on the bubble terminal velocity (Scargiali et al., 2007) was both numerically stable and sufficiently precise. Nevertheless, a more robust drag law for bubbles in shear-thinning liquid should be prioritize.

An acceptable estimation of the average gas holdup, $k_L a$, and liquid velocity was obtained from the two-phases simulations. However, in some simulations, the spatial distribution of gas fraction appeared to be more heterogeneous than what has been reported in the literature (Bombač et al., 1997). This discrepancy do not prevent the use of the CFD model for scale-up studies; they rather point out that further improvements on the closure models are needed to improve simulations fidelity.

Viscosity model and mass transfer model

The complex rheology of the liquid was implemented by considering the local shear rate, which was computed in terms of turbulent dissipation rate (Pérez et al., 2006). This approach led

to an overall accurate estimation of the average and maximum shear rates, in agreement with correlations from the literature.

The satisfactorily estimation of the liquid viscosity made it possible to use the mass transfer model obtained from the experimental analysis. In taking into account the simplification of using a global model, the average volumetric mass transfer coefficient of the simulations was found close to experimental values, with an average difference of less than 20%.

Nonetheless, it is believed that an improvement in the drag law for bubble-liquid interaction in complex liquid should lead to a greater accuracy of the model.

Coupled hydrodynamic-metabolic simulations

In order to describe the environmental conditions at which microbial cells can be exposed, the metabolic behavior of *Trichoderma reesei* was coupled to hydrodynamics and mass transfer. By using a steady-state approach, it was shown the effect of the nutrient feed rate on the substrate and oxygen distribution in the liquid phase.

The presence of substrate gradients highlighted its influence on the protein uptake, showing also that the global yield is strictly related to the feed rate. In fact, when substrate is the only limiting reactant, concentration gradients has in general a positive effect on the specific production rate.

However, when a high substrate feed rate was simulated, some zones in the tank reached an excessive nutrient content, in which the cell growth rate was not negligible anymore. In this scenario, substrate would also be used by the microorganism to grow and increase the biomass concentration, but affecting the protein yield. Particularly, simulations on a multi-impeller configuration highlighted the effect of the flow field on kinetics; due to a poor axial mixing, a difference in productivity between the top and the bottom of the tank was found.

In the end, the effect of viscosity on cell metabolism was briefly discussed. Simulations of a more concentrated broth were characterized by a low mass transfer rate; in that condition, the dissolved oxygen became the limiting reactant, The simulated case showed that, in similar conditions, fermentation would experience an increase in substrate concentration. At high feed rate, accumulation of nutrient would lead to an extra-cellular environment in which microorganism growth is solely the result, with drastic consequences on the productivity of the fed-batch process.

Perspectives

Bioprocesses constitutes a very complex domain in which several aspects — from the scale-up of the reactor to the genetic modification of the cell strains — have to be considered. Therefore, only a limited number of problems could be addressed in this research study. While answering to these problems, some other questions arose.

Experimental outlook

New information on bubble size in complex liquid was provided and dimensional correlation to estimate k_L were proposed. However, in order to better characterize the liquid-side mass transfer coefficient, measurements of $k_L a$ should be carried out with a more precise method, which would be less influenced by the presence of microbubbles in the fermentation broth or when using surface active agents.

The local description of liquid mean velocity, as well as of the fluctuating velocity, needs to be covered in future experimental campaigns. To obtain precise information in dense bubbly flows, non intrusive velocimetry techniques, as positron emission particle tracking (PEPT) or computer-automated radioactive particle tracking (CARPT), could be adopted. Besides the interest on a more precise characterization of the hydrodynamics in such systems, information of the gas-liquid flow field could be used to validate new CFD model, as discussed in the next section.

CFD improvements

The rheological model here proposed is far from being descriptive of the real shear rate distribution in an agitated reactor. To increase the confidence level on simulation of complex liquid, a turbulent model (RANS or LES) for the shear rate needs to be developed (Gori & Boghi, 2012). Moreover, a rigorous study on interfacial forces models should be conducted to improve the representation of the local gas fraction at high gas holdup.

As regards the coupling of mixing and kinetics, the steady-state description provided an interesting insight about the reaction environment inside the aerated fermenter. Substrate and oxygen distributions were predicted coherently with the metabolic response of *Trichoderma Reesei*. Nonetheless, the coupled kinetic model presented certain limitations, which narrow the range of applicability of the adopted CFD model. Firstly, to quantitatively assess the influence of reactants gradients, intra-cellular dynamics have to be taken into account (Schmalzriedt et al., 2003); in fact, the solely description of the environment would be enough if cells reacted instantaneously to their surroundings, which might not be the case. Population Balance Equations

tions could be implemented to take into account the different cells response time to substrate fluctuations. In addition to that, concentration fields should also be described in terms of particle trajectories and passage frequency between rich and poor zones (Haringa et al., 2018).

Finally, data extrapolated from the CFD model could be later used to design more predictive scale-down models. By recreating in a lab-scale the expected conditions at which microorganisms are exposed, development of better kinetic models could be achieved.

Nomenclature

A_i	Surface of the i -th bubble, m^2
a	Specific interfacial area, $\text{m}^2 \text{m}^{-3}$
a_{shape}	Prefactor used in Eq. 3.3
B	Length of the baffles, m
C, C'	Coefficients used in Equation 4.6 and 4.7
c_i	Regression coefficient used in Equation 4.1
C_P	Protein concentration, kg m^{-3}
C_S	Substrate concentration, kg m^{-3}
C_X	Biomass concentration, kg m^{-3}
C_{O_2}	Dissolved oxygen concentration, kg m^{-3}
D	Impeller diameter, m
d	Inter-probe distance, μm
d_{32}	Bubble Sauter mean diameter, m
$d_{h,32}$	Horizontal Sauter mean diameter, m
$d_{v,32}$	Vertical Sauter mean diameter, m
Da	Damköhler number
\mathcal{D}_l	Oxygen diffusivity in water and model fluids, $\text{m}^2 \text{s}^{-1}$
μ^*	Normalized growth rate

E	Bubble aspect ratio, d_v/d_h
EO	Eötvös number
Fl_g	Gas flow number
Fr	Impeller Froude number
g	Gravitational acceleration constant, 9.81 m s^{-2}
H	Liquid height
H_A	Henry constant, $\text{Pa kg}^{-1} \text{ m}^{-3}$
h_D	Clearance of the turbine, m
h_S	Clearance of the gas sparger, m
J	Mass flux, $\text{kg}^2 \text{ m}^{-1} \text{ s}^{-1}$
K	Consistency index, Pa s^n
k	Turbulent kinetic energy, $\text{m}^2 \text{ s}^{-1}$
k_G	Gas-side mass transfer coefficient, m s^{-1}
K_L	Overall mass transfer coefficient, m s^{-1}
k_L	Liquid-side mass transfer coefficient, m s^{-1}
k_{La}	Volumetric mass transfer coefficient, s^{-1}
k_s	Metzner-Otto constant, Pa s^n
m	Oxygen concentration ratio
N	Impeller rotation speed, s^{-1}
n	Flow behavior index
N_F	Flooding impeller speed, s^{-1}
N_P	Impeller power number
N_R	Minimum impeller speed for fully recirculation regime, s^{-1}
P	Pressure, Pa
P_0	Power input without gas in the system, W

P_g	Power input in aerated vessel, W
q_P^*	Normalized production rate
q_{feed}	Substrate feed rate
R_g	Eulerian correlation coefficient
$\frac{P_g}{V}$	Volumetric power input, W m ⁻³
Q_g	Gas flow rate, m ³ s ⁻¹
s	Impeller disk thickness
S_A, S_B	Normalized signals carried by the sensor
T	Tank diameter, m
T_0	Reference diameter, 1 m
U_g	Superficial gas velocity m s ⁻¹
U_t	Bubble terminal velocity m s ⁻¹
V	Reactor volume, m ³
V_I	Volume swempt by the impeller, m ³
V_i	Volume of the <i>i</i> -th bubble, m ³

Greek symbols

α_g	Global gas holdup
$\dot{\gamma}_{av}$	Average shear rate, s ⁻¹
Γ	Torque, N m
μ	Viscosity, Pa s ⁻¹
μ_{app}	Apparent viscosity, Pa s ⁻¹
ν	Kinematic viscosity, m ² s ⁻¹
ρ	Density, kg m ⁻³
θ_{95}	Mixing time to reach the 95% of homogeneity, s
θ_S	Reaction timescale, s

ε Turbulent dissipation rate, m s^{-3}

Superscripts and subscripts

G, g Gas phase

h Bubble's horizontal axis

L, l Liquid phase

v Bubble's vertical axis

θ Relative to the unaerated condition

Abbreviations

CC Cross-correlation

CFD Computational fluid dynamics

CMC Carboxymethyl cellulose

DNS Direct numerical simulation

EDCF Energy dissipation circulation function

LES Large eddy simulation

MRF Multiple reference frame

OTR Oxygen transfer rate

RANS Reynolds-averaged Naviers-stokes

RPD Relative power demand

RSD Relative standard deviation

SM Sliding mesh

XG Xanthan gum

Tensors and vectors

τ Stress tensor, Pa

D Rate-of-deformation tensor, s^{-1}

g Body forces tensor, Pa m^{-1}

<i>I</i>	Identity matrix
<i>S</i>	Rate-of-strain tensor, s^{-1}
<i>u</i>	Instantaneous velocity, $m s^{-1}$

References

- Akita, K., & Yoshida, F. (1974). Bubble size, interfacial area, and liquid-phase mass transfer coefficient in bubble columns. *Industrial & Engineering Chemistry Process Design and Development*, 13(1), 84–91.
- Al-Rubeai, M., et al. (2015). *Animal cell culture*. Springer.
- Alm eras,  . (2014). * tude des propri et es de transport et de m elange dans les  coulements   bulles*. Ph.D. thesis, Toulouse, INPT.
- Alm eras, E., Plais, C., Euzenat, F., Risso, F., Roig, V., & Augier, F. (2016). Scalar mixing in bubbly flows: Experimental investigation and diffusivity modelling. *Chemical Engineering Science*, 140, 114–122.
- Alves, S. S., Maia, C. I., Vasconcelos, J., & Serralheiro, A. J. (2002). Bubble size in aerated stirred tanks. *Chemical Engineering Journal*, 89(1-3), 109–117.
- Amanullah, A., J usten, P., Davies, A., Paul, G., Nienow, A., & Thomas, C. (2000). Agitation induced mycelial fragmentation of aspergillus oryzae and penicillium chrysogenum. *Biochemical Engineering Journal*, 5(2), 109–114.
- Amer, M., Feng, Y., & Ramsey, J. D. (2019). Using CFD simulations and statistical analysis to correlate oxygen mass transfer coefficient to both geometrical parameters and operating conditions in a stirred-tank bioreactor. *Biotechnology progress*, (p. e2785).
- Ameur, H. (2016). Mixing of shear thinning fluids in cylindrical tanks: effect of the impeller blade design and operating conditions. *International Journal of Chemical Reactor Engineering*, 14(5), 1025–1033.
- Ameur, H., Kamla, Y., & Sahel, D. (2016). CFD simulations of mixing characteristics of radial impellers in cylindrical reactors. *ChemistrySelect*, 1(10), 2548–2551.
- Amirnia, S., de Bruyn, J. R., Bergougnou, M. A., & Margaritis, A. (2013). Continuous rise velocity of air bubbles in non-Newtonian biopolymer solutions. *Chemical Engineering Science*, 94, 60–68.

- Andersson, B., Andersson, R., Håkansson, L., Mortensen, M., Sudiyo, R., & van Wachem, B. (2011). *Computational Fluid Dynamics for Engineers*. Cambridge University Press.
- Andrew, S., & SPS, A. (1982). Gas-liquid mass transfer in microbiological reactors. *Transactions of the Institution of Chemical Engineers*, 60.
- ANSYS Fluent Theory Guide (2019). *ANSYS Inc, Release 2019 R2*.
- Aubin, J., Fletcher, D., & Xuereb, C. (2004). Modeling turbulent flow in stirred tanks with CFD: The influence of the modeling approach, turbulence model and numerical scheme. *Experimental Thermal and Fluid Science*, 28.
- Azadi, P., Malina, R., Barrett, S. R., & Kraft, M. (2017). The evolution of the biofuel science. *Renewable and Sustainable Energy Reviews*, 76, 1479–1484.
- Bach, C. (2018). *Modelling of Gradients in Large Scale Bioreactors*. Ph.D. thesis, Technical University of Denmark (DTU).
- Bach, C., Yang, J., Larsson, H., Stocks, S. M., Gernaey, K. V., Albaek, M. O., & Krühne, U. (2017). Evaluation of mixing and mass transfer in a stirred pilot scale bioreactor utilizing CFD. *Chemical Engineering Science*, 171, 19–26.
- Bajpai, P. (2016). Structure of lignocellulosic biomass. In *Pretreatment of lignocellulosic biomass for biofuel production*, (pp. 7–12). Springer.
- Bakker, A., & Van den Akker, H. (1994). A computational model for the gas-liquid flow in stirred reactors. *Chemical Engineering Research and Design*, 72(A4), 594–606.
- Bao, Y., Chen, L., Gao, Z., & Chen, J. (2010). Local void fraction and bubble size distributions in cold-gassed and hot-sparged stirred reactors. *Chemical Engineering Science*, 65(2), 976–984.
- Barigou, M., & Greaves, M. (1992). Bubble-size distributions in a mechanically agitated gas-liquid contactor. *Chemical Engineering Science*, 47(8), 2009–2025.
- Bhavaraju, S. M., Russell, T., & Blanch, H. (1978). The design of gas sparged devices for viscous liquid systems. *AIChE Journal*, 24(3), 454–466.
- Bhutto, A. W., Qureshi, K., Harijan, K., Abro, R., Abbas, T., Bazmi, A. A., Karim, S., & Yu, G. (2017). Insight into progress in pre-treatment of lignocellulosic biomass. *Energy*, 122, 724–745.
- Bird, R. B., Stewart, W. E., & Lightfoot, E. N. (2006). *Transport Phenomena*. Wiley International edition. Wiley.

- Bombač, A., Žun, I., Filipič, B., & Žumer, M. (1997). Gas-filled cavity structures and local void fraction distribution in aerated stirred vessel. *AIChE journal*, *43*(11), 2921–2931.
- Bouaifi, M., & Roustan, M. (1998). Bubble size and mass transfer coefficients in dual-impeller agitated reactors. *The Canadian Journal of Chemical Engineering*, *76*(3), 390–397.
- Bouaifi, M., & Roustan, M. (2001). Power consumption, mixing time and homogenisation energy in dual-impeller agitated gas–liquid reactors. *Chemical Engineering and Processing: Process Intensification*, *40*, 87–95.
- Boyer, C., Duquenne, A.-M., & Wild, G. (2002). Measuring techniques in gas–liquid and gas–liquid–solid reactors. *Chemical Engineering Science*, *57*(16), 3185 – 3215. Jean-Claude Charpentier Festschrift Issue.
- BP (2017). Bp statistical review of world energy june 2017. *BP Statistical Review, London, UK*.
- Brandt, A., Gräsvik, J., Hallett, J. P., & Welton, T. (2013). Deconstruction of lignocellulosic biomass with ionic liquids. *Green chemistry*, *15*(3), 550–583.
- Brucato, A., Grisafi, F., & Montante, G. (1998). Particle drag coefficients in turbulent fluids. *Chemical Engineering Science*, *53*(18), 3295–3314.
- Bruijn, W., Riet, K., & Smith, J. (1974). Power consumption with aerated rushton turbines. *Trans. Inst. Chem. Eng.*, *52*, 88–104.
- Bujalski, W., Nienow, A., Chatwin, S., & Cooke, M. (1987). The dependency on scale of power numbers of rushton disc turbines. *Chemical Engineering Science*, *42*(2), 317–326.
- Calderbank, P. (1958). Physical rate processes in industrial fermentations part I: The interfacial area in gas-liquid contacting with mechanical agitation. *Trans. Inst. Chem. Engrs*, *36*, 443–463.
- Calderbank, P., & Moo-Young, M. (1961). The continuous phase heat and mass-transfer properties of dispersions. *Chemical Engineering Science*, *16*(1-2), 39–54.
- Cappello, V., Plais, C., Vial, C., & Augier, F. (2020). Bubble size and liquid-side mass transfer coefficient measurements in aerated stirred tank reactors with non-Newtonian liquids. *Chemical Engineering Science*, *211*, 115280.
- Chaabane, F. B., & Marchal, R. (2013). Upgrading the hemicellulosic fraction of biomass into biofuel. *Oil & Gas Science and Technology–Revue d'IFP Energies nouvelles*, *68*(4), 663–680.

- Cheng, Y., Wei, F., & Jin, Y. (2017). *Multiphase Reactor Engineering for Clean and Low-carbon Energy Applications*. Wiley Online Library.
- Chesters, A. (1991). Modelling of coalescence processes in fluid-liquid dispersions: a review of current understanding. *Chemical engineering research and design*, 69(A4), 259–270.
- Clarke, K., & Correia, L. (2008). Oxygen transfer in hydrocarbon–aqueous dispersions and its applicability to alkane bioprocesses: a review. *Biochemical engineering journal*, 39(3), 405–429.
- Clift, R., Grace, J. R., & Weber, M. E. (2005). *Bubbles, drops, and particles*. Courier Corporation.
- Cooke, M. (1988). Mixing and mass transfer in filamentous fermentation. In *Proc. 2nd Int. Conf. on Bioreactor Fluid Dynamics, 1988*, (pp. 37–64). BHRA/Elsevier.
- Cortada-Garcia, M., Dore, V., Mazzei, L., & Angeli, P. (2017). Experimental and CFD studies of power consumption in the agitation of highly viscous shear thinning fluids. *Chemical Engineering Research and Design*, 119, 171–182.
- Cox, A. R., Aldred, D. L., & Russell, A. B. (2009). Exceptional stability of food foams using class II hydrophobin HFBII. *Food Hydrocolloids*, 23(2), 366–376.
- Cox, A. R., Cagnol, F., Russell, A. B., & Izzard, M. J. (2007). Surface properties of class II hydrophobins from *Trichoderma reesei* and influence on bubble stability. *Langmuir*, 23(15), 7995–8002.
- Dankwerts, P. (1951). Significance of liquid-film coefficients in gas absorption. *Industrial & Engineering Chemistry*, 43(6), 1460–1467.
- Deglon, D., & Meyer, C. (2006). CFD modelling of stirred tanks: Numerical considerations. *Minerals Engineering*, 19(10), 1059–1068.
- Delafosse, A., Line, A., Morchain, J., & Guiraud, P. (2008). LES and URANS simulations of hydrodynamics in mixing tank: comparison to PIV experiments. *Chemical Engineering Research and Design*, 86(12), 1322–1330.
- Devi, T. T., & Kumar, B. (2017). Mass transfer and power characteristics of stirred tank with rushton and curved blade impeller. *Engineering Science and Technology, an International Journal*, 20(2), 730–737.
- Dewsbury, K., & Karamanev, D. (2000). Dynamic behaviour of freely rising buoyant solid spheres in non-Newtonian liquids. *AIChE Journal*, 46, 46 – 51.

- Doran, P. M. (2013). Chapter 8 - mixing. In P. M. Doran (Ed.) *Bioprocess Engineering Principles (Second Edition)*, (pp. 255 – 332). Academic Press, second edition ed.
- Ein-Mozaffari, F., & Upreti, S. R. (2010). Investigation of mixing in shear thinning fluids using computational fluid dynamics. *Computational Fluid Dynamics*, (pp. 77–102).
- Elqotbi, M., Vlaev, S., Montastruc, L., & Nikov, I. (2013). CFD modelling of two-phase stirred bioreaction systems by segregated solution of the euler–euler model. *Computers & Chemical Engineering*, *48*, 113–120.
- Escudier, M., & Presti, F. (1996). Pipe flow of a thixotropic liquid. *Journal of Non-Newtonian Fluid Mechanics*, *62*(2-3), 291–306.
- Esmaeili, A., Guy, C., & Chaouki, J. (2016). Local hydrodynamic parameters of bubble column reactors operating with non-Newtonian liquids: Experiments and models development. *AIChE Journal*, *62*(4), 1382–1396.
- Etemad, S. G., Thibault, J., & Hashemabadi, S. (2003). Calculation of the pitot tube correction factor for Newtonian and non-Newtonian fluids. *ISA transactions*, *42*(4), 505–512.
- Forret, A., Schweitzer, J., Gauthier, T., Krishna, R., & Schweich, D. (2006). Scale up of slurry bubble reactors. *Oil & Gas Science and Technology-Revue de l'IFP*, *61*(3), 443–458.
- Gabelle, J.-C. (2012). *Analyse locale et globale de l'hydrodynamique et du transfert de matière dans des fluides à rhéologie complexe caractéristiques des milieux de fermentation*. Ph.D. thesis, Toulouse, INSA.
- Gabelle, J.-C., Augier, F., Carvalho, A., Rousset, R., & Morchain, J. (2011). Effect of tank size on $k_L a$ and mixing time in aerated stirred reactors with non-Newtonian fluids. *The Canadian Journal of Chemical Engineering*, *89*(5), 1139–1153.
- Gabelle, J.-C., Jourdir, E., Licht, R., Chaabane, F. B., Henaut, I., Morchain, J., & Augier, F. (2012). Impact of rheology on the mass transfer coefficient during the growth phase of *Trichoderma reesei* in stirred bioreactors. *Chemical Engineering Science*, *75*, 408–417.
- Garcia-Ochoa, F., & Gomez, E. (2009). Bioreactor scale-up and oxygen transfer rate in microbial processes: an overview. *Biotechnology Advances*, *27*(2), 153–176.
- Gemello, L. (2018). *Modelling of the hydrodynamics of bubble columns using a two-fluid model coupled with a population balance approach*. Ph.D. thesis, Politecnico di Torino.
- Gemello, L., Plais, C., Augier, F., Cloupet, A., & Marchisio, D. (2018). Hydrodynamics and bubble size in bubble columns: Effects of contaminants and spargers. *Chemical Engineering Science*, *184*, 93–102.

- Gimbun, J., Rielly, C. D., & Nagy, Z. K. (2009). Modelling of mass transfer in gas-liquid stirred tanks agitated by rushton turbine and CD-6 impeller: a scale-up study. *Chemical Engineering Research and Design*, 87(4), 437–451.
- González-Figueroa, C., Flores-Estrella, R. A., & Rojas-Rejón, O. A. (2018). Fermentation: Metabolism, kinetic models, and bioprocessing. In *Current topics in biochemical engineering*. IntechOpen.
- Gori, F., & Boghi, A. (2012). A three dimensional exact equation for the turbulent dissipation rate of generalised Newtonian fluids. *International Communications in Heat and Mass Transfer*, 39(4), 477–485.
- Gradov, D. V., Laari, A., Turunen, I., & Koironen, T. (2017). Experimentally validated CFD model for gas-liquid flow in a round-bottom stirred tank equipped with rushton turbine. *International Journal of Chemical Reactor Engineering*, 15(2).
- Grenville, R. (1992). *Blending of viscous Newtonian and pseudo-plastic fluids*. Ph.D. thesis, Cranfield University.
- Grenville, R., Giacomelli, J., Brown, D., & Padron, G. (2017). Mixing: Impeller performance in stirred tanks. *Chemical Engineering*, 124, 42.
- Grenville, R. K., & Nienow, A. W. (2004). Blending of miscible liquids. *Handbook of Industrial Mixing*, (pp. 507–539).
- Gualtieri, C., Angeloudis, A., Bombardelli, F., Jha, S., & Stoesser, T. (2017). On the values for the turbulent Schmidt number in environmental flows. *Fluids*, 2, 1–27.
- Gusakov, A. V. (2011). Alternatives to *Trichoderma reesei* in biofuel production. *Trends in biotechnology*, 29(9), 419–425.
- Hardy, N. (2016). *Identification des critères d'extrapolation du procédé de production de cellulases par *Trichoderma reesei* en utilisant l'approche "scale-down"*. Ph.D. thesis, Université Paris-Saclay.
- Hardy, N., Augier, F., Nienow, A. W., Béal, C., & Chaabane, F. B. (2017). Scale-up agitation criteria for *Trichoderma reesei* fermentation. *Chemical Engineering Science*, 172, 158–168.
- Hardy, N., Henaut, I., Augier, F., Béal, C., & Chaabane, F. B. (2015). Rhéologie des champignons filamenteux: un outil pour la compréhension d'un procédé de production de biocatalyseurs utilisés pour la production de bioéthanol. *Rhéologie*, 27, 43–48.

- Haringa, C., Deshmukh, A. T., Mudde, R. F., & Noorman, H. J. (2017). Euler-Lagrange analysis towards representative down-scaling of a 22 m³ aerobic *S. cerevisiae* fermentation. *Chemical Engineering Science*, *170*, 653–669.
- Haringa, C., Tang, W., Deshmukh, A. T., Xia, J., Reuss, M., Heijnen, J. J., Mudde, R. F., & Noorman, H. J. (2016). Euler-Lagrange computational fluid dynamics for (bio) reactor scale down: an analysis of organism lifelines. *Engineering in life sciences*, *16*(7), 652–663.
- Haringa, C., Tang, W., Wang, G., Deshmukh, A. T., van Winden, W. A., Chu, J., van Gulik, W. M., Heijnen, J. J., Mudde, R. F., & Noorman, H. J. (2018). Computational fluid dynamics simulation of an industrial *P. chrysogenum* fermentation with a coupled 9-pool metabolic model: Towards rational scale-down and design optimization. *Chemical Engineering Science*, *175*, 12–24.
- Hasan, B. O. (2017). Breakage of drops and bubbles in a stirred tank: A review of experimental studies. *Chinese journal of chemical engineering*, *25*(6), 698–711.
- Hinze, J. O. (1955). Fundamentals of the hydrodynamic mechanism of splitting in dispersion processes. *AIChE Journal*, *1*(3), 289–295.
- Ho, C. S., Ju, L.-K., & Baddour, R. F. (1988). The anomaly of oxygen diffusion in aqueous xanthan solutions. *Biotechnology and Bioengineering*, *32*(1), 8–17.
- Huang, W., & Li, K. (2013). CFD simulation of flows in stirred tank reactors through prediction of momentum source. *Nuclear Reactor Thermal Hydraulics and Other Applications*, (pp. 135–153).
- IEA (2014). World energy outlook 2014. *International Energy Agency: Paris, France*.
- IEA (2017). Tracking clean energy progress. *International Energy Agency: Paris, France*.
- Johnson, E. (2016). Integrated enzyme production lowers the cost of cellulosic ethanol. *Biofuels, Bioproducts and Biorefining*, *10*(2), 164–174.
- Joshi, G., Pandey, J. K., Rana, S., & Rawat, D. S. (2017). Challenges and opportunities for the application of biofuel. *Renewable and Sustainable Energy Reviews*, *79*, 850–866.
- Jourdier, E. (2012). *Modélisation et optimisation de la production de cellulases par Trichoderma reesei pour les bioraffineries lignocellulosiques*. Ph.D. thesis, Clermont-Ferrand 2.
- Kawase, Y., Halard, B., & Moo-Young, M. (1987). Theoretical prediction of volumetric mass transfer coefficients in bubble columns for Newtonian and non-Newtonian fluids. *Chemical Engineering Science*, *42*(7), 1609–1617.

- Kawase, Y., Halard, B., & Moo-Young, M. (1992). Liquid-phase mass transfer coefficients in bioreactors. *Biotechnology and Bioengineering*, *39*(11), 1133–1140.
- Kazemzadeh, A., Ein-Mozaffari, F., Lohi, A., & Pakzad, L. (2016). A new perspective in the evaluation of the mixing of biopolymer solutions with different coaxial mixers comprising of two dispersing impellers and a wall scraping anchor. *Chemical Engineering Research and Design*, *114*, 202–219.
- Keating, M. (2011). Accelerating CFD solutions. *ANSYS Advantage*, *V*, 48–49.
- Khapre, A., & Munshi, B. (2014). Numerical comparison of rushton turbine and CD-6 impeller in non-Newtonian fluid stirred tank. *International Scholarly Scientific Research Innovation*, *8*(11), 1260–1267.
- Khapre, A., & Munshi, B. (2015). Numerical investigation of hydrodynamic behavior of shear-thinning fluids in stirred tank. *Journal of the Taiwan Institute of Chemical Engineers*, *56*, 16–27.
- Kolev, N. I. (2005). *Multiphase flow dynamics*, vol. 1. Springer.
- Laakkonen, M., Moilanen, P., Alopaeus, V., & Aittamaa, J. (2007). Modelling local bubble size distributions in agitated vessels. *Chemical Engineering Science*, *62*(3), 721–740.
- Labík, L., Moucha, T., Petříček, R., Rejl, J., Valenz, L., & Haidl, J. (2017). Volumetric mass transfer coefficient in viscous liquid in mechanically agitated fermenters. Measurement and correlation. *Chemical Engineering Science*, *170*, 451–463.
- Lamont, J. C., & Scott, D. (1970). An eddy cell model of mass transfer into the surface of a turbulent liquid. *AIChE Journal*, *16*(4), 513–519.
- Lane, G., Schwarz, M., & Evans, G. M. (2005). Numerical modelling of gas–liquid flow in stirred tanks. *Chemical Engineering Science*, *60*(8-9), 2203–2214.
- Lane, G. L. (2017). Improving the accuracy of CFD predictions of turbulence in a tank stirred by a hydrofoil impeller. *Chemical Engineering Science*, *169*, 188–211.
- Lapin, A., Müller, D., & Reuss, M. (2004). Dynamic behavior of microbial populations in stirred bioreactors simulated with Euler-Lagrange methods: Traveling along the lifelines of single cells. *Industrial & Engineering chemistry research*, *43*(16), 4647–4656.
- Lapin, A., Schmid, J., & Reuss, M. (2006). Modeling the dynamics of *E. coli* populations in the three-dimensional turbulent field of a stirred-tank bioreactor—a structured–segregated approach. *Chemical Engineering Science*, *61*(14), 4783–4797.

- Lauder, B., & Spalding, D. (1974). The numerical computation of turbulent flows. *Computer Methods in Applied Mechanics and Engineering*, 3(2), 269 – 289.
- Li, Y., Liu, C., Bai, F., & Zhao, X. (2016). Overproduction of cellulase by *Trichoderma reesei* rut c30 through batch-feeding of synthesized low-cost sugar mixture. *Bioresource technology*, 216, 503–510.
- Liangchao, L., Ning, C., Kefeng, X., & Beiping, X. (2018). A comparative CFD study on gas-liquid dispersion in a stirred tank with low and high gas loadings. *International Journal of Chemical Reactor Engineering*, 16(8).
- Linek, V., Kordač, M., Fugasová, M., & Moucha, T. (2004). Gas-liquid mass transfer coefficient in stirred tanks interpreted through models of idealized eddy structure of turbulence in the bubble vicinity. *Chemical Engineering and Processing: Process Intensification*, 43(12), 1511–1517.
- Linek, V., Kordač, M., & Moucha, T. (2005). Mechanism of mass transfer from bubbles in dispersions: part II: mass transfer coefficients in stirred gas-liquid reactor and bubble column. *Chemical Engineering and Processing: Process Intensification*, 44(1), 121–130.
- Lynd, L. R., Liang, X., Bidy, M. J., Allee, A., Cai, H., Foust, T., Himmel, M. E., Laser, M. S., Wang, M., & Wyman, C. E. (2017). Cellulosic ethanol: status and innovation. *Current opinion in biotechnology*, 45, 202–211.
- Machon, V., Pacek, A., & Nienow, A. (1997). Bubble sizes in electrolyte and alcohol solutions in a turbulent stirred vessel. *Chemical Engineering Research and Design*, 75(3), 339–348.
- Margaritis, A., te Bokkel, D. W., & Karamanev, D. G. (1999). Bubble rise velocities and drag coefficients in non-Newtonian polysaccharide solutions. *Biotechnology and bioengineering*, 64(3), 257–266.
- Mendelson, H. D. (1967). The prediction of bubble terminal velocities from wave theory. *AIChE Journal*, 13(2), 250–253.
- Metzner, A. B., & Otto, R. E. (1957). Agitation of non-Newtonian fluids. *AIChE Journal*, 3(1), 3–10.
- Michel, B. J., & Miller, S. A. (1962). Power requirements of gas-liquid agitated systems. *AIChE Journal*, 8(2), 262–266.
- Middleton, J. (1979). Measurement of circulation within large mixing vessels. In *Proc 3rd Euro Conf on Mixing, BHRG, Cranfield*, (pp. 15–36).

- Mohd Sauid, S., Krishnan, J., Huey Ling, T., & Veluri, M. V. (2013). Enhancement of oxygen mass transfer and gas holdup using palm oil in stirred tank bioreactors with xanthan solutions as simulated viscous fermentation broths. *BioMed research international*, 2013.
- Moilanen, P., Laakkonen, M., & Aittamaa, J. (2006). Modeling aerated fermenters with computational fluid dynamics. *Industrial & engineering chemistry research*, 45(25), 8656–8663.
- Momiroski, V., Bhattacharya, S., Davoody, M., Abdul Raman, A. A. B., & Parthasarathy, R. (2018). Size distribution of bubbles in agitated viscous Newtonian and non-Newtonian solutions. *Asia-Pacific Journal of Chemical Engineering*, 13(6), e2267.
- Montante, G., Horn, D., & Paglianti, A. (2008). Gas–liquid flow and bubble size distribution in stirred tanks. *Chemical Engineering Science*, 63(8), 2107–2118.
- Montante, G., Laurenzi, F., Paglianti, A., & Magelli, F. (2010). Two-phase flow and bubble size distribution in air-sparged and surface-aerated vessels stirred by a dual impeller. *Industrial & Engineering Chemistry Research*, 49(6), 2613–2623.
- Montante, G., Moštěk, M., Jahoda, M., & Magelli, F. (2005). CFD simulations and experimental validation of homogenisation curves and mixing time in stirred Newtonian and pseudoplastic liquids. *Chemical Engineering Science*, 60(8-9), 2427–2437.
- Montante, G., & Paglianti, A. (2015). Gas hold-up distribution and mixing time in gas-liquid stirred tanks. *Chemical Engineering Journal*, 279, 648 – 658.
- Montante, G., Paglianti, A., & Magelli, F. (2007). Experimental analysis and computational modelling of gas–liquid stirred vessels. *Chemical Engineering Research and Design*, 85(5), 647–653.
- Morchain, J. (2000). *Etude et modélisation des couplages entre cinétiques physiques et biologiques dans les réacteurs de grand volume*. Ph.D. thesis, Toulouse, INSA.
- Morchain, J., Gabelle, J.-C., & Cockx, A. (2014). A coupled population balance model and CFD approach for the simulation of mixing issues in lab-scale and industrial bioreactors. *AIChE Journal*, 60(1), 27–40.
- Moucha, T., Rejl, F., Kordač, M., & Labík, L. (2012). Mass transfer characteristics of multiple-impeller fermenters for their design and scale-up. *Biochemical engineering journal*, 69, 17–27.
- Nauha, E. K., Kálal, Z., Ali, J. M., & Alopaeus, V. (2018). Compartmental modeling of large stirred tank bioreactors with high gas volume fractions. *Chemical Engineering Journal*, 334, 2319–2334.

- Nienow, A. (1998). Hydrodynamics of stirred bioreactors. *Applied Mechanics Reviews*, 51(1), 3–32.
- Oosterhuis, N. M. G., Kossen, N. W. F., Olivier, A. P. C., & Schenk, E. S. (1985). Scale-down and optimization studies of the gluconic acid fermentation by *gluconobacter oxydans*. *Biotechnology and Bioengineering*, 27(5), 711–720.
- Pakzad, L., Ein-Mozaffari, F., & Chan, P. (2008). Using computational fluid dynamics modeling to study the mixing of pseudoplastic fluids with a scaba 6SRGT impeller. *Chemical Engineering and Processing: Process Intensification*, 47(12), 2218–2227.
- Paul, E. L., Atiemo-Obeng, V. A., & Kresta, S. M. (2004). *Handbook of industrial mixing: science and practice*. John Wiley & Sons.
- Paul, G. C., & Thomas, C. R. (1998). Characterisation of mycelial morphology using image analysis. In *Relation Between Morphology and Process Performances*, (pp. 1–59). Springer.
- Petitti, M., Marchisio, D. L., Vanni, M., Baldi, G., Mancini, N., & Podenzani, F. (2009). Effect of drag modeling on the prediction of critical regime transitions in agitated gas-liquid reactors with bubble size distribution modeling. *Multiphase Science and Technology*, 21(1-2).
- Pinelli, D., Liu, Z., & Magelli, F. (2010). Analysis of $k_L a$ measurement methods in stirred vessels: the role of experimental techniques and fluid dynamic models. *International Journal of Chemical Reactor Engineering*, 8(1).
- Pinho, H., Mateus, D., & Alves, S. (2018). Probability density functions for bubble size distribution in air–water systems in stirred tanks. *Chemical Engineering Communications*, 205, 1–14.
- Prasher, B. D., & Wills, G. B. (1973). Mass transfer in an agitated vessel. *Industrial & Engineering Chemistry Process Design and Development*, 12(3), 351–354.
- Pérez, J. A. S., Porcel, E. M. R., López, J. L. C., Sevilla, J. M. F., & Chisti, Y. (2006). Shear rate in stirred tank and bubble column bioreactors. *Chemical Engineering Journal*, 124(1), 1 – 5.
- Raimundo, P. M. (2015). *Analyse et modélisation de l'hydrodynamique locale dans les colonnes à bulles*. Ph.D. thesis, Université Grenoble Alpes Grenoble Alpes.
- Raimundo, P. M., Cartellier, A., Beneventi, D., Forret, A., & Augier, F. (2016). A new technique for in-situ measurements of bubble characteristics in bubble columns operated in the heterogeneous regime. *Chemical Engineering Science*, 155, 504–523.

- Ranade, V. V. (2001). *Computational flow modeling for chemical reactor engineering*, vol. 5. Elsevier.
- Rousar, I., & Van den Akker, H. (1994). LDA measurements of liquid velocities in sparged agitated tanks with single and multiple rushton turbines. *Institution of Chemical Engineers Symposium Series, 136*, 89–96.
- Rueger, P. E., & Calabrese, R. V. (2013). Dispersion of water into oil in a rotor–stator mixer. Part 1: Drop breakup in dilute systems. *Chemical Engineering Research and Design, 91*(11), 2122–2133.
- Sardeshpande, M. V., Gupta, S., & Ranade, V. V. (2017). Electrical resistance tomography for gas holdup in a gas-liquid stirred tank reactor. *Chemical Engineering Science, 170*, 476 – 490. 13th International Conference on Gas-Liquid and Gas-Liquid-Solid Reactor Engineering.
- Scargiali, F., D’Orazio, A., Grisafi, F., & Brucato, A. (2007). Modelling and simulation of gas–liquid hydrodynamics in mechanically stirred tanks. *Chemical Engineering Research and Design, 85*, 637–646.
- Schlüter, V., & Deckwer, W.-D. (1992). Gas-liquid mass transfer in stirred vessels. *Chemical engineering science, 47*(9-11), 2357–2362.
- Schmalzriedt, S., Jenne, M., Mauch, K., & Reuss, M. (2003). Integration of physiology and fluid dynamics. In *Process Integration in Biochemical Engineering*, (pp. 19–68). Springer.
- Senouci-Bereksi, M., Kies, F. K., & Bentahar, F. (2018). Hydrodynamics and bubble size distribution in a stirred reactor. *Arabian Journal for Science and Engineering, 43*(11), 5905–5917.
- Shi, P., & Rzehak, R. (2018). Bubbly flow in stirred tanks: Euler-Euler/RANS modeling. *Chemical Engineering Science, 190*, 419–435.
- Sims, R. E., Mabee, W., Saddler, J. N., & Taylor, M. (2010). An overview of second generation biofuel technologies. *Bioresource technology, 101*(6), 1570–1580.
- Singh, H., Fletcher, D. F., & Nijdam, J. J. (2011). An assessment of different turbulence models for predicting flow in a baffled tank stirred with a rushton turbine. *Chemical Engineering Science, 66*(23), 5976–5988.
- Smith, J., Lilly, M., & Fox, R. (1990). The effect of agitation on the morphology and penicillin production of *Penicillium chrysogenum*. *Biotechnology and bioengineering, 35*(10), 1011–1023.

- Smith, K., Merrill, E., Mickley, H., & Virk, P. (1967). Anomalous Pitot tube and hot film measurements in dilute polymer solutions. *Chemical Engineering Science*, *22*(4), 619–626.
- Sossa-Echeverria, J., & Taghipour, F. (2015). Computational simulation of mixing flow of shear thinning non-Newtonian fluids with various impellers in a stirred tank. *Chemical Engineering and Processing: Process Intensification*, *93*, 66–78.
- Sungkorn, R., Derksen, J., & Khinast, J. (2012). Modeling of aerated stirred tanks with shear-thinning power law liquids. *International Journal of Heat and Fluid Flow*, *36*, 153–166.
- Tchuenbou-Magaia, F., Norton, I., & Cox, P. (2009). Hydrophobins stabilised air-filled emulsions for the food industry. *Food Hydrocolloids*, *23*(7), 1877–1885.
- Trad, Z., Fontaine, J.-P., Larroche, C., & Vial, C. (2017). Experimental and numerical investigation of hydrodynamics and mixing in a dual-impeller mechanically-stirred digester. *Chemical Engineering Journal*, *329*, 142–155.
- Tzounakos, A., Karamanev, D. G., Margaritis, A., & Bergougnou, M. A. (2004). Effect of the surfactant concentration on the rise of gas bubbles in power-law non-Newtonian liquids. *Industrial & engineering chemistry research*, *43*(18), 5790–5795.
- Van't Riet, K. (1979). Review of measuring methods and results in nonviscous gas-liquid mass transfer in stirred vessels. *Industrial & Engineering Chemistry Process Design and Development*, *18*(3), 357–364.
- Vazquez, G., Alvarez, E., & Navaza, J. M. (1995). Surface tension of alcohol water + water from 20 to 50 °C. *Journal of Chemical and Engineering Data*, *40*(3), 611–614.
- Venneker, B. C., Derksen, J. J., & Van den Akker, H. E. (2010). Turbulent flow of shear-thinning liquids in stirred tanks—the effects of reynolds number and flow index. *Chemical Engineering Research and Design*, *88*(7), 827–843.
- Venneker, B. C. H. (1999). *Turbulent flow and gas dispersion in stirred vessels with pseudoplastic liquids..* Ph.D. thesis, Technische Universiteit Delft, Netherlands.
- Virk, P. S. (1975). Drag reduction fundamentals. *AIChE Journal*, *21*(4), 625–656.
- Wang, H., Jia, X., Wang, X., Zhou, Z., Wen, J., & Zhang, J. (2014). CFD modeling of hydrodynamic characteristics of a gas-liquid two-phase stirred tank. *Applied Mathematical Modelling*, *38*(1), 63–92.
- Wellek, R., Agrawal, A., & Skelland, A. (1966). Shape of liquid drops moving in liquid media. *AIChE Journal*, *12*(5), 854–862.

- Wichterle, K. (1981). Threshold of mixing of non-Newtonian liquids. *Int. Chem. Eng.*, *21*, 116–120.
- Wichterle, K., Kadlec, M., ŽÁK, L., & Mitschka, P. (1984). Shear rates on turbine impeller blades. *Chemical Engineering Communications*, *26*(1-3), 25–32.
- Yang, F., Zhou, S., & An, X. (2015). Gas–liquid hydrodynamics in a vessel stirred by dual dislocated-blade rushton impellers. *Chinese Journal of Chemical Engineering*, *23*(11), 1746–1754.
- Zadghaffari, R., & Moghaddas, J. S. (2010). Evaluation of drag force effect on hold-up in a gas–liquid stirred tank reactor. *Journal of chemical engineering of Japan*, *43*(10), 833–840.
- Zhang, C., Gu, J., Qin, H., Xu, Q., Li, W., Jia, X., & Zhang, J. (2017). CFD analysis of flow pattern and power consumption for viscous fluids in in-line high shear mixers. *Chemical Engineering Research and Design*, *117*, 190–204.
- Zhang, Z., & Thomas, C. R. (1995). Eddy number distribution in isotropic turbulence and its application for estimating mass transfer coefficients. *Chemical Engineering Communications*, *140*(1), 207–217.

List of publications

Full papers

Cappello, V., Plais, C., Vial, C., Augier, F. (submitted). Scale-up of aerated bioreactors: CFD validation and application to the enzyme production by *Trichoderma reesei*. *Chemical Engineering Science*.

Cappello, V., Plais, C., Vial, C., Augier, F. (2020). Bubble size and liquid-side mass transfer coefficient measurements in aerated stirred tank reactors with non-newtonian liquids. *Chemical Engineering Science*, 211, 115280.

Gemello, L., Cappello, V., Augier, F., Marchisio, D., Plais, C. (2018). CFD-based scale-up of hydrodynamics and mixing in bubble columns. *Chemical Engineering Research and Design*, 136, 846–858.

Conference papers

Cappello, V., Augier, F., Plais, C., Vial, C. (2018). Experimental characterization of the gas distribution in non-Newtonian fluid: bubble size measurement in aerated stirred tanks. 16th European Conference on Mixing.

Cappello, V., Augier, F., Plais, C., Vial, C. (2019). CFD simulations of aerated non-Newtonian fermentations: a focus on mixing and mass transfer performance. 14th International Conference on Gas-Liquid and Gas-Liquid-Solid Reactor Engineering.

Acknowledgments

According to Sicilian writer Luigi Pirandello, every man in Sicily is born an "island inside an island". In the "immense sea" that was this PhD research, I was very lucky to find a lot of great people that contributed not only to accomplishing this challenging study but also to making me feel like less of an island.

The first series of thanks goes to my supervisors: Cécile, Frédéric, and Christophe. Cécile, thank you for your constant encouragement during the toughest moments of the thesis. Working on a research project that comprises both experimental and numerical studies can be quite challenging — as you often reminded me — especially when difficulties arise on both fronts. I am grateful that I could count on your experience and support throughout the project. Then comes my other supervisor at IFPEN: Fred, it was a pleasure working with and learning from you. Thank you for trusting me to start such a complex project and for your patience with my French level! Every meeting with Cécile and you always helped me to look at problems from a different perspective. In fact, apart from elements of chemical engineering and fluid mechanics, from you I learned how to feel proud of hard-achieved results and that was all thanks to your supervision. *Merci beaucoup!* Finally, thank you Christophe for your warm welcome every time I visited Clermont-Ferrand; the level of this research surely benefited from your suggestions and expertise in reactor numerical simulation.

Furthermore, I want to express my gratitude to the technicians of the lab Lapis-Lazuli at IFPEN. Charly, Pierre, Vanessa, Robert, Mikael, Medhi, and Stephan, thank you for the priceless aid in the lab and the welcoming spirit you all have showed me.

Next on the list come the interns, who helped lighten the load of both experimental and numerical work. Bastien, Dimitri, Yanis, your passion and independence in the laboratory was remarkable. Enrico, thank you for your precious help in screening between the different numerical approaches and models. I definitely chose the wrong moment during the thesis to tear my ligament, but your diligence and willingness to learn were crucial to obtaining the first valuable results during the CFD study.

Outside the sphere of the project, I want to thank the engineers of the IFPEN Chemical

Engineering department (& Lionel!) with whom I had the chance to talk. Thank you all for contributing to a vibrant work environment and for all the tips on Fluent and CFD.

This paragraph is dedicated to my other traveling companions: Ana Rita, Damien, Hanane, Gabriel, Giulia, Luca, Marco, Olivier, Phoung, Stephan, Venkat, Vittorio, and Ziad. I value every single (bad) coffee and chat I had the chance to have with every one of you. Thank you all for the time shared at IPFEN and around Lyon.

Finally, a huge thanks goes to my family, my fiancée Morgan, and friends, who have provided a limitless source of support during my four years in France.